SULFIDE BASED NANOMATERIALS SYNTHESIS FOR USE AS CATALYST OF ELECTROCHEMICAL AND PHOTOCHEMICAL REDOX REACTIONS IN RELATION TO ENERGY AND ENVIRONMENTAL APPLICATIONS

Thesis submitted to the

Jadavpur University

For award of the degree

of

Doctor of Philosophy (Science)

by

Anupam Chowdhury

PHYSICAL CHEMISTRY SECTION

DEPARTMENT OF CHEMISTRY

JADAVPUR UNIVERSITY

KOLKATA 700032, INDIA

AUGUST 2024

PHYSICAL CHEMISTRY SECTION
DEPARTMENT OF CHEMISTRY
JADAVPUR UNIVERSITY
KOLKATA 700032, INDIA

AMBIKESH MAHAPATRA
Email: ambikeshju@gmail.com &
ambikesh.mahapatra@jadavpuruniversity.in
Tel: 033-2457 2770 (Office), 033-2432 4586 (Residence)
Mobile: +91 9433468795 & 9051030776
Fax: +91 33 2414 6333

Index No.: 157/22/Chem./28

Date: 28|08|2024

CERTIFICATE FROM THE SUPERVISOR

This is to certify that the thesis entitled **"Sulfide Based Nanomaterials Synthesis For Use As Catalyst Of Electrochemical And Photochemical Redox Reactions In Relation To Energy And Environmental Applications"** submitted by Sri Anupam Chowdhury, who got his registered on 13th June 2022 for the award of Ph.D. (Science) degree of Jadavpur University, is absolutely based upon his own work under the supervision of Prof. Ambikesh Mahapatra and that neither this thesis nor any part of it has been submitted for either any degree/diploma or any other academic award anywhere before.

A. Mahapatra

.....

(Signature of the Supervisor, date with official seal)

Ambikesh Mahapatra
Professor of Chemistry
Jadavpur University
Kolkata-700032

Index No.: 157/22/Chem./28

DECLARATION OF THE SCHOLAR

I, hereby declare that the research work assimilated in the present thesis has been carried out by me in the Physical Chemistry Laboratory, Department of Chemistry, Jadavpur university under the supervision of Prof. Swapan Kumar Bhattacharya (Retired) & Prof. Ambikesh Mahapatra, Physical Chemistry Section, Department of Chemistry, Jadavpur university, Kolkata 700032. Neither this thesis nor any part of it has been submitted for either any degree/diploma or any other academic award anywhere before.

Anupam Chowdhury 28.8.2024

(Signature of the Scholar with date)


Dedicated
To
All My Guru's

ACKNOWLEDGEMENT

I am lucky and fortunate to have Prof. Swapan Kumar Bhattacharya (Retired), Physical Chemistry Section, Department of Chemistry, Jadavpur University, Kolkata-700032 as a supervisor, teacher and motivator in my path of research journey where he has held my hands and walking till today and promised me continue to walk with me in my research endeavor. Research is a continuous process where human mind is always fighting with their ego and came up a with a long-lasting idea for betterment of living beings and also uplift them from normal being to human being till the day when they are actually realized their real purpose of struggle in this beautiful earth and saw unity and bring uniformity in every creature of time being. I would like to express my heartfelt gratitude to him for his unconditional support and guidance throughout my research endeavor. I am also fortunate to have respected, dynamic and a well-known educationist Prof. Ambikesh Mahapatra as my current supervisor who whole heartedly supported in every step and encouraged me to work with fullest devotion. I also pay my respect and gratitude to him for his unconditional support and guidance.

I am also lucky in being a family member of prestigious Department of Chemistry, Jadavpur University and grateful to the department for giving me an opportunity to carry out my research to providing necessary instrumental, infrastructural facilities. I would like to thank Dean of Science and head of the Chemistry Department for assisting me with library, laboratory and other facilities during my research work. I would also like to thank all the staff members of this department, especially physical chemistry section whom have made all my research works easier by their assistance.

I would like to express my gratitude to all the physical chemistry sectional heads from the first day in my research lab, currently Prof. Arup Gayen and Prof. Pradip Kumar Mahapatra, Prof. Sujit Kumar Ghosh, Prof. Chittaranjan Sinha, Prof. Sourav Das, Prof. Sachindranath Das (subject expert), Prof. Sanjoy Kumar (Department of Physics) and also all the respected faculty members of Physical Chemistry section, for their constant encouragement and providing instrumental facilities also.

I would also like to express my gratitude our collaborator Prof. Subrata Kundu (CECRI), co-author Aditi Dey for their support during my experimental and instrumental studies.

I would also like to express my gratitude to Dr. Kallol Mukherjee (Sir), Dr. Dulal Bhattacharya (Sir), Dr. Subhabrata Banerjee (Sir), Dr. Dipanwita Majumdar (Madam), Dr. Rajyasri Neogi (Principal Madam), Dr. Dasarath Mal and Dr. Debopam Sinha for their constant encouragement and support through my journey.

I would also like to thank Dr. Kamal Kanti Bera, Dr. Malay Chakraborty, Moisilee, Nirmal Sir, Pradip dada, Bappa dada, Mousumi, Mithun dada, Souvik, Mizanur, Stuti, Banali, Madhu, Taposhi and other my dear Scholar-friends of Chemistry Department for their valuable suggestions and constant support during my PhD journey.

I would like to express my sincere gratitude to my parents, sister and my family members (including my pets) for their constant inspiration, support and blessings.

Last but not the least, grateful to Ramakrishna Vivekananda literature, which has great significance to awakening my thinking mind. It's helped me immensely during my research works and pay my humble pranam to lotus feet of Thakur, Maa, Swamiji for their blessings and teaching to inspire me to think for welfare of entire living beings on the earth.

Physical Chemistry Section,
Department of Chemistry,
Jadavpur University, Kol-700032, India

.....
Anupam Chowdhury

List of Abbreviations

Abbreviations	Descriptions
ABS	**$AgBi_3S_5$(Silver bismuth sulfide)**
BS	**Bi_2S_3 (bismuth sulfide)**
AS	**Ag_2S (Silver sulfide)**
CBS	**$CuBiS_2$ (Copper bismuth sulfide)**
XRD	**X-ray Diffraction**
FESEM	**Field Emission Scanning Electron Microscopy**
SEM	**Scanning Electron Microscopy**
BET	**Brunauer-Emmett-Teller**
XPS	**X-ray photon electron spectroscopy**
Uv-vis	**Ultraviolet-visible spectroscopy**
PL	**Photoluminescence spectroscopy**
CV	**Cyclic Voltammetry**
CA	**Chronoamperometry**
EIS	**Electrochemical Impedance Spectroscopy**
SAED	**Selected area electron diffraction**
TEM	**Transmission Electron Microscopy**
HRTEM	**High resolution Transmission Electron Microscopy**
HER	**Hydrogen evolution reaction**
OER	**Oxygen evolution reaction**
ECSA	**Electrochemical surface area**
Cdl	**Double-layer capacitance**
GC-MS	**Gas chromatography-mass spectroscopy**
AD	**Acceleration degradation**

Abstract

Index No.: 157/22/Chem./28

Title: "SULFIDE BASED NANOMATERIALS SYNTHESIS FOR USE AS CATALYST OF ELECTROCHEMICAL AND PHOTOCHEMICAL REDOX REACTIONS IN RELATION TO ENERGY AND ENVIRONMENTAL APPLICATIONS"

Submitted by: **Anupam Chowdhury**

Energy and environment are two principal issues of the contemporary world for sustainable development. Energy is a prime entity to create acceleration in beings or objects, though the form of energy is different for various purposes. If the easily available resource of energy does not have any adverse effects on the environment, then it can play a pivotal role in bringing perfect equilibrium between energy resources and respective energy creation. The recent rise of carbon emission from limited fossil fuel resources causes environmental pollution as a result of carbon dioxide emission in the environment, which is also one of the key reasons to bring natural calamity and global warming. To counter such threats and for the sake of sustainable development, people are shifting towards renewable energy resources, which brings a sense of joy to the natural face of Mother Earth. Having characteristic features like high energy content, feasibility, storage capabilities, etc., water splitting for hydrogen generation, electrochemical fuel cells serve vital role where methanol plays a significant task to generate green, clean and sustainable energy. Electrochemical methanol oxidation overcomes some outbreaks towards direct methanol fuel cell applications due to some of special quality like less pollution, less harming, high energy density and even effective in functioning at low temperature. Direct methanol fuel cells create tremendous potentiality in the electronic field especially portable electrical device, power supplier in the automobile sectors and may play a crucial role to replace conventional use of batteries in these sectors. Electrochemical oxidation method has a significant contribution towards above-described applications which make huge differences to bring technological revolution in the coming days and this method also has environmental contribution towards waste water treatment and remove toxic component from it and also produce formate like valuable chemicals from this method. On the other hand, Water is one of the most precious, essential and subtle molecules on earth, which requires top most priority for attention and purity to maintain an equilibrium ecosystem for sustainable future. It plays like a bridge by which all beings, objects complete their life cycle path from start to end. So, development of water management and related ecosystem are much more important than that found in the present scenario to explore its highest utilization for the sake of existence of both inanimate and life.

In the context of proper conversion, storage and utilization of energy, a facile fast synthetic route is designed in our study to prepare a versatile nano electrocatalyst, $AgBi_3S_5$ (ABS) for the generation of green fuel, H_2 via water electrolysis. XRD pattern confirms the major formation of monoclinic phase $AgBi_3S_5$(ABS) along with binary phase Ag_2S (AS) and Bi_2S_3 (BS). Another variant $CuBiS_2$(CBS) nanoparticle is synthesized to compare the electrochemical result with the unique sustainable as-synthesized nanoparticles of ABS compound. Microscopy (HR-TEM) as well as spectroscopy (FTIR) studies provide confirmed evidence of the syntheses of ABS, AS, BS, and CBS respectively while the XPS study confirms the presence of Ag, Bi, and S in ABS. From the electrochemical analysis, it is evident that ABS shows lower overpotential value of 47 mV compare to that of other variants (AS – 93 mV, BS – 191 mV, CBS – 603 mV), lower Tafel slope values(mV/dec) (75.99) compare to others (AS – 101.54, BS - 120.29, CBS - 265.2) which are the key aspects to analyze the catalytic activity performance of the catalyst. It is also proved that the rate-determining step of the reaction proceeds through the Volmer-Heyrovsky step. *Lower EIS values* of 9.84 Ω with higher active surface area value of 0.092 cm^2 of ABS indicate superior and effective electron charge transfer kinetics on the electrode-electrolyte interface and elevated activity compared to other electrocatalysts (AS- 15.24 Ω and 0.035 cm^2, BS- 16.01 Ω and 0.014 cm^2, and CBS- 19 Ω and 0.005 cm^2). On top of that acceleration degradation (AD) study before and after analysis performed at 100 mVs^{-1} for 500 cycles in acidic solution disclose the fact while comparing two LSV curves a small hike (8 mV at 10

mA/cm^2) suggesting higher stability and low catalyst degradation for ABS. Chronoamperometric studies with a fixed applied potential of -0.065 V vs RHE also reveal that the catalyst (ABS) shows retention of activity after a 72-hour long-term process under a cathodic environment.

To show the application of light in H_2 generation, the as synthesized $AgBi_3S_5$-Bi_2S_3 nano composite is characterized by Rietveld analysis with XRD data along with FTIR and XPS studies confirming the formation of the synthesized photocatalyst. The morphological study like FESEM, TEM, EDS also support the result from the characteristic analysis of data and determines their elemental composition in the synthesized nanocomposite. The performance of this nano composite in the hydrogen production reaction in presence of light is convincible due to its catalytic ability is reported for the first time in presence of light where all the major determining factors are well synchronized and outperform in presence of light compare to that in absence of light. The robustness and longtime durability along with catalytic efficacy are also proved by the result outcome from the studied parameters like overpotential, Tafel analysis, electron charge transfer kinetics, double layer capacitance, electrochemical surface area and chronoamperometric analyses.

In search of non-noble metal anode catalyst for fuel cell applications, we synthesized Cu_9S_5 versatile nanomaterials using a new designing synthesis route and followed by unveiling its new catalytic wing towards electrochemical methanol oxidation reaction. Cu_9S_5 and its supported alloys in different forms and structures used in the various fields such as semiconductor, asymmetric supercapacitors, anodes for high performance lithium-ion and sodium-ion batteries, efficient catalyst for water splitting, in broad band high performance electromagnetic wave absorber, used for microfiltration, as an environmental pollution removal and photothermal conversion, as a photothermal agent with 25.7% heat conversion efficiency for photothermal ablation of cancer cells in vivo and in multimodal tumor therapy. We demonstrated electrochemical and photochemical oxidation of methanol for the first time. The increased current peak on consecutive cycling in cyclic voltammetry appears in the negative potential zone. Significantly it is achieved in absence of any noble metal in the constitution of anode. The catalyst also exhibits efficiency in presence of light. Hopefully this new insight regarding Cu_9S_5 nanomaterials towards electrochemical oxidation helps researcher in designing the catalyst without support of any noble metal. It also enlightens new direction to better optimization of its stability and makes them feasible for commercial purpose.

In the context of remediation of atmosphere from the contamination of water by toxic dye, Rhodamine-B, nanoparticles of n-$AgBi_3S_5$, n-Bi_2S_3 and n-n $AgBi_3S_5$ - Bi_2S_3 nanocomposite were synthesized by facile one pot hot chemical (90 °C) method using ethylene glycol as medium without further calcination. The nanocomposite on exposure to natural sunlight exhibits significant and synergistic photo-catalytic activity towards degradation of pollutant dye Rhodamine-B(Rh-B) in aqueous solution. The as synthesized monoclinic $AgBi_3S_5$, orthorhombic Bi_2S_3, and their nanocomposite were identified and characterized by various spectroscopic, diffraction (XRD) and microscopic techniques. The UV-visible spectroscopic study reveals significant absorption of visible light and narrow band gaps/eV: 2.8 and 1.9 for synthesized Bi_2S_3 and $AgBi_3S_5$ respectively. The spectroscopically evaluated maximum % of degradation of Rh-B (99.9) and related high-rate constant (0.059 min^{-1}) were achieved within 25 minutes with 0.7 g/L $AgBi_3S_5$-Bi_2S_3 nanocomposite at pH 3. The radical trapping experiments reveal that both $^{\bullet}O_2^-$ and $^{\bullet}OH$ are almost equally involved in the degradation, while hole, h^+ is the main initiator of the degradation as usual. Studies of the products of degradation reveals both de-ethylation and ring breaking of Rh-B indicating simultaneous absorption of sunlight by it and the catalyst. The very high efficiency and synergistic effect of the nanocomposite might be due to either/ both Z scheme/ S scheme charge separation. The 95% retention of the photocatalytic activity by 5th time used catalyst, $AgBi_3S_5$-Bi_2S_3 signifies its superiority by auto surface improvement during reaction. Hope, the present work on the sulfide-based catalyst will have significant contribution in science and build up solid edifice in the development of emission less energy converters and remediation of atmosphere for our sustainable future.

Contents

Chapter 6: Conclusion and future prospect

Chapter 1

Introduction

1. Introduction

Energy and environment are two prime issues for the present world for sustainable development. Energy management has been evolving as a key factor in the present context for proper storage, conversion and utilization of energy barring environmental hazards. On the other hand, the required industrial growth is always associated with some unavoidable environmental pollution which needs continuous monitoring and immediate remediation **[1]**.

Energy security is the one of the sensitive issues all over the world. Researchers are searching for such solution by using vast and renewable natural sources to generate clean energy without disturbing other environmental parameters. It is expected that such efforts would be fruitful to fulfill the energy demand which are rising day by day due to rapid development of the society along with growth of population. So, it is very much necessary to explore an alternative clean, green and sustainable energy resource as soon as possible. That kind of approach allows us to shift slowly from conventional fossil fuel resources which are not environment friendly to renewable energy sources which are friendlier towards environment **[2-3]**. The approach also mitigates the plenty of problems related to natural calamity like frequent disasters in every calendar year in different parts of the world **[4-6]**. In that context, search of green fuel hydrogen (H_2) is an excellent choice **[7]**. It evolving with a rapid manner also everyone as a clean energy supplier due to its sufficient availability, easy producing capability and also high gravimetric energy density which is about 142 $MJkg^{-1}$ **[8]**. Although there are various methods, H_2 is mostly generated through steam reformation of fossil resources, where CO_2 is formed as a byproduct of these reactions. This is the main concern for facing problems like global warming **[9-14]**. To counter such threats methods like electrochemical, photochemical, photo-electrochemical water splitting grow as H_2 producer as clean, competent and sustainable methods, since energy generated as a result of H_2 combustion reproduce only water which has great significance in the cycle of H_2 economy **[15]**. Catalysts play significant roles in green H_2 production via above mentioned methods. For this we mainly synthesized sulfide-based nanomaterials and used these as catalysts in electrochemical and photochemical water splitting reactions. In the context of proper conversion, storage and utilization of energy, one way of getting high energy density of the most usable form of energy, viz electricity with reduced pollution is to use the fuel cell which converts chemical energy to electrical energy directly without Carnot's efficiency loss **[16]**. The development of stable, economically viable

anode and cathode catalysts for fuel cell is therefore an important topic of present research. Synthesizing and using sulfide nanomaterials, cathode and anode catalysts are studied here for hydrogen production and alcohol oxidation in dark and illuminated environment.

Water is one of the most important and essential substantial entityes for existence of living being as well as industry. Water management system plays a key role to develop an equilibrium in between two major users of it. There is various source of waste water available from the distinct industries such as pharmaceutical, bleaching, textile, agriculture, printing ink, rubber, plastic, leather, food stuff, photographic, paper, pulp etc. where portable water is mostly consumed by textile industry **[17-19]**. Dyes are the most common commodity in textile industry and the effluents come out from this process have several toxic effects due to presence of different organic pollutant moietyes in it. Commercially more than hundred million kinds of dyes are available and similarly demand for this dye in present era as well as pigments dramatically increases and these are primarily responsible to generate waste water **[20]**. Lots of contaminated metals which have adverse effects in the biological system are in the mixed phase with effluents come from the different industries **[21]**. So, methods like photochemical oxidation have been evolved to nullify the effect with an accuracy, to diminish the toxic effect of it through its mechanistic outbreak and make this water available for reuse in the main stream and also contributed in the water management system on the earth. For this again, some sulfide-based nanomaterials are used as photocatalysts to degrade the toxic dye, Rhodamine B in aqueous solution in presence of natural sunlight. The study includes different synthetic procedures of sulfide-based nanomaterials and the roles of Sulphur in electrocatalytic, photocatalytic and photo-electrocatalytic reactions related to energy and environment. Hope, the study would contribute significant findings and notes in the related fields of science and help other researchers for further study.

1.1 Principle of water splitting

Traditional water splitting is an electrochemical process and requires an assistance in a three-component system where anode, cathode and the electrolyte are parts of the set up as shown in figure 1.1. Generally, this process involves two half-cell systems where water reduction occurs on the cathodic half-cell and water oxidation is carried out in anodic half-cell portions. The processes popularly known as HER and OER where HER stands for hydrogen evolution reaction and OER implies as Oxygen evolution reaction carried out on the cathode and anode of the cell respectively. Different electrolytes are used in this process and based on their nature different of electrochemical reactions occurred on the respective electrodes but these do not have any special effects on the overall reaction **[22, 23]**.

The mechanism of the reaction is shown below based on the different electrolytes.

When acid is used as an electrolyte and the reactions are

In cathodic compartment: $2H^+ + 2e^- \longrightarrow H_2(g)$ where $E^\circ c = 0.0$ V

In anodic compartment: $2H_2O(l) \longrightarrow O_2(g) + 4H^+ + 4e^-$ where $E^\circ a = 1.23$ V

In presence of non-acidic aqueous electrolytes, the reactions are

In cathodic compartment: $2H_2O + 2e^- \longrightarrow H_2(g) + 2OH^-$ where $E^\circ c = -0.40$ V

In anodic compartment: $4OH^- \longrightarrow O_2 + 2H_2O + 4e^-$ where Ea = 0.83 V

Overall reaction: $2H_2O(l) \longrightarrow 2H_2(g) + O_2(g)$

Thus, the theoretical value of water splitting is 1.23 V from thermodynamical point of view irrespective of the reaction medium. The above standard electrode potential values of respective cathode (Ec) and anode (Ea) are calculated with respect to standard hydrogen electrode (SHE). In reality, the potential required for water splitting is greater compare to thermodynamic potential value and the surplus potential is responsible for bringing inherent hindrances like interaction susceptibility and solution permeability in both the electrode and the surplus potential termed as overpotential as denoted by η in water splitting system. Based on the above context, the actual operational potential for the water splitting reaction presented like

E_{OP} = 1.23 V + $|\eta_a|$+ $|\eta_c|$ + $|\eta_{other}|$and this equation leads us towards actual operational potential for water splitting reaction, which is responsible for actual performance. The overpotential values in the above equations are efficiently degrading through developing right kind of catalysts as well as electrolyte for respective HER and OER reactions.

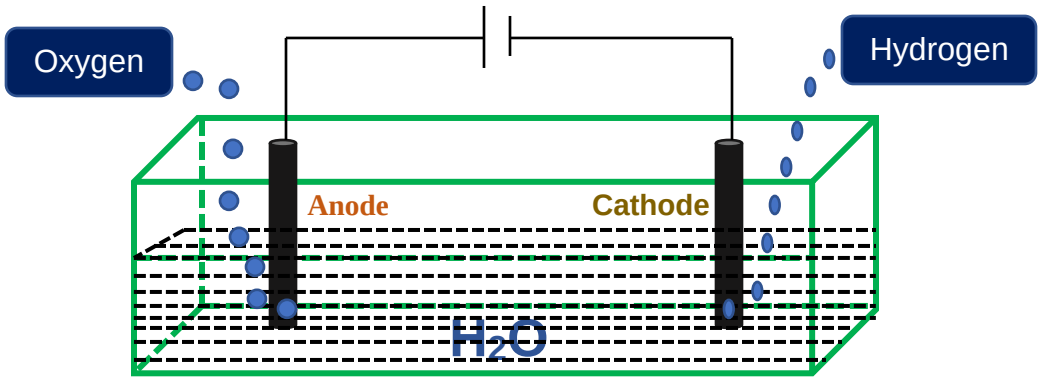

Figure 1.1 Schematic representation of water splitting

1.1.1 Hydrogen evolution reaction (HER) & Oxygen evolution reaction (OER)

HER operated via two electron exchange process where multiple steps are involved in cathodic chamber and it goes through two distinct paths associated with mainly three processes.

In case of acidic electrolyte medium, hydronium cations take an electron from the cathode to generate intermediate immobilized hydrogen on the respective surface of the electrode catalyst ($H_3O^+ + e^- \rightarrow H^{\#} + H_2O$) and the reaction followed via path of Volmer reaction. And then deposited hydrogen intermediate transform into H_2 through Heyrovsky path ($H^{\#} + H_3O^+ + e^- \rightarrow H_2 + H_2O$). The intermediate hydrogens in the vicinity of the system interacts to form H_2 followed by Tafel reaction path ($H^{\#} + H^{\#} \rightarrow H_2$).

In alkaline medium, the hydrogen evolution reaction slows down compare to acidic medium due to formation of intermediate $H^{\#}$ from H_2O dissociation steps **[24]**. And then as a result of that adsorbed $H^{\#}$ is formed through Volmer reaction ($H_2O + e^- \longrightarrow H^{\#} + OH^-$**)** and the remaining parts of the reaction is carried through either Heyrovsky path or Tafel reaction path as like in acid.

The change of free energy of hydrogen adsorption (ΔG_H) in between adsorbed H_2 and the electrocatalyst was calculated by density functional theory (DFT), which was well accepted throughout in the field **[25]**. ΔG_H value has a significant role to identify whether the rate determining step proceeds through either Heyrovsky or Tafel path or Volmer path. When ΔG_H value shows large negative value, it indicates that the rate determining step goes through Heyrovsky or Tafel path and the corresponding rate of H_2 adsorption on the electrode is much easier than rate of desorption. On the other hand, large positive value of ΔG_H signifies that the rate determining step proceeds via Volmer path and the respective interaction of H_2 is comparatively weaker. The rate of adsorption of H_2 on the electrode comes in equilibrium with rate of desorption. It implies that ΔG_H value poses near zero due to the better performance of catalyst in the HER reaction.

The rate of OER reaction is usually slower compare to that of HER because it has to overcome larger overpotential value to reach the activated state and the associated reaction goes through complicated four proton transfer process **[26]**. The possible mechanism and the general reaction pathways of HER and OER are shown below as figure no. **1.2** through schematic representation

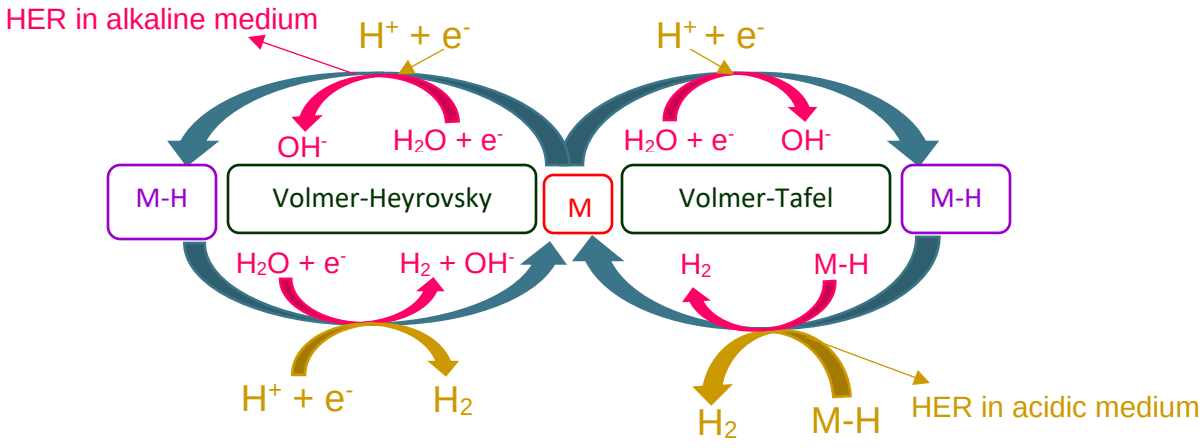

Figure 1.2 Schematic representation of reaction mechanism for the HER in acidic medium and alkaline medium

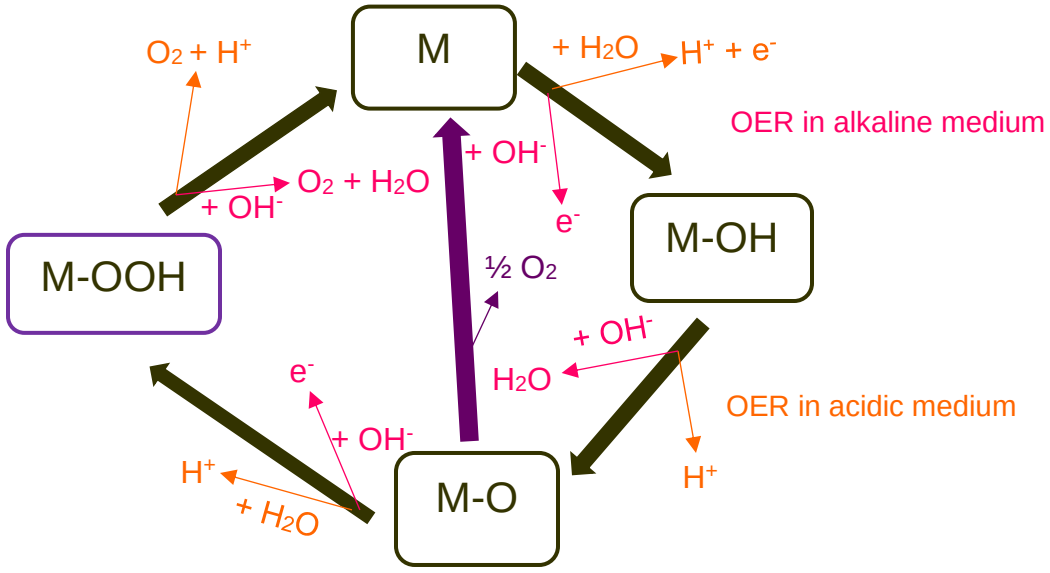

Figure 1.3 Schematic representation of reaction mechanism for the OER in acidic and alkaline medium, green and violet color arrows represent two possible intermediates of OER reactions.

In figure **1.3** intermediate M-O associates with H_2O at acid medium to generate O_2 and combining with OH^- in basic medium to form M-OOH which afterwards transform into O_2. M-OH intermediate in OER reaction also generates same intermediate like M-O and two M-O units link each other to generate O_2 in that respective reaction. Intermediates like M-O, M-OH and M-OOH have great significance to identify the electrocatalytic OER activity **[27]**. Tafel slope value assists in determining the rate determining step **[24]**. If its value is near about 120 mV dec^{-1} then the M to M-OH intermediate path acts as a rate determining step and if it is close to 40 mV dec^{-1} it indicates that the intermediate M-OH to M-O is the rate determining step of the OER.

The thermodynamic parameters like Gibbs free energy for OER determined by Rossmeisl et al. considering four reactions and the associated subsequent Gibbs free energy equation is $\Delta G_{\mathbf{i}} = \Delta G_{product} - \Delta G_{reactant} - eU - k_B T \ln[H^+]$ where **i**= 1 to 4 with an applied potential U, temperature T and kB implies the Boltzmann constant **[28]**. The relationship between theoretical overpotential for OER (η^{OER}) and the Gibbs free energy ΔG^{OER} **[29]** within standard conditions ($U_{SHE} = 0$) is as $\eta^{OER} = (\Delta G^{OER} / e) - 1.23$ V. When overpotential value is zero, the ideal Gibbs free energy is 1.23 eV and in reality, the value differs with the actual outcome owing to poor selectivity of the catalyst makes the OER reaction slower.

1.2 Methods of H_2 production

The resources available in nature are fossil fuels, biomass, seawater, hydrogen sulfide and fresh water where, hydrogen can be found as an abundant element. Sometimes by product like carbon di oxide and other pollutants are separated to obtain green hydrogen from resources like fossil fuels. Prime energy sources like thermal, photonic, electrical, biochemical energy along with some hybrid energy such photonic-biochemical, electrical photonic and electrical thermal are employed to generate net zero, clean hydrogen from the respective resources. There are several methods such as electrolysis, thermolysis, thermochemical processes of water splitting, photocatalysis, photoelectrochemical, PV electrolysis, dark fermentation, hybrid thermochemical cycles, high temperature electrolysis, coal gasification, bio photolysis, photo fermentation, fossil fuel reforming, photo electrolysis, artificial photosynthesis etc. **[30-34]** are used to generate environment friendly hydrogen from their corresponding source materials. Few of the above-mentioned methods are discussed as follows:

1.2.1 H_2 production through Electrolysis

Electrolysis is one of the most important method to generate electricity from energy resources such as solar, geothermal, biomass, wind, ocean and other available renewable energy resources and the waste heat available from different electrolysis systems are used to run several power generating systems. Electrolysis can be associated with different types of energy sources like wind, solar, geo thermal, photovoltaic system, flash cycle, etc. Water converted through electrolysis to generate H_2 and O_2 and the reaction is shown as follows

$$2H_2O \longrightarrow 2H_2 + O_2 \quad E_0 = -1.229\ V$$

1.2.2 H_2 production through Thermolysis

H_2 generated via thermolysis which is conventionally one step reaction process and the required heat was supplied by solar system for completion of such reaction. The optimum temperature required for dissociation of H_2O is near about 2500 K. And such single step reaction expressed as

$$H_2O \longrightarrow H_2 + ½\ O_2$$

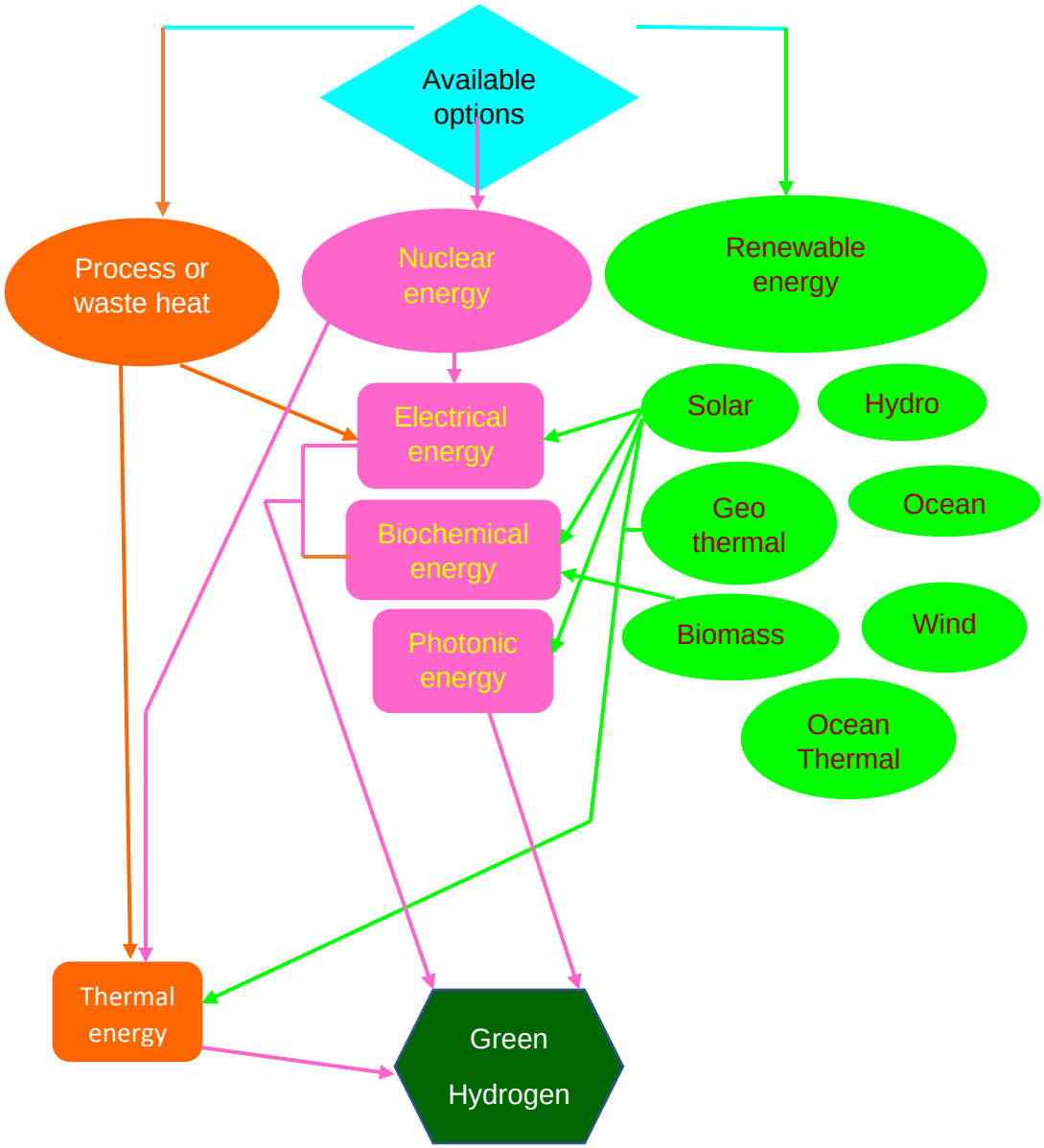

Figure 1.4 Schematic presentation for H_2 production from four different energy sources.

1.2.3 H_2 production through Photocatalysis

In Photocatalysis method where, catalyst activated via photon exposure from sunlight to generate an electron hole pair and the respective electrical charge responsible for splits water and generate hydrogen from it. Band gap play an important role to forwarded this reaction, specific band gap creates specific environment between conduction bands (CBs) and valance bands (VBs) for specific redox reactions. Characteristic feature of the desired catalyst helped to generate electron hole pairs as well as charge separation in between with faster rate. The respective photo-oxidation and photo-reduction of water splitting via photocatalysis are expressed as follows

$$2H_2O + 2e^- \xrightarrow{h\upsilon} H_2 + 2OH^- \quad \text{……Photoreduction}$$

$$2H_2O \xrightarrow{h\upsilon} O_2 + 4H^+ + 4\,e^- \quad \text{……..Photo-oxidation}$$

1.2.4 H_2 production through thermochemical processes

Thermochemical reaction driven by simple heat without assist of any catalyst for production of catalyst. The key features of this type reaction are that no requirement of any electrical energy, operation temperature range in between 600-1200 K, separation process of H_2 and O_2 was done without any membranes and the required energy for this reaction mainly supplied by geothermal, solar, nuclear electricity, biomass combustion. Biomass combustion is responsible for generate hydrogen via gasification process with biomass conversion. Some examples related to H_2 production through the thermochemical process shown below

$$C_xH_y + x\,H_2O \xrightarrow{\text{Temperature, } \Delta} (y/2+x)\,H_2 + x\,CO$$

1.2.5 H_2 production through Photo-electrochemical cells

Photo anode and photo-cathode are two integral components of photo-electrochemical cells. The reaction mechanistic approach of photo-electrochemical cells resembles with photovoltaic cells. The intrinsic characteristic patterns in electrochemical cells utilized solar energy more efficiently and its combines in electrolysis and photocatalysis of H_2O as a united single element.

1.2.6 H_2 production through Dark fermentation

The bio chemical energy stored in organic waste can be converted in other forms of energy with an assistance of Dark fermentation processes without any irradiation. H_2 is produced by living

creatures using the biochemical energy in them without any assistance of light. The hydrogen production costs would be reduced by using organic waste which is easily available and economic friendly via dark fermentation processes.

1.2.7 H_2 production through Hybrid thermochemical cycles

The main advantage of this process is that it can be operated with the help of recyclable chemicals at low temperature compare to heat assisted water splitting and produced hydrogen be used to produce environment friendly thermal energy like industrial heat, nuclear heat, solar heat, geothermal heat and waste heat generated from numerous power plants.

1.2.8 H_2 production via Photo electrolysis

Photo- electrocatalysis is conducted with an assistance of electrical energy in the electrolysis cell under solar irradiation. The key mechanistic steps followed during the photo electrolysis method are, flow of electrons from anode to cathode responsible for generating current, gaseous oxygen and protons formed as a result of water decomposition, hydrogen produced in the gaseous form as a reduction of photons in the cathodic compartment, generation of electron-hole pairs by photonic energy having higher energy than that energy of the band gap of corresponding p-n junction.

1.2.9 H_2 production via bio-photolysis and photo-fermentation

The photobioreactor is designed for microorganisms which are light sensitive and play as a biological converter in the bio-photolysis system. Microalgae microorganism has better efficiency rate compare to that of others microorganism due to their nature of culturing. The production of H_2 via bio-photolysis is pro-environmental in nature but still confined up to laboratory regions. Some examples related to bio-photolysis driven production of H_2 are stated below

$$6\,H_2O + 6CO_2 \xrightarrow{h\upsilon} C_6H_{12}O_6 + 6\,O_2$$

$$C_6H_{12}O_6 + 6\,H_2O \xrightarrow{h\upsilon} 6CO_2 + 2\,H_2$$

1.2.10 H_2 production via Artificial photosynthesis

Artificial photosynthesis method has a tremendous potentiality towards green H_2 production, in the dry agriculture field as well as electricity generation with an assistance of solar energy. The decomposition of water via electrolytically achieved followed by the method which was acting

like a photosynthesis. This method was not commercially viable for large scale H_2 production due to low efficiency **[35]** and production cost are high but researchers are too keen to find new strategy for further improvement of this method.

1.3 Role of parameters for Hydrogen and Oxygen evolution reaction

The catalytic activity of the synthesized catalyst in HER and OER depends on few important factors like Tafel slopes, Overpotential, turnover frequency, stability and faradaic efficiency of that reaction **[36-40]**.

1.3.1 Effects of overpotential on HER and OER

Overpotential is defined as extra amount of energy required to overcome the internal kinetic barrier. It also drove the catalyst from its equilibrium state to initiation of the reaction of HER and OER. Cyclic voltammetry, linear sweep voltammetry measurements are studied for determination of overpotential value of this reaction. Low overpotential value emphasized. better electrochemical study and vice versa also.

1.3.2 Effects of Tafel plot on HER and OER

Tafel slope from the respective Tafel plot was determined performing linear sweep voltammetry study at lower scan rate which associated with the electrochemical reaction and effects on the electrochemical kinetics of that reaction. The equation is shown below as fitted line with the linear portions of the Tafel plot $\eta = a + b \log j$, where η stands for overpotential value, j stands for current density and b represents Tafel slope. Exchange current density (j^0) are determined from the above linear equation when $\eta=0$ and expressed the intrinsic efficiency of the catalyst in water electrolysis reaction. Effective catalyst signified with lower Tafel slope value along with higher electron density value in an electrolysis of water system.

1.3.3 Effects of Turnover Frequency (TOF) on HER and OER

Turn over frequency was assisted to quantify the subsequent catalytic efficiency of the catalyst active site with respect to reaction conditions from which no. of reactions site per unit time are occurring in the electrolysis of water. Equation related to TOF are $TOF = (jA)/(\alpha Fn)$ where A

implies for surface area of the electrode, α represent no. of electrons of the catalyst, j denoted by current density with respect to overpotential from the linear sweep voltammetry study, F presented as Faradays constant and n stands for no. of moles derived from mass loading compensated with associated concentrations.

1.3.4 Effects of Stability on HER and OER

Stability is one of the prime factors to determine the efficacy of the used catalyst in the particular reaction and proved their stability using cyclic voltammetry studied up to thousand cycles and also catalytic performance and robust behavior of the catalyst explored through chronoamperometry study at fixed potential up to 24 hours and also beyond that time.

1.3.5 Effects of Faradaic efficiency on HER and OER

Faradaic efficiency is also assisted to find out the catalytic efficiency of electron transfer involved to driving the electrochemical reaction. Faradaic efficiency determined through comparing amount of gas produced experimentally with known amount of gas generated from the theoretical perspective. Gas chromatography is used to determine the amount of gas such as H_2 or O_2 generating on the respective electrode.

1.4 Fuel cell and its importance

Fuel cell is based on simple mechanistic device where chemical energy converts into electrical energy without creating disorder in the environment. The efficiency rate of energy creation via this route is high during the reaction process. Fuel cell-based technology is evolving in the current energy sector due to their efficiency, productivity and robust nature. The numerous characteristic features of fuel cell drawn their attention in portable energy device like laptop, mobile phone, in others electronic device as an energy supplier and also raised a very tough competitions with battery industry. Fuel cell generates continuous electricity as much as fuel and air are available in it and which bypassed recharging mechanism but battery has limited fuel generating substance and oxidant, degraded certain after time of utilization **[41,42]**. Traditionally fuel cell combines with hydrogen and a supporting oxidant through electrochemically without any exposure to heating. Fuel cells play a key role in renewable energy generation sectors due to zero pollutant created in this path. Combustion of fuel generates electrical energy directly if the process carried on in the

electrochemical cell which also restricts intermediate thermal and mechanical energy generation where Carnot limitation significantly not indulge in it **[16]**. Sir William Robert Grove was the first man who developed fuel cell in 1839 and demonstrated to took H_2 and O_2 in fuel cell while H_2SO_4 as an electrolyte and platinum as an electrode **[43]**. Another two scientist, Charles Langer and Ludwig Mond was used the term fuel cell for the first time in 1889 and they were shown fuel cell application with took coal gas as a fuel **[44]**. And the alkaline fuel cell (AFC) was first coming up under the research of prof. Francis Bacon who modified the equipment of Charles Langer and Ludwig Mond.

There are different types of fuel cell evolving till date and few of them such direct alcohol fuel cells (DAFCs), alkaline fuel cells (AFCs) and proton exchange membrane fuel cells (PEMFCs) are attracting more due to their efficiency, productivity, operational capability at low temperature and most importantly friendlier towards environment **[45]**. Specifically direct methanol fuel cell (DMFC) was performing well due to its characteristic feature like high energy density, structural simplification, higher conversional rate and zero pollutant emitter **[46-48]**.

1.4.1 Principle of Anodic Oxidation of Fuel Cell

The general mechanistic part of direct methanol fuel cell (DMFC) consists of two parts, in the anodic part where methanol going through electro-oxidation to form CO_2 and the subsequent reaction **[48]** is $CH_3OH + H_2O \longrightarrow CO_2 + 6H^+ + 6\,e^-$ $E^0 = -0.8485$ V

Oxygen mostly as an air goes through electro-reduction to from water or steam at the second part i.e., cathodic part.

The electrolytes used in this system are mainly aqueous acid or alkaline solution. Methanol, alkali such as potassium hydroxide or sodium hydroxide and water mixtures are circulating in adjacent to anodic part, oxygen is circulating near the cathodic part of that direct methanol fuel cell mechanistic system. Specific characteristic features regarding the electrochemical oxidation and reduction reaction occurred at their respective electrode compartmental zone as well as inter conversion between their specific forms understood more conveniently with observed the direction of the reaction path and extent of rate of electron flow across the reaction surface interface at orderly manner.

In our research we are concentration on designing new sulfide-based nanomaterial for mainly methanol oxidation along with other higher homologous alcohol without taking any kind of assistance from any novel metal. And optimized their new electrochemical study, revelation of mechanistic path as well as through analysis of product outcome are shown in their respective thesis chapters.

1.5 Water remediation through photochemical oxidation

Photochemical oxidation primarily known as a special kind of oxidation occurs with an assistance of light. This method is very much useful, convenient for purify the waste water coming from different industry and specifically dye industry where harmful organic pollutants are mixed with that waste water. Now in current context, this technique is attracted and evolving due to its pro environmental nature as well as economically viable character and also efficient to function under natural sunlight.

Photocatalyst has several characteristic features such ability to adsorbed the light in its surface, operated easily in visible or near visible region, environment friendlier and economically sustainable **[49]**. Photocatalyst has a unique role in this method. Efficient catalysts are driving this process with a short time frame which was desirable from the commercial point of view. We are demonstrating sulfide-based semiconductor nanomaterials play a pivotal role as an efficient photocatalyst in this method for water remediation to contribute towards water management system for sustainable ecosystem among the natural resources available in this earth.

Photocatalyst divided in to two categories, one is homogenous and other one is heterogenous photocatalyst where catalyst remain with the same phase with the reactant are called homogenous photocatalyst. Heterogenous photocatalyst has two active phases where photoreaction is carried on the surface of a catalyst and the catalyst adsorbed the light became excited then involved in reaction surface with the adsorbate molecule available in the ground state, the overall scenario is popularly known as catalyzed driven photoreaction or semiconductor assisted photocatalysis or also photoreaction through sensitized semiconductor **[50]**.

Dyes are different types like acid, basic, aniline black, direct, azoic, vat, mordant, disperse, reactive dye and metal complex dye from application point of view and indigoid, stilbene, triphenyl methyl dye, quinoline, nitro, azo and nitroso etc. from parent structure contexts and crystal violet, methyl

green, alizarin, naphthalene green B, methyl orange, methyl blue from generally available from industrial point of view **[51]**. Some dyestuffs have different chromophore groups which are responsible for light absorption and lights reflection through shown color and has immense capability to alter the properties of the experimental substance from physical and chemical context.

Chromophore and auxochromes are two components of dyes responsible for characteristic changes in it where the preceding one is responsible for color and the next one acts as electron donor or acceptor substituent which has ability to increase the affinity of that dye molecule for better solubility in water. Some of the specific feature in auxochrome are that these contain one or more number of nonbonding electron pairs which have tendency to extend conjugation for better color resolution of chromophore. Few significant chromophores are nitro group ($-NO_2$), azo (-N=N-), methine (-CH=) and carbonyl (-C=O) groups along with some common auxochromes are amino ($-NH_2$), hydroxyl (-OH), methyl ($-CH_3$), carboxyl (-COOH) and Chloro (-Cl). The constituents like metals, rings, other material in dye molecules which have several adverse effects towards aquatic system, certain marine life, available in natural ecosystem, among them azo dye belongs to longer chain class of synthetic dyes and its reduced form is carcinogenic in nature **[52, 53]**. Azo dyes are popular in synthetic organic reaction due to its flexible behavior during coupling reaction, shown structural adaptability in different applications. The specific characteristic features of azo dyes improve the biological along with chemical stability in overall dyes which has tendency to resist them from collapse during the exposure of natural light or by soap and aqueous medium.

The presence of azo dyes in aquatic system as well as their subsequent adverse effects specifically towards biological system of human life becomes vulnerable and complex diseases come out with several potential damages in liver, kidney and others organs of biological system of any beings **[54, 55]**.

There are mainly two kinds of methods available for removal of pollutant from dye contaminated water. One is separative method which includes physical and physicochemical and another is degradation method which includes chemical and biological methods. Chemical methods proceed through ozonization, oxidation and photochemical method. Advanced oxidation method is evolving as an efficient method among them because of their efficiency, capability towards oxidation process and most importantly environment friendly in nature. The mechanistic outbreak of this process in where they produce strong oxidizing agent as hydroxyl radical. Fenton method

is familiar in advanced oxidation process where H_2O_2 and iron salt mixture is familiar as Fenton's reagent, played effective role in the degradation of organic pollutant **[56]** H_2O_2 activated without any assistance of any energy which is main advantage of Fenton's method. Formation of hydroxyl radical is initiated the following reaction **[57].**

$$Fe^{2+} + H_2O_2 \longrightarrow Fe^{3+} + OH^{\bullet} + OH^{-}$$

$$Fe^{2+} + H_2O + H^{+} \longrightarrow Fe^{3+} + OH^{\bullet} + H_2O$$

Ionized form of H_2O_2 reacts with ozone to formed $OH^{\bullet}$ [32]

$$O_3 + HO_2^{-} \longrightarrow O_2 + OH^{\bullet} + O_2^{\bullet -}$$

The formation of hydroxyl radical further improved in presence of UV light and then its termed as photo Fenton's or solar Fenton method **[58]**.

Photochemical method driven by photocatalyst through photocatalysis is the advanced oxidation process due to simple, efficient, pro-environmental and economically sustainable for pollutant removal from toxic dye **[59]**. Enhance the generation of electron hole pairs assisted through radical production depends on excitation of efficient semiconductor **[60]**.

1.6 Overview of Materials Synthesis techniques

The synthetic route is very much important to develop a certain specific and unique character driven nanomaterials whose effective performance is responsible to lead us to explore various applications. There are several methods are available for sulfide-based semiconductor nanomaterials development for energy and environmental application such as Hydrothermal, solvothermal, ball milling, exfoliation, solid phase synthesis, chemical vapor deposition, electrochemical deposition, hot chemical treatment **[61-68]**. We chose hot chemical treatment method for specifically time efficient, simple, initiated with optimum temperature like characteristic features and also took less time for completion. Different types of materials synthesized followed by this method. Nanomaterials of different size and shape optimization was flexible in this method.

1.6.1 Hot Chemical treatment method

The optimum molar ratio of the source metals was weighed out for the synthesized materials and then soluble in the desired solvent based on their solubility, made a homogenous solution for individual source metals salt in the individual reaction vessel. An optimum temperature was preplanned for the synthesis based on the type of source metals participated in the desired nanomaterial synthesis. If we want to synthesized $A_xB_yC_z$ materials then at first, we mixed the homogenous mixture of source metal A and B in a reaction vessel and then put it on a pre-sated (90°C) temperature-controlled heating mantel under ambient condition. When temperature reached at desired temperature then homogenous solution of source metal C poured into main reaction vessel where solution of homogenous mixture of source metal A and B are there and then the reaction was carried on that temperature up to two hours. After end of the reaction, switched off the heating mantle and allowed the appeared mass of desired synthesize materials, then followed by centrifuged with that appeared mass and afterwards washed it with Millipore water and ethanol several times, dried at 70 °C for 24 hours.

1.7 Overview of Materials characterizations techniques

The synthesized nanomaterials were characterized by different sophisticated tools to reveals the nanomaterial's identity from structural, morphological and electrochemical point of view.

1.7.1 Overview of Electrochemical characterization

The electrochemical study was measured by cyclic voltammetry (CV), chronoamperometry (CA) and with electrochemical impedance spectroscopy (EIS)

1.7.1.1 Overview of Cyclic Voltammetry

Cyclic voltammetry is a reversible method where peak potential at the oxidation zone i.e., anodic part and subsequent peak potential at reduction zone known as cathodic compartment stimulated the electrochemical response with the support of applied potential field. Conventional three electrode set up are used to analyzed the electrochemical outcome through systematic cyclic

voltammetry study where carbon cloth or graphite carbon electrode or glassy carbon electrode used as a working electrode, inert material like platinum wire or platinum sheet are used as a counter electrode and saturated calomel electrode (SCE) or Ag/AgCl used as reference electrode in an electrochemical system. Cyclic voltammetry study was optimized through current (A) vs. potential (V) profiles at different scan rate. Catalytic stability has checked through number of cycles performed via CV analyzer until reached at saturation state of the catalyst. The Tafel plot was analyzed from the relation between log scale of current density with steady potential in a low scan rate following typical Butler Volmer equation.

$$\eta = b \times \log j + a \quad \text{……. (1)}$$

$$b = ((\eta - a)/ \log j) \quad \text{…….. (2)}$$

a, b, j and η implies as reaction constant, Tafel slope, current density and overpotential respectively.

1.7.1.2 Overview of Chronoamperometry (CA) analysis

The chronoamperometry study was done with same typical three electrode set up discussed in cyclic voltammetry optimization sections and scrutinized via current (A) vs. time (sec) profiles at fixed potential. Robustness and stability of the effective catalyst was optimized with fixed potential up to longer time exposure of catalyst surface in electrochemical system. CA study are also revealed different electrode kinetics phenomenon at the electrode electrolyte surface interface.

1.7.1.3 Overview of EIS analysis

EIS analysis was measured for charge transfer resistance in the electrode electrolyte surface along with several factors such as solution resistance and other kinetic parameter when compared the profiles of real Z with imaginary Z fitted in an optimized circuit and the plot popularly known in electrochemistry as Nyquist plot.

1.7.2 Overview of structural characterization

1.7.2.1 Overview of XRD analysis

X-ray diffraction (XRD) analysis was employed to understand the repeated and periodic arrangement of unit cell at different diffraction angle under exposure of the X-ray following the

traditional Bragg's law $n\lambda = 2d\sin\Theta$ where λ stands for wavelength of the incident X-ray, d implies the interplanar distance and Θ represented as a diffracted angle. The analysis reveals the important information for identification of different compound and their phase, nature of crystallinity, size etc.

1.7.2.2 Overview of FTIR analysis

The presence of functional group, presence of different bonds among the elements presents in synthesized materials optimized through FTIR analysis. Nature of stretching and bending vibration between two elements identify at specific wave number zone through FTIR characterization tool.

1.7.2.3 Overview of XPS analysis

The X-ray photoelectron spectroscopy is a characteristic tool to analysis the elemental composition of the synthesized materials surface, electronic and chemical state of corresponding constituent element, empirical formula of synthesized elements and their atomic percentage, uniformity of all the elements present in the materials. XPS techniques is mainly based on photo-ionization effect and escape of electrons from analyzed materials surface when exposure with high energized X-ray photons.

1.7.3 Overview of morphological characterization

1.7.3.1 Overview of Scanning electron microscopy (SEM) analysis

SEM is a useful technique to analyze the morphology and topology of the synthesized sample using high energized beam of electron for overview of intrinsic structural peripheral state of the materials surface. The resolving ability of microscope and minimum separation resolved through microscope predicted by the equation as such, $d = \lambda/2n\sin\Theta$ where λ, n, Θ stands for wavelength, refractive index, half angle of the cone of light from the objects. Resolving power inversely propagated with the respective wavelength. The range of optical resolution of that microscope varies from 0.2 μm or 200 nm. Lanthanum hexaboride (LaB_6) or Tungsten (W) are being used primarily as cathode for high melting point and the range of energy produced by electrons in the cathode is 0.1 to 0.30 keV. Conducting film of gold or platinum near about 5 nm is used to made on the experimental sample for conductivity improvement purposes and as a result of that electrons remove effectively along with decrease the effectivity of space charge.

1.7.3.2 Overview of Transmission electron microscopy (TEM) analysis

TEM is a generally used to investigate the morphology and intrinsic structure of the experimental materials and the configuration of TEM also very much similar with SEM. The energy used to accelerate electrons is much higher 100 to 400 keV compare to that of SEM. The sample should be sufficiently thinner for better penetration of the electron beam has optimum physical strength along with chemical durability for withstand the high vacuum atmosphere.

1.7.3.3 Overview of Energy-dispersive X-ray Spectroscopy (EDS or EDX)

This technique is generally part of both SEM and TEM analysis and provide information related to chemical composition of an experimental samples in particular selected region of that corresponding surface.

1.8 Overview of UV-vis spectroscopy:

The fundamental principle behind the adsorption driven by the generation of electron hole pairs as a product of optical excitation of electrons from the region of valance band to region of conduction band. The processes follow behind this technique are obeying the fundamental law of energy and momentum conservation and which are driven by the fact that minimum quantum energy sufficient for excitation of electron from valance band region to conduction band region is equal to band gap of the semiconductor. Band gap energy (E_g) of semiconductor materials determined from the measurement of the fundamental absorption spectroscopy. The profile of $(\alpha h\upsilon)^2$ vs. $h\upsilon$ conventionally known as Tauc plot for the allowed electronic transition where α, h, υ implies the absorption coefficient, plank constant and incident light. And the direct band gap was determined from following relations, $(\alpha h\upsilon)^2 = h\upsilon - E_g$

1.9 Overview of High-Performance Liquid chromatography (HPLC):

HPLC technique provides us enhanced separations under short period of time utilizing small particles, small column diameter with high liquid pressures. Martin and Synge in 1941 discovered the liquid-liquid partition chromatography and also laid the foundation of Gas-liquid chromatography and high-performance liquid chromatography. Kirkland and Hub developed HPLC in 1969 and proposed systems capable to operate at pressure up to 3000 psi and particle size 30 µm supported to 1-3 mm column has been used to injected eluent pumped through the

column at higher flow rate. When the mixtures of analyte introduce in HPLC column, affinity towards stationary phase assisted to travel accordingly. Affinity of the analyte towards adsorbent travel slowly and affinity towards stationary phase direct the analyte move fast pace. The components present in analyte easily separated by these techniques because of distinct affinity shown respective components towards stationary phase.

1.10 Literature Review

Clean energy resources have a vital impact in the field of renewable energy generation due to its zero adverse effects towards environment. Among the resources, electrolysis of water for hydrogen production acts as clean energy with their high energy conversion rate along with commendable gravimetric energy density which provides an alternative solution for countering problem like exhaustion of conventional fossil fuel and environmental disorder. So, sulfide- based materials have been exclusively explored as efficient, effective, widely popular and available as alternative to precious metals for energy applications like water splitting specifically for green hydrogen production, alkaline fuel cell oxidation, etc. for contribution towards renewable energy generation and environmental application related to water remediation for organic pollutant removal under natural resources for better water management and eco system on the earth.

Sulfur (S) atom has crucial role for designing new catalyst for energy and environmental application. Although sulfur atom usually plays a secondary role in the desired sulfide-based materials and metal plays the primary roles. It can play a significant role towards specific structure, effective area, defects etc. among abundant sulfide- based materials. Contribution is needed to understand the key step in electrochemical and photochemical redox reactions and to decide whether ‘S’ atoms play a direct role or indirect role in that said application.

Some exposed and vacancies of ‘S’ atoms on the specific basal plane of desired sulfide-based nanomaterials can have crucial effect on the electrocatalytic or photocatalytic hydrogen evolution reaction which is recognized as direct role of sulfur atoms in that reaction. Researchers like Jaramillo et al. established some facts based on the theoretical as well as experimental results is that the active sites of MoS_2 in the HER application, the position of ‘S’ atoms may be on the edges in low H environment (1\4 ML) **[69]** and basal plane has greater ‘S’ vacancies in the layered 2H-MoS_2 may contribute in the HER reaction for better enhanced performance and this is one of the

most powerful method for improving performance of HER reaction. One of the contexts where 'S' vacancies can recreate a new environment in between adjacent metal atoms, lesser reoriented atoms shown more activity and will prevail better intrinsic electrochemical performance. On the other point of view, vacancies of 'S' atoms can generate more active sites also increase the total number of active spots. New active sites due to 'S' vacancies on the inactive basal plane of 2H-MoS_2, the gap available in near to fermi level can assist direct H binding with the Mo active sites.

'S' atoms played an indirect role in HER reaction when metal atoms in an active state gets place for adhesion and separation of hydrogen generated. Dong et al. study with Ni_3S_2 nano porous system and theoretically established fact related to adjacent sites, where he showed that H_2O was specifically adsorbed on the sites of Ni through the Volmer steps and 'S' sites preferentially suited for hydrogen production via Tafel stage **[70]**. Staszak-Jirkovsky et. al proved the indirect role of sulfur through their experiment to take (Co^{2+} / Mo^{4+}) sulfide-based system where metal plays on active role to increase the slow water dissociation in basic medium and the adsorbed hydrogen recombined in the 'S' sites **[71]**.

From the above analysis it was clearly evident that role of 'S' atoms and its vacancies in the sulfide-based materials for water splitting along with other application creates new enthusiasm for scheming new active electrocatalysts. But systematic research approach is very much essential for revealing the exact roles of this participating atoms in this main reaction periphery which leads immensely for accelerating the development process with the sulfide-based material specifically for hydrogen generation.

Different morphological outbreaks also assist to increase the no. of active sites which further leads to increase the surface area of the synthesized sulfide-based materials **[72-76]**. Scientist like Kibsgaard et al. showed structural surface optimization of MoS_2 to developing mesopores orderly into the MoS_2 film with double gyroid exposing more active sites, beneficial for HER **[74]**. Alignment of MoS_2 nanosheets vertically leads to expose more reaction sites by increasing density of the active sites **[76-79]**. Constructing cracks on the surfaces leads through abundant defects which may be responsible for high density exposed reaction sites **[80-89]**. Xie et al. demonstrating controllable defect engineering with ultrathin MoS_2 exhibited better HER performance **[88]**. Lukowski et al. shown phase control on 2013 onwards, in situ dynamics of 1T MoS_2 features lead to better conductivity, electrode kinetics, surface area brings efficiency in the performance of HER

reaction also emphasis with different phase and their interconversion ability one phase to another, sometimes alters their stability in MoS_2 or WS_2 reaction moiety leads to better HER **[90-98]**. Yu et al. demonstrated with 1T MoS_2 developing pure metallic phase of that synthesized crystals along with resizes with more than hundreds of micrometers for better HER reaction **[99]**. Liu et al described different strategy to generate stable metallic phase one after another in WS_2 for efficient HER reaction **[100]**. Disordered structures along with isotropic properties are developing abundant highly exposed active sites mainly for amorphous materials leads to better catalytic efficacy in HER reaction **[101-103]**. MoS_2 with amorphous nature first developed through electrochemical deposition approach on 2011 **[104]**. Amorphous MoS_2 film incorporated through transition metal ion like Fe, Co, Ni leads to increased better surface area for catalyst loading brings change in catalytic performance of HER reaction **[105]**. Highly conductive substrates depositing on amorphous molybdenum sulfides leads to better performance in HER reaction **[106-108]**. DFT calculation revealed that amorphous MoS_2 in its surface was unstable but initially transformed in to preferred active amorphous form to the crystalline form in presence of H and which was cause for deactivation of the catalyst due to extended operation and subsequently more exposure of inert basal plane reaction sites to the electrolyte observed **[109]**. Corrosion and reductive activation further analyzed through developing correlation between quantity of S atoms with MoS_2 film leads to assist designing efficient and stable electrocatalyst for HER **[110-114]**. Expansion of interlayers MoS_2 leads to bring modification in electronic structures along with electrical conductivity on the edges of MoS_2 active sites, enhanced the HER performance **[115-119]**. Gao. et al. demonstrated through microwave assisted strategy for interlayers expanded form of MoS_2 nanosheets for better HER performance **[117]**. Sun et al. developed expanded interlayer MoS_2 on monolayer sheets of reduced graphene oxide, modification brings better changes in HER performance **[118]**. Several strategies related to activation of basal plane along with S-terminated sites has been developed to incorporate heteroatoms like (Pt, Fe, Ni, Co, O, P, N) **[120-123]**. Deng et al. incorporating Pt atoms into MoS_2 surface leads to better H adsorption on the S terminated sites brings better HER performance **[124]**. Shi et al. also demonstrated incorporating Co on the surface of WS_2 leads better H bonding also change in formation energy of S-vacancies sites accelerate better HER outcome **[125]**. Nonmetallic atoms such P, N doping on MoS_2 surface strategy leads to better HER activity **[126-130]**. Li et al. developed new strategy like generating strained S vacancies on basal plane of 2H MoS_2 for consistence HER performance **[131]**. Layered -MoS_2 formed through

assembling following composite engineering supported with conductive substrate like graphene **[132-137]** supported by conductive material such carbon paper, carbon nanotubes, carbon nanosheets, Ni foam for enhancement of HER activities **[138-142]**. Li et al. strategically modified MoS_2 with rGO sheets through using solvothermal method for better HER outcome **[143]**. The slow kinetics of HER in alkaline medium was improved by incorporating metal hydroxide with MS_2 **[144-148]**. Hu et al. demonstrating NiCo double hydroxides hybridized with MoS_2 sheets [144]. Luo et al. developed Cobalt hydroxide supported with layered MoS_2 nanosheet via two steps synthetic process increases the rate H_2 generation **[147]**. Anjum et. al modified a method inheriting S-deficient, defect-rich, expanded interlayer and Mo-edge in metallic 1T-MoS_2 for efficient water splitting **[149]**. Materials supported by cobalt sulfide along different stochiometric variant of respective sulfide materials fulfilled different parameters, with different morphologies such microwire, nanowire related to efficient HER activities **[150-153]**. Nickel sulfide along with different stoichiometric variant fulfilled all the important parameters like low cost, rich valance state, ecofriendly in nature for better HER process **[154-163]**. Jing et. al developed few crystals form of Nickel sulfide variant via microwave assisted route **[164]**. Wang et al. prepared a mixed phase of nickel sulfide incorporated platinum nickel in it, demonstration better synergistic effect for better performance of HER reaction **[165]**. Other variant Mn incorporated in nickel sulfide **[166]**, N-anion decorated nickel sulfide **[167]** has been reported so far regarding nickel-based materials optimization for HER application. FeS_2 among the other stoichiometric variant of iron most often addressed for HER application **[168-171]**. Jasion et al. prepared different variant of iron sulfide changing the ratio between Fe and S **[172]**. Wang et al improvised new strategy doping cobalt, carbon nanotube both simultaneously on iron sulfide varying different stoichiometric ration bring change in HER performance **[173-175]**. Long et al. developed nickel, iron double layers hydroxide for superior HER activities **[176]**. Konkena et al. developed different stoichiometric ratio of iron, nickel and sulfur mixed materials along with different temperature variant for better HER reaction **[177-179]**. Jing et al developed different hollow shaped nickel cobalt sulfide following solvothermal route for efficient HER performance **[180]**. Wu et al. proposed a new strategy to weakening the H-S bond via N doping into nickel cobalt sulfide materials **[181]**. Sheng et al. modified with Pd doped in nickel cobalt sulfide for HER catalysis **[182]**. Zinc cobalt sulfide was evolving recently for better HER reaction **[183, 184]**.

After studying all the catalyst along with their structural modification, we developed $AgBi_3S_5$, versatile new catalyst optimized through new synthetic route and also demonstrating first time as an efficient electrocatalyst for HER.

For alkaline fuel cell specifically electrochemical as well as photochemical methanol oxidation, we developed non novel metal-based cost-effective catalyst such as Cu_9S_5 and experimentally outbreak its characteristic features first time towards methanol oxidation reaction. Graphitic carbon nitride-based catalyst showed some activity towards direct methanol fuel cell **[185]** but not as much efficient like synthesized Cu_9S_5 nanomaterials.

Sulfide based nanomaterials also showed their photochemical activity in the water remediation process from different organic pollutants specially like Rhodamine-B dye and review outcome related to such kind of catalyst is briefly shown in below.

Li et al. on 2016 were demonstrated Rh-B degradation with CdS NPs **[186]**, Meng et al. on 2017 onwards exploring Rh-B degradation with $CdS/InVO_4$ **[187]**. Yao et al. on 2021 was shown efficient degradation of Rh-B with $CeO_2/CdS/rGO_8$ **[188]**. Zhao et al. showed the degradation efficiency of Rh-B with an assistance of $PbS/CdS/TiO_2$ **[189]**. Sun et al. & Zhou et al. both were separately demonstrated Rh-B degradation with CdS/TiO_2 **[190, 191]** on the subsequent year of 2016 and 2017. Peng et al. showed the degradation efficacy on 2016 onwards with mixed $CdS/Au/g\text{-}C_3N_4$ **[192]**. Basu et al. demonstrated the degradation with CuS **[193]**. Researchers like Ajibade and Oluwalana were demonstrated Rh-B degradation with CuS NPs **[194]**. Shamraiz et al. experimentally exploring the degradation efficiency of Rh-B with $CuS\text{-}Cu_2S$ **[195]**. Neelgund and Oki on 2021 was demonstrated Rh-B degradation with GO/FA/CuS **[196]**. Song et al. showed the degradation efficiency with CuS/ZnS **[197]** and CuS/CdS **[198]** on 2023 onwards. Zhou et al. was exploring the degradation potentiality with CuS/Bi_2WO_6 **[199]**. El-Hout et al showed the degradation efficiency with the rGO/CuS **[200]**. Liu et al. on 2013 onwards showed the degradation efficiency with FeS_2 **[201]**. Wie et al. was demonstrated the degradation efficiency with FeS_2/ $g\text{-}C_3N_4$ **[202]**. Arun Kumar et al. showed the Rh-B degradation efficacy with $BiFeO_3/SnS_2$ **[203]**. Zhao et al. used Cr: SnS_2 **[204]** for Rh-B degradation on 2018 onwards. Mahmood et al. was demonstrated catalysis efficacy of NiS_2/TiO_2/Cu **[205**] for the Rh-B degradation. Vattikuti et al. was demonstrated with MoS_2 MWNR **[206].** Zhang et a. was examined the catalytic efficiency of MoS_2 & MoS_2/rGO **[207]** for Rh-B degradation. Li et al was shown Rh-

B degradation with MoS_2/ g-C_3N_4 **[208].** Wang et al was shown with Fe/ MoS_2/ g-C_3N_4 **[209].** Zhu et al was demonstrated with MoS_2/ g-C_3N_4 **[210].** Li et al. demonstrated with MoS_2/CdS **[211].** Nguyen et al was examined with C-MoS_2/TiO_2 **[212]**. Piriyanon et al. was demonstrated catalytic efficacy of MoS_2/Ag_3PO_4 **[213]** in Rh-B degradation. Guo et al. shown with Fe_3O_4@ MoS_2/Ag_3PO_4 **[214]**. Hong at al. on 2023 explored catalytic efficiency of MoS_2/InO_2 **[215]** for Rh-B degradation purpose. Li et al. showed with MoS_2/BiOI **[216].** Nandigana et al was demonstrated degradation with Sn: MoS_2 **[217]**. Khan et al showed with Ni: MoS_2 **[218]**. Caglar et al demonstrated with Bi_2S_3 **[219]**. Jia et al. explored the catalytic potentiality of Bi_2S_3-BiOBr/TiO_2 **[220]** in Rh-B degradation. Cao et al. showed with Bi_2S_3-BiOCl **[221]**. Tao et al was demonstrated with Sb_2S_3/graphene **[222]**. Dashairya et al. was exploring with Sb_2S_3/PCS & Sb_2S_3/rGO **[223]** for Rh-B degradation. Xu & Zhao et al was demonstrated Rh-B degradation with Sb_2S_3@ MoS_2 **[224]**. Oluwalana and Ajibade was explored catalytic efficiency of PbS **[225]** for Rh-B degradation, Aziz et al. was shown degradation efficiency with CdS/PbS/TiO_2 **[226]**. Suganya et al. showed catalytic demonstration with Mo/PbS **[227]**. La Porta et al was demonstrated with α-ZnS [228]. Palanisamy showed catalytic efficiency of ZnS/Ag/$CoFe_2O_4$ & ZnS/Bi/β-Bi_2O_4 **[229, 230]** for Rh-B degradation on 2020 and 2021 respectively. Varghese showed degradation efficacy with CuS-ZnS/rGO **[231]**. Danish and Muneer was demonstrated Rh-B degradation efficiency with ZnS/SnO_2/ g-C_3N_4 **[232]** where Lee at al. on the year 2017 was demonstrated degradation efficiency of ZnS/SnO2 **[233]** specifically for Rh-B.

W synthesized $AgBi_3S_5$-Bi_2S_3 nanocomposites based on the above literature review and showed the catalytic efficacy with this nanocomposite for the first time in photochemical degradation of Rh-B under natural sunlight illumination briefly in chapter 5.

1.11 Scope and objectives

Optimization of catalytic efficiency of a synthesized catalyst is a continuous working process in any application and its best performance comes with several experimental studies. Creativity is a natural process which cultivates a positive energy in human nature for moving in the forward direction with a greater cause through breaking the limitation by this driving force. In this context, contribution to generate clean and green energy towards renewable energy sectors always demands

for new effective catalyst design for the better results. Recycling the water to contribute in water management system for future endeavor also creates opportunity for designing new catalyst, new efficient methods, for removal of the different organic pollutants mixed with the water. Such efforts make them harder and hazardous coming from different sources using natural resources and bringing back the water for use in the main stream.

To provide an appropriate solution on the basis of above important scopes available in the current research field of green energy and water remediation, relates to green, clean and sustainable future. The thesis primarily is focused on synthesis by designing new synthesis route of simple, cost effective, environment friendly, sulfide-based nanomaterials like Ag_2S, Bi_2S_3, $AgBi_3S_5$, $CuBiS_2$ catalysts and using them for the first time in the field of green hydrogen generation and non -novel metal-based nanomaterial, Cu_9S_5 developed via new synthetic route for the first time and reveals its characteristic feature experimentally towards anode catalysis of fuel cells along with photo assisted fuel cells. $AgBi_3S_5$-Bi_2S_3 nanocomposites is also synthesized as a catalyst for green hydrogen generation and also for photochemical pollutant degradation. The catalytic efficiency of the said catalysts is shown for that first time in the above-mentioned field.

1.11.1 Choice of electrolyte medium for HER

HER reaction is operated via two electron exchange processes where multiple steps are involved in cathodic chamber and it goes through two distinct paths associated with mainly three reactions. Electrolyte medium plays a significant role for efficient HER reaction and we are chosen acidic medium over alkaline medium due to following reasons.

In case of acidic electrolyte medium, hydronium cation takes an electron from the subsequent electrolyte to generate intermediate immobilized hydrogen on the respective surface of the catalyst as shown by $H_3O^+ + e^- \rightarrow H^\# + H_2O$, which is Volmer reaction. And then deposited hydrogen intermediate transforms into H_2 either through Heyrovsky path $H^\# + H_3O^+ + e^- \rightarrow H_2 + H_2O$, or by Tafel reaction path $H^\# + H^\# \rightarrow H_2$.

In alkaline medium, the hydrogen evolution reaction slows down compare to acidic medium due to formation of intermediate $H^\#$ from H_2O dissociation steps **[234]** and then as a result of that adsorbed $H^\#$ was formed through follows Volmer reaction ($H_2O + e^- \longrightarrow H^\# + OH^-$) and the

remaining parts of the reaction carried through either Heyrovsky path or Tafel reaction path as like acidic conditions.

1.11.2 Choice of fuel

Choice of fuel has played a significant role in fuel cell technology. Some of the characteristic features are needed such high availability, high energy density, easily manageable storage system and less toxicity. Liquid alcohol fuels have several advantages compared to gaseous fuels in terms of high energy density and usable without reforming, etc. Better flexibility with respect of storage and transportation of alcohol, its use in the portable electronic device is welcome as an energy provider. Methanol has emerged as an appropriate fuel compare to other fuels for direct alcohol fuel cells (DAFC) **[235]**. Having a single carbon atom, relatively lower molar mass, rapid anodic oxidation rate, high energy density near about (6.2 $kWhkg^{-1}$), it has simple structural framework and easily producible from available natural resources. The system is compact where direct methanol fuel cell activated directly feed methanol to the reactor system without any reformer **[236]**. Methanol as an effective fuel due to its cost effectivity, high conversion efficiency and others characteristic features is used as a power supplier in familiar portable electronic devices like mobile phones, notebooks and PCs **[237]** etc.

1.11.3 Choice of medium for Direct methanol fuel cell

Medium has an effective role in the fuel-cell electrochemical oxidation. Alkaline medium was preferred over acid medium due to sufficient availability of OH^- ion concentration along with additional adsorption of OH^- on the surface of the catalyst removes CO_2 and H^+ from the system, higher pH suited the oxidation process. On the other hand, in acid medium the process is slower and produced poisonous carbonaceous intermediate further interrupted and reduced the fuel cell efficacy. The corrosive nature is high in case of neutral and mild basic system causes less durability.

1.11.4 Choice of Dye

Generally, Rhodamine-B (Rh-B) dye basic in nature with high solubility belongs to xanthene class. It is mostly used as colorant in plastic, glass, paint drawing, paper textiles, dyed pesticides. The

characteristic features like bright color, cost effectivity attracted towards food industry **[238, 239]**. Rh-B has several adverse effects towards environment as well as biological systems of living beings, specifically neuro toxic, mutagenic, carcinogenic and also causes problem like respiratory tract, irritations to eyes and skins **[240-243]**. The inner moiety based on xanthene ring where N-ethyl groups attached both side of the ring. We targeted Rh-B as our preferred dye for degradation under natural light on a short span of time with our newly and first-time synthesized nanocomposites used as catalyst in this cost-effective degradation process.

1.11.5 Choice of catalyst

Catalyst has a vital role to enhance the reaction rate and also provide stability of that reaction system. We chose sulfide-based catalyst for the energy and environmental related applications due to their various characteristic features. Mixed ion metal sulfide shows excellent characteristics of enhancing the performance compare to mono metal sulfides in terms of higher electronic conductivity, higher specific capacitance, higher surface area and inherent higher redox properties **[244-246]**. The characteristics improvement of performance along with synergistic effect in metal ion metal sulfide emerged as a promising electrode material in the field of water splitting like application and their dynamic feature unveils the wings in the field of bifunctional electrocatalyst **[247-250]**. Another important role of the S atom in the case of the hydrogen evolution reaction is the formation of a place for hydrogen adhesion and separation when the metal atom is in the place of the effective site of the plane and the S atom can participate indirectly **[251]**.

The basic idea behind the choosing Ag, Bi and S elements in our catalyst is that plenty of compositions made from these elements have versatile applications towards photocatalysis, solar cells, photovoltaic devices, photodynamic capabilities, efficiency in high optothermal conversion, synergistic imaging, photothermal driven anticancer treatment, applicable as an antibacterial agent, demonstrated in the treatment of multi model malignant tumor **[252-257]**. We designed a new time-efficient environment-friendly synthesis route to prepare a low-cost, free-of-toxic element, versatile sulfur-based ternary bismuth chalcogenide, $AgBi_3S_5$ as ABS nano catalyst for mainly hydrogen evolution reaction. Ag and Bi compounds possess low band gaps. So, charge separation and availability of electrons for reduction are easy. The presence of two nuclei causes the molecule to be more defective in the nature of the crystal and S vacancy develops which is responsible for

greater H^+ adsorptions required for HER. This study further advances the knowledge in this particular field.

$AgBi_3S_5$ is chosen since it is quite stable in nature and found in earth as a part of Pavonite mineral ($Ag_{0.75}Cu_{0.25}Bi_{2.25}Pb_{0.75}S_5$). In addition, the band structure of Bi_2S_3 brackets(covers) the valence band (VB) of $AgBi_3S_5$, which makes them a suitable structure in $AgBi_3S_5$-Bi_2S_3 nanocomposite for Z-scheme and S-scheme electronic transition on excitation under sunlight. The expectation is found to be true in the study with excellent and synergistic catalytic activity obtained from the nanocomposite of $AgBi_3S_5$ and Bi_2S_3 in the degradation of Rh-B.

Cu_9S_5 is chosen as an efficient catalyst for direct methanol fuel cell oxidation for the following reasons. We synthesize Cu_9S_5 versatile nanomaterials following a newly designed synthesis route and also unveiling its new catalytic wing towards electrochemical methanol oxidation reaction. Cu_9S_5 and its supported alloys in different forms and structures used in the various fields as semiconductor, asymmetric supercapacitors, as anodes for high performance lithium-ion and sodium-ion batteries, efficient catalyst for water splitting, in broad band high performance electromagnetic wave absorber, as an environmental pollution removal and photothermal conversion, as a photothermal agent with nearly 26% heat conversion efficiency for photothermal ablation of cancer cells in vivo and in multimodal tumor therapy **[258-266]**. We demonstrated electrochemical and photochemical oxidation of methanol in lower negative potential zone without supporting of any noble metal and also shown its catalytic efficiency increases in presence of light. Hopefully this new insight regarding Cu_9S_5 nanomaterials towards electrochemical oxidation helps researcher to designing catalyst without support of any noble metal also give new direction to better optimization of its stability and make them feasible for commercial purpose.

1.11.6 Objectives of the present work

To provide some knowledge to an appropriate solution and simultaneously contribute in the current research field of green energy generation and water remediation for sustainable and economically viable future, are the primary and main objectives of our present work. For that we designed new catalyst along with new synthesis route which were efficient, effective and environment friendly. For fulfillment of our objectives, we synthesized by designing new synthesis route of simple, cost effective, environment friendly, sulfide-based nanomaterials such as Ag_2S, Bi_2S_3, $AgBi_3S_5$,

$CuBiS_2$ catalysts and used them for the first time in the field of green hydrogen generation. Non - noble metal-based nanomaterial, Cu_9S_5 developed also via new synthetic route for the first time and its characteristic feature revealed experimentally for anode catalysis in fuel cells along with photo assisted fuel cells. $AgBi_3S_5$-Bi_2S_3 nanocomposites were synthesized and used as a catalyst for green hydrogen generation and also for photochemical pollutant degradation. The said catalyst is used to show the catalytic efficiency for the first time in the above-mentioned field.

1.11.7 Organization of the Thesis Chapters

A total six chapters are integrated in the present thesis and summarized the whole work and highlighted the main findings along with their novelty, exploring the scopes of the future work related to Green Energy and Environmental field as presented in Chapter 6.

Chapter 1

In chapter 1, we discussed the necessity of our current work in today's globalized world identified the problems evolving to energy and environment fields as problems of us and all the potential components acting as raw materials to make a bridge for one earth and one family through which we are easily connected more effortlessly to each other and probably find out solution of each other's complex problems. The chapter describes thoroughly fundamentals of water splitting for hydrogen generation, different kinds of method involved related to it, types of parameters effecting such processes, fundamentals of Fuel cells applications and their contribution towards renewable energy generation, fundamental of water remediation highlighting the positive outbreak how organic pollutants from the different industry become potential contender towards water management system. Finally, literature review related to involvement of sulfide-based materials to this said application fields along with scopes and objectives of our research, brief explanation for choosing different components related to bring efficiency of such applications.

Chapter 2

Mainly deals with the new synthesis procedures followed by characterization of newly synthesized nanomaterials ($AgBi_3S_5$, Bi_2S_3, Ag_2S, $CuBiS_2$), and highlights their contribution in catalysis towards electrochemical hydrogen generation, optimization of their performance through specific

techniques such LSV, CV, CA, EIS etc. and determining the faradaic efficiency of hydrogen production. It also establishes the catalytic fate of the best electrocatalyst after use in electrochemical water splitting reaction, conclusion through characteristics findings and indicates the future prospects of such materials.

Chapter 3

Explores the photochemical water splitting reaction with newly synthesized $AgBi_3S_5$-Bi_2S_3 nanocomposites as catalyst, characterization with respect to their formation with XRD, FTIR, XPS, SEM, TEM, SAED, ELEMENTAL MAPPING like tools, highlighting the performance in photochemical water splitting, optimized the performance of this synthesized nanomaterials in absence and presence of light through CV, LSV, CA, EIS like techniques. Finally, it establishes robustness of the synthesized material in photochemical water splitting with photocurrent measurement and CA like techniques. Notable findings are discussed in the conclusion part.

Chapter 4

This chapter primarily deals with revealing the electrochemical and photochemical anodic methanol oxidation through newly developed novel metal free catalyst Cu_9S_5, optimization of its formation via XRD, FTIR, SEM, TEM, EDX, ELEMENTAL MAPPING like techniques. Optimization of electrochemical performance with CV, CA, EIS like studies, product identified via HPLC method, and suggesting probable reaction mechanism of such electrochemical oxidation on the basis of product identification, showing the efficiency of this process in presence of light, finally summarized all the unique findings in the conclusion section.

Chapter 5

Chapter 5 apparently highlights the water remediation from the organic pollutant, Rh-B dye by degradation in presence of newly synthesized $AgBi_3S_5$-Bi_2S_3 nanocomposite in presence of natural sunlight. It also verifies its formation through XRD, FTIR, XPS, SEM, TEM, EDX, ELEMENTAL MAPPING like techniques, spectral studies through UV, PL,TCSPC like experimental techniques, optimization of Rh-B degradation performance in presence of $AgBi_3S_5$-Bi_2S_3 catalyst under natural light illumination via measurement of absorption with the assistance of UV-vis spectroscopy, photo-current experiment, TCSPC spectral techniques, verified performance at

optimum pH with zeta potential like techniques, identified the main scavenger responsible for this process as well product identification via mass spectrometry and demonstrated mechanism of such process. Finally optimized the catalytic efficacy of synthesized $AgBi_3S_5$-Bi_2S_3 via recyclization techniques, BET, EDX, FTIR, XRD like studies. In conclusion main highlighted findings are mentioned.

Chapter 6

It briefly summarizes the significant outcome of previous chapters and future prospect of these materials in the respective prominent fields.

References:

1. Seh, Z. W.; Kibsgaard, J.; Dickens, C. F.; Chorkendorff, I. B.; Nørskov, J. K.; & Jaramillo, T. F. Combining theory and experiment in electrocatalysis: Insights into materials design. *Science*. **2017**, *355*(6321), eaad4998.
2. Walter, M. G.; Warren, E. L.; McKone, J. R.; Boettcher, S. W.; Mi, Q., Santori, E. A.; & Lewis, N. S. Solar water splitting cells. *Chemical reviews*, **2010**, *110*(11), 6446-6473.
3. Balat, M.; & Balat, H. Biogas as a renewable energy source—a review. *Energy Sources, Part A*. **2009**, *31*(14), 1280-1293.
4. Byrne, J.; Hughes, K.; Rickerson, W.; & Kurdgelashvili, L. American policy conflict in the greenhouse: Divergent trends in federal, regional, state, and local green energy and climate change policy. *Energy Policy*. **2007**, *35*(9), 4555-4573.
5. Solomon, S.; Plattner, G. K.; Knutti, R.; & Friedlingstein, P. Irreversible climate change due to carbon dioxide emissions. *Proceedings of the national academy of sciences*, **2009**, *106*(6), 1704-1709.
6. Di Primio, R.; Horsfield, B.; & Guzman-Vega, M. A. Determining the temperature of petroleum formation from the kinetic properties of petroleum asphaltenes. *Nature*. **2000**, *406*(6792), 173-176.
7. Chandrasekaran, S.; Yao, L.; Deng, L.; Bowen, C.; Zhang, Y.; Chen, S.; ... & Zhang, P. Recent advances in metal sulfides: from controlled fabrication to electrocatalytic,

photocatalytic and photoelectrochemical water splitting and beyond. *Chemical Society Reviews*. **2019**, *48*(15), 4178-4280.

8. Schlapbach, L.; & Züttel, A. Hydrogen-storage materials for mobile applications. *Nature*. **2001**, *414*(6861), 353-358.
9. Roger, I.; Shipman, M. A.; & Symes, M. D. Earth-abundant catalysts for electrochemical and photoelectrochemical water splitting. *Nature Reviews Chemistry*. **2017**, *1*(1), 1-13.
10. Lewis, N. S. Research opportunities to advance solar energy utilization. *Science*, **2016**, *351*(6271), aad1920.
11. Wang, J.; Shi, W.; Liu, D.; Zhang, Z.; Zhu, Y.; & Wang, D. Supramolecular organic nanofibers with highly efficient and stable visible light photooxidation performance. *Applied Catalysis B: Environmental*. **2017**, *202*, 289-297.
12. Wei, Z.; Hu, J.; Zhu, K.; Wei, W.; Ma, X.; & Zhu, Y. Self-assembled polymer phenylethnylcopper nanowires for photoelectrochemical and photocatalytic performance under visible light. *Applied Catalysis B: Environmental*. **2018**, *226*, 616-623.
13. Hughes, T. P.; Kerry, J. T.; Álvarez-Noriega, M.; Álvarez-Romero, J. G.; Anderson, K. D.; Baird, A. H.; ... & Wilson, S. K. Global warming and recurrent mass bleaching of corals. *Nature*. **2017**, *543*(7645), 373-377.
14. AghaKouchak, A.; Cheng, L.; Mazdiyasni, O.; & Farahmand, A. Global warming and changes in risk of concurrent climate extremes: Insights from the 2014 California drought. *Geophysical Research Letters*. **2014**, *41*(24), 8847-8852.
15. Lancaster, K. M.; George, S. D.; Yokoyama, K.; Richards, J. H.; & Gray, H. B. Type-zero copper proteins. *Nature chemistry*. **2009**, *1*(9), 711-715.
16. Brockris, J. O. M.; & Srinivasan, S. Fuel cells: their electrochemistry. **1969**.
17. Holkar, C. R.; Jadhav, A. J.; Pinjari, D. V.; Mahamuni, N. M.; & Pandit, A. B. A critical review on textile wastewater treatments: possible approaches. *Journal of environmental management*. **2016**, *182*, 351-366.
18. Damodhar, U.; & Vikram Reddy, M. Impact of pharmaceutical industry treated effluents on the water quality of river Uppanar, South east coast of India: a case study. *Applied Water Science*. **2013**, *3*, 501-514.

19. Yaseen, D. A.; & Scholz, M. Textile dye wastewater characteristics and constituents of synthetic effluents: a critical review. *International journal of environmental science and technology*. **2019**, *16*, 1193-1226.
20. Gürses, A.; Açıkyıldız, M.; Güneş, K.; & Gürses, M. S. *Dyes and pigments*. Springer. **2016.**
21. Hassaan, M. A.; El Nemr, A.; & Hassaan, A. Health and environmental impacts of dyes: mini review. *American Journal of Environmental Science and Engineering*. **2017**, *1*(3), 64-67.
22. Yan, Y.; Xia, B. Y.; Zhao, B.; & Wang, X. A review on noble-metal-free bifunctional heterogeneous catalysts for overall electrochemical water splitting. *Journal of Materials Chemistry A*. **2016**, *4*(45), 17587-17603.
23. Tao, Z.; Wang, T.; Wang, X.; Zheng, J.; & Li, X. MOF-derived noble metal free catalysts for electrochemical water splitting. *ACS applied materials & interfaces*, **2016**, *8*(51), 35390-35397.
24. Mahmood, N.; Yao, Y.; Zhang, J. W.; Pan, L.; Zhang, X.; & Zou, J. J. Electrocatalysts for hydrogen evolution in alkaline electrolytes: mechanisms, challenges, and prospective solutions. *Advanced Science*. **2018**, *5*(2), 1700464.
25. Ojha, K.; Saha, S.; Dagar, P.; & Ganguli, A. K. Nanocatalysts for hydrogen evolution reactions. *Physical Chemistry Chemical Physics*. **2018**, *20*(10), 6777-6799.
26. Guo, Y.; Park, T.; Yi, J. W.; Henzie, J.; Kim, J.; Wang, Z.; ... & Yamauchi, Y. Nanoarchitectonics for transition-metal-sulfide-based electrocatalysts for water splitting. *Advanced Materials*. **2019**, *31*(17), 1807134.
27. Liu, Z.; Zhang, C.; Liu, H.; & Feng, L. Efficient synergism of NiSe2 nanoparticle/NiO nanosheet for energy-relevant water and urea electrocatalysis. *Applied Catalysis B: Environmental*. **2020**, *276*, 119165.
28. Rossmeisl, J.; Qu, Z. W.; Zhu, H.; Kroes, G. J.; & Nørskov, J. K. Electrolysis of water on oxide surfaces. *Journal of Electroanalytical Chemistry*. **2007**, *607*(1-2), 83-89.
29. Joo, J.; Kim, T.; Lee, J.; Choi, S. I.; & Lee, K. Morphology-controlled metal sulfides and phosphides for electrochemical water splitting. *Advanced materials*. **2019**, *31*(14), 1806682.
30. Dincer, I. Green methods for hydrogen production. *International journal of hydrogen energy*. **2012**, *37*(2), 1954-1971.

31. Dincer, I.; & Naterer, G. F. Overview of hydrogen production research in the Clean Energy Research Laboratory (CERL) at UOIT. *International journal of hydrogen energy*. **2014**, *39*(35), 20592-20613.
32. Orhan, M. F.; Dincer, I.; Rosen, M. A.; & Kanoglu, M. Integrated hydrogen production options based on renewable and nuclear energy sources. *Renewable and Sustainable Energy Reviews*. **2012**, *16*(8), 6059-6082.
33. Dincer, I.; & Rosen, M. A. Sustainability aspects of hydrogen and fuel cell systems. *Energy for sustainable development*. **2011**, *15*(2), 137-146.
34. Dincer, I.; & Zamfirescu, C. Sustainable hydrogen production options and the role of IAHE. *International Journal of Hydrogen Energy*. **2012**, *37*(21), 16266-16286.
35. Acar, C.; & Dincer, I. Comparative assessment of hydrogen production methods from renewable and non-renewable sources. *International journal of hydrogen energy*. **2014**, *39*(1), 1-12.
36. Anantharaj, S.; Ede, S. R.; Karthick, K.; Sankar, S. S.; Sangeetha, K.; Karthik, P. E.; & Kundu, S. Precision and correctness in the evaluation of electrocatalytic water splitting: revisiting activity parameters with a critical assessment. *Energy & Environmental Science*. **2018**, *11*(4), 744-771.
37. Zou, X.; & Zhang, Y. Noble metal-free hydrogen evolution catalysts for water splitting. *Chemical Society Reviews*. **2015**, *44*(15), 5148-5180.
38. Suen, N. T.; Hung, S. F.; Quan, Q.; Zhang, N.; Xu, Y. J.; & Chen, H. M. Electrocatalysis for the oxygen evolution reaction: recent development and future perspectives. *Chemical Society Reviews*. **2017**, *46*(2), 337-365.
39. Wu, Z. P.; Lu, X. F.; Zang, S. Q.; & Lou, X. W. Non-noble-metal-based electrocatalysts toward the oxygen evolution reaction. *Advanced Functional Materials*. **2020**, *30*(15), 1910274.
40. Chen, D.; Chen, C.; Baiyee, Z. M.; Shao, Z.; & Ciucci, F. Nonstoichiometric oxides as low-cost and highly-efficient oxygen reduction/evolution catalysts for low-temperature electrochemical devices. *Chemical reviews*. **2015**, *115*(18), 9869-9921.
41. Winter, M.; & Brodd, R. J. What are batteries, fuel cells, and supercapacitors? .*Chemical reviews*. **2004**, *104*(10), 4245-4270.

42. Khaligh, A.; & Li, Z. Battery, ultracapacitor, fuel cell, and hybrid energy storage systems for electric, hybrid electric, fuel cell, and plug-in hybrid electric vehicles: State of the art. *IEEE transactions on Vehicular Technology*. **2010**, *59*(6), 2806-2814.
43. Andújar, J. M.; & Segura, F. Fuel cells: History and updating. A walk along two centuries. *Renewable and sustainable energy reviews*. **2009**, *13*(9), 2309-2322.
44. Perry, M. L.; & Fuller, T. F. A historical perspective of fuel cell technology in the 20th century. *Journal-Electrochemical Society*. **2002**, *149*(7), S59-S67.
45. Vishnyakov, V. M. Proton exchange membrane fuel cells. *Vacuum*. **2006**, *80*(10), 1053-1065.
46. Ou, D. R.; Mori, T.; Togasaki, H.; Takahashi, M.; Ye, F.; & Drennan, J. Microstructural and metal− support interactions of the Pt− CeO2/C catalysts for direct methanol fuel cell application. *Langmuir*. **2011**, *27*(7), 3859-3866.
47. Huang, Y.; Huang, H.; Liu, Y.; Xie, Y.; Liang, Z.; & Liu, C. Facile synthesis of poly (amidoamine)-modified carbon nanospheres supported Pt nanoparticles for direct methanol fuel cells. *Journal of Power Sources*. **2012**, *201*, 81-87.
48. Lamy, C.; Lima, A.; LeRhun, V.; Delime, F.; Coutanceau, C.; & Léger, J. M. Recent advances in the development of direct alcohol fuel cells (DAFC). *Journal of Power Sources*. **2002**, *105*(2), 283-296.
49. Mills, A.; & Le Hunte, S. An overview of semiconductor photocatalysis. *Journal of photochemistry and photobiology A: Chemistry*. **1997**, *108*(1), 1-35.
50. Hisatomi, T.; Kubota, J.; & Domen, K. Recent advances in semiconductors for photocatalytic and photoelectrochemical water splitting. *Chemical Society Reviews*. **2014**, *43*(22), 7520-7535.
51. Gregory, P. Classification of dyes by chemical structure. *The chemistry and application of dyes*. **1990**, 17-47.
52. Chung, K. T. Azo dyes and human health: A review. *Journal of Environmental Science and Health, Part C*. **2016**, *34*(4), 233-261.
53. Lucas, M. S.; Dias, A. A.; Sampaio, A.; Amaral, C.; & Peres, J. A. Degradation of a textile reactive Azo dye by a combined chemical–biological process: Fenton's reagent-yeast. *Water research*. **2007**, *41*(5), 1103-1109.

54. Foo, K. Y.; & Hameed, B. H. Decontamination of textile wastewater via TiO2/activated carbon composite materials. *Advances in colloid and interface science*. **2010**, *159*(2), 130-143.
55. Verma, A. K.; Dash, R. R., & Bhunia, P. A review on chemical coagulation/flocculation technologies for removal of colour from textile wastewaters. *Journal of environmental management*. **2012**, *93*(1), 154-168.
56. Gogate, P. R.; & Pandit, A. B. A review of imperative technologies for wastewater treatment I: oxidation technologies at ambient conditions. *Advances in environmental research*, **2004**, *8*(3-4), 501-551.
57. Nidheesh, P. V.; Gandhimathi, R.; & Ramesh, S. T. Degradation of dyes from aqueous solution by Fenton processes: a review. *Environmental Science and Pollution Research*. **2013**, *20*, 2099-2132.
58. Muruganandham, M.; & Swaminathan, M. Decolourisation of Reactive Orange 4 by Fenton and photo-Fenton oxidation technology. *Dyes and pigments*. **2004**, *63*(3), 315-321.
59. Sudhaik, A.; Raizada, P.; Shandilya, P.; Jeong, D. Y.; Lim, J. H.; & Singh, P. Review on fabrication of graphitic carbon nitride based efficient nanocomposites for photodegradation of aqueous phase organic pollutants. *Journal of Industrial and Engineering Chemistry*. **2018**, *67*, 28-51.
60. Hasija, V.; Raizada, P.; Sudhaik, A.; Sharma, K.; Kumar, A.; Singh, P.; ... & Thakur, V. K. Recent advances in noble metal free doped graphitic carbon nitride based nanohybrids for photocatalysis of organic contaminants in water: a review. *Applied Materials Today*. **2019**, *15*, 494-524.
61. Han, S. A.; Bhatia, R.; & Kim, S. W. Synthesis, properties and potential applications of two-dimensional transition metal dichalcogenides. *Nano Convergence*. **2015**, *2*, 1-14.
62. Li, H.; Wu, J.; Yin, Z.; & Zhang, H. Preparation and applications of mechanically exfoliated single-layer and multilayer MoS2 and WSe2 nanosheets. *Accounts of chemical research*. **2014**, *47*(4), 1067-1075.
63. Li, Z.; Young, R. J.; Backes, C.; Zhao, W.; Zhang, X.; Zhukov, A. A.; ... & Coleman, J. N. Mechanisms of liquid-phase exfoliation for the production of graphene. *ACS nano*, **2020**, *14*(9), 10976-10985.

64. Coleman, J. N.; Lotya, M.; O'Neill, A.; Bergin, S. D.; King, P. J.; Khan, U.; ... & Nicolosi, V. Two-dimensional nanosheets produced by liquid exfoliation of layered materials. *Science*. **2011**, *331*(6017), 568-571.
65. Varrla, E.; Backes, C.; Paton, K. R.; Harvey, A.; Gholamvand, Z.; McCauley, J.; & Coleman, J. N. Large-scale production of size-controlled MoS2 nanosheets by shear exfoliation. *Chemistry of Materials*. **2015**, *27*(3), 1129-1139.
66. Ambrosi, A.; Chia, X.; Sofer, Z.; & Pumera, M. Enhancement of electrochemical and catalytic properties of MoS2 through ball-milling. *Electrochemistry Communications*. **2015**, *54*, 36-40.
67. Luo, P.; Zhang, H.; Liu, L.; Zhang, Y.; Deng, J.; Xu, C.; ... & Wang, Y. Targeted synthesis of unique nickel sulfide (NiS, NiS2) microarchitectures and the applications for the enhanced water splitting system. *ACS applied materials & interfaces*. **2017**, *9*(3), 2500-2508.
68. Dong, W.; Wang, X.; Li, B.; Wang, L.; Chen, B.; Li, C.; ... & Shi, Z. Hydrothermal synthesis and structure evolution of hierarchical cobalt sulfide nanostructures. *Dalton Transactions*. **2011**, *40*(1), 243-248.
69. Jaramillo, T. F.; Jørgensen, K. P.; Bonde, J.; Nielsen, J. H.; Horch, S.; & Chorkendorff, I. Identification of active edge sites for electrochemical H2 evolution from MoS2 nanocatalysts. *Science*. **2007**, *317*(5834), 100-102.
70. Dong, J.; Zhang, F. Q.; Yang, Y.; Zhang, Y. B.; He, H.; Huang, X.; ... & Zhang, X. M. (003)-Facet-exposed Ni3S2 nanoporous thin films on nickel foil for efficient water splitting. *Applied Catalysis B: Environmental*. **2019**, *243*, 693-702.
71. Staszak-Jirkovský, J.; Malliakas, C. D.; Lopes, P. P.; Danilovic, N.; Kota, S. S.; Chang, K. C.; ... & Markovic, N. M. Design of active and stable Co–Mo–S x chalcogels as pH-universal catalysts for the hydrogen evolution reaction. *Nature materials*. **2016**, *15*(2), 197-203.
72. Shang, X.; Hu, W. H.; Li, X., Dong, B.; Liu, Y. R.; Han, G. Q.; ... & Liu, C. G. Oriented stacking along vertical (002) planes of MoS2: a novel assembling style to enhance activity for hydrogen evolution. *Electrochimica Acta*. **2017**, *224*, 25-31.

73. Kong, D.; Wang, H.; Cha, J. J.; Pasta, M.; Koski, K. J.; Yao, J.; & Cui, Y. Synthesis of MoS2 and MoSe2 films with vertically aligned layers. *Nano letters*. **2013**, *13*(3), 1341-1347.
74. Kibsgaard, J.; Chen, Z.; Reinecke, B. N.; & Jaramillo, T. F. Engineering the surface structure of MoS2 to preferentially expose active edge sites for electrocatalysis. *Nature materials*. **2012**, *11*(11), 963-969.
75. Deng, J.; Haobo, L.; Suheng, W.; Ding, D.; Mingshu, C.; Chuan, L.; Zhongqun, T. "Multiscale structural and electronic control of molybdenum disulfide foam for highly efficient hydrogen production." *Nature communications.* **2017,** 8 (1) 14430.
76. Yang, Y.; Fei, H.; Ruan, G.; Li, Y.; & Tour, J. M. Vertically aligned WS2 nanosheets for water splitting. *Advanced Functional Materials*. **2015**, *25*(39), 6199-6204.
77. Shang, X.; Yan, K. L.; Liu, Z. Z.; Lu, S. S.; Dong, B.; Chi, J. Q.; ... & Liu, C. G. Oxidized carbon fiber supported vertical WS2 nanosheets arrays as efficient 3 D nanostructure electrocatalyts for hydrogen evolution reaction. Applied Surface Science. **2017**, 402, 120-128.
78. Yu, J. H.; Lee, H. R.; Hong, S. S.; Kong, D.; Lee, H. W.; Wang, H.; ... & Cui, Y. Vertical heterostructure of two-dimensional MoS2 and WSe2 with vertically aligned layers. Nano letters. **2015**, 15(2), 1031-1035.
79. Huang, L. B.; Zhao, L.; Zhang, Y.; Chen, Y. Y.; Zhang, Q. H.; Luo, H.; ... & Hu, J. S. Self-limited on-site conversion of MoO3 nanodots into vertically aligned ultrasmall monolayer MoS2 for efficient hydrogen evolution. Advanced Energy Materials. **2018**, 8(21), 1800734.
80. Xie, J.; Qu, H.; Xin, J.; Zhang, X.; Cui, G.; Zhang, X.; ... & Xie, Y. Defect-rich MoS 2 nanowall catalyst for efficient hydrogen evolution reaction. Nano Research. **2017**, 10, 1178-1188.
81. Chen, Y.; Huang, S.; Ji, X.; Adepalli, K.; Yin, K.; Ling, X.; ... & Yildiz, B. Tuning electronic structure of single layer MoS2 through defect and interface engineering. *ACS nano*. **2018**, *12*(3), 2569-2579.
82. Bertolazzi, S.; Bonacchi, S.; Nan, G.; Pershin, A.; Beljonne, D.; & Samorì, P. Engineering chemically active defects in monolayer MoS2 transistors via ion-beam irradiation and their healing via vapor deposition of alkanethiols. *Advanced materials*. **2017**, *29*(18), 1606760.

83. Qi, K.; Yu, S.; Wang, Q.; Zhang, W.; Fan, J.; Zheng, W.; & Cui, X. Decoration of the inert basal plane of defect-rich MoS 2 with Pd atoms for achieving Pt-similar HER activity. *Journal of Materials Chemistry A*. **2016**, *4*(11), 4025-4031.
84. Ouyang, Y.; Ling, C.; Chen, Q.; Wang, Z.; Shi, L.; & Wang, J. Activating inert basal planes of MoS2 for hydrogen evolution reaction through the formation of different intrinsic defects. *Chemistry of Materials*. **2016**, *28*(12), 4390-4396.
85. Xie, J.; Zhang, J.; Li, S.; Grote, F.; Zhang, X.; Zhang, H.; ... & Xie, Y. Controllable disorder engineering in oxygen-incorporated MoS2 ultrathin nanosheets for efficient hydrogen evolution. *Journal of the American Chemical Society*. **2013**, *135*(47), 17881-17888.
86. Yang, L.; Zhou, W.; Lu, J.; Hou, D.; Ke, Y.; Li, G.; ... & Chen, S. Hierarchical spheres constructed by defect-rich MoS2/carbon nanosheets for efficient electrocatalytic hydrogen evolution. *Nano energy*. **2016**, *22*, 490-498.
87. Ye, G.; Gong, Y.; Lin, J.; Li, B.; He, Y.; Pantelides, S. T.; ... & Ajayan, P. M. Defects engineered monolayer MoS2 for improved hydrogen evolution reaction. *Nano letters*. **2016**, *16*(2), 1097-1103.
88. Xie, J.; Zhang, H.; Li, S.; Wang, R.; Sun, X.; Zhou, M.; ... & Xie, Y. Defect-rich MoS2 ultrathin nanosheets with additional active edge sites for enhanced electrocatalytic hydrogen evolution. *Advanced materials*. **2013**, (40), 5807-5813.
89. Zhu, P.; Chen, Y.; Zhou, Y.; Yang, Z.; Wu, D.; Xiong, X.; & Ouyang, F. Defect-rich MoS2 nanosheets vertically grown on graphene-protected Ni foams for high efficient electrocatalytic hydrogen evolution. *International Journal of Hydrogen Energy*. **2018**, *43*(31), 14087-14095.
90. Lukowski, M. A.; Daniel, A. S.; Meng, F.; Forticaux, A.; Li, L.; & Jin, S. Enhanced hydrogen evolution catalysis from chemically exfoliated metallic MoS2 nanosheets. *Journal of the American Chemical Society*. **2013**, *135*(28), 10274-10277.
91. Wang, J.; Tang, J.; Guo, T.; Zhang, S.; Xia, W.; Tan, H.; ... & Yamauchi, Y. C 3 N 4-digested 3D construction of hierarchical metallic phase MoS 2 nanostructures. *Journal of Materials Chemistry A*. **2019**, *7*(31), 18388-18396.
92. Voiry, D.; Yamaguchi, H.; Li, J.; Silva, R.; Alves, D. C.; Fujita, T.; ... & Chhowalla, M. Enhanced catalytic activity in strained chemically exfoliated WS2 nanosheets for hydrogen evolution. *Nature materials*. **2013**, *12*(9), 850-855.

93. Lin, Y. C.; Dumcenco, D. O.; Huang, Y. S.; & Suenaga, K. Atomic mechanism of the semiconducting-to-metallic phase transition in single-layered MoS2. *Nature nanotechnology*. **2014**, *9*(5), 391-396.
94. Kang, Y.; Najmaei, S.; Liu, Z.; Bao, Y.; Wang, Y.; Zhu, X.; ... & Fang, Z. Plasmonic hot electron induced structural phase transition in a MoS2 monolayer. *Advanced materials*. **2014**, *26*(37), 6467-6471.
95. Duerloo, K. A. N.; Li, Y.; & Reed, E. J. Structural phase transitions in two-dimensional Mo-and W-dichalcogenide monolayers. *Nature communications*. **2014**, *5*(1), 4214.
96. Mahler, B.; Hoepfner, V.; Liao, K.; & Ozin, G. A. Colloidal synthesis of 1T-WS2 and 2H-WS2 nanosheets: applications for photocatalytic hydrogen evolution. *Journal of the American Chemical Society*, **2014**, *136*(40), 14121-14127.
97. Voiry, D.; Goswami, A.; Kappera, R.; Silva, C. D. C. C. E.; Kaplan, D.; Fujita, T.; ... & Chhowalla, M. Covalent functionalization of monolayered transition metal dichalcogenides by phase engineering. *Nature chemistry*. **2015**, *7*(1), 45-49.
98. Acerce, M.; Voiry, D.; & Chhowalla, M. Metallic 1T phase MoS2 nanosheets as supercapacitor electrode materials. *Nature nanotechnology*. **2015**, *10*(4), 313-318.
99. Yu, Y.; Nam, G. H.; He, Q.; Wu, X. J.; Zhang, K.; Yang, Z.; ... & Zhang, H. High phase-purity 1T′-MoS2-and 1T′-MoSe2-layered crystals. *Nature chemistry*. **2018**, *10*(6), 638-643.
100. Liu, Z.; Li, N.; Su, C.; Zhao, H.; Xu, L.; Yin, Z.; ... & Du, Y. Colloidal synthesis of 1T'phase dominated WS2 towards endurable electrocatalysis. *Nano Energy*. **2018**, *50*, 176-181.
101. He, W.; Ifraemov, R.; Raslin, A.; & Hod, I. Room-temperature electrochemical conversion of metal–organic frameworks into porous amorphous metal sulfides with tailored composition and hydrogen evolution activity. *Advanced Functional Materials*. **2018**, *28*(18), 1707244.
102. Dinda, D.; Ahmed, M. E.; Mandal, S.; Mondal, B.; & Saha, S. K. Amorphous molybdenum sulfide quantum dots: an efficient hydrogen evolution electrocatalyst in neutral medium. *Journal of Materials Chemistry A*. **2016**, *4*(40), 15486-15493.
103. Vrubel, H.; & Hu, X. Growth and activation of an amorphous molybdenum sulfide hydrogen evolving catalyst. *Acs Catalysis*. **2013**, *3*(9), 2002-2011.

104. Merki, D.; Fierro, S.; Vrubel, H.; & Hu, X. Amorphous molybdenum sulfide films as catalysts for electrochemical hydrogen production in water. Chem Sci. **2011**, 2, 1262–1267.

105. Merki, D.; Vrubel, H.; Rovelli, L.; Fierro, S.; & Hu, X. Fe, Co, and Ni ions promote the catalytic activity of amorphous molybdenum sulfide films for hydrogen evolution. *Chemical Science*. **2012**, *3*(8), 2515-2525.

106. Chang, Y. H.; Lin, C. T.; Chen, T. Y.; Hsu, C. L.; Lee, Y. H.; Zhang, W.; ... & Li, L. J. Highly efficient electrocatalytic hydrogen production by MoSx grown on graphene-protected 3D Ni foams. *Advanced materials*. **2013**, *25*(5), 756-760.

107. Ge, X.; Chen, L.; Zhang, L.; Wen, Y.; Hirata, A.; & Chen, M. Nanoporous metal enhanced catalytic activities of amorphous molybdenum sulfide for high-efficiency hydrogen production. *Advanced Materials (Deerfield Beach, Fla.)*. **2014**, *26*(19), 3100-3104.

108. Li, D. J.; Maiti, U. N.; Lim, J.; Choi, D. S.; Lee, W. J.; Oh, Y.; ... & Kim, S. O. Molybdenum sulfide/N-doped CNT forest hybrid catalysts for high-performance hydrogen evolution reaction. *Nano letters*. **2014**, *14*(3), 1228-1233.

109. Lee, S. C.; Benck, J. D.; Tsai, C.; Park, J.; Koh, A. L.; Abild-Pedersen, F.; ... & Sinclair, R. Chemical and phase evolution of amorphous molybdenum sulfide catalysts for electrochemical hydrogen production. *ACS nano*. **2016**, *10*(1), 624-632.

110. Lassalle-Kaiser, B.; Merki, D.; Vrubel, H.; Gul, S.; Yachandra, V. K.; Hu, X.; & Yano, J. Evidence from in situ X-ray absorption spectroscopy for the involvement of terminal disulfide in the reduction of protons by an amorphous molybdenum sulfide electrocatalyst. *Journal of the American Chemical Society*. **2015**, *137*(1), 314-321.

111. Ting, L. R. L.; Deng, Y.; Ma, L.; Zhang, Y. J.; Peterson, A. A.; & Yeo, B. S. Catalytic activities of sulfur atoms in amorphous molybdenum sulfide for the electrochemical hydrogen evolution reaction. *Acs Catalysis*. **2016**, *6*(2), 861-867.

112. Tran, P. D.; Tran, T. V.; Orio, M.; Torelli, S.; Truong, Q. D.; Nayuki, K.; ... & Artero, V. Coordination polymer structure and revisited hydrogen evolution catalytic mechanism for amorphous molybdenum sulfide. *Nature materials*. **2016**, *15*(6), 640-646.

113. Deng, Y.; Ting, L. R. L.; Neo, P. H. L.; Zhang, Y. J.; Peterson, A. A.; & Yeo, B. S. Operando Raman spectroscopy of amorphous molybdenum sulfide (MoS x) during the

electrochemical hydrogen evolution reaction: Identification of sulfur atoms as catalytically active sites for H+ reduction. *ACS catalysis*. **2016**, *6*(11), 7790-7798.

114. Kibsgaard, J.; Jaramillo, T. F.; & Besenbacher, F. Building an appropriate active-site motif into a hydrogen-evolution catalyst with thiomolybdate [Mo3S13] 2− clusters. *Nature chemistry*. **2014**, *6*(3), 248-253.
115. Attanayake, N. H.; Abeyweera, S. C.; Thenuwara, A. C.; Anasori, B.; Gogotsi, Y.; Sun, Y.; & Strongin, D. R. Vertically aligned MoS 2 on Ti 3 C 2 (MXene) as an improved HER catalyst. *Journal of Materials Chemistry A*. **2018**, *6*(35), 16882-16889.
116. Xu, Y.; Wang, L.; Liu, X.; Zhang, S.; Liu, C.; Yan, D.; ... & Luo, S. Monolayer MoS 2 with S vacancies from interlayer spacing expanded counterparts for highly efficient electrochemical hydrogen production. *Journal of Materials Chemistry A*. **2016**, *4*(42), 16524-16530.
117. Gao, M. R.; Chan, M. K.; & Sun, Y. Edge-terminated molybdenum disulfide with a 9.4-Å interlayer spacing for electrochemical hydrogen production. *Nature communications*. **2015**, *6*(1), 7493.
118. Sun, Y.; Alimohammadi, F.; Zhang, D.; & Guo, G. Enabling colloidal synthesis of edge-oriented MoS2 with expanded interlayer spacing for enhanced HER catalysis. *Nano letters*. **2017**, *17*(3), 1963-1969.
119. Tang, Y. J.; Wang, Y.; Wang, X. L.; Li, S. L.; Huang, W.; Dong, L. Z.; ... & Lan, Y. Q. Molybdenum disulfide/nitrogen-doped reduced graphene oxide nanocomposite with enlarged interlayer spacing for electrocatalytic hydrogen evolution. *Advanced Energy Materials*. **2016**, *6*(12), 1600116.
120. Qi, K.; Yu, S.; Wang, Q.; Zhang, W.; Fan, J.; Zheng, W.; & Cui, X. Decoration of the inert basal plane of defect-rich MoS 2 with Pd atoms for achieving Pt-similar HER activity. *Journal of Materials Chemistry A*. **2016**, *4*(11), 4025-4031.
121. Wang, H.; Tsai, C.; Kong, D.; Chan, K.; Abild-Pedersen, F.; Nørskov, J. K.; & Cui, Y. Transition-metal doped edge sites in vertically aligned MoS 2 catalysts for enhanced hydrogen evolution. *Nano Research*. **2015**, *8*, 566-575.
122. Cheng, Y.; Lu, S.; Liao, F.; Liu, L.; Li, Y.; & Shao, M. Rh□ MoS2 Nanocomposite Catalysts with Pt-Like Activity for Hydrogen Evolution Reaction. *Advanced Functional Materials*. **2017**, *27*(23), 1700359.

123. Tang, K.; Wang, X.; Li, Q.; & Yan, C. High Edge Selectivity of In Situ Electrochemical Pt Deposition on Edge-Rich Layered WS2 Nanosheets. *Advanced Materials*. **2018**, *30*(7), 1704779.

124. Deng, J.; Li, H., Xiao, J.; Tu, Y.; Deng, D.; Yang, H.; ... & Bao, X. Triggering the electrocatalytic hydrogen evolution activity of the inert two-dimensional MoS 2 surface via single-atom metal doping. *Energy & environmental science*. **2015**, *8*(5), 1594-1601.

125. Shi, X.; Fields, M.; Park, J.; McEnaney, J. M.; Yan, H.; Zhang, Y.; ... & Zheng, X. Rapid flame doping of Co to WS 2 for efficient hydrogen evolution. *Energy & Environmental Science*. **2018**, *11*(8), 2270-2277.

126. Nipane, A.; Karmakar, D.; Kaushik, N.; Karande, S.; & Lodha, S. Few-layer MoS2 p-type devices enabled by selective doping using low energy phosphorus implantation. *ACS nano*. **2016**, *10*(2), 2128-2137.

127. Xiao, W.; Liu, P.; Zhang, J.; Song, W.; Feng, Y. P.; Gao, D.; & Ding, J. Dual-functional N dopants in edges and basal plane of MoS2 nanosheets toward efficient and durable hydrogen evolution. *Advanced Energy Materials*. **2017**, *7*(7), 1602086.

128. Ye, R.; Vicente, P. D. A.; Liu, Y.; Arellano-Jimenez, J.; Peng, Z.; Wang, T.; ... & Tour, J. M. High-performance hydrogen evolution from MoS2 (1− x) Px solid solution. *Advanced Materials (Deerfield Beach, Fla.)*. **2016**, *28*(7), 1427.

129. Huang, X.; Leng, M.; Xiao, W.; Li, M.; Ding, J.; Tan, T. L.; ... & Xue, J. Activating basal planes and S-terminated edges of MoS2 toward more efficient hydrogen evolution. *Advanced functional materials*. 2017, *27*(6), 1604943.

130. Liu, P., Zhu, J., Zhang, J., Xi, P., Tao, K., Gao, D., & Xue, D. (2017). P dopants triggered new basal plane active sites and enlarged interlayer spacing in MoS2 nanosheets toward electrocatalytic hydrogen evolution. *ACS Energy Letters*, *2*(4), 745-752.

131. Li, H.; Tsai, C.; Koh, A. L.; Cai, L.; Contryman, A. W.; Fragapane, A. H.; ... & Zheng, X. Activating and optimizing MoS2 basal planes for hydrogen evolution through the formation of strained sulphur vacancies. *Nature materials*. **2016**, *15*(1), 48-53.

132. Sun, Y.; Alimohammadi, F.; Zhang, D.; & Guo, G. Enabling colloidal synthesis of edge-oriented MoS2 with expanded interlayer spacing for enhanced HER catalysis. *Nano letters*. **2017**, *17*(3), 1963-1969.

133. Xiong, P.; Ma, R.; Sakai, N.; Nurdiwijayanto, L.; & Sasaki, T. Unilamellar metallic MoS2/graphene superlattice for efficient sodium storage and hydrogen evolution. *ACS Energy Letters*. **2018**, *3*(4), 997-1005.

134. Liao, L.; Zhu, J.; Bian, X.; Zhu, L.; Scanlon, M. D.; Girault, H. H.; & Liu, B. MoS2 formed on mesoporous graphene as a highly active catalyst for hydrogen evolution. *Advanced Functional Materials*. **2013**, *23*(42), 5326-5333.

135. Behranginia, A.; Asadi, M.; Liu, C.; Yasaei, P.; Kumar, B.; Phillips, P.; ... & Salehi-Khojin, A. Highly efficient hydrogen evolution reaction using crystalline layered three-dimensional molybdenum disulfides grown on graphene film. *Chemistry of Materials*. **2016**, *28*(2), 549-555.

136. Yu, H.; Xue, Y.; Hui, L.; Zhang, C.; Zhao, Y.; Li, Z.; & Li, Y. Controlled growth of MoS2 nanosheets on 2D N-doped graphdiyne nanolayers for highly associated effects on water reduction. *Advanced Functional Materials*, **2018**, *28*(19), 1707564.

137. Duan, J.; Chen, S.; Chambers, B. A.; Andersson, G. G.; & Qiao, S. Z. 3D WS 2 Nanolayers@ Heteroatom-Doped Graphene Films as Hydrogen Evolution Catalyst Electrodes. *Advanced Materials*. **2015**, *28*(27), 4234-4241.

138. Yang, L.; Zhou, W.; Lu, J.; Hou, D.; Ke, Y.; Li, G.; ... & Chen, S. Hierarchical spheres constructed by defect-rich MoS2/carbon nanosheets for efficient electrocatalytic hydrogen evolution. *Nano energy*. **2016**, *22*, 490-498.

139. Li, D. J.; Maiti, U. N.; Lim, J.; Choi, D. S.; Lee, W. J.; Oh, Y.; ... & Kim, S. O. Molybdenum sulfide/N-doped CNT forest hybrid catalysts for high-performance hydrogen evolution reaction. *Nano letters*. **2014**, *14*(3), 1228-1233.

140. Ye, T. N.; Lv, L. B.; Xu, M.; Zhang, B.; Wang, K. X.; Su, J.; ... & Chen, J. S. Hierarchical carbon nanopapers coupled with ultrathin MoS2 nanosheets: Highly efficient large-area electrodes for hydrogen evolution. *Nano Energy*. **2015**, *15*, 335-342.

141. Zhao, Z.; Qin, F.; Kasiraju, S.; Xie, L.; Alam, M. K.; Chen, S.; ... & Bao, J. Vertically aligned MoS2/Mo2C hybrid nanosheets grown on carbon paper for efficient electrocatalytic hydrogen evolution. *ACS Catalysis*. **2017**, *7*(10), 7312-7318.

142. Geng, X.; Wu, W.; Li, N.; Sun, W.; Armstrong, J.; Al-hilo, A.; ... & Chen, T. P. Three-dimensional structures of MoS2 nanosheets with ultrahigh hydrogen evolution reaction in water reduction. *Advanced Functional Materials*. **2014**, *24*(39), 6123-6129.

143. Li, Y.; Wang, H.; Xie, L.; Liang, Y.; Hong, G.; & Dai, H. MoS2 nanoparticles grown on graphene: an advanced catalyst for the hydrogen evolution reaction. *Journal of the American Chemical Society*. **2011**, *133*(19), 7296-7299.

144. Hu, J.; Zhang, C.; Jiang, L.; Lin, H.; An, Y.; Zhou, D.; ... & Yang, S. Nanohybridization of MoS2 with layered double hydroxides efficiently synergizes the hydrogen evolution in alkaline media. *Joule*. **2017**, *1*(2), 383-393.

145. Zhang, B.; Liu, J.; Wang, J.; Ruan, Y.; Ji, X.; Xu, K.; ... & Jiang, J. Interface engineering: the Ni (OH) 2/MoS2 heterostructure for highly efficient alkaline hydrogen evolution. *Nano Energy*. **2017**, *37*, 74-80.

146. Zhang, X.; & Liang, Y. Nickel hydr (oxy) oxide nanoparticles on metallic MoS2 nanosheets: a synergistic electrocatalyst for hydrogen evolution reaction. *Advanced Science*. **2018**, *5*(2), 1700644.

147. Luo, Y.; Li, X.; Cai, X.; Zou, X.; Kang, F.; Cheng, H. M.; & Liu, B. Two-dimensional MoS2 confined Co (OH) 2 electrocatalysts for hydrogen evolution in alkaline electrolytes. *ACS nano*. **2018**, *12*(5), 4565-4573.

148. Zhu, Z.; Yin, H.; He, C. T.; Al-Mamun, M.; Liu, P.; Jiang, L.; ... & Zhao, H. Ultrathin transition metal dichalcogenide/3d metal hydroxide hybridized nanosheets to enhance hydrogen evolution activity. *Advanced Materials*. **2018**, *30*(28), 1801171.

149. Anjum, M. A. R.; Jeong, H. Y.; Lee, M. H.; Shin, H. S.; & Lee, J. S. Efficient hydrogen evolution reaction catalysis in alkaline media by all-in-one MoS2 with multifunctional active sites. *Advanced Materials*. **2018**, *30*(20), 1707105.

150. Wang, J.; Zhong, H. X.; Wang, Z. L.; Meng, F. L.; & Zhang, X. B. Integrated three-dimensional carbon paper/carbon tubes/cobalt-sulfide sheets as an efficient electrode for overall water splitting. *ACS nano*. **2016**, *10*(2), 2342-2348.

151. Zhang, H.; Li, Y.; Zhang, G.; Wan, P.; Xu, T.; Wu, X.; & Sun, X. Highly crystallized cubic cattierite CoS2 for electrochemically hydrogen evolution over wide pH range from 0 to 14. *Electrochimica Acta*. **2014**, *148*, 170-174.

152. Peng, S.; Li, L.; Han, X.; Sun, W.; Srinivasan, M.; Mhaisalkar, S. G.; ... & Ramakrishna, S. Cobalt sulfide nanosheet/graphene/carbon nanotube nanocomposites as flexible electrodes for hydrogen evolution. *Angewandte Chemie*. **2014**, *126*(46), 12802-12807.

153. Faber, M. S.; Dziedzic, R.; Lukowski, M. A.; Kaiser, N. S.; Ding, Q.; & Jin, S. High-performance electrocatalysis using metallic cobalt pyrite (CoS2) micro-and nanostructures. *Journal of the American Chemical Society*. **2014**, *136*(28), 10053-10061.

154. Jayaramulu, K.; Masa, J.; Tomanec, O.; Peeters, D.; Ranc, V.; Schneemann, A.; ... & Fischer, R. A. Nanoporous nitrogen-doped graphene oxide/nickel sulfide composite sheets derived from a metal-organic framework as an efficient electrocatalyst for hydrogen and oxygen evolution. *Advanced Functional Materials*. **2017**, *27*(33), 1700451.

155. Jiang, N.; Bogoev, L.; Popova, M.; Gul, S.; Yano, J.; & Sun, Y. Electrodeposited nickel-sulfide films as competent hydrogen evolution catalysts in neutral water. *Journal of Materials Chemistry A*. **2014**, *2*(45), 19407-19414.

156. Tian, T.; Huang, L.; Ai, L.; & Jiang, J. Surface anion-rich NiS 2 hollow microspheres derived from metal–organic frameworks as a robust electrocatalyst for the hydrogen evolution reaction. *Journal of materials chemistry A*. **2017**, *5*(39), 20985-20992.

157. Zhu, W.; Yue, X.; Zhang, W.; Yu, S.; Zhang, Y.; Wang, J.; & Wang, J. Nickel sulfide microsphere film on Ni foam as an efficient bifunctional electrocatalyst for overall water splitting. *Chemical communications*. **2016**, *52*(7), 1486-1489.

158. Lin, T. W.; Liu, C. J.; & Dai, C. S. Ni3S2/carbon nanotube nanocomposite as electrode material for hydrogen evolution reaction in alkaline electrolyte and enzyme-free glucose detection. *Applied Catalysis B: Environmental*. **2014**, *154*, 213-220.

159. Yang, C.; Gao, M. Y.; Zhang, Q. B.; Zeng, J. R.; Li, X. T.; & Abbott, A. P. In-situ activation of self-supported 3D hierarchically porous Ni3S2 films grown on nanoporous copper as excellent pH-universal electrocatalysts for hydrogen evolution reaction. *Nano Energy*. **2017**, *36*, 85-94.

160. Tang, C.; Pu, Z.; Liu, Q.; Asiri, A. M.; Luo, Y.; & Sun, X. Ni3S2 nanosheets array supported on Ni foam: A novel efficient three-dimensional hydrogen-evolving electrocatalyst in both neutral and basic solutions. *International Journal of Hydrogen Energy*. **2015**, *40*(14), 4727-4732.

161. Yu, F.; Yao, H.; Wang, B.; Zhang, K.; Zhang, Z.; Xie, L.; ... & Shi, W. Nickel foam derived nitrogen doped nickel sulfide nanowires as an efficient electrocatalyst for the hydrogen evolution reaction. *Dalton Transactions*. **2018**, *47*(29), 9871-9876.

162. Luo, P.; Zhang, H.; Liu, L.; Zhang, Y.; Deng, J.; Xu, C.; ... & Wang, Y. Targeted synthesis of unique nickel sulfide (NiS, NiS2) microarchitectures and the applications for the enhanced water splitting system. *ACS applied materials & interfaces*. **2017**, *9*(3), 2500-2508.

163. You, B.; & Sun, Y. Hierarchically porous nickel sulfide multifunctional superstructures. *Adv. Energy Mater*. **2016**, *6*(7), 1502333.

164. Jiang, N.; Tang, Q.; Sheng, M.; You, B.; Jiang, D. E.; & Sun, Y. Nickel sulfides for electrocatalytic hydrogen evolution under alkaline conditions: a case study of crystalline NiS, NiS 2, and Ni 3 S 2 nanoparticles. *Catalysis Science & Technology*. **2016**, *6*(4), 1077-1084.

165. Wang, P.; Zhang, X.; Zhang, J.; Wan, S.; Guo, S.; Lu, G.; ... & Huang, X. Precise tuning in platinum-nickel/nickel sulfide interface nanowires for synergistic hydrogen evolution catalysis. *Nature communications*. **2017**, *8*(1), 14580.

166. Du, H.; Kong, R.; Qu, F.; & Lu, L. Enhanced electrocatalysis for alkaline hydrogen evolution by Mn doping in a Ni 3 S 2 nanosheet array. *Chemical Communications*. **2018**, *54*(72), 10100-10103.

167. Chen, P.; Zhou, T.; Zhang, M.; Tong, Y.; Zhong, C.; Zhang, N.; ... & Xie, Y. 3D nitrogen-anion-decorated nickel sulfides for highly efficient overall water splitting. *Advanced Materials*. **2017**, *29*(30), 1701584.

168. Di Giovanni, C.; Wang, W. A.; Nowak, S.; Grenèche, J. M.; Lecoq, H.; Mouton, L.; ... & Tard, C. Bioinspired iron sulfide nanoparticles for cheap and long-lived electrocatalytic molecular hydrogen evolution in neutral water. *Acs Catalysis*. **2014**, *4*(2), 681-687.

169. Faber, M. S.; Lukowski, M. A.; Ding, Q.; Kaiser, N. S.; & Jin, S. Earth-abundant metal pyrites (FeS2, CoS2, NiS2, and their alloys) for highly efficient hydrogen evolution and polysulfide reduction electrocatalysis. *The Journal of Physical Chemistry C*. **2014**, *118*(37), 21347-21356.

170. Li, T.; Liu, H.; Wu, Z.; Liu, Y.; Guo, Z.; & Zhang, H. Seeded preparation of ultrathin FeS 2 nanosheets from Fe 3 O 4 nanoparticles. *Nanoscale*. **2016**, *8*(23), 11792-11796.

171. Villalba, M.; Peron, J.; Giraud, M.; & Tard, C. pH-dependence on HER electrocatalytic activity of iron sulfide pyrite nanoparticles. *Electrochemistry communications*. **2018**, *91*, 10-14.

172. Jasion, D.; Barforoush, J. M.; Qiao, Q.; Zhu, Y.; Ren, S.; & Leonard, K. C. Low-dimensional hyperthin FeS2 nanostructures for efficient and stable hydrogen evolution electrocatalysis. *ACS Catalysis*. **2015**, *5*(11), 6653-6657.

173. Wang, D. Y.; Gong, M.; Chou, H. L.; Pan, C. J.; Chen, H. A.; Wu, Y.; ... & Dai, H. Highly active and stable hybrid catalyst of cobalt-doped FeS2 nanosheets–carbon nanotubes for hydrogen evolution reaction. *Journal of the American Chemical Society*. **2015**, *137*(4), 1587-1592.

174. Xiong, W.; Guo, Z.; Li, H.; Zhao, R.; & Wang, X. Rational Bottom-Up Engineering of Electrocatalysts by Atomic Layer Deposition: A Case Study of Fe x Co1–x S y-Based Catalysts for Electrochemical Hydrogen Evolution. *ACS Energy Letters*. **2017**, *2*(12), 2778-2785.

175. Kuo, T. R.; Chen, W. T.; Liao, H. J.; Yang, Y. H.; Yen, H. C.; Liao, T. W.; ... & Wang, D. Y. Improving hydrogen evolution activity of earth-abundant cobalt-doped iron pyrite catalysts by surface modification with phosphide. *Small*. **2017**, *13*(8), 1603356.

176. Long, X.; Li, G.; Wang, Z.; Zhu, H.; Zhang, T.; Xiao, S.; ... & Yang, S. Metallic iron–nickel sulfide ultrathin nanosheets as a highly active electrocatalyst for hydrogen evolution reaction in acidic media. *Journal of the American Chemical Society*. **2015**, *137*(37), 11900-11903.

177. Konkena, B.; Junge Puring, K.; Sinev, I.; Piontek, S.; Khavryuchenko, O.; Dürholt, J. P.; ... & Apfel, U. P. Pentlandite rocks as sustainable and stable efficient electrocatalysts for hydrogen generation. *Nature communications*. **2016**, *7*(1), 12269.

178. Zegkinoglou, I.; Zendegani, A.; Sinev, I.; Kunze, S.; Mistry, H.; Jeon, H. S.; ... & Roldan Cuenya, B. Operando phonon studies of the protonation mechanism in highly active hydrogen evolution reaction pentlandite catalysts. *Journal of the American Chemical Society*. **2017**, *139*(41), 14360-14363.

179. Piontek, S.; Andronescu, C.; Zaichenko, A.; Konkena, B.; Junge Puring, K.; Marler, B.; ... & Apfel, U. P. Influence of the Fe: Ni Ratio and Reaction Temperature on the Efficiency of (Fe x Ni1–x) 9S8 Electrocatalysts Applied in the Hydrogen Evolution Reaction. *ACS Catalysis*. **2018**, *8*(2), 987-996.

180. Jiang, Y.; Qian, X.; Zhu, C.; Liu, H.; & Hou, L. Nickel cobalt sulfide double-shelled hollow nanospheres as superior bifunctional electrocatalysts for photovoltaics and alkaline hydrogen evolution. *ACS applied materials & interfaces*. **2018**, *10*(11), 9379-9389.

181. Wu, Y.; Liu, X.; Han, D.; Song, X.; Shi, L.; Song, Y.; ... & Wang, G. Electron density modulation of NiCo2S4 nanowires by nitrogen incorporation for highly efficient hydrogen evolution catalysis. *Nature communications*. **2018**, *9*(1), 1425.

182. Sheng, G.; Chen, J.; Li, Y.; Ye, H.; Hu, Z.; Fu, X. Z.; ... & Wong, C. P. Flowerlike NiCo2S4 hollow sub-microspheres with mesoporous nanoshells support Pd nanoparticles for enhanced hydrogen evolution reaction electrocatalysis in both acidic and alkaline conditions. *ACS applied materials & interfaces*. **2018**, *10*(26), 22248-22256.

183. Huang, Z. F.; Song, J.; Li, K.; Tahir, M.; Wang, Y. T.; Pan, L.; ... & Zou, J. J. Hollow cobalt-based bimetallic sulfide polyhedra for efficient all-pH-value electrochemical and photocatalytic hydrogen evolution. *Journal of the American Chemical Society*. **2016**, *138*(4), 1359-1365.

184. Zhang, B.; Yang, G.; Li, C.; Huang, K.; Wu, J.; Hao, S.; ... & Huang, Y. Phase controllable fabrication of zinc cobalt sulfide hollow polyhedra as high-performance electrocatalysts for the hydrogen evolution reaction. *Nanoscale*. **2018**, *10*(4), 1774-1778.

185. Yuda, A.; & Kumar, A. A review of g-C3N4 based catalysts for direct methanol fuel cells. *International Journal of Hydrogen Energy*. **2022**, *47*(5), 3371-3395.

186. Li, S.; Meng, D.; Hou, L.; Wang, D.; & Xie, T. The surface engineering of CdS nanocrystal for photocatalytic reaction: a strategy of modulating the trapping states and radicals' generation towards RhB degradation. Applied Surface Science. **2016**, 371, 164-171.

187. Meng, Y.; Hong, Y.; Huang, C.; & Shi, W. Fabrication of novel Z-scheme InVO 4/CdS heterojunctions with efficiently enhanced visible light photocatalytic activity. CrystEngComm. **2017**, 19(6), 982-993.

188. Yao, J.; Gao, Z.; Meng, Q.; He, G.; & Chen, H. One-step synthesis of reduced graphene oxide based ceric dioxide modified with cadmium sulfide (CeO2/CdS/RGO) heterojunction with enhanced sunlight-driven photocatalytic activity. Journal of Colloid and Interface Science. **2021**, 594, 621-634.

189. Zhao, Y.; Zhang, J.; & Fu, W. Dual-sensitized modification engineering with enhanced photocatalytic degradation for organic dye. Journal of Materials Science: Materials in Electronics. **2021**, 32, 19380-19389.

190. Zhou, P.; Xie, Y.; Fang, J.; Ling, Y.; Yu, C.; Liu, X.; ... & Zhou, D. CdS quantum dots confined in mesoporous TiO2 with exceptional photocatalytic performance for degradation of organic polutants. Chemosphere. **2017**, 178, 1-10.

191. Sun, G.; Zhu, C.; Zheng, J.; Jiang, B.; Yin, H.; Wang, H.; ... & Xue, Q. Preparation of spherical and dendritic CdS@ TiO2 hollow double-shelled nanoparticles for photocatalysis. Materials Letters. **2016**, 166, 113-115.

192. Peng, D.; Wang, H.; Yu, K.; Chang, Y.; Ma, X.; & Dong, S. Photochemical preparation of the ternary composite CdS/Au/gC 3 N 4 with enhanced visible light photocatalytic performance and its microstructure. RSC advances. **2016**, 6(81), 77760-77767.

193. Basu, M.; Sinha, A. K.; Pradhan, M.; Sarkar, S.; Negishi, Y.; & Pal, T. Evolution of hierarchical hexagonal stacked plates of CuS from liquid− liquid interface and its photocatalytic application for oxidative degradation of different dyes under indoor lighting. Environmental science & technology. **2010**, 44(16), 6313-6318.

194. Ajibade, P. A.; & Oluwalana, A. E. Enhanced photocatalytic degradation of ternary dyes by copper sulfide nanoparticles. Nanomaterials. **2021**, 11(8), 2000.

195. Shamraiz, U.; Badshah, A.; Hussain, R. A.; Nadeem, M. A.; & Saba, S. Surfactant free fabrication of copper sulphide (CuS–Cu2S) nanoparticles from single source precursor for photocatalytic applications. Journal of Saudi Chemical Society. **2017**, 21(4), 390-398.

196. Neelgund, G. M.; & Oki, A. Folic acid and CuS conjugated graphene oxide: An efficient photocatalyst for explicit degradation of toxic dyes. Applied Surface Science. **2021**, 566, 150648.

197. Song, Z.; Liu, Y.; Zhang, B.; Song, S.; Zhou, Z.; Huang, Y.; & Zhao, Z. Magnetic grinding synthesis of copper sulfide-based photocatalytic composites for the degradation of organic dyes under visible light. New Journal of Chemistry. **2023**, 47(5), 2286-2295.

198. Zhou, J.; Zhang, Z.; Kong, X.; He, F.; Zhao, R.; Wu, R.; ... & Feng, J. A. novel PN heterojunction with staggered energy level based on ZnFe2O4 decorating SnS2 nanosheet for efficient photocatalytic degradation. Applied Surface Science. **2020**, 510, 145442.

199. El-Hout, S. I.; El-Sheikh, S. M.; Gaber, A.; Shawky, A.; & Ahmed, A. I. Highly efficient sunlight-driven photocatalytic degradation of malachite green dye over reduced graphene oxide-supported CuS nanoparticles. Journal of Alloys and Compounds. **2020**, 849, 156573.

200. Liu, S.; Li, M.; Li, S.; Li, H.; & Yan, L. Synthesis and adsorption/photocatalysis performance of pyrite FeS2. Applied surface science. **2013**, 268, 213-217.

201. Wei, B.; Wang, C.; He, Y.; Ran, G.; & Song, Q. A novel FeS2@ g-C3N4 composite with enhanced photo-Fenton catalytic activity for pollutant degradation. Composites Communications. **2021**, 24, 100652.

202. Arunkumar, M.; Veerakumar, S.; Mohanavel, V.; Vairamuthu, J.; Vijayan, V.; & Senthilkumar, N. A novel visible light-driven p-type BiFeO3/n-type SnS2 heterojunction photocatalyst for efficient charge separation and enhanced photocatalytic activity. Journal of Cluster Science. **2021**, 32(5), 1431-1439.

203. Zhao, W.; Wei, Z.; Zhang, L.; Wu, X.; & Wang, X. Cr doped SnS2 nanoflowers: Preparation, characterization and photocatalytic decolorization. Materials Science in Semiconductor Processing. **2018**, 88, 173-180

204. Mahmood, P. H.; Amiri, O.; Ahmed, S. S.; & Hama, J. R. Simple microwave synthesis of TiO2/NiS2 nanocomposite and TiO2/NiS2/Cu nanocomposite as an efficient visible driven photocatalyst. Ceramics International. **2019**, 45(11), 14167-14172.

205. Vattikuti, S. P.; Byon, C.; & Reddy, C. V. Synthesis of MoS2 multi-wall nanotubes using wet chemical method with H2O2 as growth promoter. Superlattices and Microstructures, **2015**, 85, 124-132.

206. Zhang, L.; Sun, L.; Liu, S.; Huang, Y.; Xu, K.; & Ma, F. Effective charge separation and enhanced photocatalytic activity by the heterointerface in MoS 2/reduced graphene oxide composites. Rsc Advances. **2016**, 6(65), 60318-60326

207. Li, J.; Liu, E.; Ma, Y.; Hu, X.; Wan, J.; Sun, L.; & Fan, J. Synthesis of MoS2/g-C3N4 nanosheets as 2D heterojunction photocatalysts with enhanced visible light activity. Applied Surface Science. **2016**, 364, 694-702.

208. Wang, Xiu.; Mingzhu, Hong.; Fuwei, Zhang.; Zanyong, Zhuang.; and Yan, Yu. "Recyclable nanoscale zero valent iron doped g-C3N4/MoS2 for efficient photocatalysis of RhB and Cr (VI) driven by visible light." ACS Sustainable Chemistry & Engineering. **2016**, 4, 7, 4055-4063.

209. Zhu, K.; Luan, X.; Matras-Postolek, K.; & Yang, P. 2D/2D MoS2/g-C3N4 layered heterojunctions with enhanced interfacial electron coupling effect. Journal of Electroanalytical Chemistry. **2021**, 893, 115350.

210. Li, L.; Yin, X.; & Sun, Y. Facile synthesized low-cost MoS2/CdS nanodots-on-nanorods heterostructures for highly efficient pollution degradation under visible-light irradiation. Separation and Purification Technology. **2019**, 212, 135-141.

211. Mady, A. H.; Mahadadalkar, M. A.; Baynosa, M. L.; Kumar, D. R.; Rabie, A. M.; Lee, J.; ... & Shim, J. J. Highly active Z-scheme heterojunction photocatalyst of anatase TiO2 octahedra covered with C-MoS2 nanosheets for efficient degradation of organic pollutants under solar light. Journal of Colloid and Interface Science. **2022**, 606, 337-352.

212. Piriyanon, J.; Chankhanittha, T.; Youngme, S.; Hemavibool, K.; Nijpanich, S.; Juabrum, S.; ... & Nanan, S. Fabrication of MoS 2/Ag 3 PO 4 S-scheme photocatalyst for visible-light-active degradation of organic dye and antibiotic in wastewater. Journal of Materials Science: Materials in Electronics. **2021**, 32, 19798-19819.

213. Wang, L.; Chai, Y.; Ren, J.; Ding, J.; Liu, Q.; & Dai, W. L. Ag 3 PO 4 nanoparticles loaded on 3D flower-like spherical MoS 2: a highly efficient hierarchical heterojunction photocatalyst. Dalton Transactions. **2015**, 44(33), 14625-14634.

214. Guo, N.; Li, H.; Xu, X.; & Yu, H. Hierarchical Fe3O4@ MoS2/Ag3PO4 magnetic nanocomposites: enhanced and stable photocatalytic performance for water purification under visible light irradiation. Applied Surface Science. **2016**, 389, 227-239.

215. Hong, Y.; Yang, L.; Tian, Y.; Lin, X.; Liu, E.; Sun, W.; ... & Shi, J. Rational design 2D/3D MoS2/In2O3 composites for great boosting photocatalytic H2 production coupled with dye degradation. Journal of the Taiwan Institute of Chemical Engineers. **2023**, 146, 104862.

216. Li, X.; Xia, J.; Zhu, W.; Di, J.; Wang, B.; Yin, S.; ... & Li, H. Facile synthesis of few-layered MoS2 modified BiOI with enhanced visible-light photocatalytic activity. Colloids and Surfaces A: Physicochemical and Engineering Aspects. **2016**, 511, 1-7.

217. Nandigana, P.; Mahato, S.; Dhandapani, M.; Pradhan, B.; Subramanian, B.; & Panda, S. K. Lyophilized tin-doped MoS2 as an efficient photocatalyst for overall degradation of Rhodamine B dye. Journal of Alloys and Compounds. **2022**, 907, 164470.

218. Khan, M. I.; Hasan, M. S.; Bhatti, K. A.; Rizvi, H.; Wahab, A.; Rehman, S. U.; ... & Iqbal, M. Effect of Ni doping on the structural, optical and photocatalytic activity of MoS2, prepared by Hydrothermal method. Materials Research Express. **2020**, 7(1), 015061.

219. Caglar, B.; Guner, E. K.; Ersoy, S.; Caglar, S.; Özdemir, A. O.; Özdokur, K. V.; ... & Çırak, Ç. Bi2S3 nanorods decorated on bentonite nanocomposite for enhanced visible-light-driven photocatalytic performance towards degradation of organic dyes. Journal of Alloys and Compounds. **2021**, 885, 160964.

220. Jia, Y.; Liu, P.; Wang, Q.; Wu, Y.; Cao, D.; & Qiao, Q. A. Construction of Bi2S3-BiOBr nanosheets on TiO2 NTA as the effective photocatalysts: Pollutant removal, photoelectric conversion and hydrogen generation. Journal of Colloid and Interface Science. **2021**, 585, 459-469.

221. Cao, J.; Xu, B.; Lin, H.; Luo, B.; & Chen, S. Novel Bi2S3-sensitized BiOCl with highly visible light photocatalytic activity for the removal of rhodamine B. Catalysis Communications. **2012**, 26, 204-208.

222. Tao, W.; Chang, J.; Wu, D.; Gao, Z.; Duan, X.; Xu, F.; & Jiang, K. Solvothermal synthesis of graphene-Sb2S3 composite and the degradation activity under visible light. Materials Research Bulletin. **2013**, 48(2), 538-543.

223. Dashairya, L.; Sharma, S.; Rathi, A.; Saha, P.; & Basu, S. Solar-light-driven photocatalysis by Sb2S3/carbonbased composites towards degradation of noxious organic pollutants. Materials Chemistry and Physics. **2021**, 273, 125120.

224. Xu, M.; & Zhao, J. Facile Synthesis of 1D/2D Core–Shell Structured Sb 2 S 3@ MoS 2 Nanorods with Enhanced Photocatalytic Performance. Electronic Materials Letters. **2018**, 14, 499-504.

225. Oluwalana, A. E.; & Ajibade, P. A. Structural, optical and photocatalytic studies of oleylamine capped PbS nanoparticles. Optical and Quantum Electronics. **2021**, 53, 1-13.

226. Aziz, M. I.; Mughal, F.; Naeem, H. M.; Zeb, A.; Tahir, M. A.; & Basit, M. A. Evolution of photovoltaic and photocatalytic activity in anatase-TiO2 under visible light via simplistic deposition of CdS and PbS quantum-dots. Materials Chemistry and Physics. **2019**, 229, 508-513.

227. Suganya, M.; Baskaran, R.; Nagarethinam, V. S.; & Balu, A. R. Photoconductive and Antimicrobial Properties of Psidium guajava Leaf Extract Mediated Green Synthesized

SnS2–CdO and SnS2–NiO Nanocomposites. International Journal of Nanoscience. **2021**, 20(04), 2150034.

228. La Porta, F. D. A.; Nogueira, A. E.; Gracia, L.; Pereira, W. S.; Botelho, G.; Mulinari, T. A.; ... & Longo, E. An experimental and theoretical investigation on the optical and photocatalytic properties of ZnS nanoparticles. Journal of Physics and Chemistry of Solids. **2017**, 103, 179-189.
229. Palanisamy, V. K.; Manoharan, K.; Raman, K.; & Sundaram, R. Efficient sunlight-driven photocatalytic behavior of zinc sulfide nanorods towards Rose Bengal degradation. Journal of Materials Science: Materials in Electronics. **2020**, 31, 14795-14809.47.
230. Palanisamy, G.; Bhuvaneswari, K.; Bharathi, G.; Pazhanivel, T.; & Dhanalakshmi, M. Improved photocatalytic performance of magnetically recoverable Bi2Te3/CdS/CuFe2O4 nanocomposite for MB dye under visible light exposure. Solid State Sciences. **2021**, 115, 106584.
231. Varghese, J. CuS–ZnS decorated graphene nanocomposites: Synthesis and photocatalytic properties. Journal of Physics and Chemistry of Solids. **2021**, 156, 109911.
232. Danish, M.; & Muneer, M. Novel ZnSQDs-SnO2/g-C3N4 nanocomposite with enhanced photocatalytic performance for the degradation of different organic pollutants in aqueous suspension under visible light. Journal of Physics and Chemistry of Solids. **2021**, 149, 109785.
233. Lee, J.; Ham, S.; & Jang, D. J. Facile fabrication of Cu-exchanged ZnS nanoadsorbents for highly efficient removal of contaminants. Journal of environmental chemical engineering. **2017**, 5(5), 4431-4440.
234. Mahmood, N.; Yao, Y.; Zhang, J. W.; Pan, L.; Zhang, X.; & Zou, J. J. Electrocatalysts for hydrogen evolution in alkaline electrolytes: mechanisms, challenges, and prospective solutions. *Advanced Science*. **2018**, *5*(2), 1700464.
235. Wasmus, S.; & Küver, A. Methanol oxidation and direct methanol fuel cells: a selective review. *Journal of Electroanalytical Chemistry*. **1999**, *461*(1-2), 14-31.
236. Qian, W.; Wilkinson, D. P.; Shen, J.; Wang, H.; & Zhang, J. Architecture for portable direct liquid fuel cells. *Journal of power sources*. **2006**, *154*(1), 202-213.

237. Kamarudin, S. K.; Achmad, F.; & Daud, W. R. W. Overview on the application of direct methanol fuel cell (DMFC) for portable electronic devices. *International Journal of hydrogen energy*. **2009**, *34*(16), 6902-6916.

238. Brantom, P. G. Review of the Toxicology of a Number of Dyes Illegally Present in Food in the EU. *EFSA J*. **2005**, *263*, 1-71.

239. Kornbrust, D.; & Barfknecht, T. Testing of 24 food, drug, cosmetic, and fabric dyes in the in vitro and the in vivo/in vitro rat hepatocyte primary culture DNA repair assays. *Environmental mutagenesis*. **1985**, *7*(1), 101-120.

240. Merouani, S.; Hamdaoui, O.; Saoudi, F.; Chiha, M.; & Pétrier, C. Influence of bicarbonate and carbonate ions on sonochemical degradation of Rhodamine B in aqueous phase. *Journal of hazardous materials*. **2010**, *175*(1-3), 593-599.

241. Wuebbles, B. J.; & Felton, J. S. Evaluation of laser dye mutagenicity using the Ames/Salmonella microsome test. *Environmental Mutagenesis*. **1985**, *7*(4), 511-522.

242. Sweatman, T. W.; Seshadri, R.; & Israel, M. Metabolism and elimination of rhodamine 123 in the rat. *Cancer chemotherapy and pharmacology*. **1990**, *27*(3), 205-210.

243. Rochat, J.; Demenge, P.; & Rerat, J. C. Toxicologic study of a fluorescent tracer: rhodamine B. *Toxicological European research. Recherche europeenne en toxicologie*. **1978**, *1*(1), 23-26.

244. Chen, H.; Jiang, J.; Zhang, L.; Wan, H.; Qi, T.; & Xia, D. Highly conductive NiCo2 S 4 urchin-like nanostructures for high-rate pseudocapacitors. *Nanoscale*. **2013**, *5*(19), 8879-8883.

245. Shen, L.; Yu, L.; Wu, H. B.; Yu, X. Y.; Zhang, X.; & Lou, X. W. Formation of nickel cobalt sulfide ball-in-ball hollow spheres with enhanced electrochemical pseudocapacitive properties. *Nature communications*. **2015**, *6*(1), 6694.

246. Staszak-Jirkovský, J.; Malliakas, C. D.; Lopes, P. P.; Danilovic, N.; Kota, S. S.; Chang, K. C.; ... & Markovic, N. M. Design of active and stable Co–Mo–S x chalcogels as pH-universal catalysts for the hydrogen evolution reaction. *Nature materials*. **2016**, *15*(2), 197-203.

247. Chen, H.; Jiang, J.; Zhang, L.; Xia, D.; Zhao, Y.; Guo, D.; ... & Wan, H. In situ growth of NiCo2S4 nanotube arrays on Ni foam for supercapacitors: maximizing utilization

efficiency at high mass loading to achieve ultrahigh areal pseudocapacitance. *Journal of Power Sources*. **2014**, *254*, 249-257.

248. Liu, D.; Lu, Q.; Luo, Y.; Sun, X.; & Asiri, A. M. NiCo 2 S 4 nanowires array as an efficient bifunctional electrocatalyst for full water splitting with superior activity. *Nanoscale*. **2015**, *7*(37), 15122-15126.

249. Sivanantham, A.; Ganesan, P.; & Shanmugam, S. Hierarchical NiCo2S4 nanowire arrays supported on Ni foam: an efficient and durable bifunctional electrocatalyst for oxygen and hydrogen evolution reactions. *Advanced Functional Materials*. **2016**, *26*(26), 4661-4672.

250. Liu, Q.; Jin, J.; & Zhang, J. NiCo2S4@ graphene as a bifunctional electrocatalyst for oxygen reduction and evolution reactions. *ACS applied materials & interfaces*. **2013**, *5*(11), 5002-5008.

251. Dong, J.; Zhang, F. Q.; Yang, Y.; Zhang, Y. B.; He, H.; Huang, X.; ... & Zhang, X. M. (003)-Facet-exposed Ni3S2 nanoporous thin films on nickel foil for efficient water splitting. *Applied Catalysis B: Environmental*. **2019**, *243*, 693-702.

252. Ganguly, P.; Mathew, S.; Clarizia, L.; Akande, A.; Hinder, S.; Breen, A.; & Pillai, S. C. Theoretical and experimental investigation of visible light responsive AgBiS2-TiO2 heterojunctions for enhanced photocatalytic applications. *Applied Catalysis B: Environmental*. **2019**, *253*, 401-418.

253. Bernechea, M.; Cates, N.; Xercavins, G.; So, D.; Stavrinadis, A.; & Konstantatos, G. Solution-processed solar cells based on environmentally friendly AgBiS2 nanocrystals. *Nature Photonics*, **2016**, *10*(8), 521-525.

254. Pai, N.; Lu, J.; Senevirathna, D. C.; Chesman, A. S.; Gengenbach, T.; Chatti, M.; ... & Simonov, A. N. Spray deposition of AgBiS 2 and Cu 3 BiS 3 thin films for photovoltaic applications. *Journal of Materials Chemistry C*. **2018**, *6*(10), 2483-2494.

255. Lei, P.; An, R.; Zheng, X.; Zhang, P.; Du, K.; Zhang, M.; ... & Zhang, H. Ultrafast synthesis of ultrasmall polyethylenimine-protected AgBiS 2 nanodots by “rookie method” for in vivo dual-modal CT/PA imaging and simultaneous photothermal therapy. *Nanoscale*. **2018**, *10*(35), 16765-16774.

256. Cheng, J.; Wang, W.; Xu, X.; Lin, Z.; Xie, C.; Zhang, Y.; ... & Li, Q. AgBiS2 nanoparticles with synergistic photodynamic and bioimaging properties for enhanced malignant tumor phototherapy. *Materials Science and Engineering: C*. **2020**, *107*, 110324.

257. Sun, M.; Yang, D.; Wang, C.; Bi, H.; Zhou, Y.; Wang, X.; ... & Yang, P. AgBiS 2-TPP nanocomposite for mitochondrial targeting photodynamic therapy, photothermal therapy and bio-imaging under 808 nm NIR laser irradiation. *Biomaterials science*. **2019**, *7*(11), 4769-4781.

258. Itzhak, A.; Teblum, E.; Girshevitz, O.; Okashy, S.; Turkulets, Y.; Burlaka, L.; ... & Nessim, G. D. Digenite (Cu9S5): layered p-type semiconductor grown by reactive annealing of copper. *Chemistry of Materials*. **2018**, *30*(7), 2379-2388.

259. Guo, L.; Li, F.; Ji, C.; Liu, Y.; He, W.; Xing, H.; ... & Zheng, X. Effect of Annealing on the Defects and Morphology of Cu9S5: Implication for Advanced Electrode for Asymmetric Supercapacitors. *Journal of Electrochemical Energy Conversion and Storage*. **2023**, *20*(1), 011002.

260. Lu, R.; Zhou, S.; Chai, S.; Zhong, Y.; Zhang, H.; Chen, J.; ... & Pan, A. Cu9S5 nanoparticles encapsulated in N, S co-doped carbon nanofibers as anodes for high-performance lithium-ion and sodium-ion batteries. *Journal of Physics D: Applied Physics*. **2022**, *55*(33), 334001.

261. Qin, N.; Dai, F.; Xue, Y.; Gao, D.; Liu, Y.; Zhang, Y.; ... & Yang, Q. Acanthosphere-like bimetallic sulfide Cu9S5/Mo2S3/NF as bifunctional catalyst for water splitting. *Journal of Electroanalytical Chemistry*. **2024**, *964*, 118338.

262. Chen, W.; Xing, H.; Gao, S.; Yang, P.; & Ji, X. Bi-semiconductor heterojunction Cu9S5@ VO2 microspheres with morphology regulation as broadband high-performance electromagnetic wave absorber. *Applied Surface Science*. **2023**, *610*, 155539.

263. Tao, F.; Zhang, Y.; Zhang, F.; An, Y.; Dong, L.; & Yin, Y. Structural evolution from CuS nanoflowers to Cu 9 S 5 nanosheets and their applications in environmental pollution removal and photothermal conversion. *RSC advances*. **2016**, *6*(68), 63820-63826.

264. Yepseu, A. P.; Girardet, T.; Nyamen, L. D.; Fleutot, S.; Ketchemen, K. I.; Cleymand, F.; & Ndifon, P. T. Copper (II) heterocyclic thiosemicarbazone complexes as single-source precursors for the preparation of Cu9S5 nanoparticles: application in photocatalytic degradation of methylene blue. *Catalysts*. **2022**, *12*(1), 61.

265. Tian, Q.; Jiang, F.; Zou, R.; Liu, Q.; Chen, Z.; Zhu, M.; ... & Hu, J. Hydrophilic Cu9S5 nanocrystals: a photothermal agent with a 25.7% heat conversion efficiency for photothermal ablation of cancer cells in vivo. *ACS nano*. **2011**, *5*(12), 9761-9771.

266. Xu, T.; Liu, S.; Wei, Z.; Zhang, W.; Zhang, G. Y.; Liu, T.; ... & Song, Y. Ultrathin Cu9S5 Nanosheets with Sulfur Vacancy for Multimodal Tumor Therapy. *ACS Applied Materials & Interfaces*. **2024**, *16*(12), 14489-14502.

Chapter 2

Designing $AgBi_3S_5$ as an Efficient Electrocatalyst for Hydrogen Evolution Reaction

2.1 Introduction

Energy is a prime entity to create acceleration in beings or objects, though the source of energy is different for various purposes. If the easily available resource of energy does not have any adverse effects on the environment, then it can play a pivotal role in bringing perfect equilibrium between energy resources and respective energy creation. The recent rise of carbon emission from easily limited fossil fuel resources causes environmental pollution as a result of carbon dioxide emission in the environment, which is also one of the key reasons to bring natural calamity and global warming **[1-6]**. To counter such threats for the sake of other Earth's health conditions, people are shifting towards renewable energy resources, which brings a sense of joy to the natural face of Mother Earth **[7-10]**. Now we concentrate on such technologies which utilize clean environment-friendly renewable energy from natural resources like wind power, hydropower, geothermal energy, bioenergy, and precious solar energy **[11-15]**. In the present context, H_2 gas is evolving as one of the key contenders as a resource of clean, green, carbon-zero energy source with exceptional gravimetric energy density, higher efficiency rates towards energy conversion, also having a great ability to solve problems like conventional fossil fuel exhaustion and environmental pollution. For these characteristic features of H_2 towards the contribution of green energy generation, water electrolysis creates a tremendous potentiality in the research fields as well as related technical fields **[16-18]**. Earth-abundant, transition metal-based mixed sulfides, in the nanoscale range have emerged as potential electrocatalysts which are also economically feasible and better alternatives to precious metal-based catalysts for the application of electrochemical water splitting reactions **[19-24]**. Mixed ion metal sulfide shows excellent characteristics of enhancing performance compared to mono metal sulfides in terms of higher electronic conductivity, higher specific capacitance, higher surface area, and inherent higher redox properties **[25-27]**. The characteristics improvement of performance along with synergistic effect in metal ion metal sulfide emerged as a promising electrode material in the field of water splitting like application and their dynamic feature unveils the wings in the field of bifunctional electrocatalyst **[28-31]**. Catalytic activity has a significant role for best outcome in water splitting. It depends on the variety of composition and structure of the catalyst and their adjustability features **[32-35]**. Water splitting performance is greatly enhanced by varying stoichiometric adjustability of these materials **[20, 36-37]** Electrocatalytic improvement in hydrogen evolution reaction is affected by some of the exposed S atoms and vacancies created because of that atom on the edges of the transition metal sulfide-

based catalyst. Jaramillo et al. identified and reported, mainly based on their experimental as well as theoretical results, that the S atom of active sites of MoS_2 could be low hydrogen adsorption near the edges (1/4 ML) **[38]** during the hydrogen evolution reaction. Further enhancement reveals that S vacancies present on the edge of the layered 2H-MoS_2 have a contribution towards enhancing Hydrogen Evolution Reaction **[39]**. Some of the key aspects regarding S vacancies are changes in the coordination environment of the adjacent metal atom due to the absence of 'S' in the appropriate edges of the plane. Metal atoms with low coordination numbers can show more activity, over and above have higher intrinsic electrocatalytic activity and S vacancies can also generate more active sites to play an active role in increasing more active sites on the edges of the metal plane. As a consequence, S vacancies help to introduce key reactive site more efficiently in the inert plane of 2H-metal sulfide where the gap near the fermi level assists to bind hydrogen with reactive metal sites appropriately. Another important role of the S atom for HER, to develop an appropriate place for hydrogen adhesion and separation when the metal atom is in the place of the effective site of the plane and the S atom can participate indirectly **[40]**. Dong et al. experimented on Ni_3S_2 nano porous thin films with exposed (003) faces in hydrogen evolution reaction and came to a conclusion based on a theoretical calculation. They showed that the rate of H_2O adsorption on the surface of Ni sites carried through Volmer Process, on the other hand S sites were seemingly reactive for the generation of H_2 in the Tafel stage **[40]**. The basic idea behind choosing Ag, Bi, and S elements compared to other cost-effective earth-abundant elements like Ni, Mn, Fe, etc. in our synthesized materials is that plenty of composition made from these elements has versatile applications towards photocatalysis, solar cells, photovoltaic devices, photodynamic capabilities, efficiency in high optothermal conversion, synergistic imaging, photothermal driven anticancer treatment, applicable as an antibacterial agent, demonstrated in the treatment of multi-model malignant tumor **[41-46]**. In previous studies authors have shown the thermoelectric property of $AgBi_3S_5$ having ultralow thermal conductivity **[47-49]**.

In the study, we designed a new time-efficient environment-friendly synthesis route to prepare a low-cost, free-of-toxic element, versatile sulfur-based ternary bismuth chalcogenide, $AgBi_3S_5$ as ABS nano catalyst for mainly hydrogen evolution reaction. Ag and Bi compounds possess low band gaps. So, charge separation and availability of electrons for reduction are easy. The presence of two nuclei causes the molecule to be more defective in the nature of the crystal and S vacancy develops which is responsible for greater H^+ adsorptions required for HER. S possesses a slightly

negative charge compared to Ag and Bi in the compounds. Due to S vacancy conduction capabilities of Ag and Bi increase. Moreover, greater S vacancy in ABS (due to the presence of two atoms of different sizes and valency) compared to AS and BS, causes S to become the potential centers of H^+ adsorption in ABS. So, a synergistic effect is found between Ag, Bi, and S. This study further advances the knowledge in this particular field. Following the same synthesis procedure, we also prepared Ag_2S as (AS), Bi_2S_3 as (BS), and $CuBiS_2$ as (CBS). Here in this study, $AgBi_3S_5$ was chosen because $AgBi_3S_5$ is quite stable and it occurs in nature as a pavonine mineral compared to the other intermates of Ag_2S and Bi_2S_3.In general, $CuBiS_2$ was chosen which are new compound in this application along with another specification as Cu is present in the same period of Ag and mixed catalysts often show synergistic behavior. It may also contain more defects and S-vacancies which will enhance the catalytic capabilities of synthesized materials. Pertaining to this investigation, it is explored that ABS performed better as a catalyst compared to others in an electrochemical hydrogen evolution reaction. The details are described briefly in the electrochemical analysis part.

2.2 Experimental Section

2.2.1 Materials

Silver nitrate ($AgNO_3$, 99.99% Merck), Thiourea (H_2N-C(=S)-NH_2, 99.99% Merck). Copper nitrate (Cu $(NO_3)_2.2H_2O$, 99.99%, Merck), Ethylene glycol ($C_2H_6O_2$, 99.99% Merck) and Bismuth nitrate (Bi $(NO_3)_3.5H_2O$, 99.99%, Merck) are used in this study. The double distilled water was thoroughly used during the reaction.

2.2.2 Synthesis of the $AgBi_3S_5$ as (ABS):

2.12 g of $AgNO_3$ was taken in a beaker that contained 25 mL ethylene glycol solution. The mixture was sonicated for up to 15 minutes to prepare a uniform homogeneous solution (A). In another beaker, 6.06 g of bismuth nitrate was dissolved in a 25 mL ethylene glycol solution and then sonicated it for 15 minutes. The mixture was termed as (B). Subsequently in another beaker 1.903 g of thiourea was dispersed in a 25 mL ethylene glycol solution and sonicated for 15 minutes and it was termed as mixture C. Solution B was poured into A and the resultant solution A & B was sonicated about 20 minutes, placed it into a temperature-controllable heating mantel under ambient conditions and the temperature was set at 90 °C (± 5°C). When the temperature reached 90° C, the reaction mixture C was poured into it and the mixed solution was kept for 2 hours maintaining the same condition. Heating mantel was switched off after the reaction, subsequently the appeared mass allows to settle down at normal temperature. The synthesized residue was collected after centrifugation followed by washing several times with double distilled water as well as absolute alcohol respectively. The collected mass was dried in an air oven at about 80°C for next 20 hrs.

2.2.3 Synthesis of the Ag_2S as (AS)

0.85 g of $AgNO_3$ was dissolved in 25 mL ethylene glycol taken in a beaker and the mixture was sonicated for 15 minutes and termed as mixture A. In another beaker, 0.76 g of thiourea was dispersed in 25 mL ethylene glycol solution and homogenized for 15 minutes by sonication. Then the reaction mixture A was placed into the heating mantel under ambient conditions. When the temperature reached 90°C, the solution B was poured into it, carried out the respective reaction up to 2 hours maintaining the same reaction condition. Then the mixed solution was allowed to settle

at 25°C. As synthesized residue was collected after centrifugation followed by washing with double distilled water, absolute alcohol one after another subsequently. Dried at 80°C for 24 h.

2.2.4 Synthesis of the Bi_2S_3 as (BS)

1.21 g of bismuth nitrate was taken in a beaker containing 25 mL ethylene glycol and the mixture was sonicated for 15 minutes. In another beaker, 5.09 g of thiourea was dissolved in a 25 mL ethylene glycol and the solution was made homogenous by subsequent sonication for 15 minutes. The first mixture was placed at a temperature-controlled heating mantel under ambient conditions and then the second solution was poured into the first reaction mixture when the temperature reached 90° C. The reaction mixture was kept in the same environment for 2 hours, Then the mixed solution was allowed to settle at 25°C. As synthesized residue was collected after centrifugation followed by washing with double distilled water, absolute alcohol one at a time, dried at 80°C for 24 h.

2.2.5 Synthesis of the $CuBiS_2$ as (CBS)

0.60 g of copper nitrate was dissolved in a 25 mL ethylene glycol and the mixture was sonicated for 15 minutes. In another beaker 1.21 g of bismuth nitrate was dispersed in a 25 mL ethylene glycol solution and the mixture was made after 15 minutes subsequent sonication. Then second reaction mixture was poured into the first and the resulting mixture was sonicated for 20 minutes and the resultant mixture was placed in the heating mantel under ambient conditions. When the temperature reached 90° C, 3.88 g of thiourea solution was added into it and the reaction carried for 2 hours maintaining the same condition, followed by settling down to room temperature. Then the synthesized residue was washing with double distilled water, absolute alcohol one at a time, dried at 80°C for 24 h.

2.2.6 Electrochemical measurement

AURT-M204 was used at room temperature as electrochemical analyzer to perform the electrochemical study where 0.5 M H_2SO_4 was used as an electrolyte throughout the experiments. Conventional three electrode system was placed for the experiment in which carbon cloth was used as a working electrode, saturated calomel electrode (SCE) was used as reference electrode and

graphite carbon rod was used as a counter electrode. Double distilled water was used thoroughly during the reaction.

2.2.7 Fabrication of electrode:

The catalyst solution drop-casted over the PTFE coated carbon cloth used as a working electrode which effective surface area was 0.5 cm^2. 3 mg of catalyst was weight out in a 3 mL glass bottle and 1 mL ethanol was added to it and the mixture solution was bath sonicated up to 30 to 40 minutes at room temperature. Then 34.5 µL of catalyst solution was drop-casted over carbon cloth and dried at room temperature up to 12 hours in an inert atmosphere and then 5 µL of 0.5 % Nafion solution was drop-casted over catalyst solution as a binder and then it was kept in an inert atmosphere up to 20 hours. 0.1 mg/cm^2 was the catalytic mass loading on the surface of working electrode. The cyclic voltammetry was performed with that working electrode in a three-electrode conventional set up at a scan rate of 50 mv/s and after 20 cycles of completion, the liner sweep voltammetry (LSV) was performed at 2 mv/s with that activated electrode. The Tafel slope values was determined from the LSV curves and all the data throughout the measurements were 50% iR-corrected in manual mode with that Rs values obtained from the electrochemical impedance studies (EIS). EIS study was analyzed at a scan range from 0.1 to 10,000 Hz at 5 mv amplitude potential in which it could reach to benchmarking current i.e., 10 mA/cm^2. The electrochemical data was used in RHE scale throughout the experiments.

The Nernst equation was used for the conversion of LSV data in the potential (V) regions.

$$\mathbf{E_{RHE} = E_{SCE} + 0.059 \times 0.3 + 0.241}$$

Overpotential values has determined using the following equation

$$\mathbf{\eta = 0 - E_{RHE}\ (V)}$$

The Tafel slopes values has determined from the relation between current density in log scale and potential which is known as Tafel plot. The Butler-Volmer equation assisted to find out the Tafel slope values which related as

$$\mathbf{\eta = b \times \log j + a \ldots\ldots\ldots\ldots\ldots\ (1)}$$

$$\mathbf{b = ((\eta - a)/ \log j) \ldots\ldots\ldots\ldots\ldots\ldots\ (2)}$$

a, b, j and η implies as reaction constant, Tafel slope, current density and overpotential respectively.

The electrochemical double layer capacitance value was determined analyzing the data from the non-faradic region and with that electrochemical surface area (ECSA) values were find out comparing the following equation

$i_c = \upsilon \times C_{dl}$ …….(3)

$ECSA = C_{dl} / C_s$ ……(4)

Whereas i_c, υ, C_s, represents double layer charging current, scan rate (υ), specific capacitance value (0.040 $mFcm^{-2}$, reference value) respectively and all the electrochemical data used throughout the experiments after correlation of iR drop.

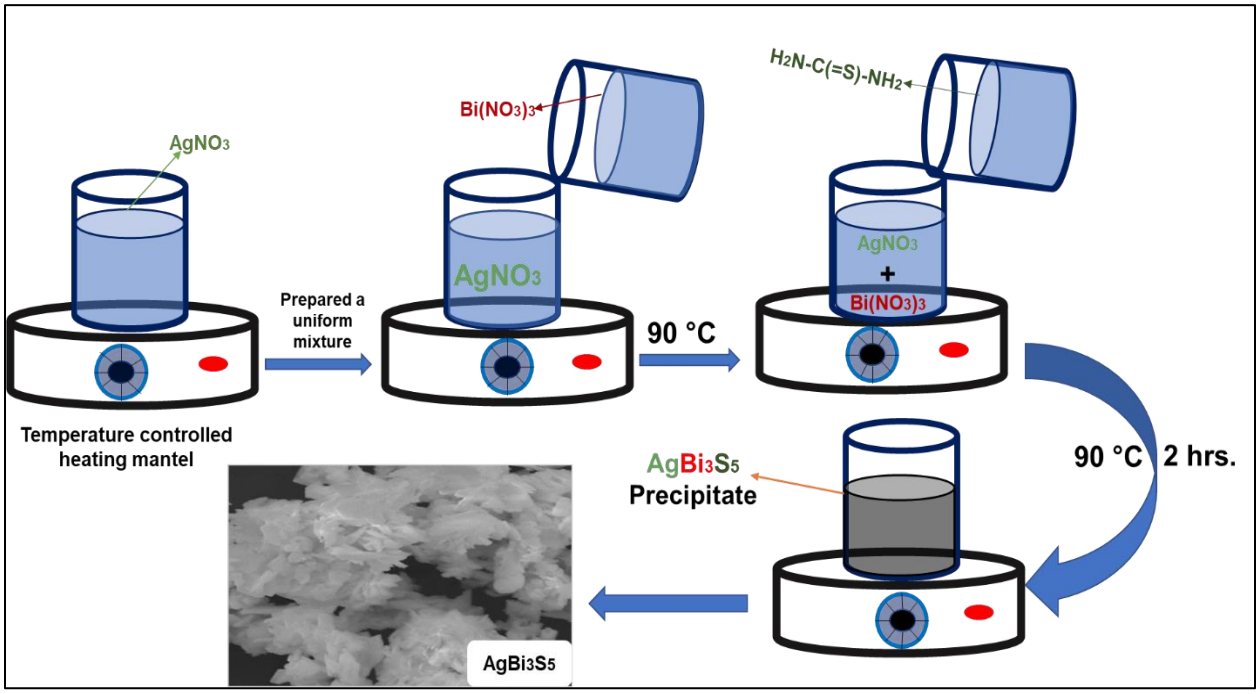

Scheme 2.1: Schematic diagram of synthesis procedure of $AgBi_3S_5$

2.3 Results and discussion

2.3.1 XRD analysis

XRD patterns of synthesized monoclinic silver sulfide, Ag_2S (AS); orthorhombic bismuth sulfide, Bi_2S_3 (BS); monoclinic silver bismuth sulfide, $AgBi_3S_5$ (ABS); orthorhombic copper bismuth sulfide $CuBiS_2$ (CBS) and the profiles corresponding to JCPDS data are depicted in **Figure 2.1(a).** The sharp diffraction peaks of Ag_2S are found at 2θ values (°) around 25.92, 26.32,28.95, 31.54, 33.657, 34.425, 36.826, 37.717, 40.834 and 43.352, which are due to maximum diffraction from the planes (101), (012), (111), ($\bar{1}$12), (120), ($\bar{1}$21), (121), (103), (031), (200) (JCPDS NO. 89-3840). The peaks found for (220), (230), (301), and (521) planes of orthorhombic Bi_2S_3 arise at 2θ values (°) 22.32, 28.57, 32.90 and 49.30 respectively (JCPDS NO.89-8965). The major diffraction peaks of silver bismuth sulfide arise at 2θ values (°) 21.77, 22.98, 27.78, 28.53, 29.92, 31.392, 31.473, 32.52, 34.913, 36.431, 37.165, 38.447, 40.82. These are attributed to the planes (203), (110), (401), (113), ($\bar{3}$10), ($\bar{3}$12), (114), (403), ($\bar{3}$13), ($\bar{3}$14), (405), (007), (116) respectively of monoclinic $AgBi_3S_5$ (JCPDS NO. 83-2051). The major diffraction peaks of $CuBiS_2$ (CBS) are found at 2θ values (°) 24.4, 27.616, 29.281, 31.615, 32.805, 34.24, 41.6, 46.09, 51.97, and the respective diffracted planes are (040), (111), (031), (220), (131), (230), (151), (170), (321) which matched with reference JCPDS NO. 10-0474.

2.3.2 FTIR analysis

The FTIR spectra of ABS, AS, BS, and CBS are presented in **Figure 2.1(b)** where the peaks at 533 cm^{-1} present in ABS and AS indicate the characteristic vibration modes of sulfur **[37]** inferring the presence of Ag-S bond. The peaks around 590 to 650 (cm^{-1}) indicate the vibration of Bi-S **[50]**. Frequencies in the range 3100-3300 cm^{-1} and at around 1649 cm^{-1} for the samples AS and ABS are plausibly presence of bending and stretching vibrations of the O-H bond in adsorbed H_2O at the surface of Ag_2S **[51-52]**. Peaks appeared at 1336 cm^{-1} and 872 – 900 cm^{-1} in sample ABS, BS, and CBS are seemingly presence of bending and stretching vibrations frequency of Bi-S bond.

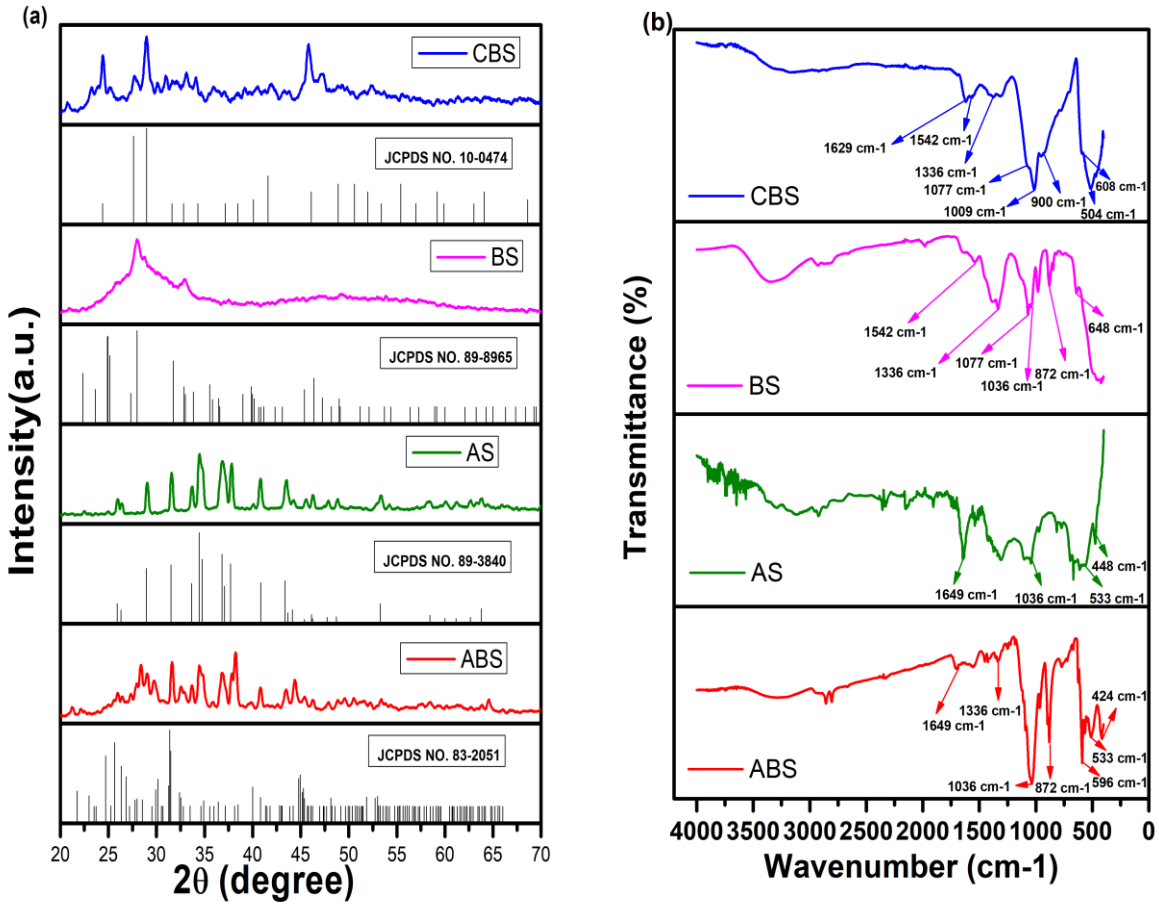

Figure 2.1: (a) Powder XRD patterns of the synthesized ABS, AS, BS, CBS nano-crystals along with the corresponding JCPDS data profiles from bottom to top respectively (b) FTIR spectra of ABS, AS, BS, CBS nano-crystals from down to up respectively

2.3.3 XPS analysis

From the close XPS analysis, doublet peaks seemed at 373.7 eV and 367.7 in the fine Ag 3d spectrum, as identified for Ag $3d_{3/2}$ and Ag $3d_{5/2}$ of the Ag^{+} respectively was shown in **figure 2.2a [53]**. Likewise, the Bi 4f doublet peaks seemed at 158.8 eV (Bi $4f_{7/2}$) and 164.1 eV (Bi $4f_{5/2}$) was shown in **figure 2.2b**. The positions which are measured in between those of bismuth metal (Bi $4f_{7/2}$, 157 eV) and bismuth oxides (Bi $4f_{7/2}$, 159 eV), may be indicative for conventional bismuth sulfide **[53]**. The consequence of above investigation directed that both silver (Ag (I)) and bismuth (Bi (III)) were existing as metal sulfides as approved with previous studies **[54-55]**. The Bi 4f

region and S 2p region are merged so closely that they are visible as a single peak in the survey scan which we have given in the **figure 3**. As a result of that two low-intensity peaks appeared after deconvolution in between the Bi 4f region where 162.7 eV for S $2p_{1/2}$,162.1 eV for S $2p_{3/2}$. In addition, peaks arise at 227.1 eV for S 2s (zero), subsequently another peak appeared at 232.6 eV for II states of S 2s **(Figure 2.2c)**. **Figure 2.3a** represented the surface spectrum where a broad peak at 532.03 eV was assigned for the O 1s region for adsorption of water molecule at the metal sulfide surfaces of the catalyst **[56]**. The catalyst was drop casted on the surface of the silicon wafer during the XPS analysis and the peak appeared around 100-150 eV regions signifying the corresponding observance. One of the broad peaks highlighted around binding energy 286.6 eV due to calibration peak, appeared for C 1s and is also known as the adventitious carbon peak **[57]**. From **Figure 2.3(b)** representation where two small peaks appeared after deconvolution which signified the presence of S 2p.

Table 2.1 The outcome of XPS analysis regarding elemental composition and subsequent chemical states of synthesized ABS represented as a tabular form.

Element	**peak**	**Positions (B.E) eV**
Ag 3d	Ag^{+} $3d_{5/2}$	373.7
	Ag^{+} $3d_{3/2}$	367.7
Bi 4f	Bi (III) $4f_{7/2}$	158.8
	Bi (III) $4f_{5/2}$	164.1
S 2p	S^{2-} $2p_{3/2}$	162.1
	S^{2-} $2p_{1/2}$	162.7
S 2s	S 2s (0)	227.1
	S 2s (II)	232.6

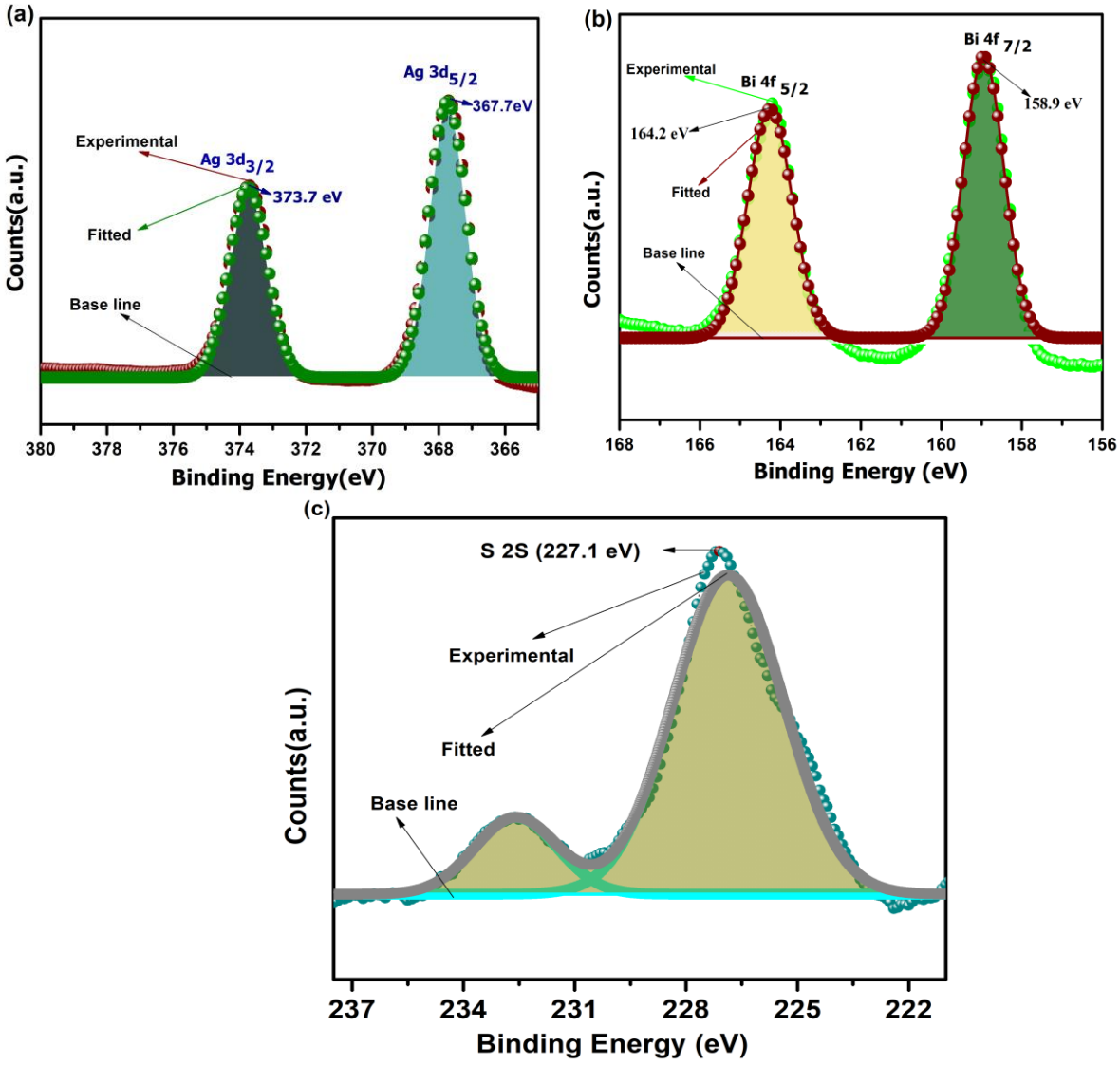

Figure 2.2*:* Fine XPS spectra of synthesized $AgBi_3S_5$ where (a-c) depicted as Ag (3d), Bi (4f) & S (2s) respectively

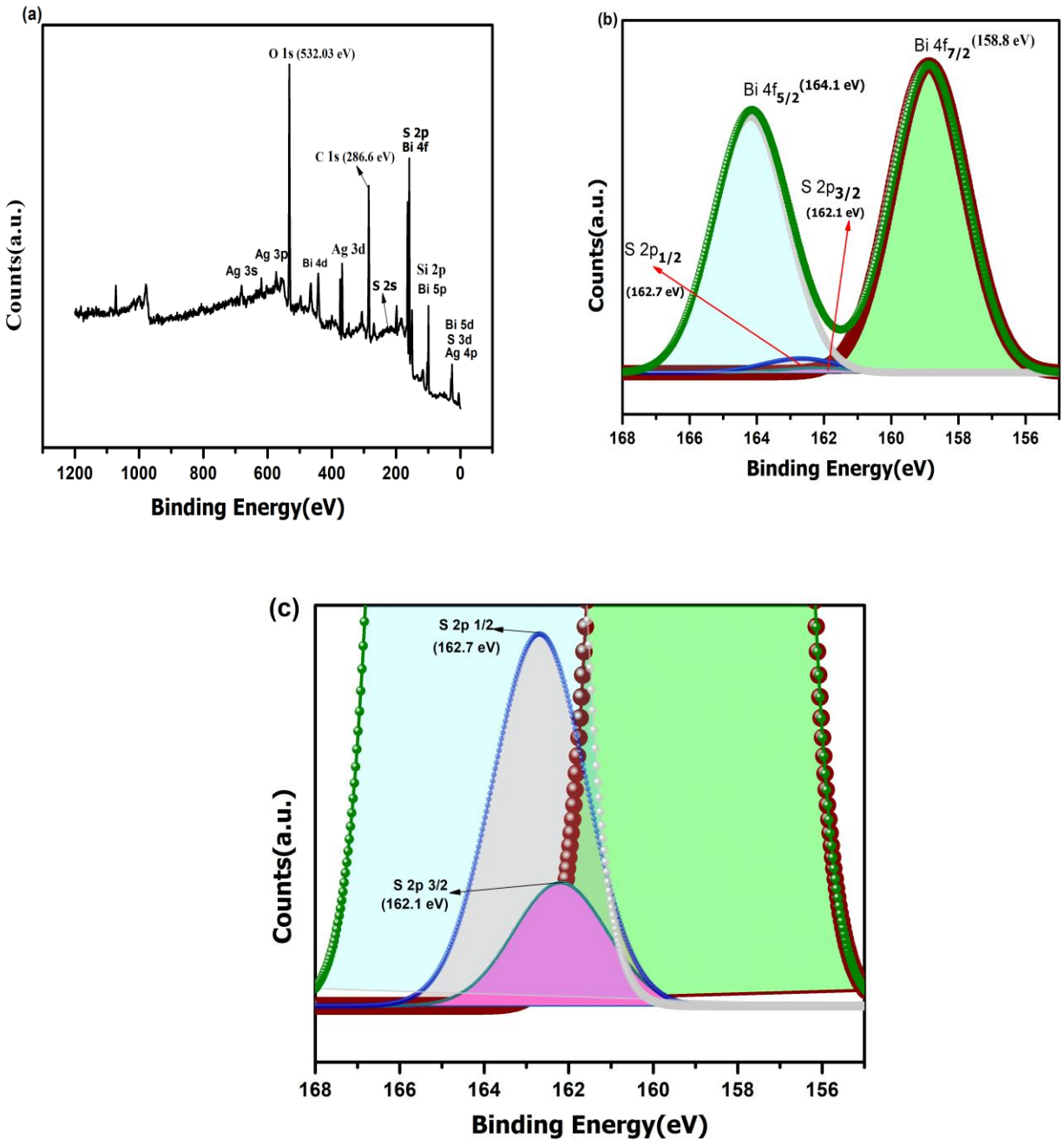

Figure 2.3 (a) Fine survey XPS spectra of ABS and (b) XPS spectrum of Bi and S together of ABS after deconvolution and (c) extent of figure (b) with lower counts of Y axis scale.

2.3.4 Morphological analysis

Figure 2.4 (a-b) shows SEM images of ABS at different magnifications which altogether reveal that the plates on cotton-like structures of ABS are constructed by heaping small rods which in turn are formed from elongated spheres of the material. **Figure 2.5** reveals SEM images of AS, and BS where both particles become distorted agglomerated, and CBS shows rounded flower-like structures. The building blocks of these narrow structures have sizes/diameters in the order of a few nanometers. The shape and size described in **Figure 2.5** are more exposed in a higher magnification scale. The changes in shape and morphology that occurred for the samples AS, BS, and ABS might be due to the presence of different interactions arising from the presence of different relative concentrations of NO_3^-, thiourea, and ethylene glycol with respect to that of the nucleus, Ag/Bi/ Ag & Bi of the synthesized compounds.

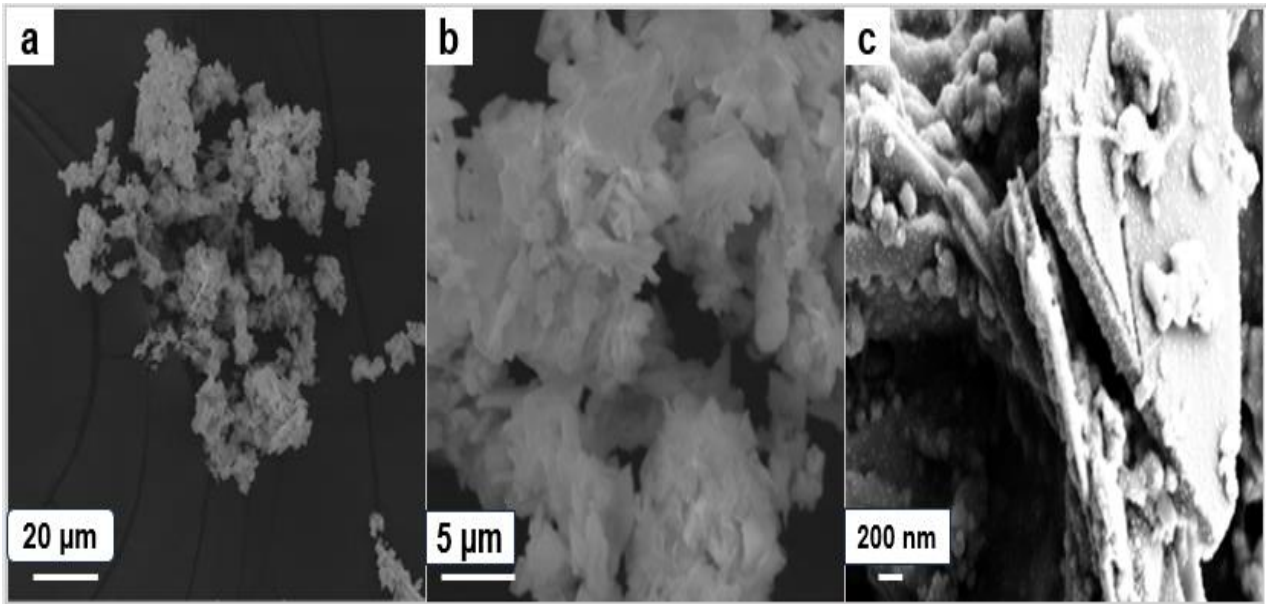

Figure 2.4*:* SEM images of synthesized $AgBi_3S_5$ where (a) depicted lower and (b) represented higher magnification respectively. (c) the FESEM image of ABS.

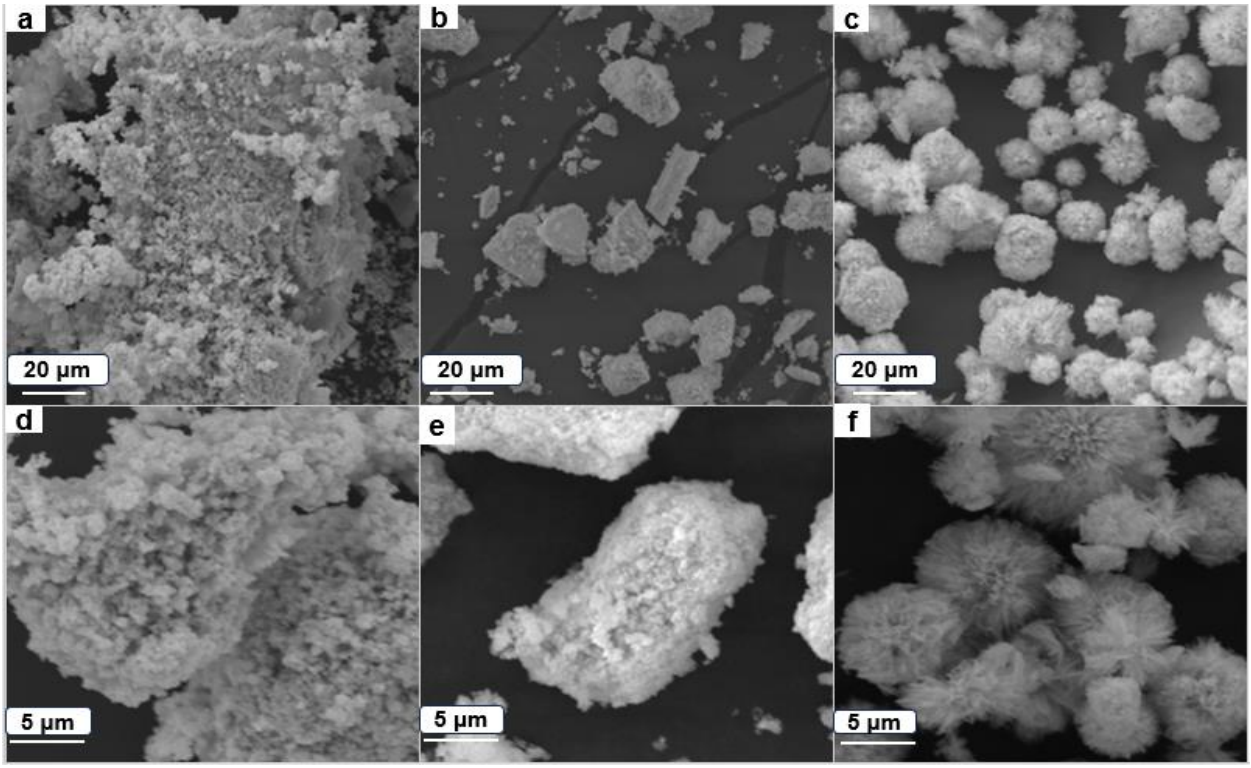

Figure 2.5*:* The SEM images at low (a,b,c) and high (d,c,f) magnification of AS, BS, CBS respectively.

The surface morphology, elemental detection, and compound recognition of the best electrocatalyst ABS were accomplished by TEM, HRTEM, and SAED pattern as presented in **Figure 2.8(a), (b),** and **(c)** respectively. Ash-colored irregular lumps of material $AgBi_3S_5$ are heaped together to form a rough material surface. The lumps are loosely bound and several holes and gaps are formed for every junction of material parts. Certain portions of the whole micrograph in colored black, seemingly due to the accumulation of several layers one after another in the portions. The key benefit of including a HAADF image in **Figure 2.8** and **9** is that it provides much stronger selectivity for the elements present in that selected portion and allows to accommodate higher resolution images that may help to identify the actual morphology of that synthesized compounds (ABS, AS, BS, and CBS) more realistically. Structural information at the atomic level is profoundly revealed from these techniques. HR-TEM profiles in **Figure 2.8b** reveals the presence of two different planes (206) and (112) of monoclinic $AgBi_3S_5$. The SAED profile indicates the presence of several planes of the compound including (200), (112), and (206) as marked**. Figures 2.8(d-h)** show areas selected for color mapping of combined and constituent

elements namely Ag, Bi, and S. The almost uniform distribution of the elements within the entire area supports the formation of the compound $AgBi_3S_5$. **Figure 2.9a** presents the TEM image of an Ag_2S (AS)- lump whose cylinder-like portion has about 50 nm diameter. **Figure 2.9(b-d)** shows the area selected and the color mapping of Ag and S respectively. The similar distribution of Ag and S signifies the formation of Ag_2S. **Figure 2.9e** reveals the formation of mixtures of some wire and rod-like structures of about 10 nm diameter for Bi_2S_3. **Figure 2.9 (f-h)** shows the selected area and the color mapping of Bi and S respectively. **Figure 2.9i** depicted the formation of kind of structure which look like broad wires having diameters in between 16-82 nm. **Figure 2.9(j-m)** displays the selected area and distributions of Cu, Bi, and S respectively. The distribution is almost uniform supporting the probable formation of $CuBiS_2$. The interplanar spacing and respective plane supported the XRD data of synthesized electrocatalyst AS, BS, and CBS respectively. The EDS spectra of synthesized ABS, AS, BS, and CBS are also provided in **Figure 2.7**, where clearly indicating that the respective constituents of synthesized nanoparticles present in it. The average size of synthesized ABS was determined from SEM analysis and the respective outcome showed in **figure 2.6**.

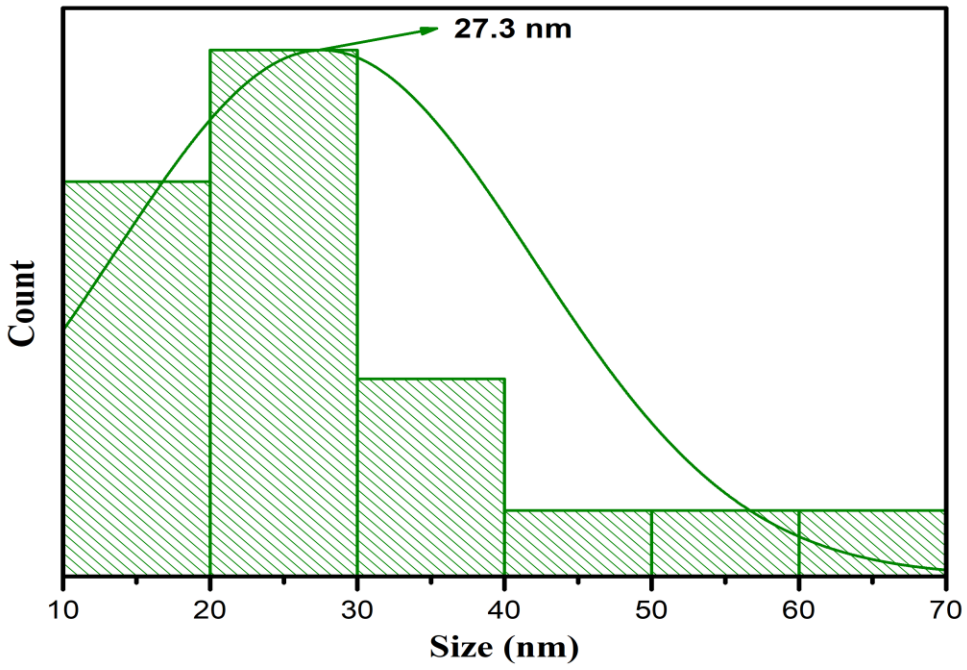

Figure 2.6: Size distribution histogram for ABS

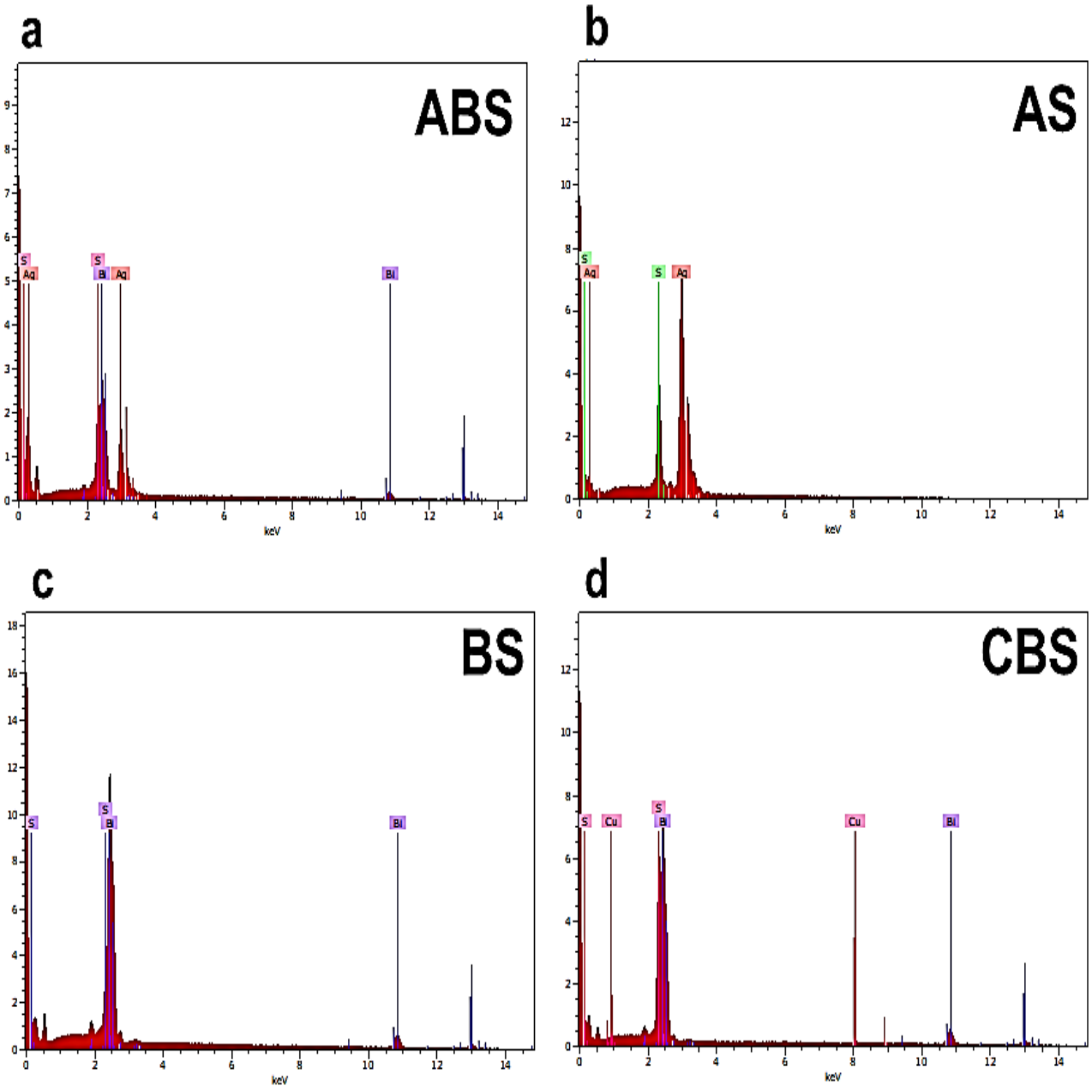

Figure 2.7: (a, b, c, d) represents the EDS spectrum of ABS, AS, BS, and CBS electrocatalysts respectively

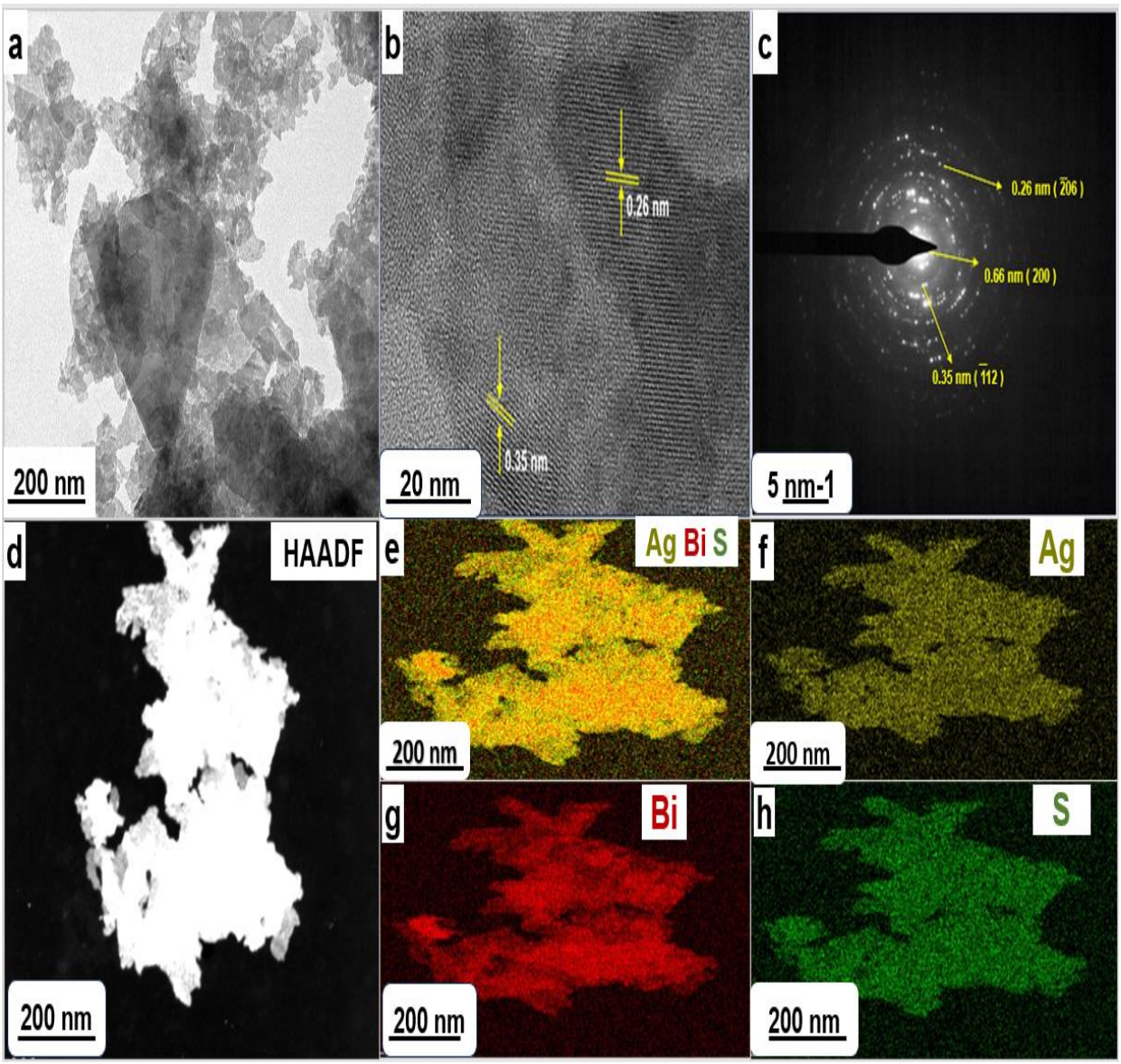

Figure 2.8*:* (a) The TEM image of ABS electrocatalyst; (b) HRTEM image of ABS electrocatalyst; (c) SAED pattern of ABS electrocatalyst; (d) HAADF color mapping for selected area of ABS and (e-h) color mapping mix, Ag, Bi, S elenments respectively.

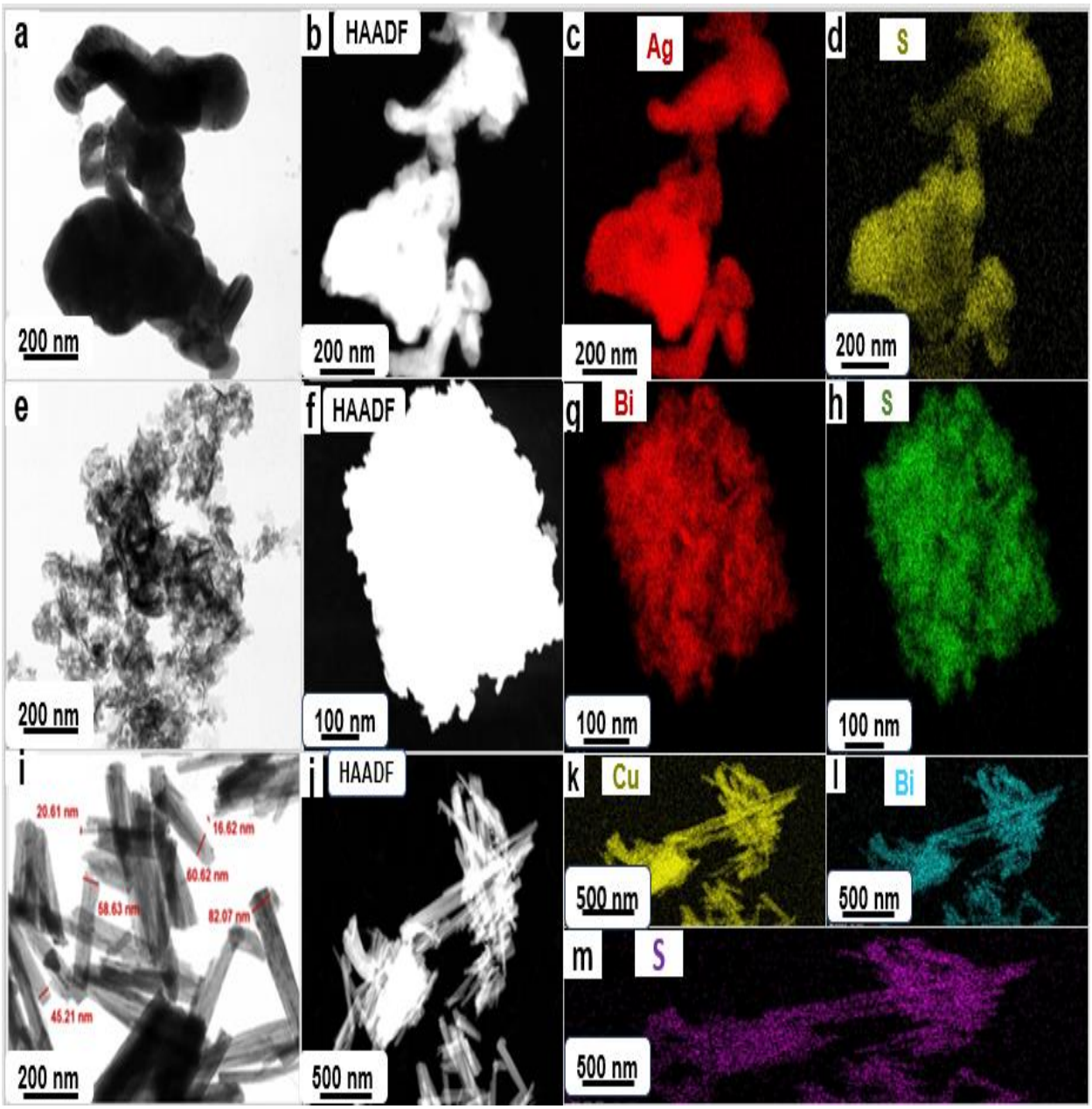

Figure 2.9*:* (a) TEM image of AS electrocatalyst; (b) HAADF color mapping for selected area of AS; (c-d) color mapping of Ag, S respectively; (e) TEM image of BS electrocatalyst; (f) HAADF color mapping for selected area of BS; (g-h) color mapping of Bi, S respectively; (i) TEM image of CBS electrocatalyst; (j) area selected for HAADF color mapping of CBS; (k-m) color mapping of Cu, Bi, S respectively.

2.3.5 Electrochemical Hydrogen Evolution Reaction

The electrocatalytic HER experiment was investigated in 0.5 M H_2SO_4 for all the catalyst and their outcome are depicted in **Figure 2.10.** Here, we can see that the ABS catalyst shows the best electrochemical activity and CBS displays very less catalytic activity among all the catalysts. The rate of efficiency of electrochemical movement was first investigated by comparing their overpotential values of that synthesized catalysts. Here, we were analyzed the linear sweep voltammetry (LSV) studies in between potential window (0 to -1 V) with respect to RHE scales to scrutinize the electrochemical activity after collecting the iR-corrected LSV outcomes at 5 mV/sec scan rate value for all the catalysts and the capability towards the HER is substantiated by evaluating the overpotential value at 10 mA/cm^2 benchmarking current density value. Commercial platinum was used as a standard catalyst for comparing the electrochemical performance in terms of overpotential values with other synthesized catalysts. **(Figure-2.10a) [61]**. Pt/C, ABS, AS, BS, and CBS electrocatalysts show 34 mV, 47 mV, 93 mV, 191 mV, and 603 mV of respective overpotential values **[62]**. **Figure 2.10b** portrays a bar diagram of all overpotential values with the same catalysts loading for a better understanding of the comparison of all HER overpotential values. The next important factor for analysis of the performance of the synthesized catalyst is Tafel slope determination. The extent of charge transfer kinetics was determined from the outcome of the Tafel slope values which was also assist to determine the probable mechanistic pathway in HER. The range of Tafel slope values in between 40-120 mV/dec indicates that, HER takes place via the Volmer−Heyrovsky pathway and if the range is in between 30 and 40 mV/dec, the mechanism occurs via the Volmer−Tafel pathway. Here, the corresponding Tafel slope values were 75.99, 101.54, 120.29, and 265.2 mV/dec for ABS, AS, BS, and CBS respectively **(Figure-2.10c)**. The lowest Tafel slope value (75.99 mV/dec) of the best active catalyst ABS proves that the reaction proceeds through the Volmer-Heyrovsky path which was also the rate determining step **[63]**. Charge transfer resistance (Rct) through EIS studies was another key parameter which was assist to determine the effective electron charge transfer in near the reaction interface. The calculated EIS values are 9.84, 15.24, 16.01, and 19 Ω for ABS, AS, BS, and CBS respectively **(Figure 2.10d)**. The lower R_{ct} value for ABS indicates that, better rate of charge transfer was executed in the reaction interface related to other electrocatalysts. Feasibility of better charge transfer kinetics for ABS catalyst might be derived from the highly exposed surface area for H adsorption. To approve the above-mentioned statement additionally, the electrochemical surface

area (ECSA) study was performed in between non-Faradaic potential region (0.2 to 0.3 V) with respect to SCE **[64]**.

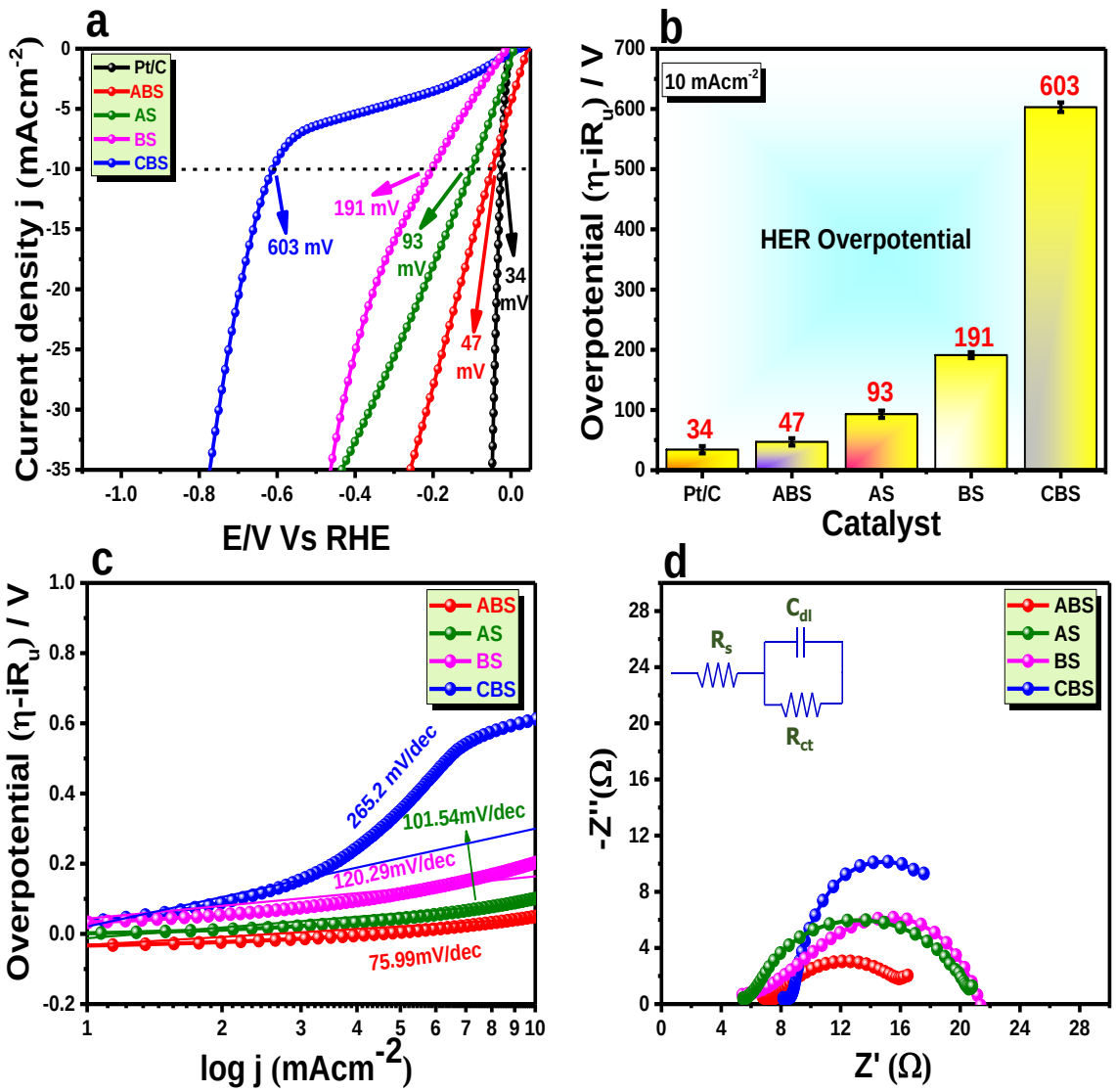

Figure 2.10: (a) LSV profiles of synthesized electrocatalysts in 0.5M H_2SO_4 solution at 5 mV/s; (b) Bar-diagram presentation of overpotential values of respective catalysts (c) Tafel plot of synthesized electrocatalysts with the 50 % iR-corrected data; (d) Electrochemical impedance spectral studies of that respected electrocatalysts with the same environment.

The resulting scan rate-reliant CV curve of all the catalysts starting from ABS, AS, BS, and CBS is given separately in **Figure 2.12(a-d)**, respectively. Afterward, the capacitance in the subsequent double layers of the reaction interface (C_{dl}) values of all the materials are evaluated from the slope of the ΔJ vs the scan rate curve given in **Figure 2.12(e)**. The calculated C_{dl} values are 3.66, 1.38, 0.598, and 0.214 μF/cm^2 for ABS, AS, BS, and CBS respectively. ECSA values were determined from the respective C_{dl} values using the formula mentioned in **equation-S3** and the obtained values are 0.092, 0.035, 0.014, 0.005 cm^2 for ABS, AS, BS, and CBS respectively. The best active catalyst ABS shows a higher active surface area value compared to other catalysts confirming again higher charge transfer kinetics. Another vital yardstick for catalyst performance is the stability of the catalyst under long-term exposure. To confirm the steadiness of the most excellent active catalyst ABS, long run catalytic efficiency was executed through the acceleration degradation (AD) study in a 0.5 M H_2SO_4 solution for 500 times at 100 mV/s scan rate **[65]**. Following the AD study, the LSV polarization analysis before and after completion of AD experiment was shown in **Figure 2.13(a)**. While comparing these two curves a marginal hike about 8 mV with reference to 10 mA/cm^2 current density is detected after the AD experiment on account of overpotential value suggesting higher stability with low catalyst degradation for ABS catalyst. EIS investigation was also studied relate to before and after AD experiment for ABS catalyst and the R_{ct} value of ABS after finishing the AD study was 12.55 Ω, which was comparatively little high prior to the AD study (**Figure 2.13b**). Here, the R_{ct} value slightly increases due to the agglomeration of certain spheres and rods to produce bigger particles. However, the routes of the reactants to the electrode surface are more cleaned and channelized during HER, so the rate of reaction and Rct value do not change much even after 500 cycles. In order to confirm more robustness of the best active catalyst ABS, the long-term durability was examined from the chronoamperometric (CA) experiment with respect to constant potential (-0.065 V) in RHE scales (**Figure 2.13c**) where the catalyst shows retention of durability after 72-hour long term process under cathodic environment **[66]**. The Faradaic efficiency value for the catalyst "*ABS*" was calculated from GC-MS studies by applying a persistent potential of "-0.074" V vs RHE for periods of 30 min.

The FE value has been calculated with respect to experimental and calculative amount of H_2 observance are using the following formula.

$$FE = \frac{Experimentally\ observed\ H_2}{Calculated\ H_2} \times 100\%$$

From the given experimental result, the calculated FE value was 91.02%. The observed FE value is consistent with high selectivity towards the HER. The decreased FE value by 9% might be due to the loss of H_2 gas during the operation of GC-MS coupled with the electrochemical analyzer. The FE outcome is portrayed in **Figure 2.11**.

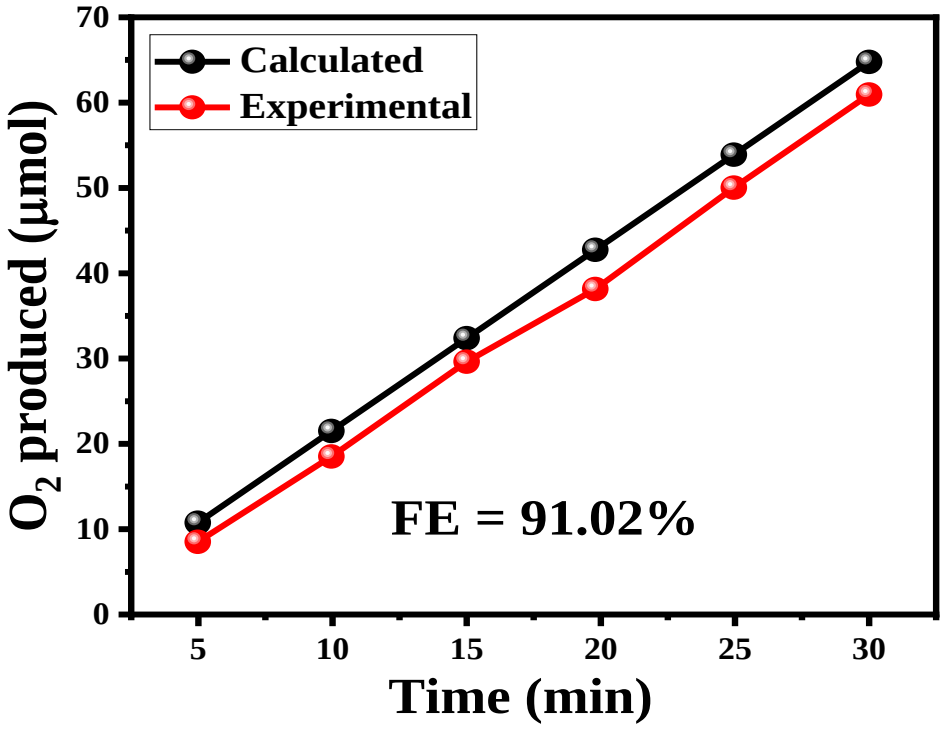

Figure 2.11: Faradaic efficiency (FE) of the ABS electrocatalyst for acidic HER solution.

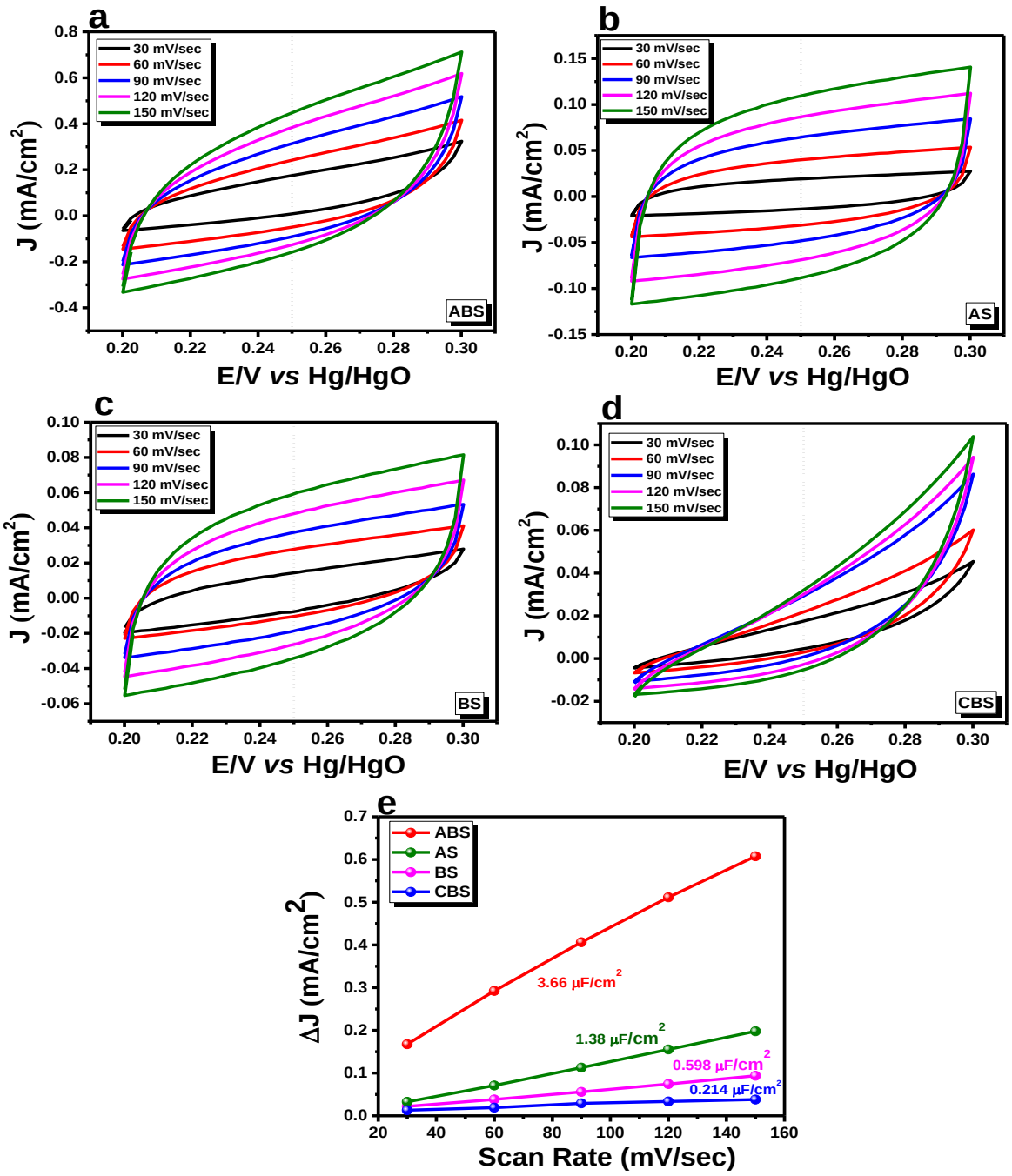

Figure 2.12: (a-d) Cyclic voltammetry profiles of ABS, AS, BS and CBS in non-faradic region with increasing scan rates in 0.5 M H_2SO_4 solution respectively (e) ΔJ versus Scan rate graph of all synthesized electrocatalysts.

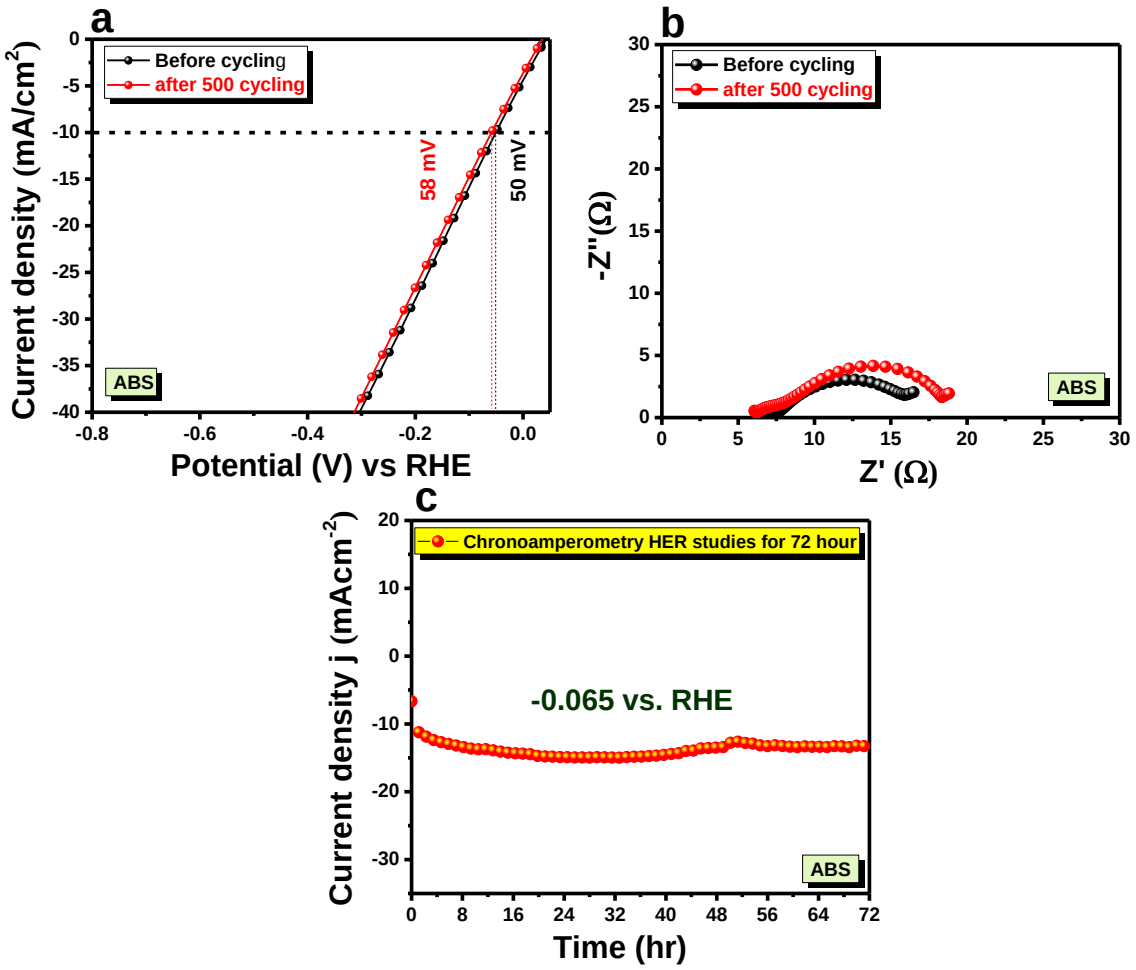

Figure 2.13: (a) LSV polarization curves of best active catalyst ABS before and after AD experiment; (b) EIS study of ABS in former and later of HER investigation (c) Chronoamperometric outcomes of ABS under aqueous solution of 0.5 M H_2SO_4 for 72 hours exposures.

2.3.6 Fate of Catalyst

In order to study the fate of the catalyst, ABS after several catalytic cycles, repeated LSV study was performed on the synthesized $AgBi_3S_5$ nano particle-deposited carbon electrode and the resulting carbon mixed $AgBi_3S_5$ particles separated from the thin film before and after use, were tested for XRD study. It is found that almost all major peaks of $AgBi_3S_5$ are retained in the same position in the X-ray profile of the catalyst used after the hydrogen evolution reaction showed in **figure 2.15**. The drop in intensity between 20 and 30 (°) 2θ is due to the baseline correction. 110

peak exists at 22.98°. For both the samples most, prominent peaks appear before 40°.The FESEM study was shown in **figure 2.14** with the same catalyst particles before and after use, reveals that spheres, plates, and rods are present in the morphology of both the catalyst materials before and after use.

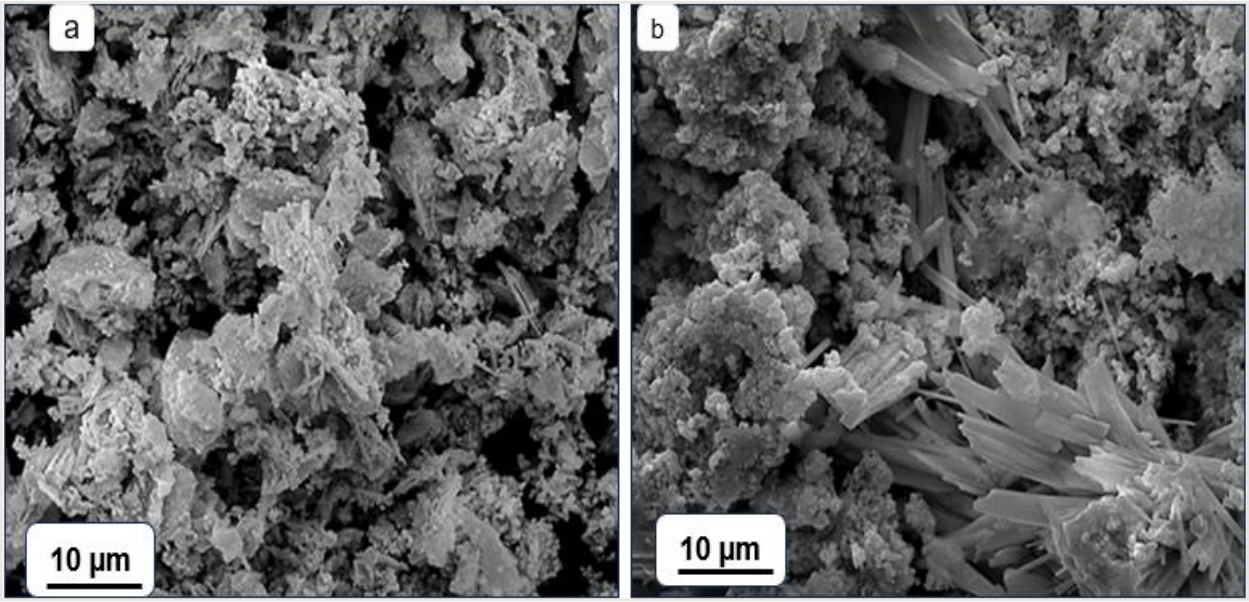

Figure 2.14: (a-b) represent the FESEM profiles of $AgBi_3S_5$ nano-catalyst before and after HER studies respectively.

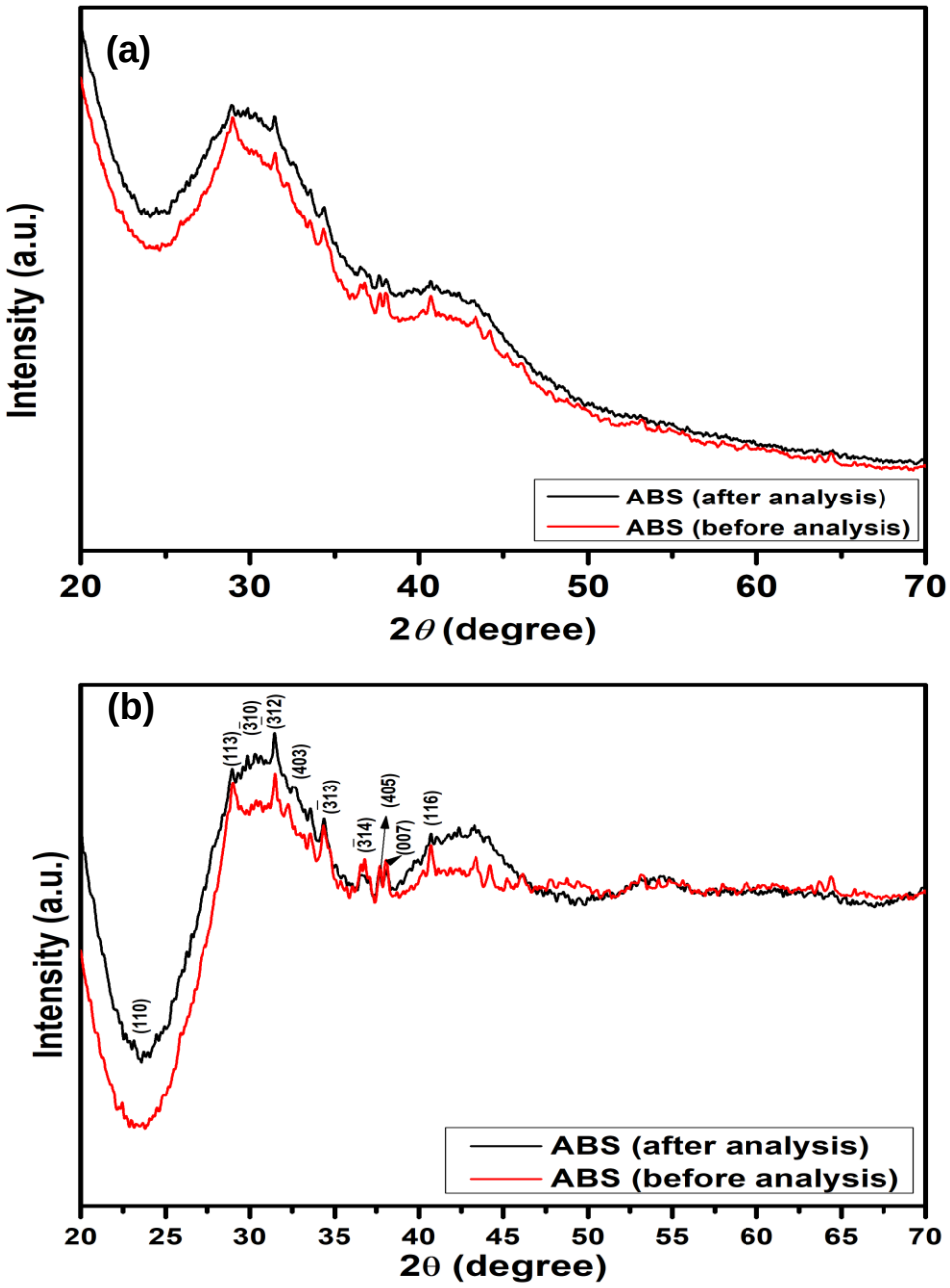

Figure 2.15: XRD profiles of the ABS electrocatalyst before and after HER in aqueous solution of 0.5 M H_2SO_4 (a) depicted without baseline correction, (b) with baseline correction respectively.

2.4 Conclusions:

Nanoparticles of different sulfides like Ag_2S, Bi_2S_3, and particularly their composites $AgBi_3S_5$, and another variant $CuBiS_2$ are synthesized for the first time by similar facile liquid phase hot chemical treatments and are used as catalysts for electrochemical HER in aqueous acid solution for the first time and are characterized by various microscopic and spectroscopic techniques. Amongst the various catalysts developed (such as ABS, AS, BS, and CBS), ABS shows comparatively lower overpotential value of 47mV/dec, lower Tafel slope value of 75.99 mV/dec related to rest of synthesized catalysts. The catalytic capability of the synthesized materials follows the sequence: ABS > AS > BS > CBS which are in the same order as that of the electrochemical surface area of the materials and EIS values. ABS is a quite stable compound from the post studies of the catalyst. Thus, at room temperature more charge separation, conductivity, and S vacancy are expected. These may increase H^+ adsorption. So, it shows more electrochemical surface area than others. Moreover, Bi of ABS may upshift the Centre of the d-band in ABS. Hence the desorption of adsorbed hydrogen in the Volmer- Heyrovsky step is facilitated. Thus, ABS outperforms the other components. The dynamic stability study reveals little deterioration of the best electrode made by $AgBi_3S_5$, even after 500 cycles in the AD study. Thus, the electrode based on $AgBi_3S_5$ can be used as a superior catalyst for HER in an acidic medium for generation of green H_2 fuel in an expanded manner. The study also provides a promising strategy to develop excellent stable Pt-group-metal-free multinuclear nano-catalysts. The study will also initiate the use of more ternary sulfide nanoparticles as catalysts in various energy studies in the near future.

References:

1. Roger, I.; Shipman, M. A.; & Symes, M. D. Earth-abundant catalysts for electrochemical and photoelectrochemical water splitting. *Nature Reviews Chemistry*. **2017**, *1*(1), 1-13.
2. Lewis, N. S. Research opportunities to advance solar energy utilization. *Science*. **2016**, *351*(6271), aad1920.
3. Wang, J.; Shi, W.; Liu, D.; Zhang, Z.; Zhu, Y.; & Wang, D. Supramolecular organic nanofibers with highly efficient and stable visible light photooxidation performance. *Applied Catalysis B: Environmental*. **2017**, *202*, 289-297.
4. Wei, Z.; Hu, J.; Zhu, K.; Wei, W.; Ma, X.; & Zhu, Y. Self-assembled polymer phenylethnylcopper nanowires for photoelectrochemical and photocatalytic performance under visible light. *Applied Catalysis B: Environmental*. **2018**, *226*, 616-623.
5. Hughes, T. P.; Kerry, J. T.; Álvarez-Noriega, M.; Álvarez-Romero, J. G.; Anderson, K. D.; Baird, A. H.; ... & Wilson, S. K. Global warming and recurrent mass bleaching of corals. *Nature*. **2017**, *543*(7645), 373-377.
6. AghaKouchak, A.; Cheng, L.; Mazdiyasni, O.; & Farahmand, A. Global warming and changes in risk of concurrent climate extremes: Insights from the 2014 California drought. *Geophysical Research Letters*. **2014**, *41*(24), 8847-8852.
7. Grätzel, M. Recent advances in sensitized mesoscopic solar cells. *Accounts of chemical research*. **2009**, *42*(11), 1788-1798.
8. Bak, T.; Nowotny, J.; Rekas, M.; & Sorrell, C. C. Photo-electrochemical hydrogen generation from water using solar energy. Materials-related aspects. *International journal of hydrogen energy*. **2002**, *27*(10), 991-1022.
9. Fujishima, A., & Honda, K. (1972). Electrochemical photolysis of water at a semiconductor electrode. *nature*, *238*(5358), 37-38.
10. Tachibana, Y.; Vayssieres, L.; & Durrant, J. R. Artificial photosynthesis for solar water-splitting. *Nature Photonics*. **2012**, *6*(8), 511-518.

11. Shortall, R.; Davidsdottir, B.; & Axelsson, G. Geothermal energy for sustainable development: A review of sustainability impacts and assessment frameworks. *Renewable and sustainable energy reviews*. **2015**, *44*, 391-406.

12. Gernaat, D. E.; Bogaart, P. W.; Vuuren, D. P. V.; Biemans, H.; & Niessink, R. High-resolution assessment of global technical and economic hydropower potential. *Nature Energy*. **2017**, *2*(10), 821-828.

13. Woolf, D.; Lehmann, J.; & Lee, D. R. Optimal bioenergy power generation for climate change mitigation with or without carbon sequestration. *Nature Communications*. **2016**, *7*(1), 13160.

14. Lewis, N. S. Research opportunities to advance solar energy utilization. Science. **2016**, 351, aad1920.

15. Herbert, G. J.; Iniyan, S.; Sreevalsan, E.; & Rajapandian, S. A review of wind energy technologies. *Renewable and sustainable energy Reviews*. **2007**, *11*(6), 1117-1145.

16. Seh, Z. W.; Kibsgaard, J.; Dickens, C. F.; Chorkendorff, I. B.; Nørskov, J. K.; & Jaramillo, T. F. Combining theory and experiment in electrocatalysis: Insights into materials design. *Science*. **2017**, *355*(6321), eaad4998.

17. Morales-Guio, C. G.; Stern, L. A.; & Hu, X. Nanostructured hydrotreating catalysts for electrochemical hydrogen evolution. *Chemical Society Reviews*. **2014**, *43*(18), 6555-6569.

18. Xu, Y.; Kraft, M.; & Xu, R. Metal-free carbonaceous electrocatalysts and photocatalysts for water splitting. *Chemical Society Reviews*. **2016**, *45*(11), 3039-3052.

19. Wu, T.; Stone, M. L.; Shearer, M. J.; Stolt, M. J.; Guzei, I. A.; Hamers, R. J.; ... & Schmidt, J. R. Crystallographic facet dependence of the hydrogen evolution reaction on CoPS: theory and experiments. *ACS Catalysis*. **2018**, *8*(2), 1143-1152.

20. Yan, Y.; Xia, B. Y.; Zhao, B.; & Wang, X. A review on noble-metal-free bifunctional heterogeneous catalysts for overall electrochemical water splitting. *Journal of Materials Chemistry A*. **2016**, *4*(45), 17587-17603.

21. Wang, F.; Shifa, T. A.; Zhan, X.; Huang, Y.; Liu, K.; Cheng, Z.; ... & He, J. Recent advances in transition-metal dichalcogenide based nanomaterials for water splitting. *Nanoscale*. **2015**, *7*(47), 19764-19788.

22. Lukowski, M. A.; Daniel, A. S.; Meng, F.; Forticaux, A.; Li, L.; & Jin, S. Enhanced hydrogen evolution catalysis from chemically exfoliated metallic MoS2 nanosheets. *Journal of the American Chemical Society*. **2013**, *135*(28), 10274-10277.

23. Xiao, P.; Chen, W.; & Wang, X. A review of phosphide-based materials for electrocatalytic hydrogen evolution. *Advanced Energy Materials*. **2015**, *5*(24), 1500985.

24. Yu, X. Y.; & Lou, X. W. Mixed metal sulfides for electrochemical energy storage and conversion. *Advanced Energy Materials*. **2018**, *8*(3), 1701592.

25. Chen, H.; Jiang, J.; Zhang, L.; Wan, H.; Qi, T.; & Xia, D. Highly conductive NiCo2 S 4 urchin-like nanostructures for high-rate pseudocapacitors. *Nanoscale*. **2013**, *5*(19), 8879-8883.

26. Shen, L.; Yu, L.; Wu, H. B.; Yu, X. Y.; Zhang, X.; & Lou, X. W. Formation of nickel cobalt sulfide ball-in-ball hollow spheres with enhanced electrochemical pseudocapacitive properties. *Nature communications*. **2015**, *6*(1), 6694.

27. Staszak-Jirkovský, J.; Malliakas, C. D.; Lopes, P. P.; Danilovic, N.; Kota, S. S.; Chang, K. C.; ... & Markovic, N. M. Design of active and stable Co–Mo–S x chalcogels as pH-universal catalysts for the hydrogen evolution reaction. *Nature materials*. **2016**,*15*(2), 197-203.

28. Chen, H.; Jiang, J.; Zhang, L.; Xia, D.; Zhao, Y.; Guo, D.; ... & Wan, H. In situ growth of NiCo2S4 nanotube arrays on Ni foam for supercapacitors: maximizing utilization efficiency at high mass loading to achieve ultrahigh areal pseudocapacitance. *Journal of Power Sources*. **2014**, *254*, 249-257.

29. Liu, D.; Lu, Q.; Luo, Y.; Sun, X.; & Asiri, A. MNiCo 2 S 4 nanowires array as an efficient bifunctional electrocatalyst for full water splitting with superior activity. *Nanoscale*. **2015**, *7*(37), 15122-15126.

30. Sivanantham, A.; Ganesan, P.; & Shanmugam, S. Hierarchical NiCo2S4 nanowire arrays supported on Ni foam: an efficient and durable bifunctional electrocatalyst for oxygen and hydrogen evolution reactions. *Advanced Functional Materials*. **2016**, *26*(26), 4661-4672.

31. Liu, Q.; Jin, J.; & Zhang, J. NiCo2S4@ graphene as a bifunctional electrocatalyst for oxygen reduction and evolution reactions. *ACS applied materials & interfaces*. **2013**, *5*(11), 5002-5008.

32. Jiang, N.; Tang, Q.; Sheng, M.; You, B.; Jiang, D. E.; & Sun, Y. Nickel sulfides for electrocatalytic hydrogen evolution under alkaline conditions: a case study of crystalline NiS, NiS 2, and Ni 3 S 2 nanoparticles. *Catalysis Science & Technology*. **2016**, *6*(4), 1077-1084.

33. Huang, Z. F.; Song, J.; Li, K.; Tahir, M.; Wang, Y. T.; Pan, L.; ... & Zou, J. J. Hollow cobalt-based bimetallic sulfide polyhedra for efficient all-pH-value electrochemical and photocatalytic hydrogen evolution. *Journal of the American Chemical Society*. **2016**, *138*(4), 1359-1365.

34. Wang, D. Y.; Gong, M.; Chou, H. L.; Pan, C. J.; Chen, H. A.; Wu, Y.; ... & Dai, H. Highly active and stable hybrid catalyst of cobalt-doped FeS2 nanosheets–carbon nanotubes for hydrogen evolution reaction. *Journal of the American Chemical Society*. **2015**, *137*(4), 1587-1592.

35. Li, P.; & Zeng, H. C. Advanced oxygen evolution catalysis by bimetallic Ni–Fe phosphide nanoparticles encapsulated in nitrogen, phosphorus, and sulphur tri-doped porous carbon. *Chemical Communications*. **2017**, *53*(44), 6025-6028.

36. Zou, X.; & Zhang, Y. Noble metal-free hydrogen evolution catalysts for water splitting. *Chemical Society Reviews*. **2015**, *44*(15), 5148-5180.

37. Anantharaj, S.; Ede, S. R.; Sakthikumar, K.; Karthick, K.; Mishra, S.; & Kundu, S. Recent trends and perspectives in electrochemical water splitting with an emphasis on sulfide, selenide, and phosphide catalysts of Fe, Co, and Ni: a review. *Acs Catalysis*. **2016**, *6*(12), 8069-8097.

38. Jaramillo, T. F.; Jørgensen, K. P.; Bonde, J.; Nielsen, J. H.; Horch, S.; & Chorkendorff, I. Identification of active edge sites for electrochemical H2 evolution from MoS2 nanocatalysts. *Science*. **2007**, *317*(5834), 100-102.

39. Sun, K.; Zeng, L.; Liu, S.; Zhao, L.; Zhu, H.; Zhao, J.; ... & Liu, C. Design of basal plane active MoS2 through one-step nitrogen and phosphorus co-doping as an efficient pH-universal electrocatalyst for hydrogen evolution. *Nano Energy*. **2019**, *58*, 862-869.

40. Dong, J.; Zhang, F. Q.; Yang, Y.; Zhang, Y. B.; He, H.; Huang, X.; ... & Zhang, X. M. (003)-Facet-exposed Ni3S2 nanoporous thin films on nickel foil for efficient water splitting. *Applied Catalysis B: Environmental*. **2019**, *243*, 693-702.

41. Ganguly, P.; Mathew, S.; Clarizia, L.; Akande, A.; Hinder, S.; Breen, A.; & Pillai, S. C. Theoretical and experimental investigation of visible light responsive AgBiS2-TiO2 heterojunctions for enhanced photocatalytic applications. *Applied Catalysis B: Environmental*. **2019**, *253*, 401-418.

42. Bernechea, M.; Cates, N.; Xercavins, G.; So, D.; Stavrinadis, A.; & Konstantatos, G. Solution-processed solar cells based on environmentally friendly AgBiS2 nanocrystals. *Nature Photonics*. **2016**, *10*(8), 521-525.

43. Pai, N.; Lu, J.; Senevirathna, D. C.; Chesman, A. S.; Gengenbach, T.; Chatti, M.; ... & Simonov, A. N. Spray deposition of AgBiS 2 and Cu 3 BiS 3 thin films for photovoltaic applications. *Journal of Materials Chemistry C*. **2018**, *6*(10), 2483-2494.

44. Lei, P.; An, R.; Zheng, X.; Zhang, P.; Du, K.; Zhang, M.; ... & Zhang, H. Ultrafast synthesis of ultrasmall polyethylenimine-protected AgBiS 2 nanodots by "rookie method" for in vivo dual-modal CT/PA imaging and simultaneous photothermal therapy. *Nanoscale*. **2018**, *10*(35), 16765-16774.

45. Cheng, J.; Wang, W.; Xu, X.; Lin, Z.; Xie, C.; Zhang, Y.; ... & Li, Q. AgBiS2 nanoparticles with synergistic photodynamic and bioimaging properties for enhanced malignant tumor phototherapy. *Materials Science and Engineering: C*. **2020**, *107*, 110324.

46. Sun, M.; Yang, D.; Wang, C.; Bi, H.; Zhou, Y.; Wang, X.; ... & Yang, P. AgBiS 2-TPP nanocomposite for mitochondrial targeting photodynamic therapy, photothermal therapy

and bio-imaging under 808 nm NIR laser irradiation. *Biomaterials science*. **2019**, *7*(11), 4769-4781.

47. Tan, G.; Hao, S.; Zhao, J.; Wolverton, C.; & Kanatzidis, M. G. High thermoelectric performance in electron-doped AgBi3S5 with ultralow thermal conductivity. *Journal of the American Chemical Society*. **2017**,*139*(18), 6467-6473.

48. Kim, J. H.; Chung, D. Y.; Bilc, D.; Loo, S.; Short, J.; Mahanti, S. D.; ... & Kanatzidis, M. G. Crystal Growth, Thermoelectric Properties, and Electronic Structure of AgBi3S5 and AgSb x Bi3-x S5 (x= 0.3). *Chemistry of materials*. **2005**, *17*(14), 3606-3614.

49. Qian, X.; Zhang, X.; Guo, H.; Ding, B.; Chen, M.; Wang, J. L.; ... & Wang, S. F. Enhancing thermoelectric performance of n-type AgBi3S5 through synergistically optimizing the effective mass and carrier mobility. *Journal of Materiomics*. **2023**, *9*(5), 874-881.

50. Sugarthi, S., Bakiyaraj, G., Abinaya, R., Navaneethan, M., Archana, J., & Shimomura, M. Effect of different growth temperature on the formation of ternary metal chalcogenides AgBiS2. *Materials Science in Semiconductor Processing*. **2020**, *107*, 104781.

51. Kim, Y. Y.; & Walsh, D. Metal sulfide nanoparticles synthesized via enzyme treatment of biopolymer stabilized nanosuspensions. *Nanoscale*. **2010**, *2*(2), 240-247.

52. Wu, D.; Jiang, Y.; Yuan, Y.; Wu, J.; & Jiang, K. ZnO–ZnS heterostructures with enhanced optical and photocatalytic properties. *Journal of Nanoparticle Research*. **2011**, *13*, 2875-2886.

53. Baer, D. R.; Artyushkova, K.; Cohen, H.; Easton, C. D.; Engelhard, M.; Gengenbach, T. R.; ... & Roberts, A. XPS guide: Charge neutralization and binding energy referencing for insulating samples. *Journal of Vacuum Science & Technology A*. **2020**, *38*(3).

54. Bernechea, M.; Cates, N.; Xercavins, G.; So, D.; Stavrinadis, A.; & Konstantatos, G. Solution-processed solar cells based on environmentally friendly AgBiS2 nanocrystals. *Nature Photonics*. **2016**, *10*(8), 521-525.

55. Pai, N.; Lu, J.; Senevirathna, D. C.; Chesman, A. S.; Gengenbach, T.; Chatti, M.; ... & Simonov, A. N. Spray deposition of AgBiS 2 and Cu 3 BiS 3 thin films for photovoltaic applications. *Journal of Materials Chemistry C*. **2018**, *6*(10), 2483-2494.

56. Cheng, W.; Guan, W.; Lin, Y.; & Lu, C. Rapid discrimination of adsorbed oxygen and lattice oxygen in catalysts by the cataluminescence method. *Analytical chemistry*. **2022**, *94*(2), 1382-1389.

57. Bai, P.; Tong, X.; Wan, J.; Gao, Y.; & Xue, S. Flower-like Bi2O2CO3-mediated selective oxidative coupling processes of amines under visible light irradiation. *Journal of Catalysis*. **2019**, *374*, 257-265.

58. Chakraborty, M.; Bera, K. K.; Chatterjee, S.; Ghosh, A.; & Bhattacharya, S. K. Synthesis of mesoporous BiOI flower and facile in-situ preparation of BiOI/BiOCl mixture for enhanced photocatalytic degradation of toxic dye, Rhodamine-B. *Journal of Photochemistry and Photobiology*. **2021**, *8*, 100077.

59. Bera, K. K.; Chowdhury, A.; Bera, S. K.; Das, M. R.; Roy, A.; Das, S.; & Bhattacharya, S. K. Pd Nanoparticle-Decorated Novel Ternary Bi2O2CO3-Bi2MoO6-CuO Heterojunction for Enhanced Photo-electrocatalytic Ethanol Oxidation. *ACS omega*. **2023**, *8*(31), 28419-28435.

60. Bera, K. K.; Chakraborty, M.; Bera, S. K.; Chowdhury, A.; Das, M. R.; Mondal, M.; & Bhattacharya, S. K. Synergistic photo-enhanced electrocatalysis of Pt–ZnO–Bi 2 O 3 heterojunction for methanol oxidation under visible light illumination. *Energy Advances*. **2022**, *1*(11), 908-925.

61. Bera, K.; Madhu, R.; Dhandapani, H. N.; Nagappan, S.; De, A.; & Kundu, S. Accelerating the electrocatalytic performance of NiFe–LDH via Sn doping toward the water oxidation reaction under alkaline condition. *Inorganic Chemistry*. **2022**, *61*(42), 16895-16904.

62. Nagappan, S.; Karmakar, A.; Madhu, R.; N Dhandapani, H.; Bera, K.; De, A.; & Kundu, S. Electronically modified Ce3+ ion doped 2D NiFe-LDH nanosheets over a 1D microfiber: a high-performance electrocatalyst for overall water splitting. *ACS Applied Energy Materials*. 2022, *5*(10), 12768-12781.

63. Karmakar, A.; Karthick, K.; Kumaravel, S.; Sankar, S. S.; & Kundu, S. Enabling and inducing oxygen vacancies in cobalt iron layer double hydroxide via selenization as

precatalysts for electrocatalytic hydrogen and oxygen evolution reactions. *Inorganic Chemistry*. **2021**, *60*(3), 2023-2036.

64. De, A.; Karmakar, A.; & Kundu, S. Enhancing the surface-active sites of bimetallic 2D hydroxide materials by introducing Fe2+ ions toward effective hydroxide adsorption for the water oxidation reaction. *ACS Applied Energy Materials*. **2023**, *6*(11), 5761-5773.

65. Kuchipudi, A.; Nagappan, S.; Karmakar, A.; Sreedhar, G.; & Kundu, S. Stabilization of Ru NPs over 3D LaCrO3 Nanostructures for High-Performance HER Catalysts in Acidic Media. *Inorganic Chemistry*. **2022**, *61*(48), 19407-19416.

66. De, A.; Madhu, R.; Bera, K.; Dhandapani, H. N.; Nagappan, S.; Roy, S. S.; & Kundu, S. Deciphering the amplification of dual catalytic active sites of Se-doped NiV LDH in water electrolysis: a hidden gem exposure of anion doping at the core-lattice LDH framework. *Journal of Materials Chemistry A*. **2023**, *11*(45), 25055-25071.

Chapter 3

Environment friendly $AgBi_3S_5$-Bi_2S_3 nano composite for efficient visible light driven photochemical H_2 evolution reaction

3.1 Introduction

Renewable energy generator plays a pivotal role to create a sustainable eco-friendly environment where two apparently opposing characters balance one another. It meets on one hand ever-lasting energy demand and on the other by developing clean energy. It prevails and prevents the prime route cause from which natural disaster like situation arises **[1-6]**. In this context photocatalytic water splitting has been evolving too fast to manage two most abundant energy resources available to us which are clean, renewable and natural **[7-11]**. The issues cause negative environmental effect, limited reserves and excessive utilization generating from fossil fuels strongly countered by the potential solution namely production of hydrogen via photocatalytic routes **[12-16]**. A few promising methods attracted convincingly towards direct conversion of solar energy to hydrogen, photoelectrochemical water splitting (PEC) is one of the methods among them **[17-22]**. Most commonly the main components which are involved in photoelectrochemical water splitting are counter electrode, aqueous electrolyte and a photoactive semiconductor electrode. The faradic efficiency of this process has been driven by photoactive semiconductor-based electrode **[23-24]**. Popular researchers like Fujishima and Honda invented the photoelectrochemical water splitting for the first time based on their development of TiO_2 based materials **[5]**. Since, then numerous oxide-based materials like SnO_2, TiO_2, ZnO came in to play in the electrochemical water splitting field after the initial break through due to their nontoxicity, outstanding photo corrosion resistance and high photocatalytic activity and other characteristic features **[25-28]**. The conversion efficiency of hydrogen production has not reached still a certain satisfactory level due to the wide range of band gap of these oxide materials. This sort of limitation leads to grow chalcogenide-based materials to contribute in the conversion efficiency because of their narrow bandgap features fit very well in this photoelectrochemical water splitting. The light absorption and photoinduced charge separation enhance when chalcogenide-based materials are coupled with metal oxide-based materials. [29-30] The developed chalcogenide materials such as PbS, PbSe, CdS, CdSe and Bi_2S_3 contributed significantly in photoelectrochemical energy conversion **[29-34]**. The commercial use is restricted with lead and cadmium-based chalcogenide materials due to their negative environmental effects. On the other side bismuth-based materials attracts more conveniently in the photoelectrochemical water splitting for their facile characteristic tunability, solution processability and pro-environmental nature **[35-36].** The previous studies have revealed that ternary bismuth-based chalcogenide materials like $AgBiS_2$ exhibited a higher photovoltaic

performance than bismuth-based chalcogenide materials like Bi_2S_3 and also the absorption coefficient enhanced in the visible region **[37]**. The potentiality of the conversion rate of hydrogen production in photoelectrochemical water splitting was influenced by the different morphological shape and form of that kind of synthesized materials. Another some important factors along with band gap engineering are the light sensitization enhanced catalysis by adding quantum dots, coupling like plasmon-exciton, photon coupling between facilitated host semiconductor and noble metal cocatalysts based nanoparticle **[38]**.

In the previous chapters, we have emphasized on electrochemical water splitting for hydrogen production from the synthesized binary and ternary sulfide-based nanomaterials and explored first time of their catalytic efficiency in this field.

Here we synthesized specifically ternary sulfide-based $AgBi_3S_5$-Bi_2S_3 nanocomposite for using it as catalyst for the first time in photoelectrochemical water splitting which improvised their catalytic performance in presence of light compare to that in absence of light in the same reaction medium.

3.2 Experimental Sections

3.2.1 Materials

Silver nitrate ($AgNO_3$, 99.9%, Merck), bismuth nitrate (Bi $(NO_3)_3.5H_2O$, 99.9%, Merck), ethylene glycol ($C_2H_6O_2$, 99.9%, Merck), thiourea (H_2N-C(=S)-NH_2, 99.9%, Merck), were used in this study without further refinement. The Millipore water was used throughout the investigation.

3.2.2 Synthesis of the $AgBi_3S_5$-Bi_2S_3

Three dried clean beakers were taken and marked as beaker A, B and C. In beaker A, 0.68 g of silver nitrate was dissolved in 20 mL ethylene glycol solution followed by 15 minutes of ultrasonication at room temperature. In beaker B, a similar solution was prepared with 2.05 g of bismuth nitrate instead of silver nitrate and 0.61 g of thiourea dissolved in 20 mL ethylene glycol solution in beaker C following the above conditions. Now solution in beaker B poured in beaker A to make a uniform solution with 15 minutes of sonication and the homogenous solution now placed under temperature (pre-adjusted at 90°C) controlled heating mantel at ambient condition.

Solution in beaker C mixed with this homogenous solution mixture when the temperature reached at 90°C and the resultant uniform mixture was kept in same reaction condition up to 2 hours. The heating mantel was stopped after 2 hours and settled down the appeared ash-colored mass in the reaction mixture at room temperature. Then the mass was collected followed by centrifugation along with washing by Millipore water and ethanol for several times and dried at 80°C up to 20 hours in air oven.

3.2.3 Rietveld refinement analysis with experimental XRD data

The Rietveld refinement analysis techniques (MAUD 2.26, software version) was mainly used to characterize with the PXRD data of synthesized micro, nano structure as well as the nano composite. Marquardt least square method is applied to minimize the differentiate parameter between the diffraction pattern of simulated and observed data. The fitting ratio of that resulting parameter was close to 1 signified its fitting quality where R_{wp} implies ratio of weighted residual error and R_{exp} signifies the residual error and the fitting is known as the goodness of fit as termed as GOF.

Where R_{wp} and R_{exp} find out from the following expressions

$$R_{wp} = \left[\frac{\sum_i w_i (I_0 - I_c)^2}{\sum_i w_i I_0^2} \right]^{1/2} \quad \text{and} \quad R_{exp} = \left[\frac{(N - P)}{\sum_i w_i I_0^2} \right]^{1/2}$$

I_0, I_c, w_i, N and P represent experimental intensity of XRD peaks, calculated intensity of XRD peaks, weighing factor ($1/I_0$), number of exponential observation and number of fitting parameters respectively [39,40].

3.2.4 Electrochemical measurement and fabrication of the electrode

AUTO-LAB was used at room temperature as electrochemical analyzer to perform the electrochemical study where 0.5 M H_2SO_4 was used as an electrolyte throughout the experiments. Conventional three electrode system was placed for the experiment in which graphite carbon rod was used as a working electrode, saturated calomel electrode (SCE) was used as reference electrode and Platinum foil was used as a counter electrode.

The catalyst solution drop-casted over the graphite carbon rod surface (previously polished with MRE-paper) and cleaned by sonication after dipping in alcohol & water used as a working electrode which effective surface area was 0.12 cm^2. 4 mg of catalyst was weight out in a 3 mL glass bottle and 1 mL ethanol was added to it and the mixture solution was bath sonicated up to 30 to 40 minutes at room temperature. Then 10 µL of catalyst solution was drop-casted over graphite carbon rod and dried at room temperature up to 2 hours in an inert atmosphere and then 5 µL of 0.5 % Nafion solution was drop-casted over catalyst solution as a binder and then it was kept in an inert atmosphere up to 20 hours. 0.3 mg/cm^2 was the catalytic mass loading on the surface of working electrode. The cyclic voltammetry was performed with that working electrode in a three-electrode conventional set up at a scan rate of 50 mv/s and after 20 cycles of completion, the liner sweep voltammetry (LSV) was performed at 2 mv/s with that activated electrode. The Tafel slope values was determined from the LSV curves and all the data throughout the measurements were 50% iR-corrected in manual mode with that Rs values obtained from the electrochemical impedance studies (EIS). EIS study was analyzed at a scan range from 0.1 to 10,000 Hz at 5 mv amplitude potential in which it could reach to benchmarking current i.e., 10 mA/cm^2. The electrochemical data was used in RHE scale throughout the experiments.

The Nernst equation was used for the conversion of LSV data in the potential (V) regions.

$$\mathbf{E_{RHE} = E_{SCE} + 0.059 \times 0.3 + 0.241}$$

Overpotential values has determined using the following equation

$$\mathbf{\eta = 0 - E_{RHE}\ (V)}$$

The Tafel slopes values has determined from the relation between current density in log scale and potential which is known as Tafel plot. The Butler-Volmer equation assisted to find out the Tafel slope values which related as

$$\mathbf{\eta = b \times \log j + a \ldots\ldots\ldots\ldots\ldots\ (1)}$$

$$\mathbf{b = ((\eta - a)/ \log j) \ldots\ldots\ldots\ldots\ldots\ldots\ (2)}$$

a, b, j and η implies as reaction constant, Tafel slope, current density and overpotential respectively.

The electrochemical double layer capacitance value was determined analyzing the data from the non-faradic region and with that electrochemical surface area (ECSA) values were find out comparing the following equation

$i_c = \upsilon \times C_{dl}$ …….(3)

$ECSA = C_{dl} / C_s$ ……(4)

Whereas i_c, υ, C_s, represents double layer charging current, scan rate (υ), specific capacitance value (0.040 $mFcm^{-2}$, reference value) respectively and all the electrochemical data used throughout the experiments after correlation of iR drop.

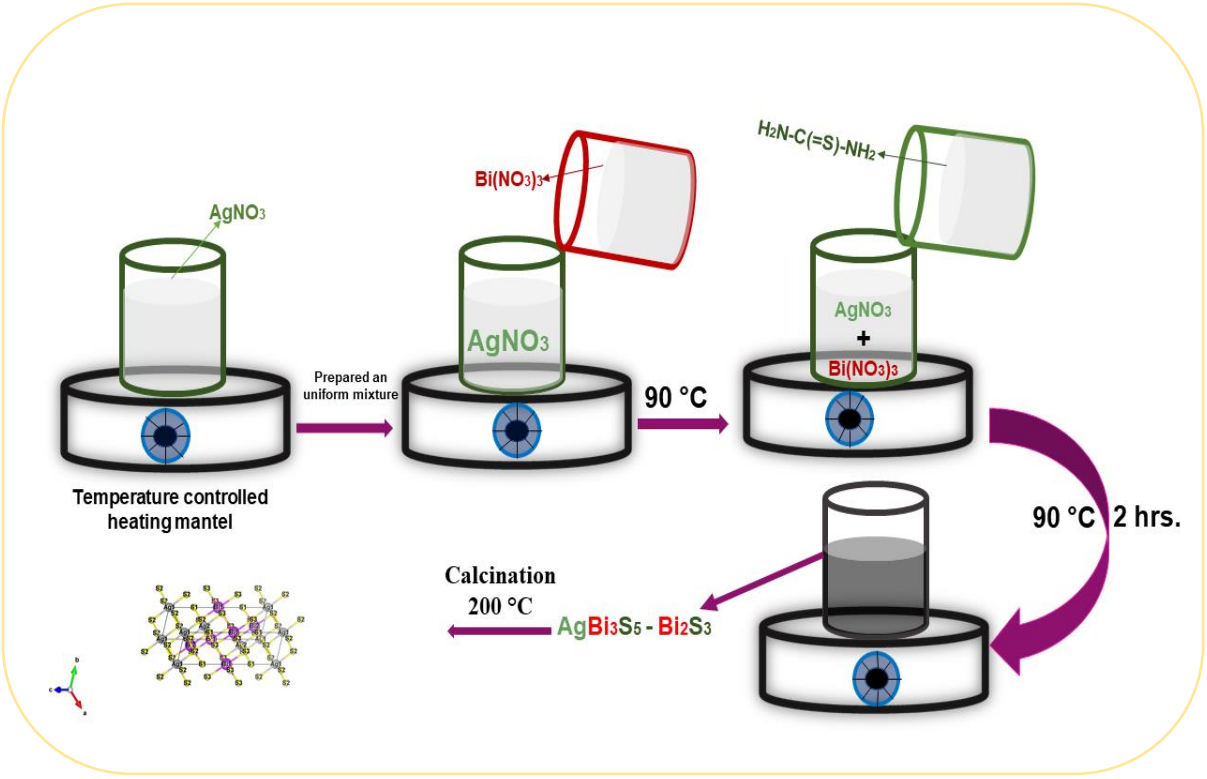

Scheme 3.1 Schematic diagram of synthesis procedure of $AgBi_3S_5$ - Bi_2S_3

3.3 Results and Discussions

The as synthesized nano composites were characterized by the X-ray diffraction (XRD), Fourier transform infrared spectroscopy (FTIR) along with X-ray photoelectron spectroscopy (XPS) and

the morphological structure of synthesized $AgBi_3S_5$ - Bi_2S_3 was studied by Transmission electron microscopy (TEM), Field emission scanning electron microscopy (FESEM) etc.

3.3.1 XRD analysis

The main diffraction planes for as synthesized nano composite ($AgBi_3S_5$-Bi_2S_3) found at (113), (310), (312), (403), (313), (314), (405), (007), (116) crystal planes. These match with the monoclinic $AgBi_3S_5$(JCPDS NO. 83-2051) and the respective diffraction peaks appear at 2Θ values (°) 28.53, 29.92, 31.39, 32.52, 34.913, 36.430, 37.165, 38.447, 40.82 respectively. The rest of the diffraction peaks and planes may be synchronized with the associated orthorhombic Bi_2S_3(JCPDS NO. 89-8965) and their 2Θ values (°) found near about 28.57, 32.90, 49.30, which are attributed with the corresponding diffraction planes (230), (301), (521) respectively. The Rietveld analysis was also confirmed the synthesis of $AgBi_3S_5$-Bi_2S_3 nano composite and the outcome of mass percentages of $AgBi_3S_5$ and Bi_2S_3 were 87% and 13% respectively and the value of weighted residual (R_{wp}) error was 6.04 where expected residual (R_{exp}) error 5.9 and their goodness of fit ratio (GOF) 1.02 which is near is 1 signifying the respective fitting quality.

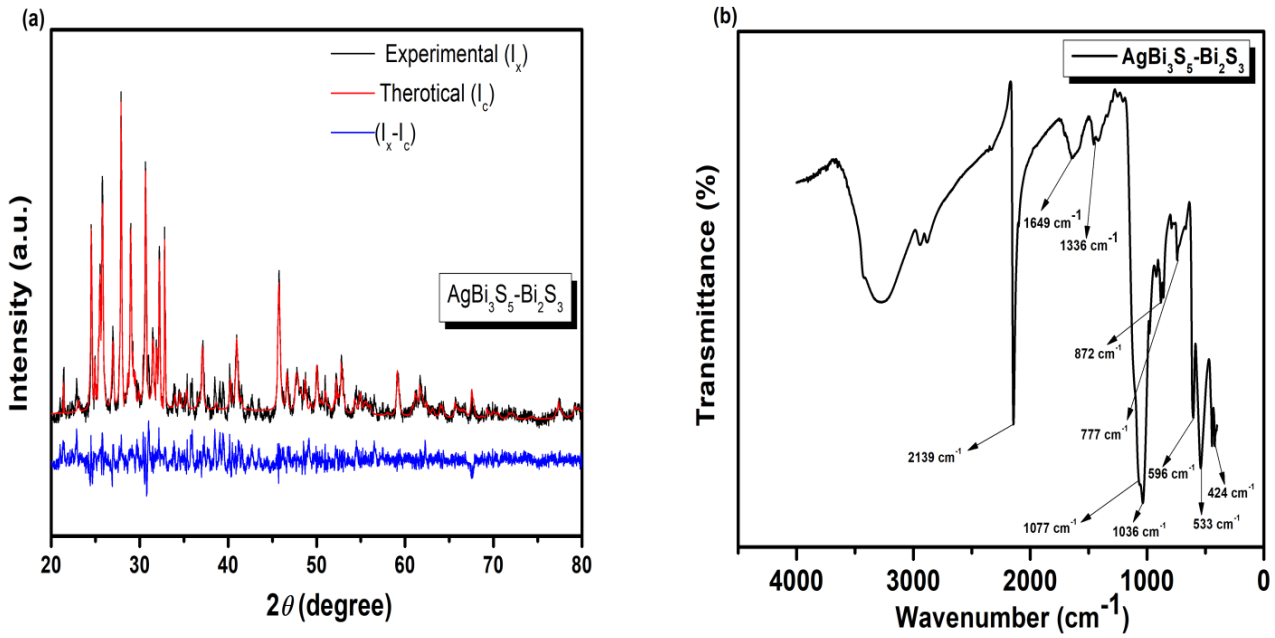

Figure 3.1 (a) Profiles of XRD and corresponding Rietveld analysis of synthesized $AgBi_3S_5$-Bi_2S_3 where black line denoted the experimental XRD pattern where red line implies the respective simulated XRD pattern and I_x – I_c stands for respective residual intensity **(b)** FTIR spectrum of synthesized $AgBi_3S_5$-Bi_2S_3 nano composite.

3.3.2 FTIR analysis

Figure **3.**1(b) represents the FTIR spectrum of $AgBi_3S_5$-Bi_2S_3 which exhibits the peak at 533 cm^{-1} indicating the characteristic vibration mode of sulfur **[41]** inferring the presence of Ag-S bond. The peaks found in range 590 cm^{-1} to 650 cm^{-1} indicate the vibration of Bi-S **[41]**. Frequencies near about 1649 cm^{-1} for $AgBi_3S_5$-Bi_2S_3 is probably due to the stretching and bending vibrations of the O-H bond of the adsorbed H_2O at the surface of $AgBi_3S_5$-Bi_2S_3 **[42, 43]**. The peak found in $AgBi_3S_5$-Bi_2S_3 around 1336 cm^{-1} and 872-900 cm^{-1} are seemingly due to the stretching and bending vibrations of the Bi-S bond.

3.3.3 XPS analysis

In the XPS analysis, survey spectrum **(figure3.2a)** shows the elements present. The doublet peaks found at 373.7 eV and 367.7 eV in Ag spectrum **(figure3.2b)** may be ascribed to Ag $_{5/2}$ and Ag $_{3/2}$ of the Ag^+ respectively **[44]**. Similarly, the Bi 4f doublet**(figure3.2c)** can also be looked at 158.9 eV (Bi 4f $_{7/2}$) and 164.2 eV (Bi 4f $_{5/2}$). The measured positions are in between those of bismuth metal (Bi 4f $_{7/2}$, 157 eV) and bismuth oxides (Bi 4f $_{7/2}$, 159 eV), which are anticipated and revealing of typical bismuth sulfide **[44].** The consequence of above investigation directed that both silver (Ag (I)) and bismuth (Bi (III)) were existing as metal sulfides as approved with previous studies **[45, 46]**. Another small peak found at 231 eV can be assigned to S 2s **(Figure 3.2(d))**. **Figure 3.2(a)** presented as surface spectrum where a broad peak at 532 eV was assigned to the O 1s region due to water molecules adsorbed at the surface of the metal sulfide of the catalyst **[47]**. The catalyst drops casted on the surface of the silicon wafer for the XPS analysis and peak appeared in around 100-150 eV region attributed the corresponding observance. One of the broad peaks emphasized around binding energy 286.6 eV appears due to C 1s calibration peak, which is also known as adventitious carbon peak **[48]**.

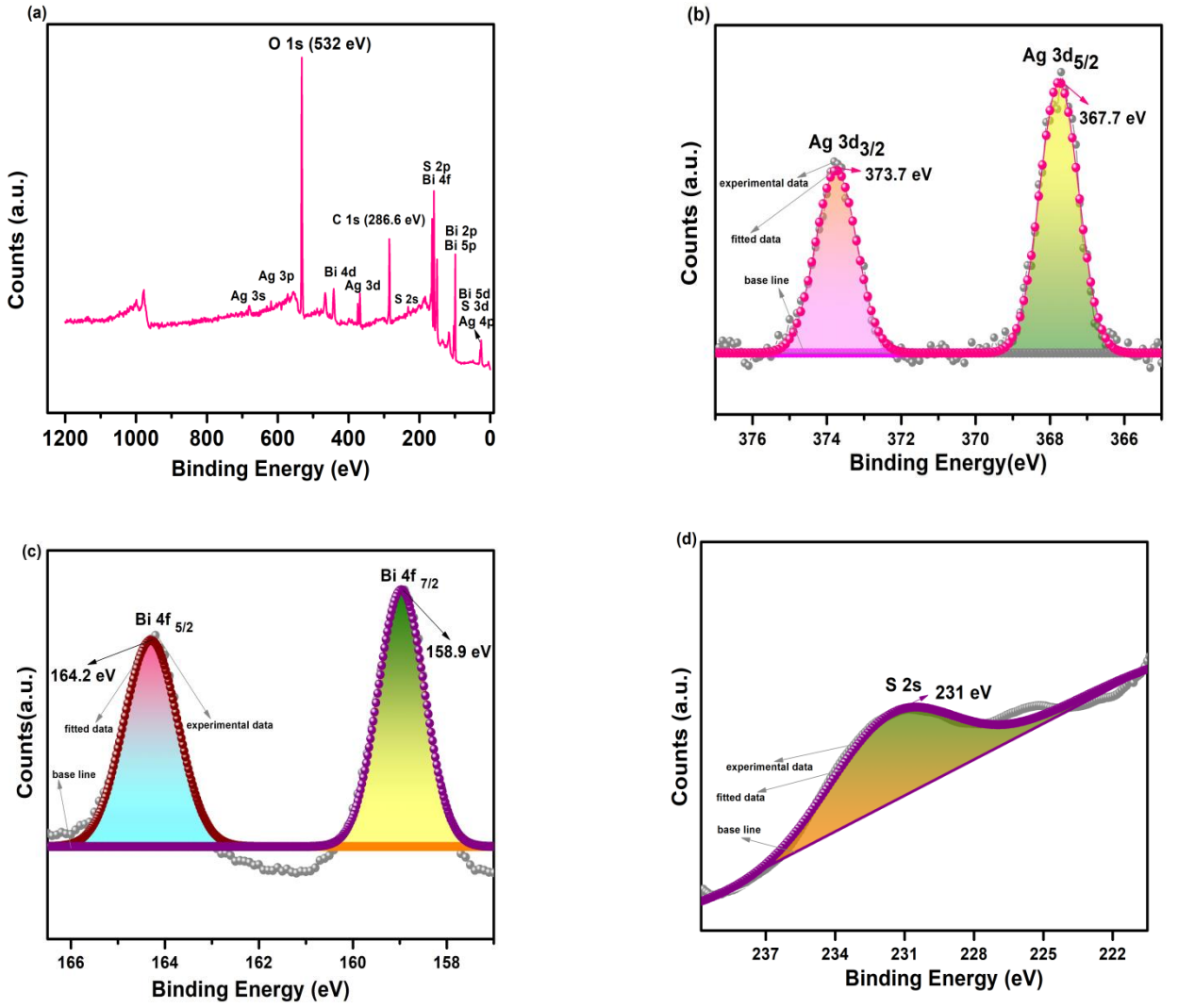

Figure 3.2: Fine XPS profiles of synthesized $AgBi_3S_5$-Bi_2S_3 where (a) survey spectrum (b) Ag 3d (c) Bi 4f and (d) S 2s spectra.

3.3.4 Morphological analysis

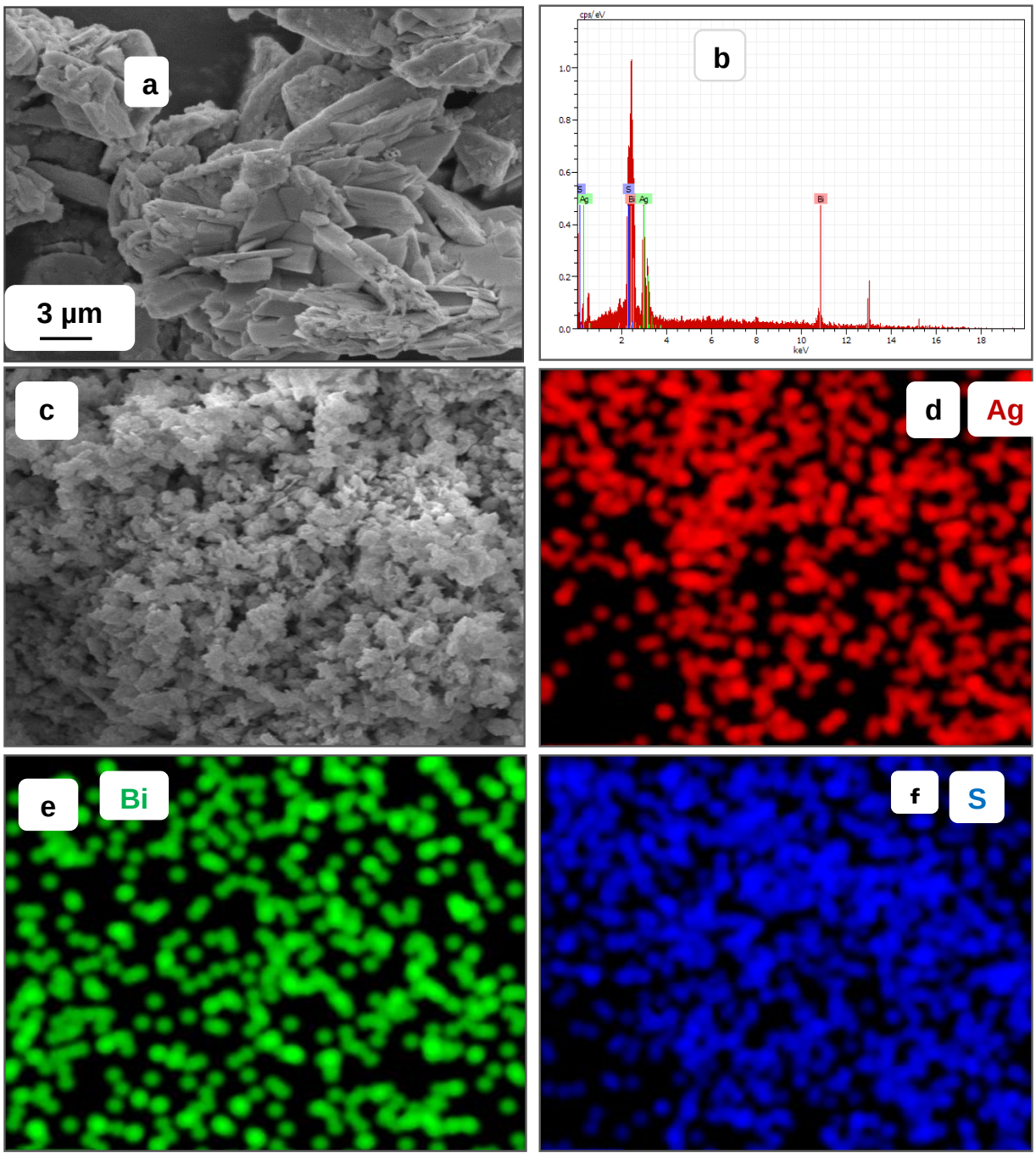

Figure 3.3 (a) *FESEM image of synthesized* $AgBi_3S_5$-Bi_2S_3 *nanocomposites (b) EDS profile of respective nanocomposite (c) area selected for EDS analysis (d, e, f) color mapping profiles of Ag, Bi, and S respectively.*

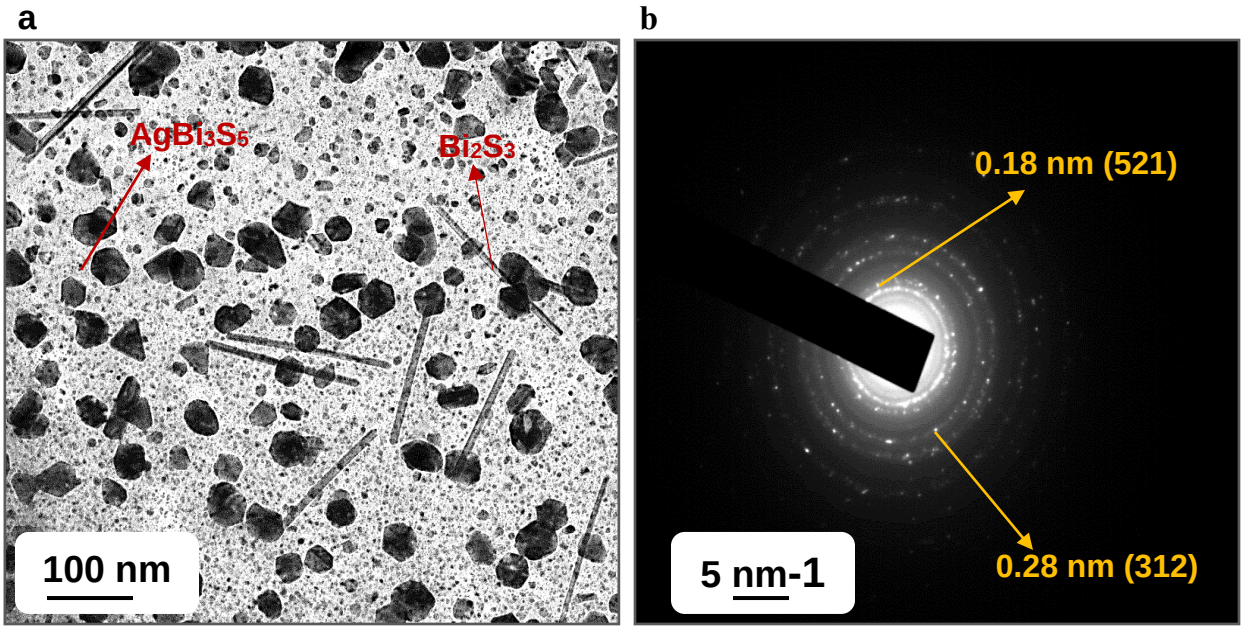

Figure 3.4: (a, b) TEM image and SAED pattern of $AgBi_3S_5$-Bi_2S_3 respectively.

The surface morphology and compound recognition of $AgBi_3S_5$-Bi_2S_3 were studied by FESEM, TEM and SAED pattern as depicted in **figure 3.3** and **3.4** respectively. **Figures 3.3(a)** illustrates the morphology of $AgBi_3S_5$-Bi_2S_3 nanocomposite. FESEM pictures exhibit plate and rod-like structures with some grains on the plates and the rods. These also reveal sufficient holes and gaps between the structures, which may help movement of the reactants and products towards and from the surface of the catalyst. The EDS spectrum of $AgBi_3S_5$-Bi_2S_3 nanocomposites also recognizes all the constituting elements **(figure 3.3b)**. **Figure 3.3(c)** represents the area selected for EDS analysis and **figures 3.3(d, e, f)** present the color mapping profiles of Ag, Bi and S respectively, each of which is almost uniformly distributed in the selected area.

The irregular small spheres of about 8 nm diameter and bigger lumps (8-40 nm) and some rod-like structure (diameter about 9 nm) can be observed in **figure 3.4 (a)**. **Figure 3.4(b)** indicated the presence of both $AgBi_3S_5$ and Bi_2S_3 as the corresponding planes (312) and (521) exposed in SAED pattern of $AgBi_3S_5$-Bi_2S_3 in **figure 3.4(b)** are synchronized with the outcome from XRD profile of synthesized $AgBi_3S_5$-Bi_2S_3 nano composite. The above result is more clearly revealed the formation of $AgBi_3S_5$-Bi_2S_3 nanocomposite.

3.3.5 Brunauer-Emmett-Teller (BET) analysis

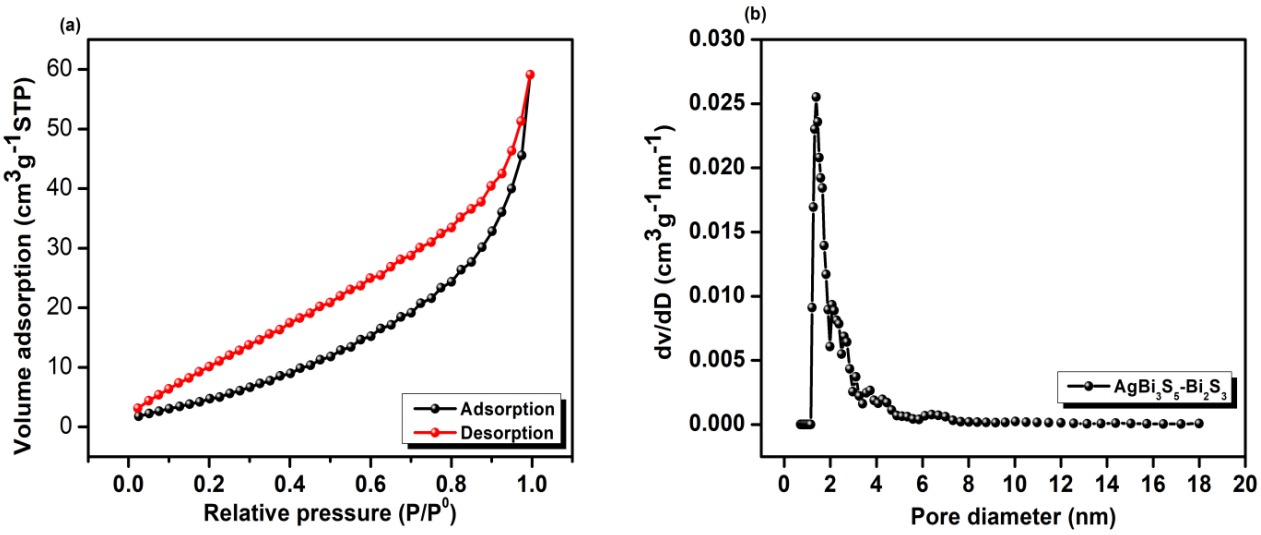

Figure 3.5 (a) N_2 adsorption-desorption isotherm where black line indicates adsorption and red line indicates desorption of synthesized $AgBi_3S_5$-Bi_2S_3 nano composite (b) pore size distribution of $AgBi_3S_5$-Bi_2S_3

The surface area and the corresponding average pore diameter found for the synthesized *$AgBi_3S_5$-Bi_2S_3* nano composite were 25.79 m^2/g and 5.29 nm respectively from the N_2 adsorption-desorption isotherm.

3.3.6 Photo-electrochemical hydrogen evolution reaction

The photoelectrochemical hydrogen evolution reaction was carried out in 0.5 M H_2SO_4 in absence of light and as well as in presence of light. The outcome from the experiment is shown in **figure 3.6.** The synthesized photocatalyst perform better in HER reaction in presence of light compare to that in absence of light.

Overpotential is one of the few parameters which are used to determine the electrochemical activities. Here we first analyzed the linear sweep voltammetry (LSV) studies in the potential range of 0 to -1 V vs. RHE to scrutinize the electrochemical activity after collecting the iR-corrected LSV outcomes at 5 mV/sec scan rate. It explores the efficacy of the synthesized photocatalyst towards HER, which is substantiated by analyzing the overpotential values at 10 mA/cm^2 standard current density value in **figure 3.6(a)**. Synthesized $AgBi_3S_5$-Bi_2S_3 nano composite photocatalyst shows the respective overpotential values 45 mV and 62 mV with respect to RHE in presence and absence of light respectively **[49]**. **Figure 3.6(b)** is expressed through bar diagram for better understanding of the comparison of overpotential values in HER reaction in absence and presence of light using the same catalyst loading. The photocatalytic behavior of the synthesized nanocomposite can also be revealed from the chronoamperometric study done both in absence and presence of light as portrayed in **figure 3.6(c)**. The outcome of current has been increased when light is ON and the subsequent observed current decreased when light is OFF in the Chronoamperometric analysis (CA) which clearly indicates the better catalytic photo-effect of that synthesized nanocomposite.

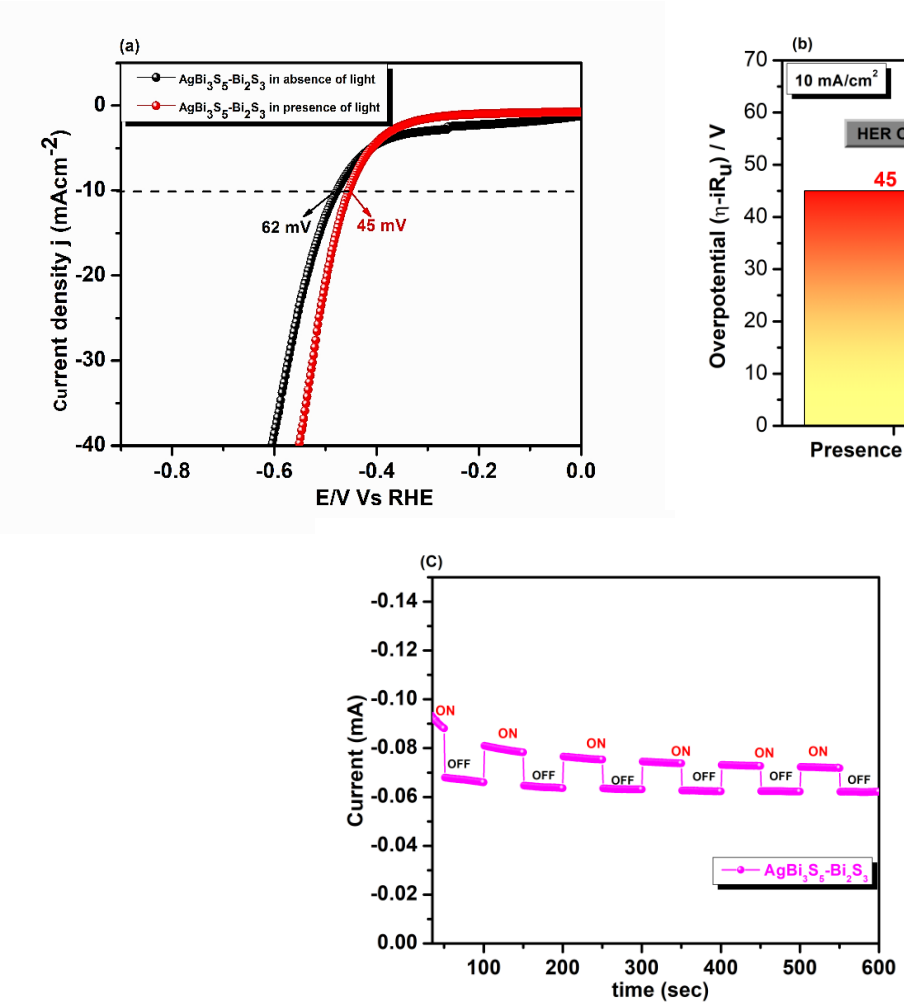

Figure 3.6 (a) LSV curves observed at 5 mV/sec in 0.5 M H_2SO_4 solution with synthesized $AgBi_3S_5$-Bi_2S_3 nanocomposite in absence and presence of light (b) bar diagram of respective nanocomposite in absence and presence of light (c) ON-OFF profile measured at -0.055V vs. RHE via chronoamperometry experiments with maintaining the same environment.

The next important factor for analysis of the performance of the synthesized catalyst is Tafel slope determination. The extent of charge transfer kinetics has been determined from the outcome of the Tafel slope values. For synthesized nanocomposite, it is 45.16 mV/sec in presence of light compare

to 77.91 mV/sec in absence of light. This implies that HER moves by Volmer-Heyrovsky path **[50]** in both the cases and specifically the synthesized photocatalyst shown better charge transfer kinetics at electrode- electrolyte surface in presence of light. The charge transfer resistance (Rct) from the electron impedance spectroscopy (EIS) analysis was the next important parameter to determine the effective electron charge transfer at the surface interface. **Figure 3.7(b)** indicates the outcome of radius of lower semicircle in presence of light in the EIS experiment compare to that in absence of light. It reveals significant charge transfer kinetics at the electrode-electrolyte interface even in the dark and it also increases in the presence of light.

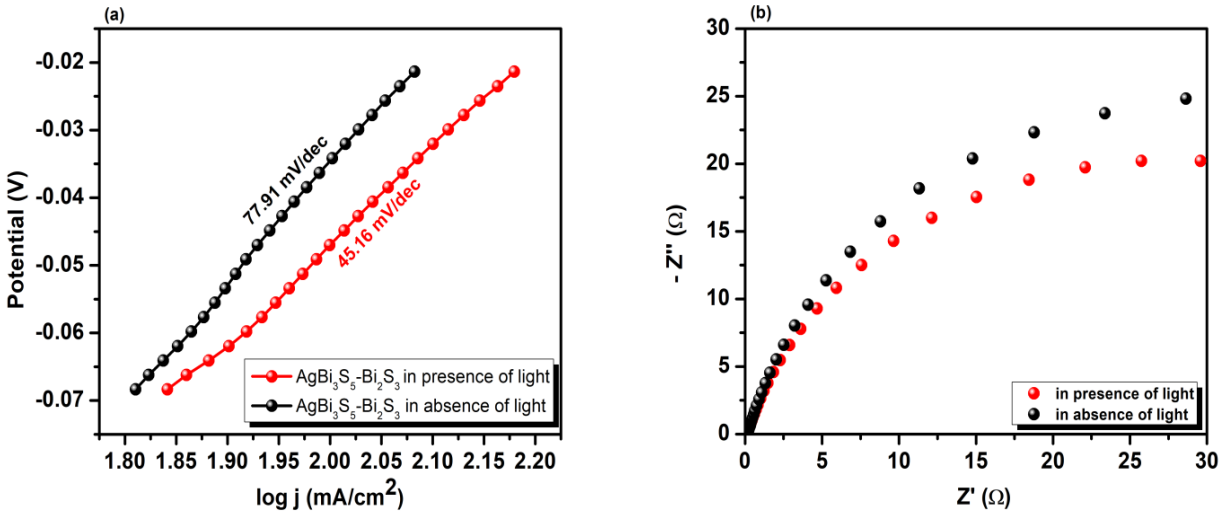

Figure 3.7 (a) Tafel plot of synthesized nanocomposite in absence and presence of light (b) electrochemical impedance spectra studies of that respected nanocomposite with the same environment.

The better H adsorption for highly exposed surface area was determined from the feasibility of high charge transfer kinetics of synthesized photocatalyst. The electrochemical active surface area was measured in the non-faradic region 0.2 to 0.3 V with respect to SCE to verify the above statement related to better H adsorption shown in **figure 3.8(a, b)** which implies the scan rate dependent cyclic voltammetry graph of the synthesized photocatalyst in absence and presence of

light respectively. The outcome of slope values from the graph of ΔJ vs. scan rate shown in **figure 3.8(c)** gives the double layer capacitance (C_{dl}) values for the synthesized nano photocatalyst in both absence and presence of light conditions and their calculated values 3.3 μF/cm^2 and 4 μF/cm^2 respectively.

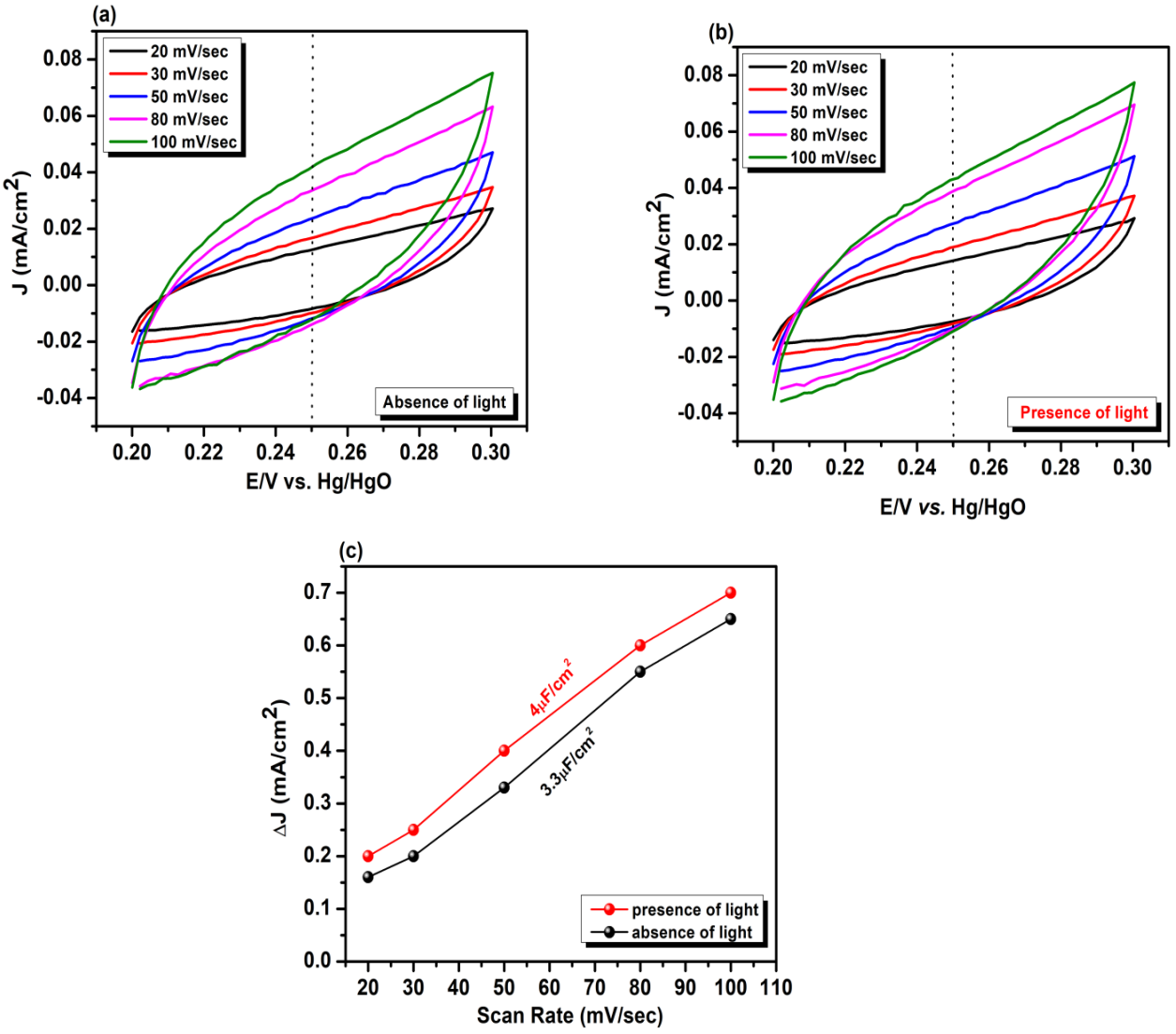

Figure 3.8 (a, b) Cyclic voltammogram executed in a non-faradic region with scan rate variation for determination of ECSA from the double layer capacitance in absence and presence of light respectively (c) plot of ΔJ vs. scan rate in absence and presence of light to find the double layer capacitance value.

The respective electrochemical surface area was determined using the equation 4 shown in section 3.4 and the values are 0.1 cm^2, 0.08 cm^2 for synthesized nanocomposite in presence of light and in absence of light respectively where the photocatalyst shown again higher charge transfer kinetics at the presence of light.

The long-term exposure of the synthesized photocatalyst in the HER reaction expressed its stability and durability which was the one of the most significant factor of catalyst performance.

The dynamic robustness study was analyzed through acceleration degradation (AD) study at 100 mV/sec for 1000 cycles in a 0.5 M H_2SO_4 solution.

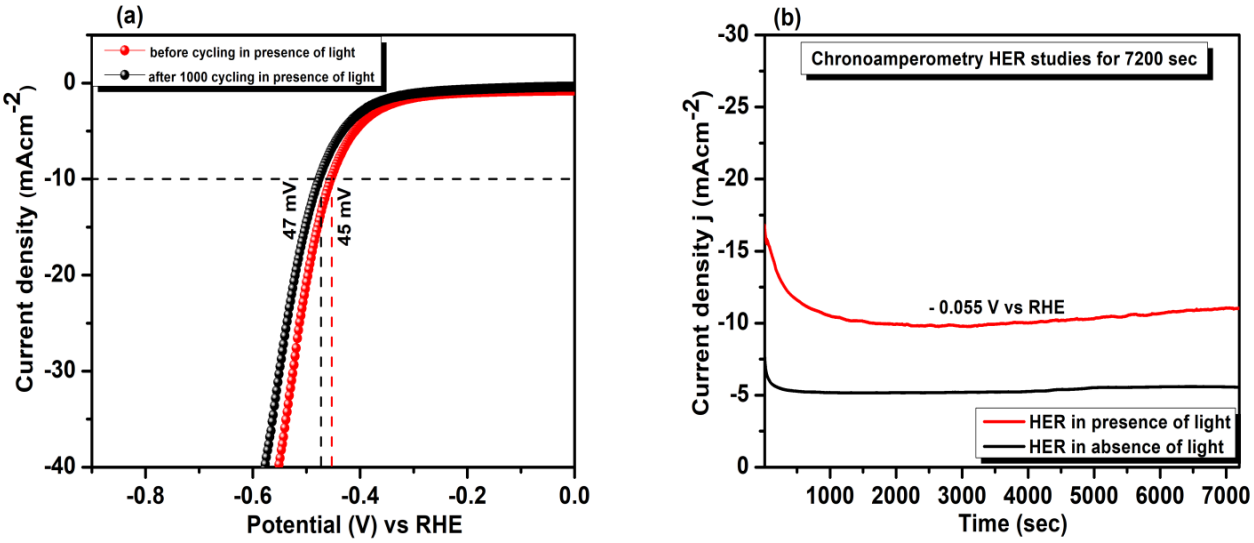

Figure 3.9 (a) Linear sweep voltammetry (LSV) of synthesized nanocomposite in presence of light before and after 1000 cycles of AD study (b)Chronoamperometry profiles of synthesized nanocomposite in presence and absence of light.

The linear sweep voltammetry polarization curve before and after (1000 cycles) AD studied in presence of light shown a little hike (2 mV at 10 mA/cm^2) in **figure 3.9(a)** of HER reaction which indicated the very low catalyst degradation with higher stability. The chronoamperometry study at fixed potential -0.055 V vs. RHE up to two hours both in presence and absence of light expressed through **figure 3.9(b)** proved and confirmed long time durability and robustness once again for the photocatalytic performance of synthesized $AgBi_3S_5$-Bi_2S_3 nano composite in cathodic environment of hydrogen production reaction.

3.4 Conclusion

The as synthesized photocatalyst $AgBi_3S_5$-Bi_2S_3 nano composite was characterized by Rietveld analysis of XRD data along with FTIR and XPS studies. The morphological study like FESEM, TEM, EDS also support the characteristic analysis data and formation of nano composite and their elemental constitution. The performance of this nano composite in the hydrogen production reaction is convincible due to its catalytic ability revealed first time in absence of light as well as in presence of light where all the major determining factors well synchronized and outperformed in presence of light compare to that in absence of light. The catalytic efficacy along with the robustness and longtime durability proved also by the result outcome from the studied parameters like overpotential, Tafel slope, electron charge transfer kinetics, double layer capacitance, electrochemical surface area and chronoamperometric analysis, etc.

References

1. Hughes, T. P.; Kerry, J. T.; Álvarez-Noriega, M.; Álvarez-Romero, J. G.; Anderson, K. D.; Baird, A. H.; ... & Wilson, S. K. Global warming and recurrent mass bleaching of corals. *Nature*. **2017**, *543*(7645), 373-377.

2. AghaKouchak, A.; Cheng, L.; Mazdiyasni, O.; & Farahmand, A. Global warming and changes in risk of concurrent climate extremes: Insights from the 2014 California drought. *Geophysical Research Letters*. **2014**, *41*(24), 8847-8852.

3. Grätzel, M. Recent advances in sensitized mesoscopic solar cells. *Accounts of chemical research*. **2009**, *42*(11), 1788-1798.

4. Bak, T.; Nowotny, J.; Rekas, M.; & Sorrell, C. C. Photo-electrochemical hydrogen generation from water using solar energy. Materials-related aspects. *International journal of hydrogen energy*. **2002**, *27*(10), 991-1022.

5. Fujishima, A.; & Honda, K. Electrochemical photolysis of water at a semiconductor electrode. *Nature*. **1972**, *238*(5358), 37-38.

6. Tachibana, Y.; Vayssieres, L.; & Durrant, J. R. Artificial photosynthesis for solar water-splitting. *Nature Photonics*. **2012**, *6*(8), 511-518.

7. Shortall, R.; Davidsdottir, B.; & Axelsson, G. Geothermal energy for sustainable development: A review of sustainability impacts and assessment frameworks. *Renewable and sustainable energy reviews*. **2015**, *44*, 391-406.

8. Gernaat, D. E.; Bogaart, P. W.; Vuuren, D. P. V.; Biemans, H.; & Niessink, R. High-resolution assessment of global technical and economic hydropower potential. *Nature Energy*. **2017**, *2*(10), 821-828.

9. Woolf, D.; Lehmann, J.; & Lee, D. R. Optimal bioenergy power generation for climate change mitigation with or without carbon sequestration. *Nature Communications*. **2016**, *7*(1), 13160.

10. Lewis, N. S. Research opportunities to advance solar energy utilization. *Science*. 2016, *351*(6271), aad1920.

11. Herbert, G. J.; Iniyan, S.; Sreevalsan, E.; & Rajapandian, S. A review of wind energy technologies. *Renewable and sustainable energy Reviews*. **2007**, *11*(6), 1117-1145.

12. Roger, I.; Shipman, M. A.; & Symes, M. D. Earth-abundant catalysts for electrochemical and photoelectrochemical water splitting. *Nature Reviews Chemistry*. **2017**, *1*(1), 1-13.

13. Lewis, N. S. Research opportunities to advance solar energy utilization. *Science*. **2016**, *351*(6271), aad1920.

14. Wang, J.; Shi, W.; Liu, D.; Zhang, Z.; Zhu, Y.; & Wang, D. Supramolecular organic nanofibers with highly efficient and stable visible light photooxidation performance. *Applied Catalysis B: Environmental*. **2017**, *202*, 289-297.

15. Wei, Z.; Hu, J.; Zhu, K.; Wei, W.; Ma, X.; & Zhu, Y. Self-assembled polymer phenylethnylcopper nanowires for photoelectrochemical and photocatalytic performance under visible light. *Applied Catalysis B: Environmental*. **2018**, *226*, 616-623.

16. Jang, J. S.; Kim, H. G.; & Lee, J. S. Heterojunction semiconductors: A strategy to develop efficient photocatalytic materials for visible light water splitting. *Catalysis today*. **2012**, *185*(1), 270-277.

17. Young, J. L.; Steiner, M. A.; Döscher, H.; France, R. M.; Turner, J. A.; & Deutsch, T. G. Direct solar-to-hydrogen conversion via inverted metamorphic multi-junction semiconductor architectures. *Nature Energy*. **2017**, *2*(4), 1-8.

18. Jacobson, M. Z.; Colella, W. G.; & Golden, D. M. Cleaning the air and improving health with hydrogen fuel-cell vehicles. *Science*. **2005**, *308*(5730), 1901-1905.

19. Service, R. F. The carbon conundrum. **2004**, 305, 962-963.

20. Nikolaidis, P.; & Poullikkas, A. A comparative overview of hydrogen production processes. *Renewable and sustainable energy reviews*. **2017**, *67*, 597-611.

21. Dincer, I. Green methods for hydrogen production. *International journal of hydrogen energy*. **2012**, *37*(2), 1954-1971.

22. Lewis, N. S.; & Nocera, D. G. Powering the planet: Chemical challenges in solar energy utilization. *Proceedings of the National Academy of Sciences*. **2006**, *103*(43), 15729-15735.

23. Shaner, M. R.; Atwater, H. A.; Lewis, N. S.; & McFarland, E. W. A comparative technoeconomic analysis of renewable hydrogen production using solar energy. *Energy & Environmental Science*. **2016**, *9*(7), 2354-2371.

24. Rongé, J.; Bosserez, T.; Huguenin, L.; Dumortier, M.; Haussener, S.; & Martens, J. A. Solar hydrogen reaching maturity. *Oil & Gas Science and Technology–Revue d'IFP Energies Nouvelles*. **2015**, *70*(5), 863-876.

25. Wolcott, A.; Smith, W. A.; Kuykendall, T. R.; Zhao, Y.; & Zhang, J. Z. Photoelectrochemical study of nanostructured ZnO thin films for hydrogen generation from water splitting. *Advanced Functional Materials*. **2009**, *19*(12), 1849-1856.

26. Cho, I. S.; Chen, Z.; Forman, A. J.; Kim, D. R.; Rao, P. M.; Jaramillo, T. F.; & Zheng, X. Branched TiO2 nanorods for photoelectrochemical hydrogen production. *Nano letters*. **2011**, *11*(11), 4978-4984.

27. Commandeur, D.; Brown, G.; Hills, E.; Spencer, J.; & Chen, Q. Defect-rich ZnO nanorod arrays for efficient solar water splitting. *ACS Applied Nano Materials*. **2019**, *2*(3), 1570-1578.

28. Mohamad Noh, M. F.; Soh, M. F.; Riza, M. A.; Safaei, J.; Mohd Nasir, S. N.; Mohamad Sapian, N. W.; ... & Mat Teridi, M. A. Effect of film thickness on photoelectrochemical performance of SnO2 prepared via AACVD. *physica status solidi (b)*. **2018**, *255*(6), 1700570.

29. Cheng, C.; Karuturi, S. K.; Liu, L.; Liu, J.; Li, H.; Su, L. T.; ... & Fan, H. J. Quantum-dot-sensitized TiO2 inverse opals for photoelectrochemical hydrogen generation. *Small (Weinheim an der Bergstrasse, Germany)*. **2011**, *8*(1), 37-42.

30. Chang, Y. S.; Choi, M.; Baek, M.; Hsieh, P. Y.; Yong, K.; & Hsu, Y. J. CdS/CdSe co-sensitized brookite H: TiO2 nanostructures: Charge carrier dynamics and

photoelectrochemical hydrogen generation. *Applied Catalysis B: Environmental*. **2018**, *225*, 379-385.

31. Kim, J. Y.; Jang, Y. J.; Park, J.; Kim, J.; Kang, J. S.; Chung, D. Y.; ... & Ko, M. J. Highly loaded PbS/Mn-doped CdS quantum dots for dual application in solar-to-electrical and solar-to-chemical energy conversion. *Applied Catalysis B: Environmental*. **2018**, *227*, 409-417.

32. Yan, Y.; Crisp, R. W.; Gu, J.; Chernomordik, B. D.; Pach, G. F.; Marshall, A. R.; ... & Beard, M. C. Multiple exciton generation for photoelectrochemical hydrogen evolution reactions with quantum yields exceeding 100%. *Nature Energy*. **2017**, *2*(5), 1-7.

33. Liao, W.; Wang, B.; & Liu, Z. Photoelectrochemical hydrogen production at peak efficiency over 10% via PbSe QDs/TiO2 nanotube array photoanodes. *International Journal of Hydrogen Energy*. **2017**, *42*(16), 10962-10970.

34. He, H.; Berglund, S. P.; Xiao, P.; Chemelewski, W. D.; Zhang, Y.; & Mullins, C. B. Nanostructured Bi 2 S 3/WO 3 heterojunction films exhibiting enhanced photoelectrochemical performance. *Journal of Materials Chemistry A*. **2013**, *1*(41), 12826-12834.

35. Ai, G.; Mo, R.; Chen, Q.; Xu, H.; Yang, S.; Li, H.; & Zhong, J. TiO 2/Bi 2 S 3 core–shell nanowire arrays for photoelectrochemical hydrogen generation. *RSC Advances*. **2015**, *5*(18), 13544-13549.

36. Cai, F.; Chen, X.; Qiu, L.; Jiang, L.; Ma, S.; Zhang, Q.; & Zhao, Y. Controlled hydrothermal synthesis and photoelectrochemical properties of Bi2S3/TiO2 nanotube arrays heterostructure. *Journal of Alloys and Compounds*. **2019**, *808*, 151770.

37. Bernechea, M.; Cates, N.; Xercavins, G.; So, D.; Stavrinadis, A.; & Konstantatos, G. Solution-processed solar cells based on environmentally friendly AgBiS2 nanocrystals. *Nature Photonics*. **2016**, *10*(8), 521-525.

38. Chen, X.; Li, P.; Tong, H.; Kako, T.; & Ye, J. Nanoarchitectonics of a Au nanoprism array on WO3 film for synergistic optoelectronic response. *Science and Technology of Advanced Materials*. **2011**, 12,44-64.

39. Nandy, A.; Dutta, A.; & Pradhan, S. K. Microstructure correlated electrical conductivity of Manganese alloyed nanocrystalline cubic zirconia synthesized by mechanical alloying. *Advanced Powder Technology*. **2017**, *28*(2), 618-628.

40. Kundu, S.; Satpati, B.; Kar, T.; & Pradhan, S. K. Microstructure characterization of hydrothermally synthesized PANI/V2O5· nH2O heterojunction photocatalyst for visible light induced photodegradation of organic pollutants and non-absorbing colorless molecules. *Journal of hazardous materials*. **2017**, *339*, 161-173.

41. Sugarthi, S.; Bakiyaraj, G.; Abinaya, R.; Navaneethan, M.; Archana, J.; & Shimomura, M. Effect of different growth temperature on the formation of ternary metal chalcogenides AgBiS2. *Materials Science in Semiconductor Processing*. **2020**, *107*, 104781.

42. Kim, Y. Y.; & Walsh, D. Metal sulfide nanoparticles synthesized via enzyme treatment of biopolymer stabilized nanosuspensions. *Nanoscale*. **2010**, *2*(2), 240-247.

43. Wu, D.; Jiang, Y.; Yuan, Y.; Wu, J.; & Jiang, K. ZnO–ZnS heterostructures with enhanced optical and photocatalytic properties. *Journal of Nanoparticle Research*. **2011**, *13*, 2875-2886.

44. Baer, D. R.; Artyushkova, K.; Cohen, H.; Easton, C. D.; Engelhard, M.; Gengenbach, T. R.; ... & Roberts, A. XPS guide: Charge neutralization and binding energy referencing for insulating samples. *Journal of Vacuum Science & Technology A*. **2020**, *38*(3).

45. Bernechea, M.; Cates, N.; Xercavins, G.; So, D.; Stavrinadis, A.; & Konstantatos, G. Solution-processed solar cells based on environmentally friendly AgBiS2 nanocrystals. *Nature Photonics*. **2016**, *10*(8), 521-525.

46. Pai, N.; Lu, J.; Senevirathna, D. C.; Chesman, A. S.; Gengenbach, T.; Chatti, M.; ... & Simonov, A. N. Spray deposition of AgBiS 2 and Cu 3 BiS 3 thin films for photovoltaic applications. *Journal of Materials Chemistry C*. **2018**, *6*(10), 2483-2494.

47. Cheng, W.; Guan, W.; Lin, Y.; & Lu, C. Rapid discrimination of adsorbed oxygen and lattice oxygen in catalysts by the cataluminescence method. *Analytical chemistry*. **2022**, *94*(2), 1382-1389.

48. Bai, P.; Tong, X.; Wan, J.; Gao, Y.; & Xue, S. Flower-like Bi2O2CO3-mediated selective oxidative coupling processes of amines under visible light irradiation. *Journal of Catalysis*. **2019**, *374*, 257-265.

49. Nagappan, S.; Karmakar, A.; Madhu, R.; N Dhandapani, H.; Bera, K.; De, A.; & Kundu, S. Electronically modified Ce3+ ion doped 2D NiFe-LDH nanosheets over a 1D microfiber: a high-performance electrocatalyst for overall water splitting. *ACS Applied Energy Materials*. **2022**, *5*(10), 12768-12781.

50. Chowdhury, A.; De, A.; Kundu, S.; & Bhattacharya, S. K. Designing AgBi3S5 as an efficient electrocatalyst for hydrogen evolution reaction. *Sustainable Energy & Fuels*. **2024**, 8, 2941-2953.

Chapter 4

Unveiling novel metal free electrochemical and photochemical anodic oxidation of methanol by newly synthesized Cu_9S_5

4.1 Introduction

Green energy resources have evolved in the current century as a game changer to fulfill the ever-increasing energy demand without effecting the key environmental parameter. It of course is a great sign of sustainable development and brings a ray of hope to decrease the developing natural disasters like situation in various parts of the earth **[1-6]**. By virtue of the characteristic features like high energy content, feasibility, storage capabilities etc., electrochemical fuel cells evolve as a key contender where methanol plays a significant role to generate green, clean, sustainable and most useful electrical energy **[7-10]**. Electrochemical methanol oxidation system overcomes some outbreaks of direct fuel cells due to some of its special quality like less pollution harming, high energy density, effective low temperature functioning, etc. **[11, 12]**. Direct methanol fuel cells create tremendous potentiality in the electronic field especially portable electrical device, power supplier in the automobile sectors and may play a crucial role to replace conventional use of batteries in these sectors **[13]**. Spontaneous electrochemical oxidation method has a significant contribution towards above-described application which makes huge differences to bring technological revolution in the coming days. This method also has environmental contribution by development of methanol sensors, waste water treatment removed it toxic components and also production of formate like valuable chemicals, etc. **[14-17]**.

Efficiency of catalysis towards electrochemical and photochemical methanol oxidation reactions lies mostly on development of efficient catalyst. Pt and Pd based nanoparticles used as catalyst in this reaction in a regular manner though they have numerous drawbacks like cost, abundance and CO poisoning **[18, 19]**. Strategy like using lower content of Pt/Pd instead of bulk metal and use of a supporting material helps to tackle situation like its limited supply and poor poison tolerance **[20-22]**. Carbon based materials have also shown significant efficiency as a support material towards electrocatalytic and photocatalytic oxidation reactions where materials like carbon black, carbon nanotube, carbon nanofibers, graphene attract most of the times due to their good electrical conductivity as well as their stability in the involved reaction **[23-29]**.

To develop and provide an alternate solution to address above mentioned drawbacks, we were synthesizing Cu_9S_5 versatile nanomaterials followed by a new designing synthesis route and also unveiling its new catalytic wing towards electrochemical methanol oxidation reaction (MOR). Cu_9S_5 and its supported alloys in different forms and structures are used in the various fields as

semiconductor, asymmetric supercapacitors, as anodes for high performance lithium-ion and sodium-ion batteries, efficient catalyst for water splitting, high performance electromagnetic wave absorber, used for microfiltration, as an environmental pollution removal and photothermal conversion in broad band, as a photothermal agent with near about 26% heat conversion efficiency for photothermal ablation of cancer cells in vivo and in multimodal tumor therapy **[30-39]**. We demonstrated electrochemical and photochemical oxidation of methanol for the first time in lower negative potential zone without supporting of any novel metals and also showed its increased catalytic efficiency in presence of light. Hopefully this new insight regarding Cu_9S_5 nanomaterials towards electrochemical oxidation helps researcher to designing catalyst without depending on any novel metal. It also gives new direction to better optimization of its stability and feasibility for using them in commercial purpose.

4.2 Experimental Sections

4.2.1 Materials

Cupper nitrate (Cu $(NO_3)_2$ $3H_2O$, 99.9%, Merck), thiourea (H_2N-C(=S)-NH_2, 99.9%, Merck), Cetyltrimethylammonium bromide (CTAB) ([$(C_{16}H_{33})$ $N(CH_3)_3$] Br, 99.9%, Merck), are used in this study without further refinement. The double distilled water was used throughout the experiments.

4.2.2 Synthesis of the Cu_9S_5(CS)

0.60 g of Cupper nitrate was weighed out and dissolved in 0.01 M CTAB aqueous solution taken in a beaker and ultrasonicated up to 15 minutes, named as solution A. In the other beaker 0.19 g of thiourea soluble in a 0.01 M CTAB solution by 15 minutes sonication marked as solution B. Now the temperature- controlled heating mantel was switched on and the temperature was set up at 90 °C. Then the solution A in the beaker was placed on the heating mantle. Solution B poured into it when desired temperature was reached and the temperature also manually checked with the thermometer. The reaction mixture was kept in this reaction condition for 2 hours and then allow to settle down the appeared green color massed in the reaction system up to room temperature. The

green color mass was collected followed by centrifugation and washed for several times with double distilled water along with ethanol. The collected mass was dried at 70 °C for 15 hrs. in an air woven.

4.2.3 Fabrication of electrodes

The electrodes were fabricated for electrochemical and photo electrochemical analyses through cyclic voltammetry (CV), Chronoamperometry (CA) and electrochemical impedance spectroscopy (EIS) in presence and absence of light with the synthesized Cu_9S_5 nanomaterial. 2 mg of the synthesized CS was taken in 1 mL ethanol containing glass bottle and it dispersed with bath sonication for 45 to 50 minutes at room temperature. Then 10 µL of catalyst solution was dropped on the flat surface of the polished graphite carbon electrode and dried at room temperature for 2.30 hours in an inert atmosphere and then 5 µL of 0.5 (w/v) % nafion solution was drop-casted on the catalyst film so produced as a binder and then it was kept in an inert atmosphere for 22 hours. 0.16 mg/cm^2 was the catalytic mass loading on the surface of working electrode [40].

4.2.4 Electrochemical and Photochemical measurement

The electrochemical and photochemical study was executed via AUTO-LAB Potentiostat at room temperature in the potential region of -0.9 V to 0.3 V where 1 M KOH aqueous solution in presence and absence of 1M MeOH solution was used as an electrolyte throughout the experiments at different scan rate. Conventional three electrode system was placed for the experiment in which polished graphite carbon electrode was used as a working electrode, saturated calomel electrode (SCE) was used as reference electrode and Platinum foil (1 cm × 1 cm) was used as a counter electrode. The Chronoamperometry (CA) analysis was executed at fixed -0.15 V potential for 600 seconds.

EIS study was performed at a constant potential -0.15 V using frequency scan range from 0.1 to 10,000 Hz at 5 mv amplitude potential in 1 M KOH aqueous solution in presence of 1M MeOH. The 30-watt LED bulb (wavelength > 400 nm) was used as a light source during the photochemical measurement and the intensity of that light source was measured by lux meter (LX-101A) where the intensity was (90 × 100 lux) **[40, 41]**.

4.2.5 HPLC Studies with anodic oxidation products

10 mL 1 M MeOH in1 M KOH was taken as an electrolyte in the electrochemical system where time coursed current density measurement was performed at constant potential -0.15 V with respect to SCE in presence and absence of light for 7200 seconds. The polished graphite carbon electrode drop casted with the synthesized CS nano materials was used as a working electrode. The resulting solution was collected in a glass bottle covered by dark papers and then the solution was studied by high performance liquid chromatography (HPLC) instrument manufactured by Shimadzu Corporation, Japan.

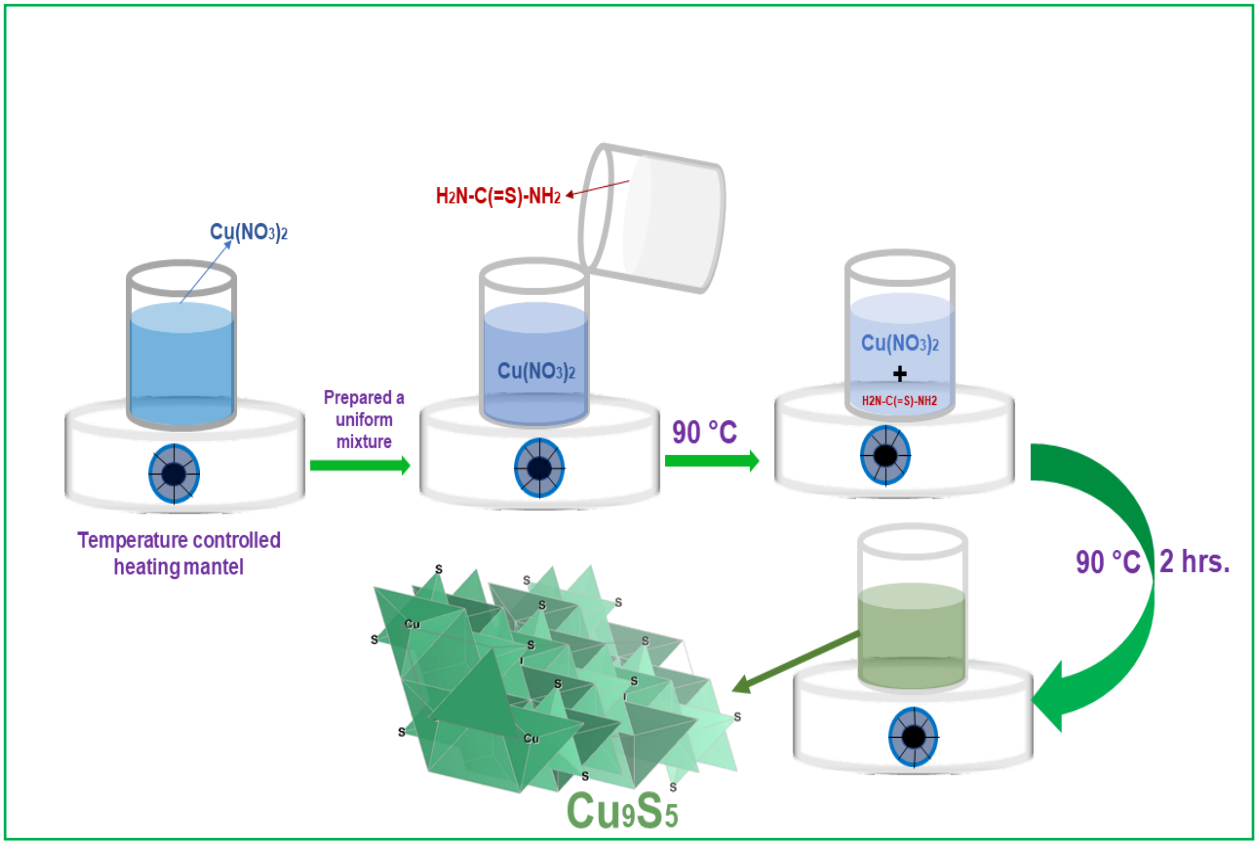

Scheme 4.1 Schematic diagram of synthesis procedure of Cu_9S_5(CS)

4.3 Results and Discussions

4.3.1 XRD analysis

The main diffraction peaks exposed at 2Θ values (°) 26.228, 29.254, 32, 35.805, 37.2, 39.270, 39.963, 42.4, 44.546, 46.159, 51.193, 54, 54.729, 56.121, 59.757, 62.171, 62.67 for as synthesized nano material (Cu_9S_5 as CS) and their respected diffraction plane appeared at (101), (107), (1010), (1013), (0114), (0021), (1016), (0117), (1019), (110), (0123), (202), (1115), (208), (0213), (0129), (0216) where maximum planes matched with the rhombohedral Cu_9S_5 (JCPDS NO. 88-2158).The above outcome from the XRD analysis (**figure 4.1(a)**) is justified the formation of Cu_9S_5 nanomaterials. The average size of the synthesized nanomaterial about 10 nm as determined using Debye Scherrer equation considering (110) planes, from which the diffractions is maximal.

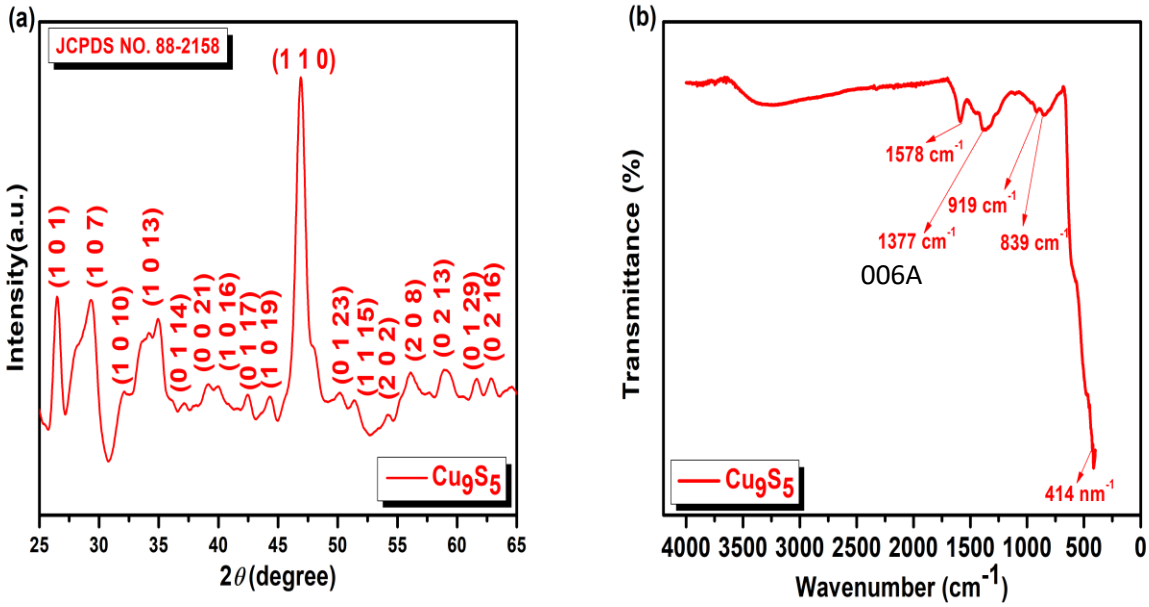

Figure 4.1 (a) Powder XRD patterns of the synthesized Cu_9S_5 along with the JCPDS number (b) FTIR spectra of Cu_9S_5 nanomaterials.

4.3.2 FTIR analysis

FTIR spectral study of synthesized nanomaterials was investigated by the instrument, Perkin Elmer, spectrum RX1. The FTIR spectra of *synthesized* Cu_9S_5 expressed in **Figure 4.1(b)** where the peaks at 414 cm^{-1} present in CS designated the characteristic vibration modes of sulfur **[35, 36, 42]** inferring the presence of Cu-S bond. The peaks existing between (839 cm^{-1} to 919 cm^{-1})

indicate the stretching and bending vibrations of Cu-S **[35, 36]**. Frequencies in the range 3100-3300 cm^{-1} and at around 1578 cm^{-1} for the samples CS plausibly due to stretching and bending vibrations of the O-H bond of the adsorbed H_2O at the surface of Cu_9S_5 **[35, 36, 43, 44]**. Peaks at around 1377 cm^{-1} and 839 – 919 cm^{-1} found in sample CS seemingly due to the stretching and bending vibrations of the Cu-S bond.

4.3.3 Morphological analysis

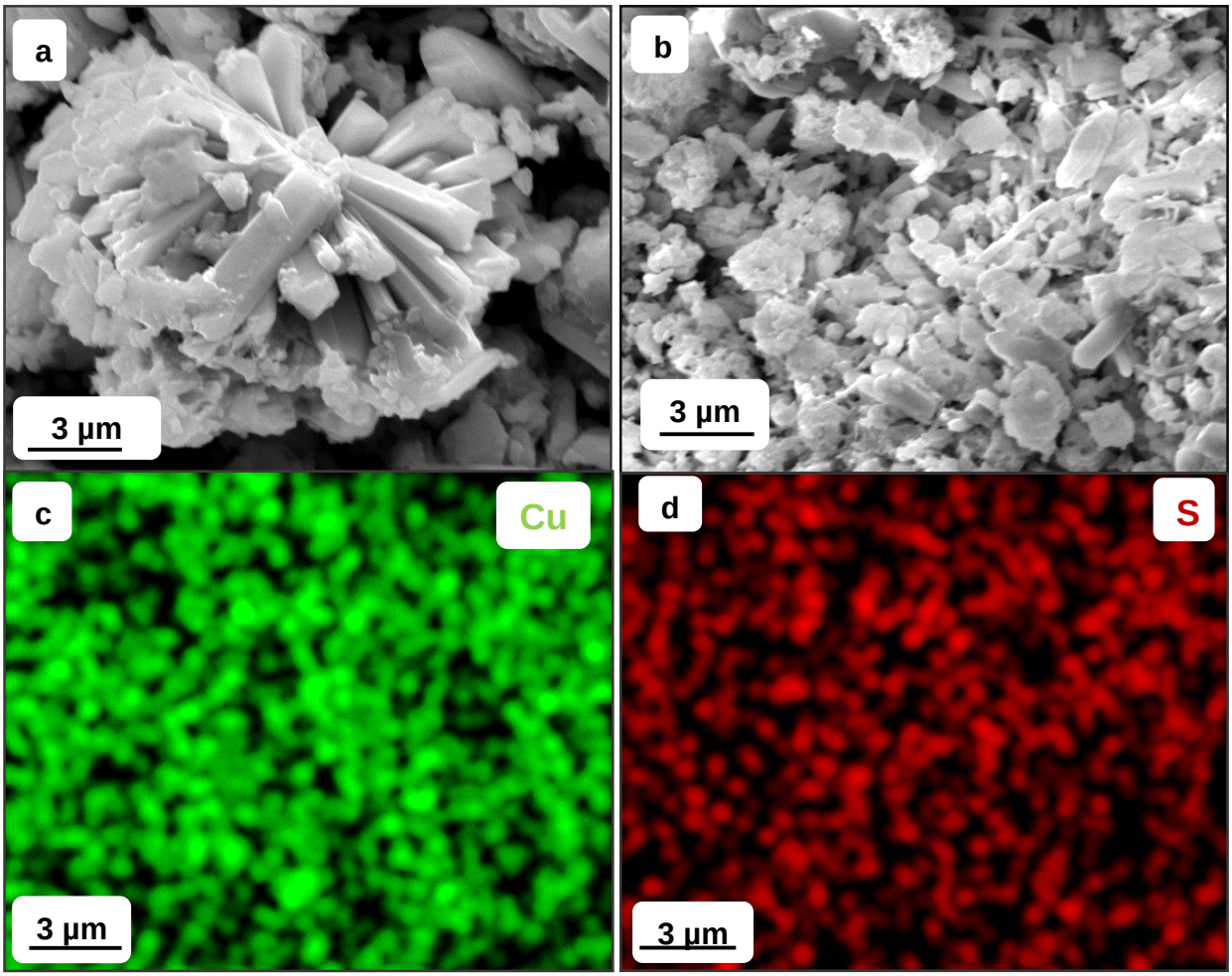

Figure 4.2 (a) FESEM image of synthesized Cu_9S_5 nanomaterial (b) area selected for EDAX spectrum (c-d) elemental mapping of Cu and S present in synthesized nanomaterial respectively.

The morphological overview of synthesized Cu_9S_5 nanomaterial investigated by scanning electron microscopy (FESEM) with a FEI INSPECT F50 instrument having a magnification range of 40X to 400 KX with an accelerating voltage near is to 0.5 to 30 kV and the respected elemental presence of synthesized nanomaterial was analyzed by Energy dispersive X-ray spectroscopy (EDS) analysis was carried out with the FESEM instrument with the images (BRUKER EDS) with a separate EDS detector connected to that instrument. The bar like structure of synthesized nanomaterial expressed in **Figure 4.2(a)**. The selected area for EDS analysis of elemental detection and the presence of Cu and S in it presented in **figure 4.2(b, c, d)** respectively. The EDS spectra of synthesized nanomaterial was shown in **figure 4.3(d)**.

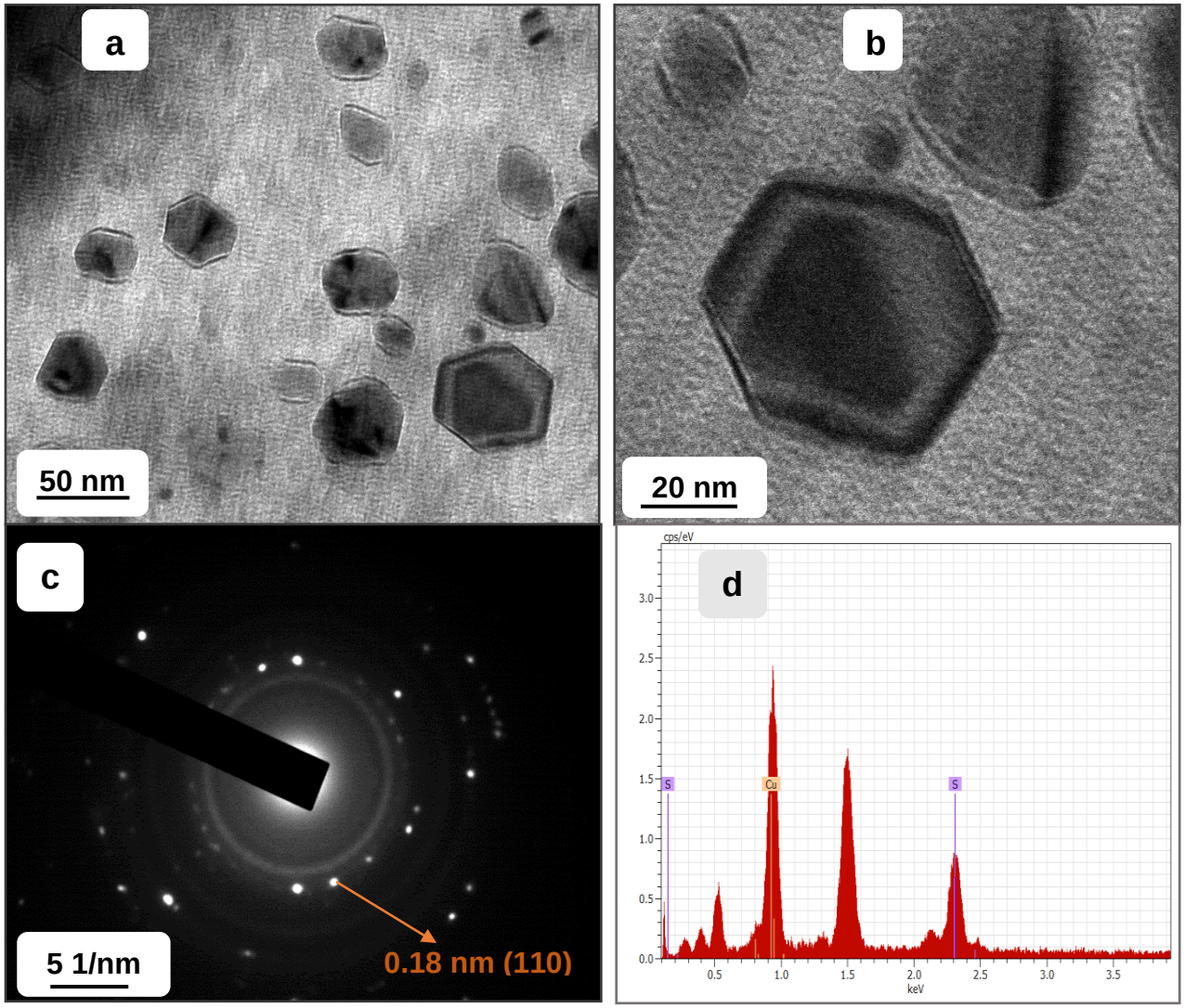

Figure 4.3 (a-b) TEM images of synthesized nanomaterial lower and higher magnification (c)SAED pattern of synthesized nanomaterial (d) EDS spectrum of synthesized nanomaterial.

The intrinsic changes of synthesized materials were investigated by Transmission electron microscopy (TEM) analyzer. Hexagonal and another some square planar like structure developed in synthesized nanomaterials reveals in **figure 4.3 (a)** and the equivalent higher resolution image was highlighted in **figure 4.3(b).** The inter planer distance and the respective diffracted planes was coming up from SAED pattern in figure **4.3(c)** synchronized with the data of XRD analysis. The diffracted plane of that main diffracted peak in synthesized nanomaterial presence in SAED patterns further approved and confirmed for the successful formation of that nanomaterial.

4.3.4 UV-visible and Photoluminescence spectral study

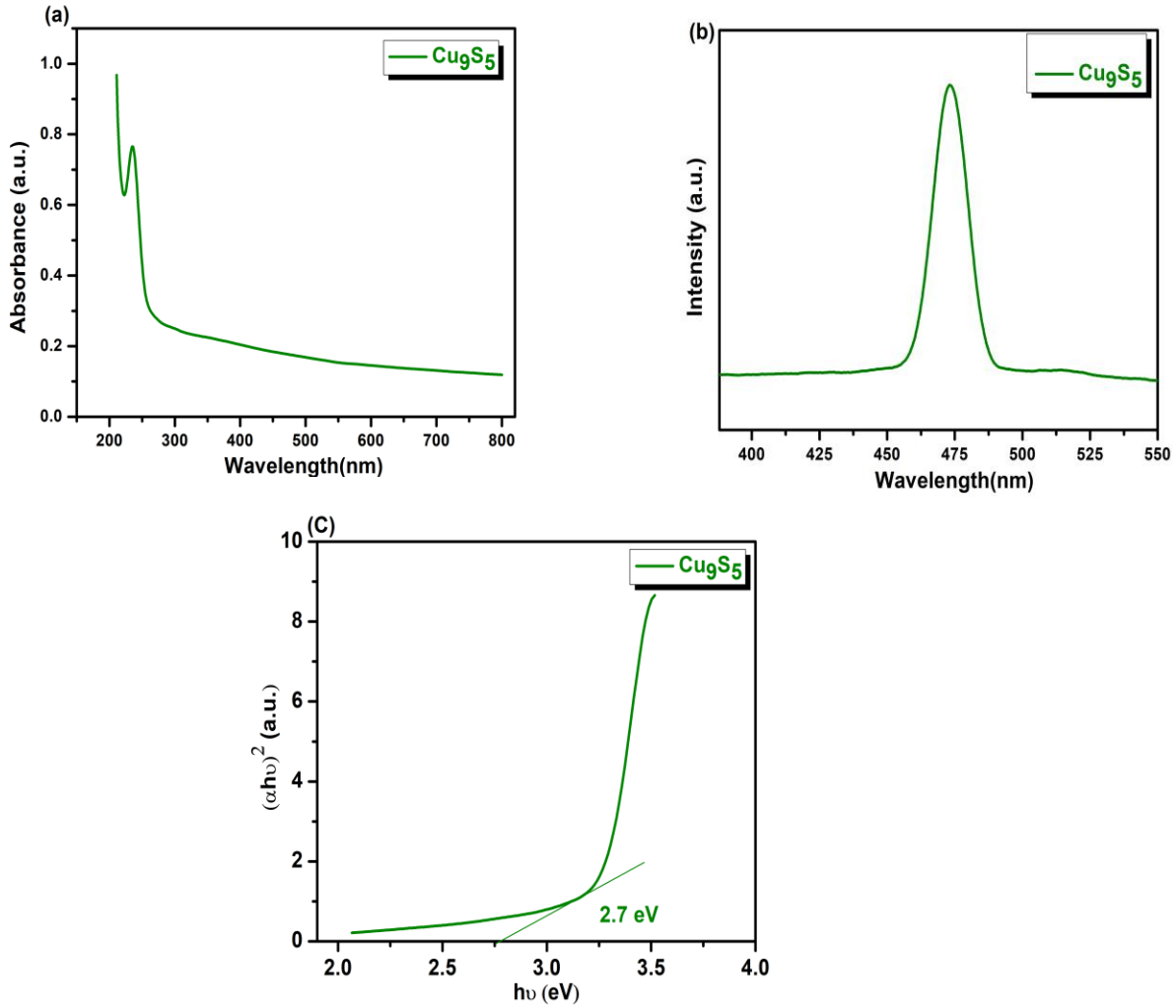

Figure 4.4 (a) UV-Visible absorption spectral study of synthesized Cu_9S_5 nanomaterial (b) Photoluminescence spectral study of synthesized nanomaterial (c) $(\alpha h\upsilon)^2$ vs. $h\upsilon$ profile of synthesized nanomaterial.

The UV visible spectral study of Cu_9S_5 denoted in **figure 4.4(a)** and the corresponding direct band gap (E_g) presented in **figure 4.4(c)** determined from the plot of $(\alpha h\nu)^2$ *vs.* hν followed by Tauc equation **[40-41]** $(\alpha h\nu)^2 = A(h\nu - Eg)$ where α, h, ν, A and Eg are the absorption coefficient, plank constant, incident light, a constant and energy of photon respectively. The outcome of band gap value of Cu_9S_5 2.7 eV well-coordinated with the former reported value **[35, 36]**.

Photoluminescence (PL) spectral outcome shown in **figure 4.4 (b)** of synthesized Cu_9S_5 and the Photo-effect of that synthesized nanomaterial dealing with recombination of charge carriers and such characteristic features coming from photoluminescence analysis. The maximum peak intensity of photoluminescence study was detected at 473 nm and the corresponding excitation wavelength was 235 nm shown in **figure 4.4(a)**. The result of PL study favors the photochemical measurements during the studies like cyclic voltammetry, chronoamperometry, impedance and photocurrent observations in presence of visible light exposure.

4.3.5 Electrochemical and Photochemical Methanol oxidation

The electrochemical measurement was carried out in the conventional three electrode system in 1 M KOH solution and 1 M CH_3OH in 1 M KOH solution, where modified or bare polished graphite carbon electrode functioned as working electrode, saturated calomel electrode (SCE) as reference electrode and platinum (1 cm × 1 cm) as counter electrode. Electrode fabrication and the respective mass deposition on the surface of polished graphite carbon electrode was discussed briefly in the experimental section. The electrochemical activity through Cyclic voltammetry (CV) revealed that when only polished graphite carbon electrode used without mass loading on to it as a working electrode in 1 M KOH electrolyte solution under three electrode system no characteristic peak was developed in the anodic zone and the respective CV outcome depicted as a relatively flat almost straight line in **figure 4.5(a).** And then the cyclic voltammetry experiment was done in the same condition keeping the same environment with synthesized nanomaterial deposited on the polished graphite carbon electrode and used it as a working electrode in three electrodes set up where the two anodic peaks appeared at the potentials of about -0.11 V and -0.41 in 1 M KOH electrolyte indicating the oxidizing capability of the catalyst as shown in **figure 4.5(a).** However, the subsequent peaks were disappeared with the increasing number of cycles which was clearly observed in **figure 4.5 (b)** due to some intermediate formed and covered gradually the catalyst

surface with the progression of the reaction in this potential region. The intermediates are plausibly (Cu_9S_5)-OH generated at potential around – 0.35 V and CuSOH at around -0.05 V respectively. The observation was totally changed when the same measurement was done in presence of 1 M MeOH in 1M KOH at the same reaction condition. Now the two peaks appearing at -0.08 V and -0.40 V respectively and persisted with increasing cycles along with increasing current density which can be observed from the **figure 4.5(c).** The observation drew the attention towards anodic oxidation of methanol at the potentials. At about -0.1 V and -0.40 V the generated intermediates viz (Cu_9S_5)-OH & CuSOH in methanol help oxidation in alkaline solution. The detail mechanism of the reactions is set to be explored, but undoubtedly the hydroxyl ion takes the key role for the reactions. Since the surface adsorbed hydroxyl in (Cu_9S_5)-OH is more active than chemically bound hydroxyl in CuSOH, the forms is responsible to oxidize methanol at lower potential (-0.4 V) than other (-0.08 V). The investigation was further done in presence of light in the same reaction atmosphere which are shown in **figure 4.5(d)** implying the photo effect of the synthesized catalyst on the oxidation process. We compared the performance in the anodic oxidation region in absence and presence of light and found that the oxidation process is facilitated in presence of light. The result further is compared with the 10 wt.% commercial platinum where performance is at per with the above outcome. The outcomes from chronoamperometry, impedance and photocurrent studies approved the efficacy of oxidation of methanol in the anodic region in presence of light which are shown in **figure 4.6.** The photoluminescence study also complimented the photochemical efficiency of synthesized nanomaterial towards the anodic oxidation process. The charge transfer kinetics at the electrode electrolyte surface of the oxidation process has been greatly influenced by some important factors. Tafel slope values from the Butler-Volmer equation which are briefly discussed in the previous chapters, one of the determining factors of electrochemical performance of synthesized catalyst. The charge transfer resistance is another important factor which is mainly obtained from EIS studies also shown the efficiency of synthesized nanomaterial towards anodic oxidation of methanol.

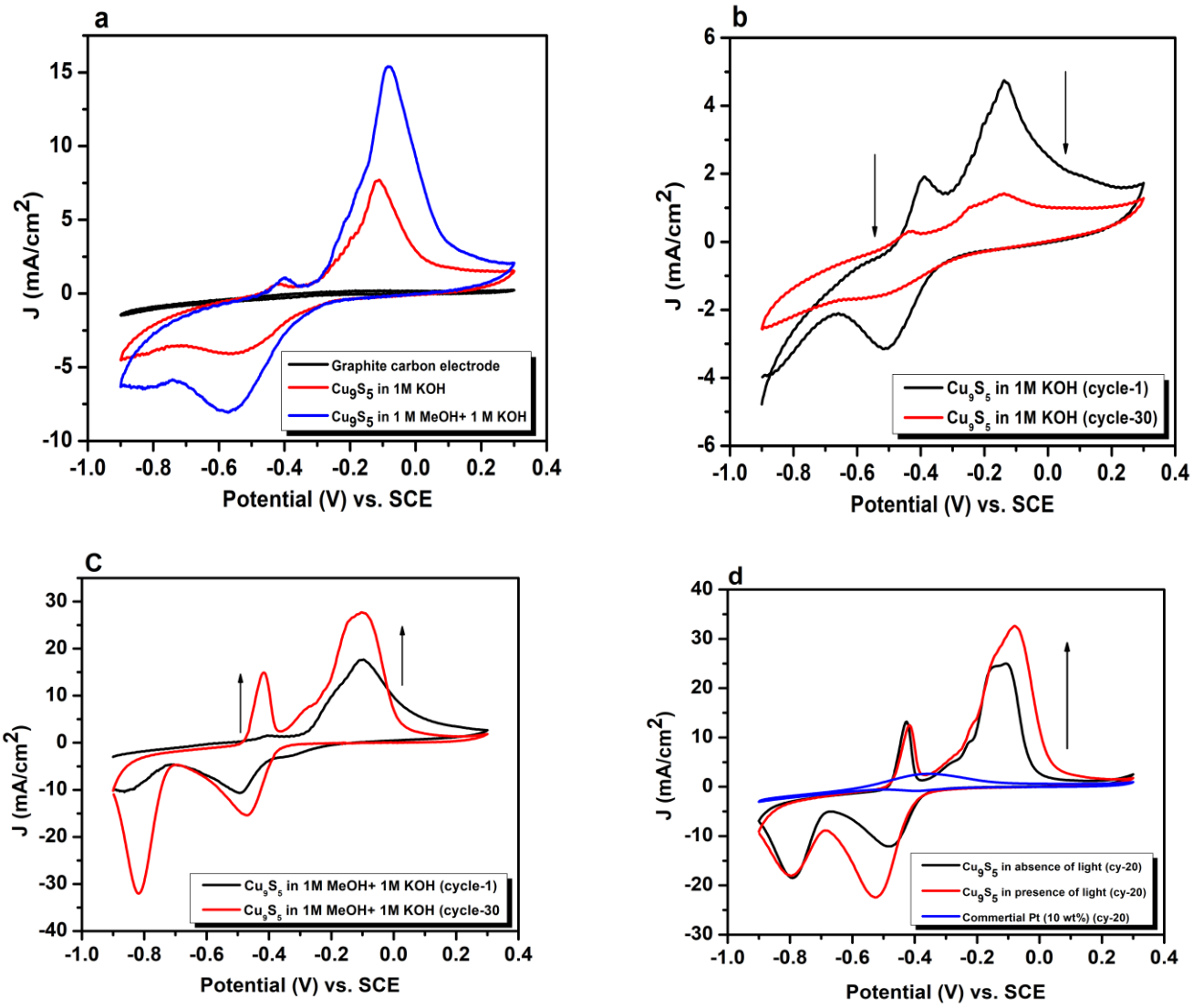

Figure 4.5 (a) Cyclic voltammogram (CV) of bare graphite carbon electrode in 1 M KOH solution and Cu_9S_5 deposited graphite carbon electrode in 1 M KOH and in 1 M MeOH in 1 M KOH at 50 mV/sec in absence of light. (b) CV of Cu_9S5 deposited graphite carbon electrode in 1M KOH solution (comparing cy-1 and 30) (c) CV of Cu_9S_5 in 1M MeOH in 1M KOH solution (comparing cy-1 and 30) (d) CV of Cu_9S_5 deposited graphite carbon electrode in 1 M MeOH in 1 M KOH solution in absence and presence of light along with CV of commercial Pt (10 wt. %).

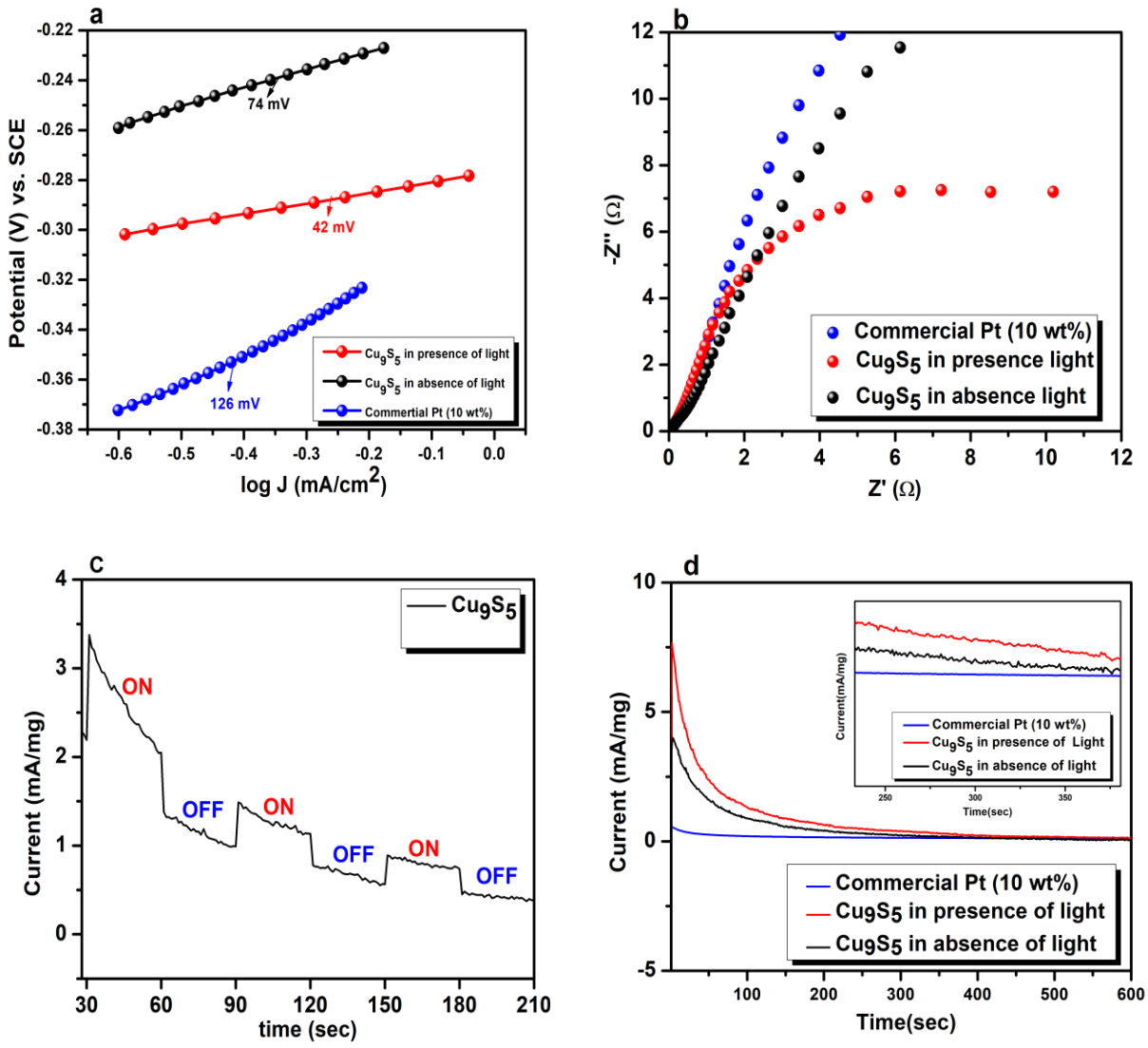

Figure 4.6 (a)Tafel plot of Cu_9S_5 in 1M MeOH in 1M KOH solution in presence and absence of light at 1mV/sec scan rate comparing with commercial Pt at same conditions. (b) Nyquist plot, of impedance spectrum profiles of Cu_9S_5 in 1M MeOH in 1M KOH solution in presence and absence of light at -0.15 V constant potential vs. SCE comparing with commercial Pt (10 wt. %). (c) photocurrent responses of synthesized materials with same conditions. (d) Chronoamperogram of Cu_9S_5 in 1M MeOH in 1M KOH solution in presence and absence of light at -0.15 V constant potential vs. SCE comparing with commercial Pt (10 wt. %).

The Tafel slope values were obtained from the potentio dynamic measurement of alcohol oxidation in 1 M CH_3OH in 1 M KOH electrolyte solution at 1 mV/sec scan rate with respect to SCE using the Butler-Volmer equation. The order of Tafel slope values i.e., 42 mV (Cu_9S_5 in presence of light) < 74 mV (Cu_9S_5 in absence of light) < 126 mv (Commercial Pt (10 wt.%)) were shown in **figure 4.6(a)** indicating the efficiency of charge transfer kinetics on Cu_9S_5 is intrinsically better than that on commercial Pt in the oxidation process. Moreover, it becomes much better in presence of light. On the other hand, the charge transfer resistance dealing with electrochemical impedance spectroscopy (EIS) depicted in **figure 4.6(b**) reveals that the radius of the semicircle follows the order: Cu_9S_5 in presence of light < Cu_9S_5 in absence of light < Commercial Pt (10 wt.%). Since the lower semicircle radius is corelated with the lower charge transfer resistance in the electrode electrolyte surface, it implies that, the catalytic activity of the electrodes is in the reverse order. The order is also agreement with the Tafel slope values.

The photocurrent measurement was done with traditional three electrode set up using the chronoamperometry studies at -0.15 V fixed potential supplied in the oxidation process and the light ON -OFF was done after 30 secs of interval. The experimental result of photocurrent measurement reveals **(figure 4.6(c))** that the photocurrent is increases when light is on and subsequently the photocurrent decreases when light is off mode. The results also compliment with the outcome from the above-mentioned experimental evidences.

The stability of the catalyst is the key factor to use it practically in commercial fuel cell. The stability of the synthesized nanomaterials is scrutinized through Chronoamperometric (CA) studies at -0.15 V fixed potential for 600 sec which was shown in **figure 4.6(d).** The consequences of CA studies indicates that Cu_9S_5 in presence of light dominates over others and shown better stability with respect to observing current at a short span of time.

The cyclic voltammetry study was done at different scan rates with respect to SCE in 1 M MeOH in 1 M KOH electrolyte solution in presence of light for further verification of the catalytic stability which was shown in **figure 4.7(a)**. The dependency of forward peak current with the square root of scan rate is also demonstrated in the **figure 4.7(b)**.

The peak current density is reached at saturation level in 60 cycles as shown in **figure 4.7(c)**. Afterwards the current density decreases but the decline rate is too low which implies the stability of the catalyst as well as the catalytic performance of the catalyst in methanol oxidation.

From the analysis of the above experimental results, it is concluded that catalytic activity of the synthesized nanomaterial enhances and the photo-effect assists better stability than that in absence of light. The results also are compared with that of polished graphite carbon working electrode loaded with same mass of Pt from a 10 wt.% of commercial platinum material. It is found that Cu_9S_5 in absence and presence of light predominates in catalytic activity over state-of-the-art catalyst, Pt.

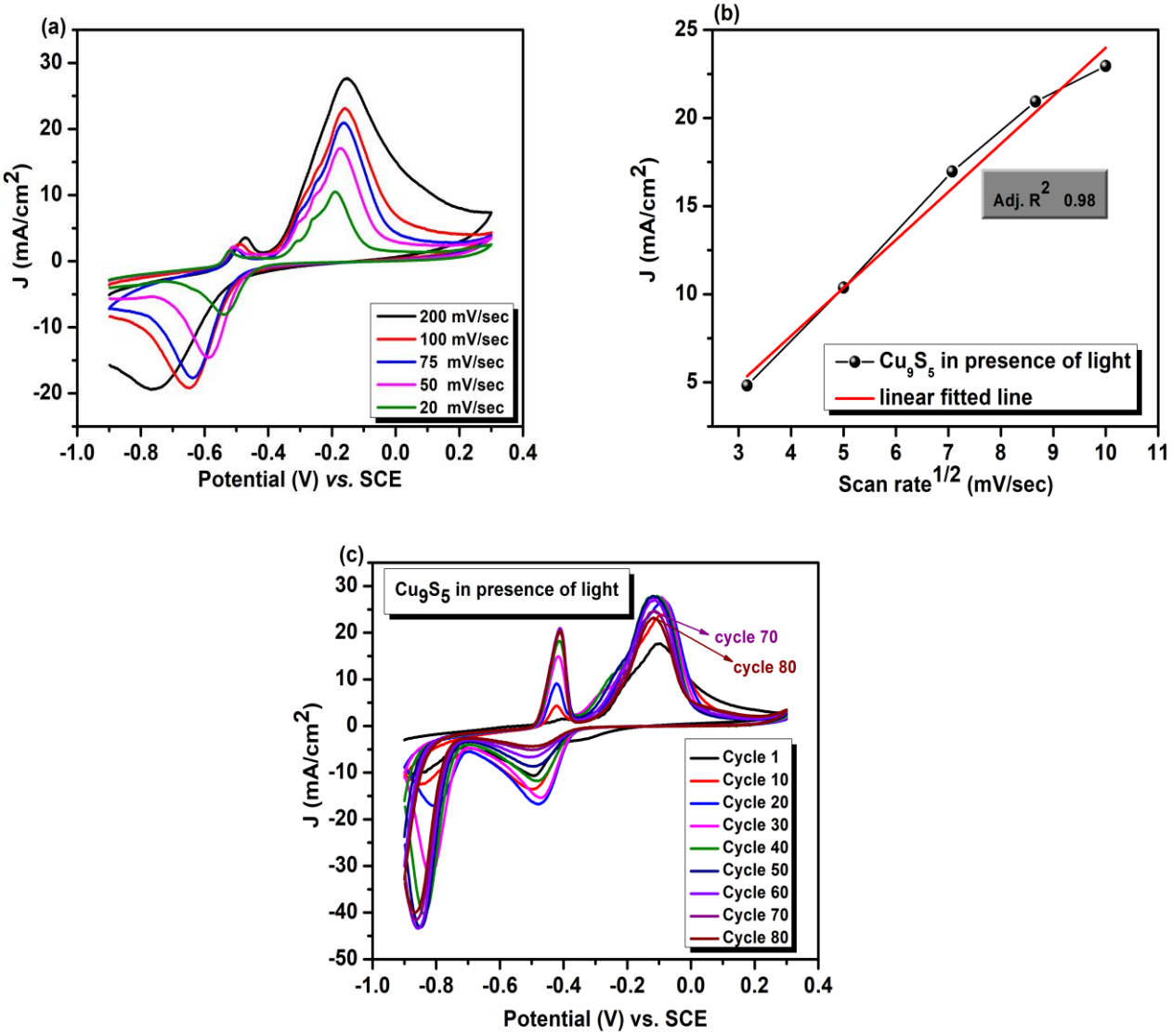

Figure 4.7 (a) Cyclic voltammograms of methanol oxidation on Cu_9S_5 at various scan rates in 1 M CH_3OH in 1M KOH solution in presence of light (b) Plot of forward peak current density vs. square root of scan rates of methanol oxidation (c) Cyclic voltammograms of graphite carbon supported synthesized Cu_9S_5 in 1 M CH_3OH + 1 M KOH solution up to 80 cycles at 50 mV/sec.

4.3.6 Identification of Methanol oxidation products

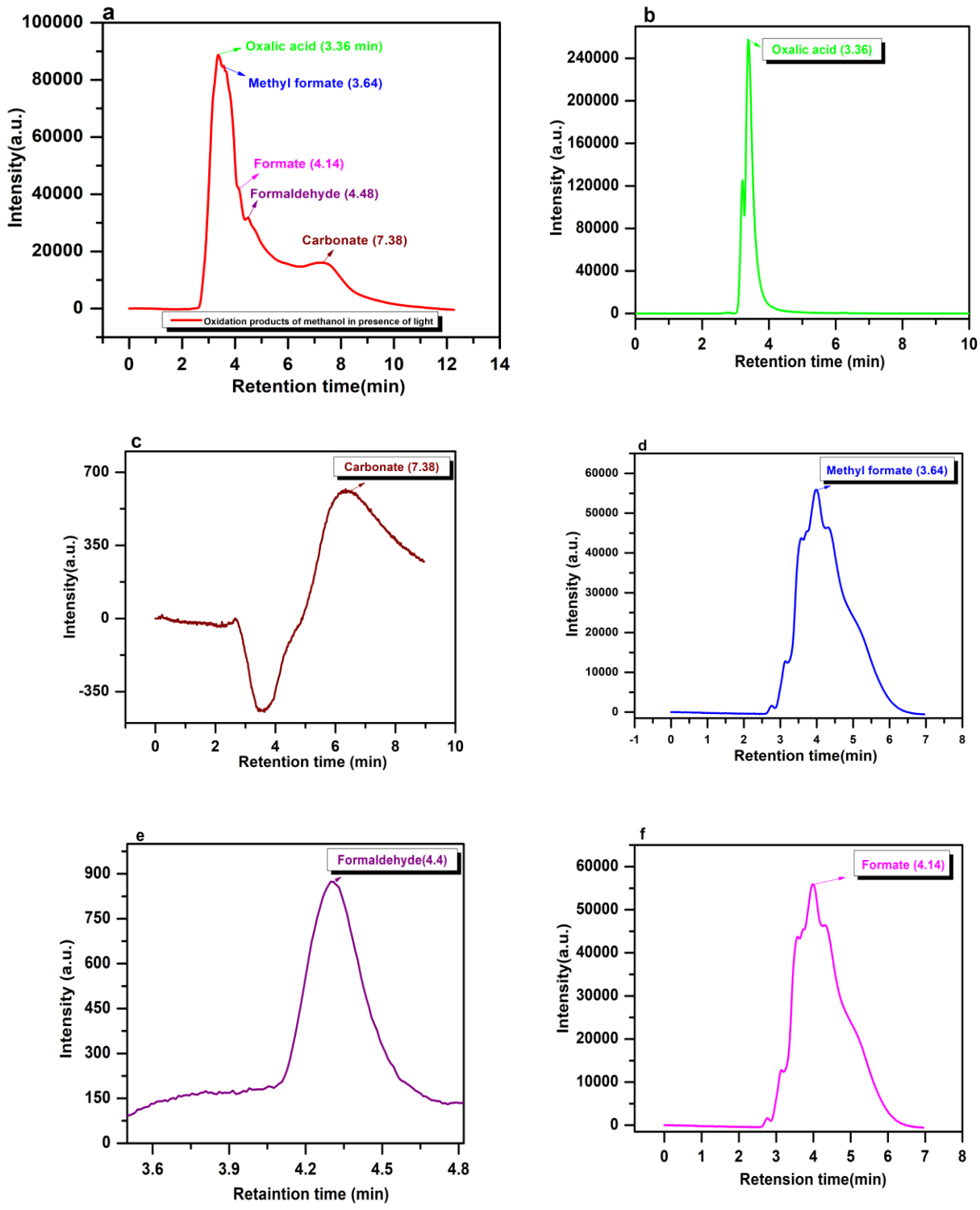

Figure 4.8 (a) High pressure liquid chromatographic (HPLC) profiles of the solution of methanol oxidation (b-f) HPLC profiles of known compounds of namely oxalic acid, carbonate, methyl formate, formaldehyde and formate respectively.

The observation of HPLC study has been shown in **figure 4.6.7(a)**. The peaks appeared at retention times (minutes) of 3.36, 3.64, 4.14, 4.48, 7.38 respectively. The peaks are identified by comparing them with the standard HPLC profiles of known compounds. The respective observation of known compounds is shown in figure **4.6.7(b-f)**. The identified peak at 3.36 minutes retention time stands for oxalic acid ($C_2H_2O_4$), peak at retention time 3.64 minutes for methyl formate ($HCOOCH_3$) formation, peak at 4.14 minutes indicates the formation of potassium formate (HCOOK), peak at 4.48 minutes represents the formation of formaldehyde (HCHO) and the peak at retention times of 7.38 minute implies the formation of carbonate CO_3^{2-}. From the peaks it can be revealed that methyl formate is the major product along with significant amount of potassium carbonate.

4.3.7 Mechanism of photochemical Methanol oxidation

The band gap energy of the synthesized Cu_9S_5 nanomaterial determined through Tauc plot of $(\alpha h\upsilon)^2$ Vs $h\upsilon$ as depicted in figure 4.4(c) is 2.7 eV. The valance band (VB) and conduction band (CB) edges of the respective synthesized material is determined following the equation:

$$E_{VB} = \chi - Ec + 0.5\ Eg$$

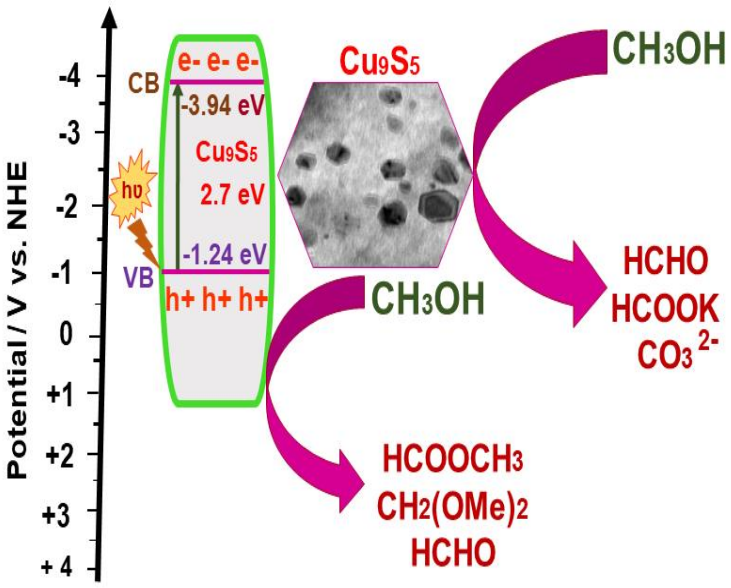

Figure 4.10 Schematic mechanism of photo chemical oxidation of methanol through synthesized Cu_9S_5 nanomaterial.

Where Ec represent the free electron energy potential with respect to NHE scale and its value equal to 4.5 eV and χ implies the absolute electronegativity of the synthesized nanomaterial which was obtained through geometric mean of the electronegativity in Mulliken scale of the constituent atom of the synthesized nanomaterial using the subsequent equation

$\chi = [\ \chi(A).\ a \times \chi(B).\ b]\ (1/\ (a + b))$ where a and b are the number of atoms of A, B in the nanomaterial [40,41]. Thus, χ values of Cu_9S_5 nanomaterial is 2.26 eV and the respective valence band (VB) and conduction band (CB) values of Cu_9S_5 nanomaterial lies at -1.24 eV and -3.94 eV respectively.

The probable mechanism of photochemical methanol oxidation may be described briefly as a reaction path where photo-assisted holes react with OH^- ions to form corresponding $OH^\bullet$ radicals. The generated holes assisting through photo effect and the $OH^\bullet$ radicals oxidized the adsorbed methanol to form formaldehyde, potassium salt of formic acid, methyl formate and potassium carbonate through intermediate $^\bullet CH_2OH$ radical.

The reaction steps involved in this photochemical oxidation of methanol are shown in below as a steps manner

$$Cu_9S_5 + h\upsilon \longrightarrow e^-_{CB} + h^+_{VB}$$

$$h^+ + OH^- \longrightarrow OH^\bullet$$

$$CH_3OH + OH^\bullet \longrightarrow {}^\bullet CH_2OH + H_2O$$

$$^\bullet CH_2OH + OH^\bullet \longrightarrow HCHO + H_2O$$

$$HCHO + OH^\bullet \longrightarrow HCOO^- + 2H^+ + e^-$$

$$CH_3OH + HCHO \longrightarrow HCOOCH_3 + H_2O$$

$$HCOO^- + OH^\bullet \longrightarrow {}^\bullet COOH + OH^-$$

$$2\ {}^\bullet COOH \longrightarrow (COOH)_2$$

4.4 Conclusions

Cost effective Cu_9S_5 nanomaterial was synthesized within a short time in an environment friendly atmosphere by designing a new reaction scheme. The synthesized nanomaterial is characterized by XRD, FTIR, FESEM, EDS, TEM like techniques and the outcome reveals the successful formation of the synthesized nanomaterial. We used Cu_9S_5 as an alternate catalyst instead of highly expensive noble metals like Pt, Pd in the valuable application of fuel oxidation and the electrochemical and photochemical results open a new door in the field of energy research, though still a few limitations are there for its improvement. Electrochemical experiments like cyclic voltammetry, chronoamperometry, photocurrent response measurement, electrochemical impedance studies reveal that synthesized Cu_9S_5 in anodic oxidation of 1 M CH_3OH in 1 M KOH performs better in presence of light compare to that in absence of light as well as 10 wt.% commercial platinum. The stability of the synthesized material was measured through consecutive cyclic voltammetry cycles at 50 mV/sec vs. SCE. The current density was saturated near 70 cycles and after that little fall in current density was observed. In absence of any noble metal that performance in terms of potential and current per surface area were impressive. This result would attract researcher to provide a new in sight to improve noble metal free cost-effective catalyst design of alkaline fuel oxidation reaction. The HPLC measurement identified the products in alkaline methanol oxidation in presence of light. The probable mechanism was also proposed on the basis of the products formed in this photo-assisted oxidation process.

References

1. Roger, I.; Shipman, M. A.; & Symes, M. D. Earth-abundant catalysts for electrochemical and photoelectrochemical water splitting. *Nature Reviews Chemistry*. **2017**, *1*(1), 1-13.

2. Lewis, N. S. Research opportunities to advance solar energy utilization. *Science*. **2016**, *351*(6271), aad1920.

3. Wang, J.; Shi, W.; Liu, D.; Zhang, Z.; Zhu, Y.; & Wang, D. Supramolecular organic nanofibers with highly efficient and stable visible light photooxidation performance. *Applied Catalysis B: Environmental*. **2017**, *202*, 289-297.

4. Wei, Z.; Hu, J.; Zhu, K.; Wei, W.; Ma, X.; & Zhu, Y. Self-assembled polymer phenylethnylcopper nanowires for photoelectrochemical and photocatalytic performance under visible light. *Applied Catalysis B: Environmental*. **2018**, *226*, 616-623.

5. Hughes, T. P.; Kerry, J. T.; Álvarez-Noriega, M.; Álvarez-Romero, J. G.; Anderson, K. D.; Baird, A. H.; ... & Wilson, S. K. Global warming and recurrent mass bleaching of corals. *Nature*. **2017**, *543*(7645), 373-377.

6. AghaKouchak, A.; Cheng, L.; Mazdiyasni, O.; & Farahmand, A. Global warming and changes in risk of concurrent climate extremes: Insights from the 2014 California drought. *Geophysical Research Letters*. **2014**, *41*(24), 8847-8852.

7. Grätzel, M. Recent advances in sensitized mesoscopic solar cells. *Accounts of chemical research*. **2009**, *42*(11), 1788-1798.

8. Bak, T.; Nowotny, J.; Rekas, M.; & Sorrell, C. C. Photo-electrochemical hydrogen generation from water using solar energy. Materials-related aspects. *International journal of hydrogen energy*. **2002**, *27*(10), 991-1022.

9. Fujishima, A.; & Honda, K. Electrochemical photolysis of water at a semiconductor electrode. *Nature*. **1972**, *238*(5358), 37-38.

10. Tachibana, Y.; Vayssieres, L.; & Durrant, J. R. Artificial photosynthesis for solar water-splitting. *Nature Photonics*. **2012**, *6*(8), 511-518.

11. Kamarudin, S. K.; Daud, W. R. W.; Ho, S. L.; & Hasran, U. A. Overview on the challenges and developments of micro-direct methanol fuel cells (DMFC). *Journal of Power Sources*. **2007**, *163*(2), 743-754.

12. Alias, M. S.; Kamarudin, S. K.; Zainoodin, A. M.; & Masdar, M. S. Active direct methanol fuel cell: An overview. *International Journal of Hydrogen Energy*. **2020**, *45*(38), 19620-19641.

13. Cano, Z. P.; Banham, D.; Ye, S.; Hintennach, A., Lu, J.; Fowler, M.; & Chen, Z. Batteries and fuel cells for emerging electric vehicle markets. *Nature energy*. **2018**, *3*(4), 279-289.

14. Majumdar, D.; & Bhattacharya, S. K. Recent Developments of Methanol Electrooxidation Using Nickel-based Nanocatalysts. *ChemistrySelect*. **2022**, *7*(40), e202201807.

15. Zhu, B.; Dong, B.; Wang, F.; Yang, Q.; He, Y.; Zhang, C.; ... & Feng, L. Unraveling a bifunctional mechanism for methanol-to-formate electro-oxidation on nickel-based hydroxides. *Nature Communications*. **2023**, *14*(1), 1686.

16. Luo, H.; Barrio, J.; Sunny, N.; Li, A.; Steier, L.; Shah, N.; ... & Titirici, M. M. Progress and perspectives in photo-and electrochemical-oxidation of biomass for sustainable chemicals and hydrogen production. *Advanced Energy Materials*. **2021**, *11*(43), 2101180.

17. Li, J.; Wei, R.; Wang, X.; Zuo, Y.; Han, X.; Arbiol, J.; ... & Cui, C. Selective methanol-to-formate electrocatalytic conversion on branched nickel carbide. *Angewandte Chemie*. **2020**, *132*(47), 21012-21016.

18. Liu, S. X.; Liao, L. W.; Tao, Q.; Chen, Y. X.; & Ye, S. The kinetics of CO pathway in methanol oxidation at Pt electrodes, a quantitative study by ATR-FTIR spectroscopy. *Physical Chemistry Chemical Physics*. **2011,** *13*(20), 9725-9735.

19. Yuda, A.; Ashok, A.; & Kumar, A. A comprehensive and critical review on recent progress in anode catalyst for methanol oxidation reaction. *Catalysis Reviews*. **2022**, *64*(1), 126-228.

20. Matin, M. A.; Kumar, A.; Bhosale, R. R.; Saad, M. S.; Almomani, F. A.; & Al-Marri, M. J. PdZn nanoparticle electrocatalysts synthesized by solution combustion for methanol oxidation reaction in an alkaline medium. *RSC advances*. **2017**, *7*(68), 42709-42717.

21. Matin, M. A.; Saad, M. A. H. S.; Kumar, A.; Al-Marri, M. J.; & Mansour, S. A. Effect of fuel content on the electrocatalytic methanol oxidation performance of Pt/ZnO nanoparticles synthesized by solution combustion. *Applied Surface Science*. **2019**, *492*, 73-81.

22. Nazir, R.; Khalfani, A.; Abdelfattah, O.; Kumar, A.; Saleh Saad, M. A.; & Ali, S. Nanosheet synthesis of mixed Co3O4/CuO via combustion method for methanol oxidation and carbon dioxide reduction. *Langmuir*. **2020**, *36*(42), 12760-12771.

23. Nazir, R.; Kumar, A.; Saad, M. A. S.; & Ashok, A. Synthesis of hydroxide nanoparticles of Co/Cu on carbon nitride surface via galvanic exchange method for electrocatalytic CO2 reduction into formate. *Colloids and Surfaces A: Physicochemical and Engineering Aspects*. **2020**, *598*, 124835.

24. Nazir, R.; Kumar, A.; Saad, M. A. S.; & Ali, S. Development of CuAg/Cu2O nanoparticles on carbon nitride surface for methanol oxidation and selective conversion of carbon dioxide into formate. *Journal of Colloid and Interface Science*. **2020**, *578*, 726-737.

25. Guo, S.; Dong, S.; & Wang, E. Constructing carbon nanotube/Pt nanoparticle hybrids using an imidazolium-salt-based ionic liquid as a linker. *Advanced Materials*. **2010**, *22*(11), 1269-1272.

26. Antolini, E.; Passos, R. R.; & Ticianelli, E. A. Effects of the carbon powder characteristics in the cathode gas diffusion layer on the performance of polymer electrolyte fuel cells. *Journal of Power Sources*. **2002**, *109*(2), 477-482.

27. Huang, H.; & Wang, X. Pd nanoparticles supported on low-defect graphene sheets: for use as high-performance electrocatalysts for formic acid and methanol oxidation. *Journal of Materials Chemistry*. **2012**, *22*(42), 22533-22541.

28. Wang, S.; & Manthiram, A. Graphene ribbon-supported Pd nanoparticles as highly durable, efficient electrocatalysts for formic acid oxidation. *Electrochimica acta*. **2013**, *88*, 565-570.

29. de Miguel, S. R.; Vilella, J. I.; Jablonski, E. L.; Scelza, O. A.; de Lecea, C. S. M.; & Linares-Solano, A. Preparation of Pt catalysts supported on activated carbon felts (ACF). *Applied Catalysis A: General*. **2002**, *232*(1-2), 237-246.

30. Itzhak, A.; Teblum, E.; Girshevitz, O.; Okashy, S.; Turkulets, Y.; Burlaka, L.; ... & Nessim, G. D. Digenite (Cu9S5): layered p-type semiconductor grown by reactive annealing of copper. *Chemistry of Materials*. **2018**, *30*(7), 2379-2388.

31. Guo, L.; Li, F.; Ji, C.; Liu, Y.; He, W.; Xing, H.; ... & Zheng, X. Effect of Annealing on the Defects and Morphology of Cu9S5: Implication for Advanced Electrode for Asymmetric Supercapacitors. *Journal of Electrochemical Energy Conversion and Storage*. **2023**, *20*(1), 011002.

32. Lu, R.; Zhou, S.; Chai, S.; Zhong, Y.; Zhang, H.; Chen, J.; ... & Pan, A. Cu9S5 nanoparticles encapsulated in N, S co-doped carbon nanofibers as anodes for high-performance lithium-ion and sodium-ion batteries. *Journal of Physics D: Applied Physics*. **2022**, *55*(33), 334001.

33. Qin, N.; Dai, F.; Xue, Y.; Gao, D.; Liu, Y.; Zhang, Y.; ... & Yang, Q. Acanthosphere-like bimetallic sulfide Cu9S5/Mo2S3/NF as bifunctional catalyst for water splitting. *Journal of Electroanalytical Chemistry*. **2024**, *964*, 118338.

34. Chen, W.; Xing, H.; Gao, S.; Yang, P.; & Ji, X. Bi-semiconductor heterojunction Cu9S5@ VO2 microspheres with morphology regulation as broadband high-performance electromagnetic wave absorber. *Applied Surface Science*. **2023**, *610*, 155539.

35. Ye, J.; Wang, H.; Wang, L.; Wang, D.; Li, X.; & Wang, X. Rod-shaped cellulose nanocrystal/Cu9S5 antibacterial nanocomposites for microfiltration. *Industrial Crops and Products*. **2024**, *216*, 118742.

36. Tao, F.; Zhang, Y.; Zhang, F.; An, Y.; Dong, L.; & Yin, Y. Structural evolution from CuS nanoflowers to Cu 9 S 5 nanosheets and their applications in environmental pollution removal and photothermal conversion. *RSC advances*. **2016**, *6*(68), 63820-63826.

37. Yepseu, A. P.; Girardet, T.; Nyamen, L. D.; Fleutot, S.; Ketchemen, K. I.; Cleymand, F.; & Ndifon, P. T. Copper (II) heterocyclic thiosemicarbazone complexes as single-source

precursors for the preparation of Cu9S5 nanoparticles: application in photocatalytic degradation of methylene blue. *Catalysts*. **2022**, *12*(1), 61.

38. Tian, Q.; Jiang, F.; Zou, R.; Liu, Q.; Chen, Z.; Zhu, M.; ... & Hu, J. Hydrophilic Cu9S5 nanocrystals: a photothermal agent with a 25.7% heat conversion efficiency for photothermal ablation of cancer cells in vivo. *ACS nano*. **2011**, *5*(12), 9761-9771.

39. Xu, T.; Liu, S.; Wei, Z.; Zhang, W.; Zhang, G. Y.; Liu, T.; ... & Song, Y. Ultrathin Cu9S5 Nanosheets with Sulfur Vacancy for Multimodal Tumor Therapy. *ACS Applied Materials & Interfaces*. **2024**, *16*(12), 14489-14502.

40. Bera, K. K.; Chowdhury, A.; Bera, S. K.; Das, M. R.; Roy, A.; Das, S.; & Bhattacharya, S. K. Pd Nanoparticle-Decorated Novel Ternary Bi2O2CO3-Bi2MoO6-CuO Heterojunction for Enhanced Photo-electrocatalytic Ethanol Oxidation. *ACS omega*. **2023**, *8*(31), 28419-28435.

41. Bera, K. K.; Chakraborty, M.; Bera, S. K.; Chowdhury, A.; Das, M. R.; Mondal, M.; & Bhattacharya, S. K. Synergistic photo-enhanced electrocatalysis of Pt–ZnO–Bi 2 O 3 heterojunction for methanol oxidation under visible light illumination. *Energy Advances*. **2022**, *1*(11), 908-925.

42. Sugarthi, S.; Bakiyaraj, G.; Abinaya, R.; Navaneethan, M.; Archana, J.; & Shimomura, M. Effect of different growth temperature on the formation of ternary metal chalcogenides AgBiS2. *Materials Science in Semiconductor Processing*. **2020**, *107*, 104781.

43. Kim, Y. Y.; & Walsh, D. Metal sulfide nanoparticles synthesized via enzyme treatment of biopolymer stabilized nanosuspensions. *Nanoscale*. **2010**, *2*(2), 240-247.

44. Wu, D.; Jiang, Y.; Yuan, Y.; Wu, J.; & Jiang, K. ZnO–ZnS heterostructures with enhanced optical and photocatalytic properties. *Journal of Nanoparticle Research*. **2011**, *13*, 2875-2886.

Chapter- 5

Unfolding photocatalytic efficiency of newly one pot synthesized n-n $AgBi_3S_5$-Bi_2S_3 photocatalyst for removal of Rhodamine-B from aqueous system under natural light illumination

CHAPTER 5

5.1 Introduction:

Water is one of the most precious, essential and subtle molecules on earth, which requires top most priority for attention and purity to maintain an equilibrium ecosystem for sustainable future. It plays like a bridge by which all beings, objects complete their life cycle path from start to end. So, development of water management and related ecosystem are much more important than that found in present scenario to explore its highest utilization for the sake of existence of both inanimate and life. But with the progress of civilization man-maid contamination of many toxic organic elements by cleaning, cooking, agricultural and industrial uses, are increased day by day **[1-3]** and simultaneously the water is not purified to its required form for reuse **[4]**. Among various industries those related to dye sector are one of the most pollutant-creator in terms of volume and effluent generation **[5,6]** and as a consequence pollutes released in water develop an uncanny situation in environment **[7-8]**. Moreover, conventional methods of treatment are not capable enough to degrade such toxic organic pollutants contaminated in water **[9-10]**. Therefore, new promising tools involving solar radiation, photocatalysis, electrocatalysis, etc. are developing as a sustainable solution to address these issues **[11-13]**. Out of these, photocatalytic degradation using sunlight is the most effective economic green method to reshape the pollutant in the form of harmless products like H_2O and CO_2 **[14-15]**. The ecofriendly sustainable nature of this advanced oxidation process has gained enough attention due to its some characteristic features like complete mineralization, simple operating condition, zero waste generation etc. **[16]** and apart from that it has too effective to treat waste water of high complexity, low biodegradability and highly concentrated organic dyes **[17]**. Several semiconductor materials considered to be a good photocatalyst in past few years towards degradation of organic pollutants like dyes where titanium di oxide (TiO_2) showed some promising result due to its nontoxicity, commercial availability, economic viability, physical chemical stability and high photocatalytic activity **[18]**. But its large band gap energy (3.2 eV) decreases its photocatalytic efficacy to some extent and makes it unable to respond the UV light of wavelength above 387 nm which mainly restricted its application towards practical field **[19-21]**. Therefore, the demand for non-titanium based visible light responsive **[22]** highly efficient, cost-effective, visible light-usable practical photocatalyst were pending from long time. Metal sulfides are attracting much more attention due to their special characteristic features like small band gap, high position of valence and conduction bands in energy scale, absorption capability of wider range of light spectrum compare to metal oxides **[23]**.

Some of the concerns raised by previous authors **[24, 25]** regarding small band gap resulting rapid charge recombination and wider absorption range, may be overcome by selecting a combination of materials forming type II heterojunction. There are several mechanistic path ways through which charge migration and separation in between two semiconductors may proceed, depending on the nature, combination and structure of heterojunctions. Recently heterojunctions pursuing step-scheme (S-scheme) has made substantial attraction in the current research progression **[26]**.

When two semiconductors connect the electron migrates one to another in S-scheme based on their work function values followed by band bending and subsequently create an environment in the interface like an internal electric field **[27]**. The internal electric field activates and enhances the ability of the respective electrons and holes which are not participated in the photocatalytic reaction due to their poor oxidation and reduction forms without disturbing those electrons and holes which participate in the photochemical reaction and also intact their efficiency. The photocatalytic efficacy of the respective catalyst is expected to improve significantly as a result of the above phenomenon **[28]**. The significant features and exceptional photocatalytic efficacy of the nanocomposite having charge carriers with strong redox ability via S-scheme pathways has been already explored by some researchers in recent time through their work in the field of photochemical application **[29-31]**.

In the previous study **[32]**, we observed that greater the absorption of sunlight as dictated by the characteristics of the materials and mixed materials and band gap management, greater is the catalytic capability for degradation of dye. So, Bi_2O_3 is replaced by Bi_2S_3 as the band gap is expected to decrease on going down a group (here chalcogen of chalcogenide) in the periodic table. Moreover, Ag-based semi-conductors have low band gaps with high absorption of sunlight and photocatalytic activity. However, they suffer from poor stability. $AgBi_3S_5$ is chosen since it is quite stable in nature and found in earth as a part of Pavonite mineral ($Ag_{0.75}$ Cu $_{0.25}$ Bi $_{2.25}$ Pb $_{0.75}$ S_5). In addition, the band structure of Bi_2S_3 brackets(covers) the valence band (VB) of $AgBi_3S_5$, which makes them a suitable structure in $AgBi_3S_5$-Bi_2S_3 nanocomposite for Z-scheme and S-scheme electronic transition on excitation under sunlight. The expectation is found to be true in the study with excellent and synergistic catalytic activity obtained from the nanocomposite of $AgBi_3S_5$ and Bi_2S_3 in reference to the pure ones in the degradation of Rh-B.

5.2 EXPERIMENTAL SECTION

5.2.1. Materials

Bismuth nitrate (Bi $(NO_3)_3.5H_2O$, 99.9%, Merck), ethylene glycol ($C_2H_6O_2$, 99.9%, Merck), silver nitrate ($AgNO_3$, 99.9%, Merck), thiourea (H_2N-C(=S)-NH_2, 99.9%, Merck), Rhodamine B (Eastman, AR) are used in the study without further purification. The double distilled water was used throughout the investigation.

5.2.2. Synthesis of the $AgBi_3S_5$

1.06 g of $AgNO_3$ was dissolved in 25 mL ethylene glycol solution followed by stirring for 15 minutes to prepare a homogenous solution, A. Simultaneously, 3.03 g of bismuth nitrate taken in 25 mL ethylene glycol solution and the mixture stirred near about 15 minutes to prepare a solution, B. As the same time in another reaction vessel where 0.95 g of thiourea dissolved in 25 mL ethylene glycol solution followed by 15 minutes stirring and the resultant solution termed as mixture, C. Mixture A taken in mixture B and resultant solution sonicated up to 20 minutes and then the homogenous mixture placed into temperature-controlled heating mantel under ambient condition and the temperature was set to 90°C. When the reaction temperature reached at 90°C then mixture C poured into it and the mixed solution kept in same temperature up to 2 hours. Switched off the heating mantel followed by settle down the reaction mixture at room temperature. The synthesized residue collected after centrifugation, washing with water and alcohol several times and dried it at 80°C for 24 h.

5.2.3. Synthesis of the Bi_2S_3

0.61 g of bismuth nitrate was taken in 25 mL ethylene glycol. The mixture sonicated for 15 minutes and the solution kept in a temperature-controlled heating mantel, set the temperature at 90°C. Subsequently, 2.55 g of thiourea dispersed in 25 mL ethylene glycol solution followed by 15 minutes stirring and poured the mixture into the previous one into the temperature-controlled heating mantel, when the reaction temperature reached at 90°C, carried the reaction up to 2 h with same environment, settled the reaction mixture at room temperature. The synthesized residue was collected followed by centrifugation, washing with water and alcohol respectively. Dried the residue at 80°C in an air oven up to 24 h.

5.2.4. Synthesis of the $AgBi_3S_5$-Bi_2S_3

0.85 g of silver nitrate dissolved in a 25 ml ethylene glycol solution and the mixture sonicated up to 15 minutes, termed as solution A. In another reaction vessel where 2.43 g of bismuth nitrate was dispersed in a 25 ml ethylene glycol solution followed by 15 minutes stirring and named the homogenous mixture as B. Now, mixture B poured into mixture A and the resultant mixture sonicated near about 20 minutes, placed the reaction mixture into a temperature-controlled heating mantel under ambient condition and set the reaction temperature at 90°C. 0.76 g of thiourea dispersed in a 25 ml ethylene glycol solution, sonicated it about 15 minutes and poured the thiourea solution into reaction mixture when the reaction temperature reached at 90°C and kept the reaction mixture in the same environment near about 2 hours. Settled down the synthesized residue in room temperature and collected it after centrifugation followed by several times washing with water, alcohol one after at a regular interval. Dried the collected residue at 80°C for 24 h.

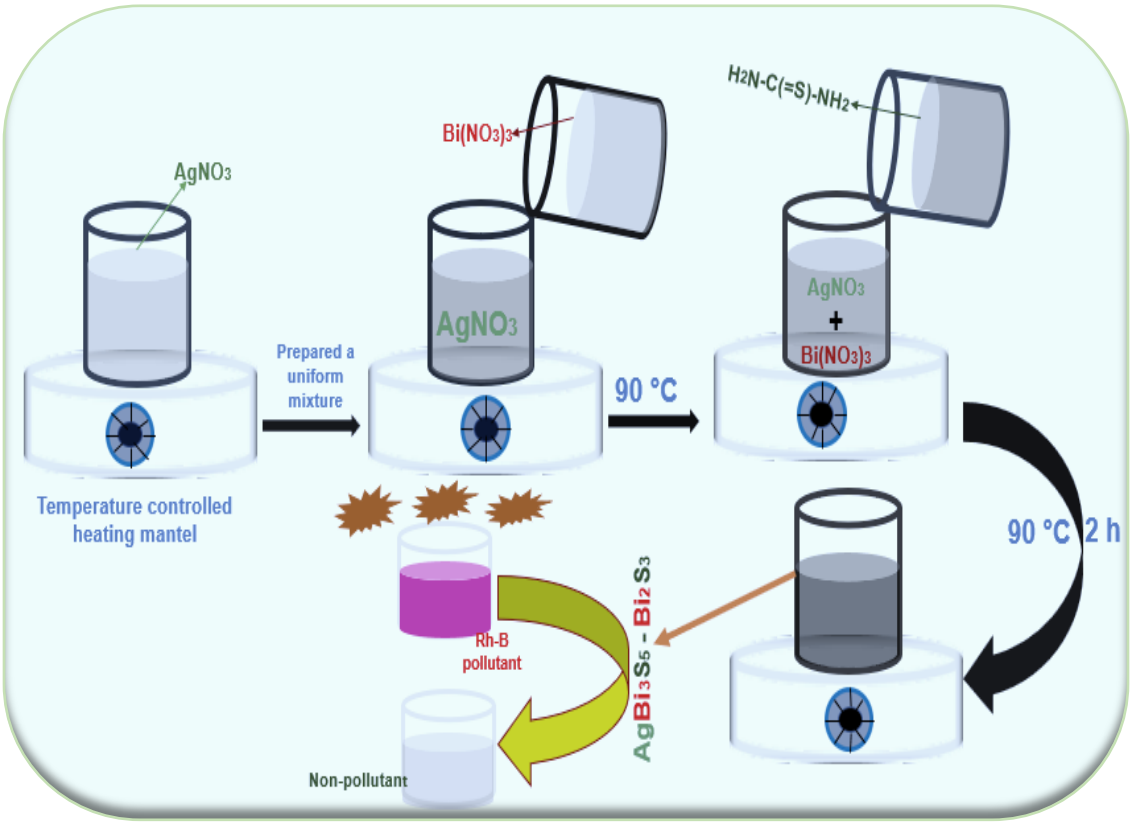

Scheme 5.1: Schematic representation for the synthesis of $AgBi_3S_5$-Bi_2S_3 nanocomposites

5.2.5 Photocatalytic experiments

The photocatalytic experiment was carried out using synthesized photocatalysts for photodegradation of Rhodamine-B under natural sunlight illumination. 0.7 gL^{-1} $AgBi_3S_5$-Bi_2S_3 was taken in a 100 mL beaker containing 50 mL of 10 ppm aqueous solution of Rhodamine-B followed by 30 minutes sonication and then stirring the suspension under magnetic stirrer around 450 rpm in a dark condition up to 1 hr. to disperse the catalyst homogeneously into the dye solution. 4 mL of this suspension was collected before exposure to the sunlight for analysis which was termed as observation at 0 min. Then it was exposed to sunlight and around 4 mL of suspension was collected every 5 minutes interval. The intensity of sunlight which was time dependent, recorded using LUX meter, model LX-101A for determining the average illumination of sunlight. The experiments were carried out during April, 2023 in between 12 pm to 2.30 pm at Jadavpur university, Jadavpur, Kolkata, India in consecutive days for maintain consistency of irradiation of natural sunlight. The collected dye suspension was analyzed using spectrophotometer and the changes of concentration of dye suspension was recorded from its characteristic changes of absorption at the wavelength of adsorption maximum around 554 nm. The percentage of photocatalytic degradation was calculated using following formula

% Of Photocatalytic degradation = $\mathbf{\{(C_0 - C_t)/ C_0\} \times 100}$

where C_0 is the initial absorbance before exposure to sunlight and C_t are the absorbance of dye suspension after exposure to sunlight in between t minute interval. The reaction followed the equation $\mathbf{\ln (C_0 / C_t) = kt}$ where k implies as an associated pseudo-first order rate constant. Recyclization experiment was carried out following above procedure, after completion of each cycle, the catalyst was collected followed by subsequent washing with water and alcohol and then dried at 80 °C up to 4 h and reused it for next cycle.

5.2.6 Trapping experiments

The trapping experiment was carried out followed by same procedure discussed in photocatalytic experiment section, in addition to that using 2mM of different scavengers like Isopropyl alcohol (IPA), Parabenzoquinone (BQ) and Disodium ethylenediaminetetraacetic acid (Na_2EDTA) as $\mathbf{^{\bullet}OH}$, $\mathbf{^{\bullet}O^{2-}}$ and $\mathbf{h^+}$ trapping agent respectively.

5.2.7 Zeta Potential experiments

The zeta potential experiment was carried to determine the responsible pH of point zero charge where at that pH solution the net charge on the surface of the adsorbents become zero. 0.7 gL^{-1} of catalyst was dispersed in a respective desired volume of water until the solution become homogeneous. Then equal amount of homogenous solution was taken in different glass bottle and the respective pH were adjusted using pH meter. The pH values of respective prepared pH solution, 1, 2, 3, 4, 5, 8 and 10 were performed for zeta potential experiment respective one solution taken at a time.

5.2.8 Measurement of Photocurrent experiments

The device was fabricated with ITO coated glass in which a narrow region (0.5 mm × 6 mm) itched using Zinc dust followed by 2 M HCl solution. Then the whole region was cleaned with soap solution, distilled water, acetone and iso propyl alcohol one after another sequentially 10 minutes each with that respective solution and then again cleaned up to 15 minutes with UV ozone plasma. 2 mg of $AgBi_3S_5$-Bi_2S_3, $AgBi_3S_5$ and Bi_2S_3 were dispersed in 1 mL of ethanol solution in separate centrifuge tube and sonicated up to half an hour. 50 µL of respective dispersed solution was drop casted in a cleaned narrow region of separate device and dried at 60 °C up to 15 minutes in a hot plate respectively. Then the photocurrent measurement was done under solar stimulator which intensity is equivalent to one sun light illumination by keithly 2602 B source-meter with 1 volt bias potential.

5.2.9 Time Resolved Photoluminescence (TRPL) Spectral experiments

0.7 gL^{-1} of $AgBi_3S_5$-Bi_2S_3 was dispersed in a 50 mL 10 ppm Rhodamine-B aqueous solution followed by 30 minutes bath sonication at room temperature and then magnetic stirring was done in dark condition up to 1 hours. pH of the respective solution was maintained to pH 3 and then 4 mL of the solution was collected using micropipette and then rest solution was exposed to light. 4 mL of the subsequent solution was also collected after 10 minutes of the irradiation. Similarly same experimental solution was prepared in absence of dye. The TRPL experiments were carried out with these collected and prepared solutions before and after exposure. In addition, the solutions containing only dye and only catalyst were also studied using two different excitation wavelengths

550 nm and 265 nm respectively. The corresponding emission wavelengths were 580 nm and 530 nm respectively.

5.3 Results and discussion

5.3.1 XRD analysis

XRD patterns of the synthesized monoclinic silver bismuth sulfide ($AgBi_3S_5$), orthorhombic bismuth sulfide (Bi_2S_3) and mixed phase of them ($AgBi_3S_5$-Bi_2S_3) are depicted in **Figure 5.1(a).** The major diffraction peaks of silver bismuth sulfide arise at 2Θ values (°) 21.77, 22.98, 27.78, 28.53, 29.92, 31.392, 31.473, 32.52, 34.913, 36.431, 37.165, 38.447, 40.82. These are attributed to the planes (203), (110), (401), (113), ($\bar{3}$10), ($\bar{3}$12), (114), (403), ($\bar{3}$13), ($\bar{3}$14), (405), (007), (116) respectively of monoclinic $AgBi_3S_5$ (JCPDS NO. 83-2051). The sharp diffraction peaks of Bi_2S_3 are found at 2Θ values (°) around 22.32, 28.57, 32.90 and 49.30 which are due to maximum diffraction from the planes (220), (230), (301), and (521) (JCPDS NO. 89-8965) respectively. The peaks found for ($AgBi_3S_5$-Bi_2S_3) matched with the (113), ($\bar{3}$10), ($\bar{3}$12), (403), ($\bar{3}$13), ($\bar{3}$14), (405), (007), (116) planes of monoclinic $AgBi_3S_5$(JCPDS NO. 83-2051) arise at 2Θ values (°) 28.53, 29.92, 31.39, 32.52, 34.913, 36.430, 37.165, 38.447, 40.82 respectively and also matched with some diffraction peaks of orthorhombic of Bi_2S_3(JCPDS NO. 89-8965) are found at 2Θ values (°) around 28.57, 32.90, 49.30, attributed to the planes (230), (301), (521) respectively. For both synthesized $AgBi_3S_5$ and Bi_2S_3, it reveals that some peaks are relatively more intense with respect to the others in comparison to that expected from JCPDS data. It signifies that some planes are fairly more developed than others in the synthesized nano particle samples. Moreover, the full width half maximum of the intense peaks is sufficiently large, exhibiting nanoparticle nature of the synthesized samples.

5.3.2 FTIR analysis

Figure 5.1(b) represented the FTIR spectra of $AgBi_3S_5$, Bi_2S_3 and $AgBi_3S_5$-Bi_2S_3 where the peaks at 533 cm^{-1} present in AgBi3S5 and $AgBi_3S_5$-Bi_2S_3 directed the typical vibration modes of sulfur **[33]** inferring the existence of Ag-S bond. The peaks found in range 590 cm^{-1} to 650 cm^{-1} designate the vibration of Bi-S **[33].** Frequencies adjacent to 1649 cm^{-1} for $AgBi_3S_5$-Bi_2S_3 and $AgBi_3S_5$ are probably owing to stretching and bending vibrations of the O-H bond of the adsorbed H_2O on the

surface of $AgBi_3S_5$ **[34,35].** The peaks observed in $AgBi_3S_5$, Bi_2S_3 and $AgBi_3S_5$-Bi_2S_3 nearby 1336 cm^{-1} and 872-900 cm^{-1} are the stretching and bending vibrations of the Bi-S bond.

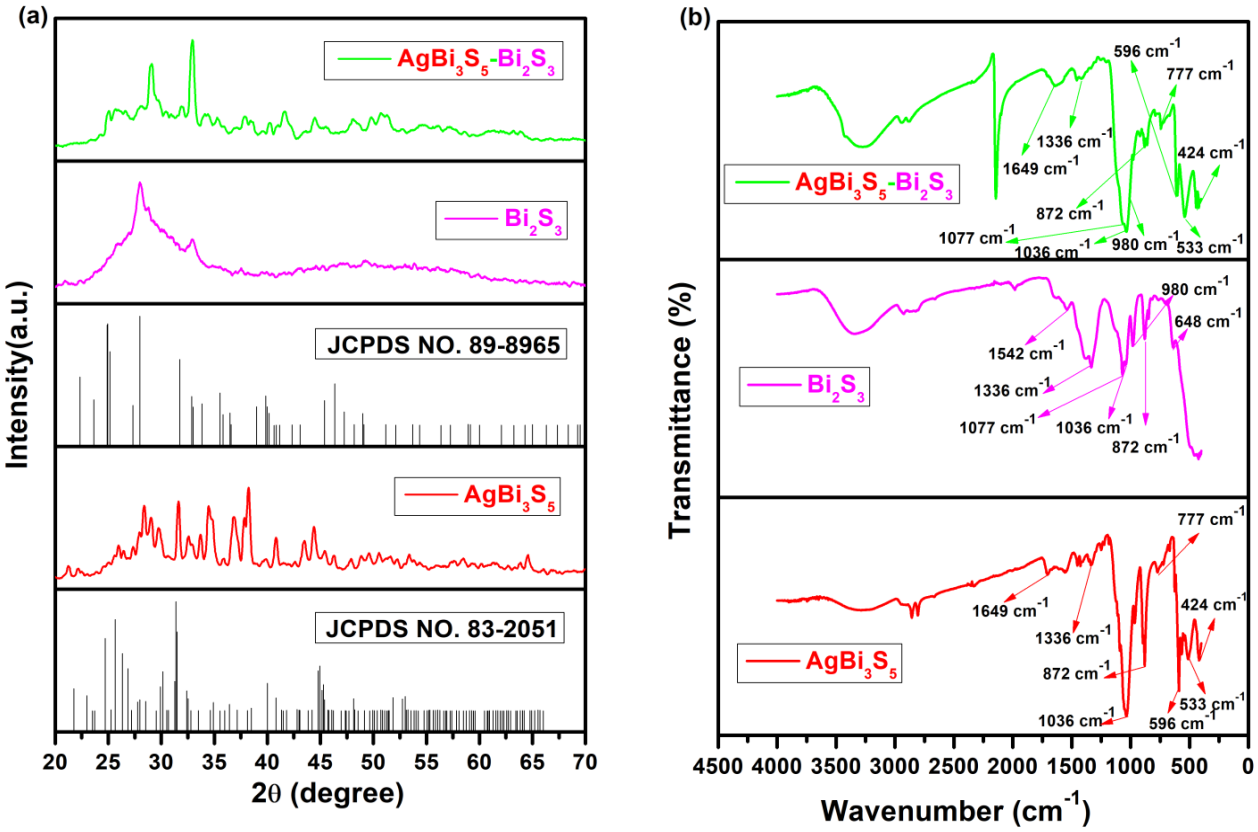

Figure 5.1: (a) Powder XRD patterns of $AgBi_3S_5$, Bi_2S_3 and $AgBi_3S_5$-Bi_2S_3 from bottom to top respectively (b) FTIR spectra of $AgBi_3S_5$, Bi_2S_3 and $AgBi_3S_5$-Bi_2S_3 from down to up respectively.

5.3.3 XPS analysis

In the XPS analysis, doublet peaks **(Figure 5.2(a))** arose at 373.7 eV and 367.7 eV in fine Ag spectrum attributed to Ag $_{5/2}$ and Ag $_{3/2}$ of the Ag^+ respectively **[36]** Similarly, the Bi 4f doublet **(figure 5.2(b))** appeared at 158.9 eV (Bi 4f $_{7/2}$) and 164.2 eV (Bi 4f $_{5/2}$). The Bi 4f locations are in between those of bismuth metal (Bi 4f $_{7/2}$, 157 eV) and bismuth oxides (Bi 4f $_{7/2}$, 159 eV), indicating characteristic bismuth sulfide **[36].** The outcome of above analysis **(Table 5.1)** directed

that both silver and bismuth were present as metal sulfides (Ag (I), Bi (III)), as complimented with previous studies **[37,38].** The Bi 4f and S 2p regions are combined to a single peak in the survey scan presented in the supporting information (Figure S1). Another small peak found at 230.7 eV which can be assigned to S 2s **(Figure 5.2(c)). Figure 5.3** presented as surface spectrum where a broad peak at 532 eV was assigned to the O 1s region due to water molecules adsorbed at the surface of the metal sulfide of the catalyst **[39].** The catalyst drops casted on the surface of the silicon wafer for the XPS analysis and peak appeared in around 100-150 eV regions attributed the corresponding observance. One of the broad peaks highlighted around binding energy 286.6 eV appears due to C 1s calibration peak, which is also known as adventitious carbon peak **[40].**

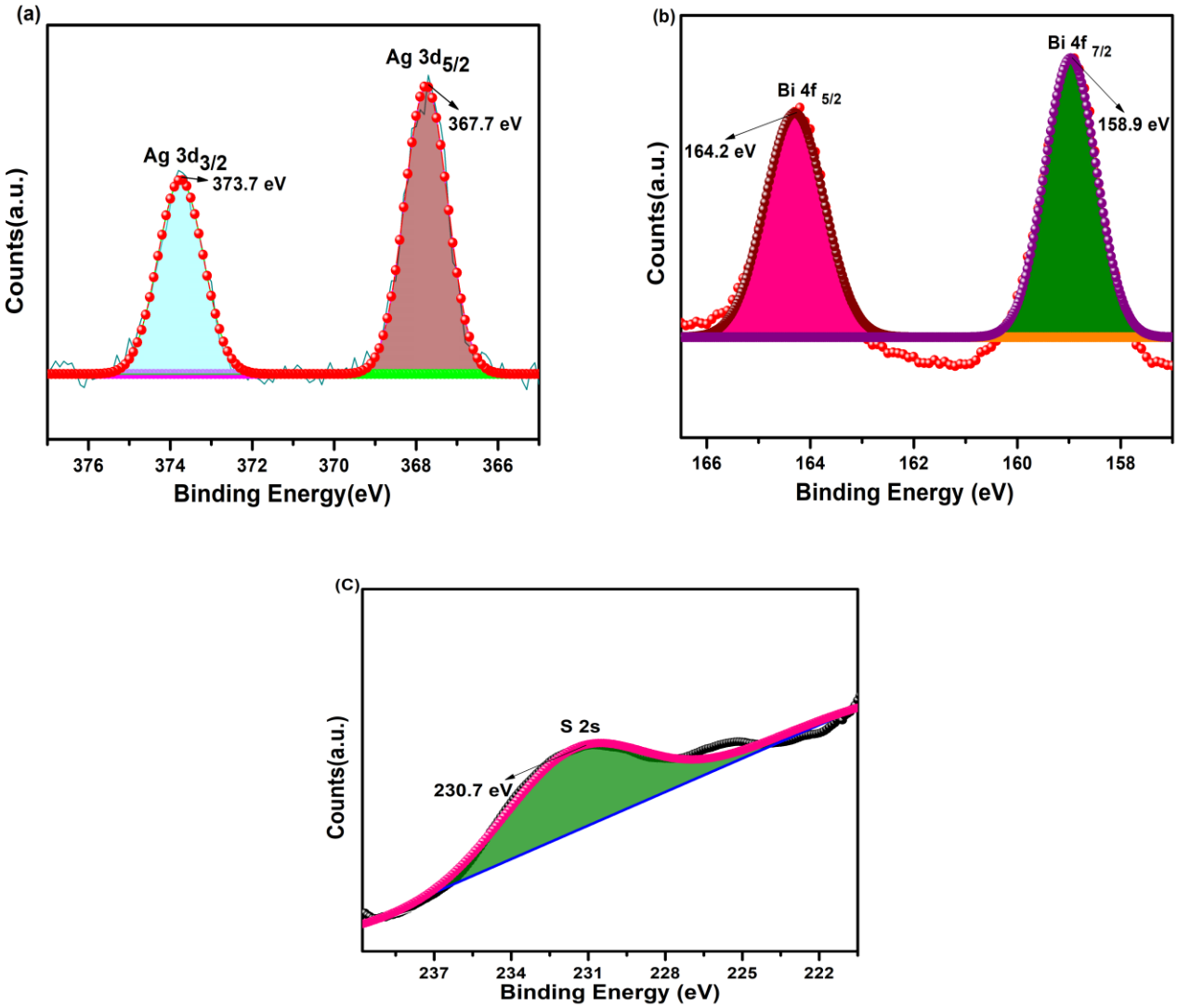

Figure 5.2: Fine XPS spectra of (a) Ag 3d (b) Bi 4f and (c) S 2s elements.

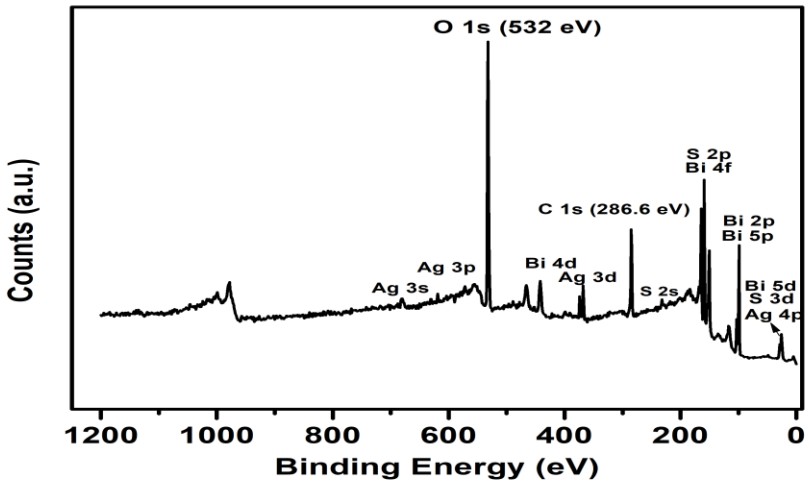

Figure 5.3: The survey spectrum of $AgBi_3S_5$-Bi_2S_3.

Table 5.1 Elemental compositions along with their chemical states of the synthesized catalyst from the XPS study.

Element	**peak**	**Positions (B.E) eV**
Ag 3d	Ag^{+} 3d $_{5/2}$	373.7
	Ag^{+} 3d $_{3/2}$	367.7
Bi 4f	Bi $^{3+}$ 4f $_{7/2}$	158.9
	Bi $^{3+}$ 4f $_{5/2}$	164.2
S 2s	S 2s	230.7

5.3.4 UV -vis spectral study

The UV-vis absorption spectra of $AgBi_3S_5$, Bi_2S_3, $AgBi_3S_5$-Bi_2S_3 are depicted in **figure 5.4(a)** and respective direct band gap (E_g) shown in **figures 5.4(b-d)** determined from the plot of $(\alpha h\upsilon)^2$ *vs.* $h\upsilon$, represent the allowed electronic transition **[41,42]** and α, h, υ are the absorption coefficient, plank constant and incident light respectively. The direct band gap values of $AgBi_3S_5$ and Bi_2S_3 are well synchronized with the previous reported values **[43-45].**

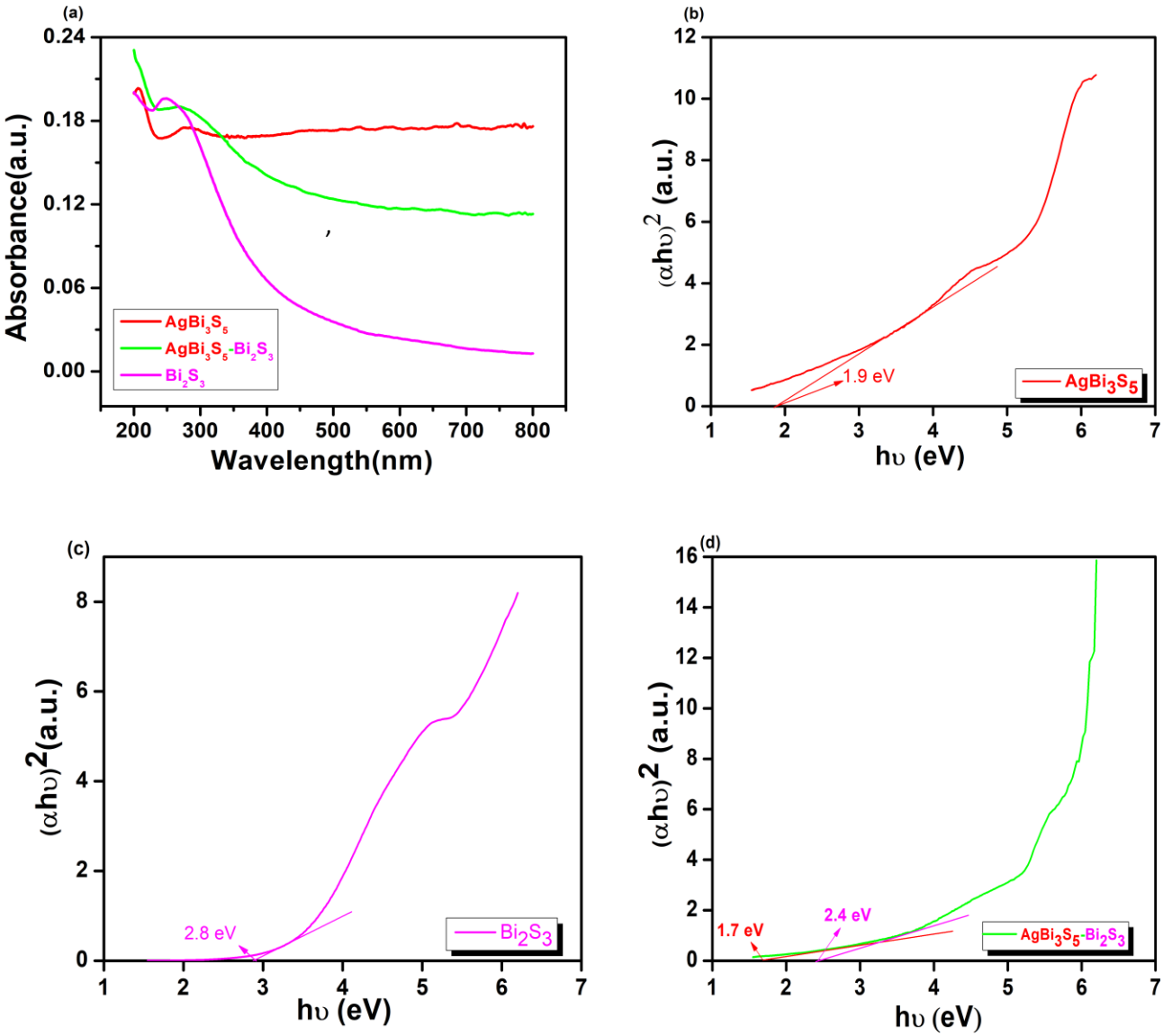

Figure 5.4: UV-vis spectra of (a) $AgBi_3S_5$, $AgBi_3S_5/Bi_2S_3$ and Bi_2S_3, (b-d) represents the $(\alpha h\upsilon)^2$ vs. $h\upsilon$ profiles of $AgBi_3S_5$, Bi_2S_3 and $AgBi_3S_5$-Bi_2S_3 photo-catalysts respectively for the determination of band gap energy.

5.3.5 Photoluminescence (PL) spectral study

Photoluminescence (PL) spectra shown in **figure 5.5(a)** of Bi_2S_3, $AgBi_3S_5$-Bi_2S_3 and $AgBi_3S_5$ respectively. Efficacy of photocatalyst depends upon recombination of charge carriers and such important characteristic information getting from photoluminescence studies, the spectra primary dealing with recombination of charge carriers. The maximum PL intensity observed at 532 nm

when the respective excitation wavelength was 265 nm. $AgBi_3S_5$-Bi_2S_3 shown lower intensity compare to others because the separation of charge carriers improved in it due to lower recombination rate and facilitate greater catalytic efficiency which complimented with the outcome of photochemical degradation reaction.

5.3.6 Photocurrent measurement

To provide additional support for better electron-hole separation efficiency of $AgBi_3S_5$-Bi_2S_3 among the synthesized photocatalysts, the transient photocurrent was measured with several ON-OFF cycles under the solar light simulator whose intensity is equivalent to one sunlight illumination. The current density versus time plot was shown in **figure 5.5(b)** highlight that the photocurrent increases gradually at first and attain a maximum current saturation then fall back when the light is turned off. The phenomenon has indicated that faster charge separation and less charge recombination for $AgBi_3S_5$-Bi_2S_3. The photo-assisted electrons move to the contact of surface of respective synthesized photocatalyst. The slow recombination process for $AgBi_3S_5$-Bi_2S_3 was complimenting the subsequent decaying of photocurrent which was also corroborated with the outcome of photoluminescence study. $AgBi_3S_5$-Bi_2S_3 was shown greater photocurrent response compare to $AgBi_3S_5$ and Bi_2S_3 which are fairly complimented with their photocatalytic performance in these degradation process.

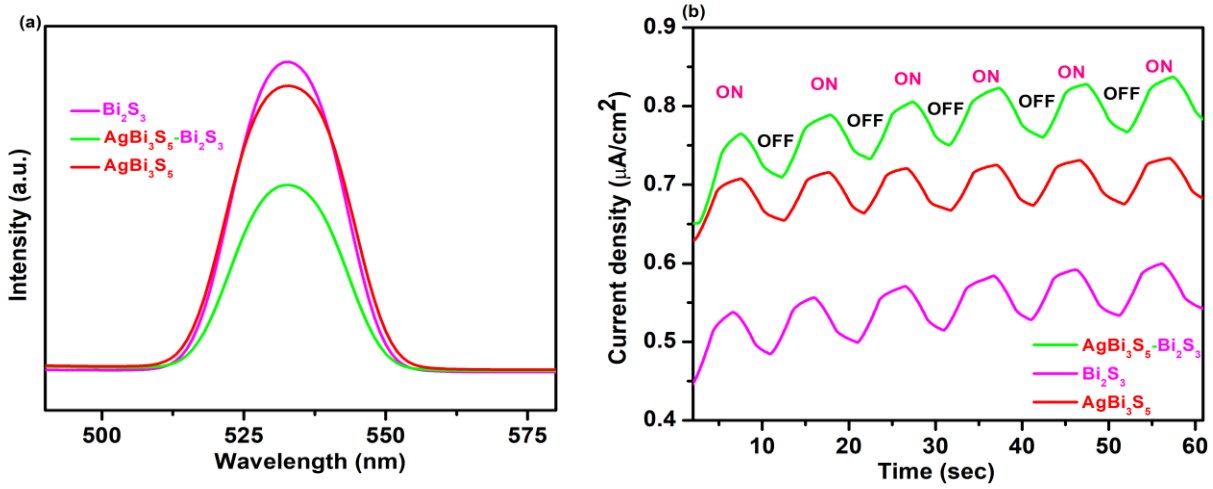

Figure 5.5: (a) Photoluminescence spectra of Bi_2S_3, $AgBi_3S_5$ and $AgBi_3S_5$-Bi_2S_3. (b) photocurrent response of $AgBi_3S_5$-Bi_2S_3, Bi_2S_3, and $AgBi_3S_5$ with the same concentration under 1V bias potential on exposure to the solar light simulator respectively.

5.3.7 Morphological study

The surface morphology and compound recognition of $AgBi_3S_5$, Bi_2S_3, $AgBi_3S_5$-Bi_2S_3 were established by FESEM, TEM and SAED pattern as depicted in **figure 5.6** and **5.7** respectively. **Figures 5.6(a)** and **5.6(b)** illustrate the morphology of $AgBi_3S_5$-Bi_2S_3 nanocomposite before and after 5th time of its use as photocatalyst in Rh-B degradation. Both FESEM pictures exhibit plate and rod-like structures with some grains on the plates and the rods. Both figures reveal sufficient holes and gaps between the structures, which may help movement of the reactants and products towards and from the surface of the catalyst. **Figure 5.6(b)** exhibits more heaped rods of bigger lengths, which might arise due to channelization of the reactants and products during reaction. **Figure 5.6(c)** represents the area selected for EDS analysis, where the elements Ag, Bi, S are found to be present. **Figures 5.6(d, e, f)** present respectively the color mapping profiles of Ag, Bi and S, each of which is almost uniformly distributed in the selected area. The EDS spectrum of $AgBi_3S_5$-Bi_2S_3 nanocomposites also recognizes all the constituting elements **(figure 5.6(g))** and the EDS spectrum of after degradation along with elemental mapping provided in **figure 5.14** also compliment with the outcome of before degradation. Ash colored irregular spheres and lumps of material, $AgBi_3S_5$ **(figure 5.7(a))** are stacked one after another to form an irregular rough surface. Holes and gaps are formed in every part of materials where the lumps are loosely bound. Few portions of whole micrograph in colored black due to the accumulation of several layers one after another in that portion. The SAED profile indicates the presence of (312) plane of $AgBi_3S_5$ is well coordinated with result of XRD studies in outlined **figure 5.7(b)**. EDS profiles of $AgBi_3S_5$, Bi_2S_3 depicted in **figure 5.7(c, d)** respectively. Figure **5.7(e)** represents the formation of some rod-like structure of Bi_2S_3 having diameter nearly 10 nm. Corresponding planes (301), (521) are outcome from the SAED profiles synchronized with respective XRD data depicted in **figure 5.7(f).** The irregular small spheres of about 10 nm diameter and bigger lumps (10-50 nm) and some rod-like structure (diameter about 10 nm) both are shown in **figure 5.7(g)** indicated presence of both $AgBi_3S_5$ and Bi_2S_3 and planes ($\bar{3}$12), (521) exposed in SAED pattern of $AgBi_3S_5$-Bi_2S_3 in **figure 5.7(h)** are also present in SAED profiles of $AgBi_3S_5$ and Bi_2S_3 respectively. The above result is more clearly indicated that both $AgBi_3S_5$ and Bi_2S_3 are present in surface of $AgBi_3S_5$-Bi_2S nanocomposite.

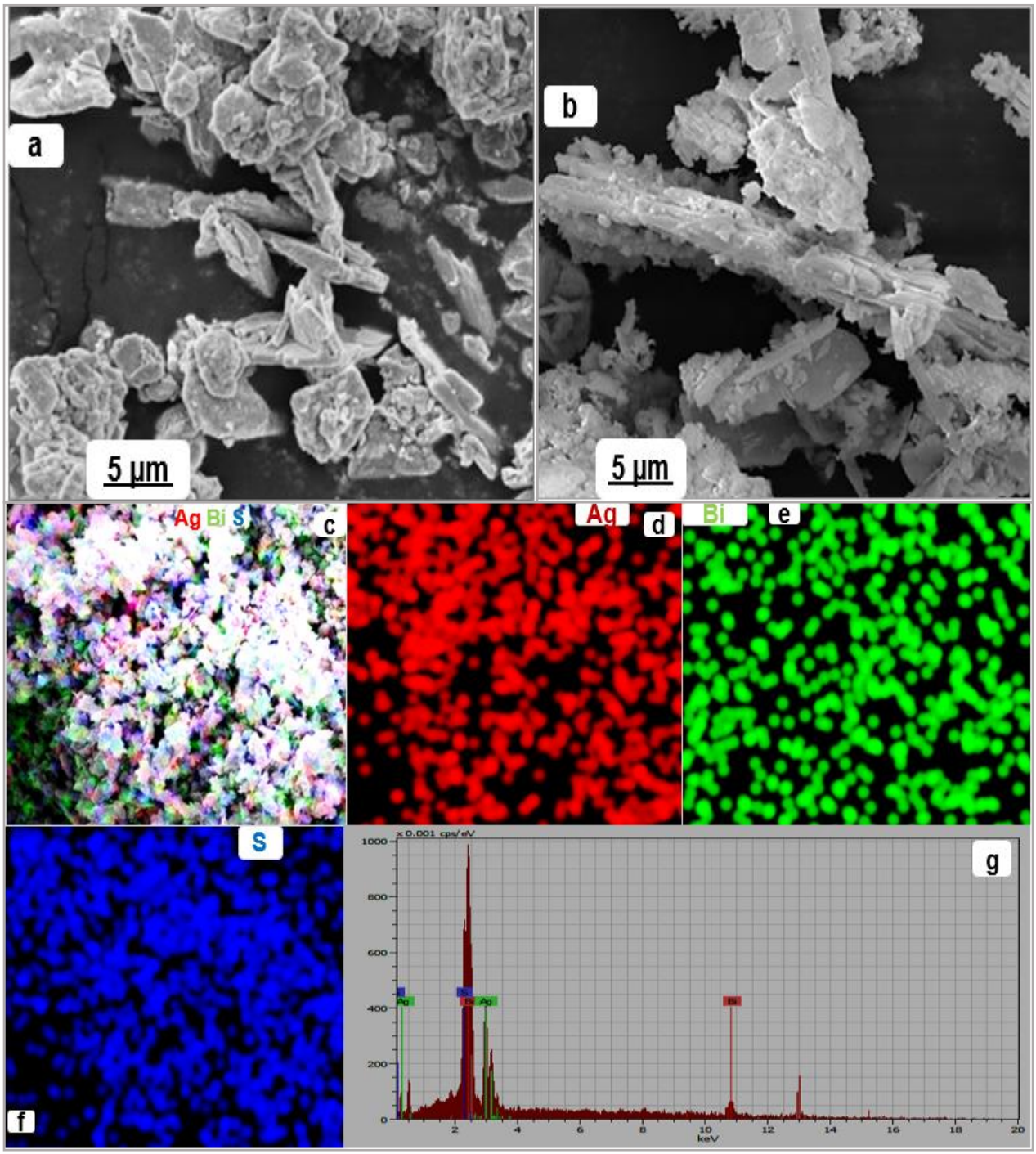

Figure 5.6: FESEM image of synthesized $AgBi_3S_5$-Bi_2S_3 nanocomposites a) before use b) after use (5th time) c) area selected for EDS analysis, d, e, f, g) color mapping profiles of Ag, Bi, S and respective EDS profile respectively.

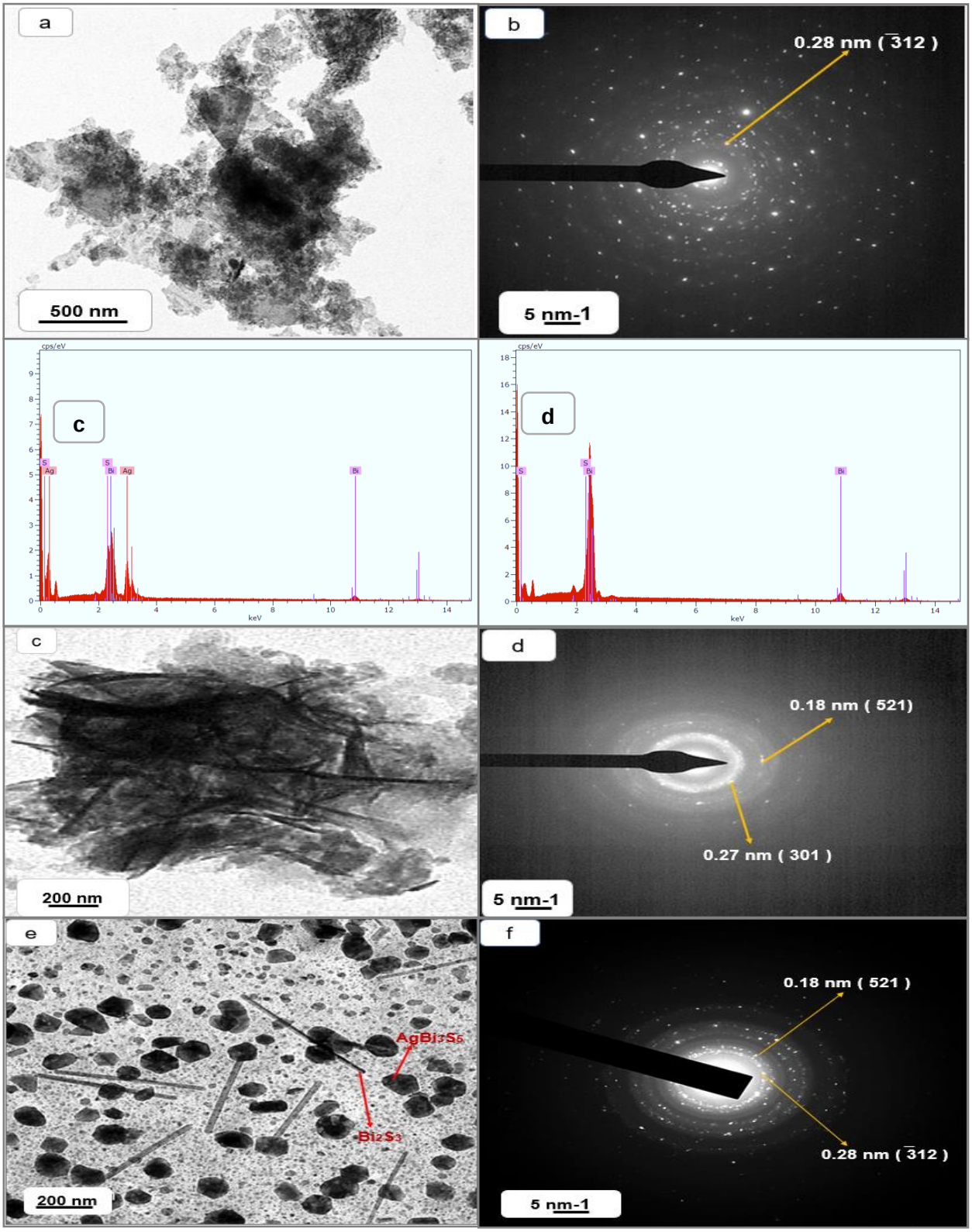

Figure 5.7: TEM image and SAED pattern of $AgBi_3S_5$(a, b), (c, d) are EDS profiles of $AgBi_3S_5$, Bi_2S_3 respectively, TEM images and SAED patterns of Bi_2S_3 (e, f) and $AgBi_3S_5$-Bi_2S_3 (g, h) photocatalysts respectively.

5.3.8 Time resolved photoluminescence (TRPL) spectral study

The time resolved photoluminescence (TRPL) spectral studied with respect to dye as well catalyst under various conditions. The analysis of graded decay of time resolved photoluminescence spectrum of dye, Rhodamine-B reveals life time of the excited state in the order of 1.66 ns. The addition of catalyst to the system reveals faster decrease of count indicating adsorption of dye to the catalyst surface leading to decrease in concentration of dye in the solutions. The count versus time profile also reveals that the number of count decreases at the much faster rate on exposure of the catalyst-dye system to visible light for 10 minutes. This transpires the removal of dye molecules from the catalyst surface by decomposition and subsequent adsorption of the catalyst by dye molecules leading to more decreased concentration of dye in solution shown in **figure 5.8(a).** The Time resolved photoluminescence decay spectrum of the catalyst, $AgBi_3S_5$-Bi_2S_3(in absence of dye) in the experimental solution of pH 3 reveals relative decrease of counts and the change in number of counts for the catalyst with respect to time is in the order shown in **figure 5.8(b):** bare catalyst>catalyst (after adsorption of dye but before degradation) > catalyst (after somewhat dye degradation). Moreover, two average life time values are obtained for each state of the catalyst corresponding to two pathways of decay of the excited states of $AgBi_3S_5$ and Bi_2S_3. The low ($\tau 1$) and high (τ_2) values of life time (Table 2) may correspond to the excited states of $AgBi_3S_5$ and Bi_2S_3 respectively according to the higher and lower coefficient values (a_1 and a_2). The same mixture of catalyst exhibits little change in the high valued life time ($\tau 2$) but almost 3 times increase of low valued life time (τ_1) in presence of dye. Moreover, a_1 is decreased while a_2 is increased. This indicates that the adsorption of dye on the surface of $AgBi_3S_5$ may increase the life time of the excited state of $AgBi_3S_5$ due to energy distribution with the dye molecules. It may be considered as delayed emission of eosin(E) type. The adsorption also decreases the value of the co-efficient a_1 in presence of dye. a_2 is increased significantly due to the fact that the excited dye also can release energy by photoluminescence emission or non-radiating transition releasing electron from its excited state to the valence band of Bi_2S_3 **[32] (Scheme 5.2)**. The absorption of energy by the dye by energy transfer (ET) is evident since the maximum emission of catalyst occurs at 530 nm and maximum absorption of dye occurs at 560 nm. Now after the exposure of the system to visible light, the dye at the surface of the catalyst is decomposed and the catalyst surface becomes relatively open for light absorption and subsequent emission. But only a fraction of the adsorbed surface is now available. So, the decay profile and $\tau 1$ and a_1 values are intermediate

between the corresponding profiles and values obtained when only catalyst remains and when maximum adsorbed catalyst (in absence of dye degradation by light) were present in the solution.

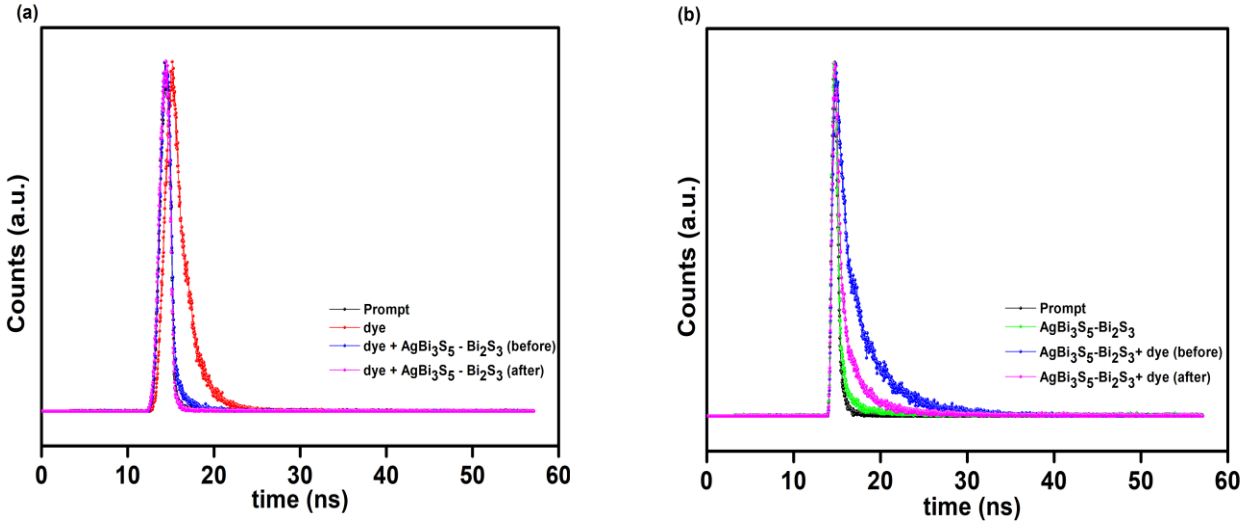

Figure 5.8: (a) Time resolved photoluminescence (TRPL) spectra of 10 ppm Rh-B with $AgBi_3S_5$-Bi_2S_3 (before and after exposure to light along with prompt) at excitation wavelength 550 nm and emission wavelength 580 nm (b) TRPL spectra of $AgBi_3S_5$-Bi_2S_3 with Rh-B (before and after irradiation along with prompt) at excitation wavelength 265 nm and emission wavelength 530 nm.

Table 5.2:

Life time and coefficient values of Dye and $AgBi_3S_5$-Bi_2S_3 after and before exposure to light from Time resolved photoluminescence spectral experiment

System	Condition	Life time τ1 (ns)	Life time τ2 (ns)	Coefficient (a_1)	Coefficient (a_2)
$AgBi_3S_5$-Bi_2S_3	**in absence of dye**	0.345	2.9	0.167	0.004
$AgBi_3S_5$-Bi_2S_3 + dye	**before irradiation**	0.939	3.8	0.044	0.030
$AgBi_3S_5$-Bi_2S_3 + dye	**after irradiation**	0.536	2.9	0.080	0.012
Dye	**in absence of $AgBi_3S_5$-Bi_2S_3**		1.66		0.040
Dye + $AgBi_3S_5$-Bi_2S_3	**before exposure to light**	0.084	1.3	0.369	0.005
Dye + $AgBi_3S_5$-Bi_2S_3	**after exposure to light**	0.064	0.5	0.540	0.006

5.3.9 Effect of characteristic parameters on Photocatalytic degradation of Rhodamine-B:

To identify the best photocatalyst among the newly synthesized photocatalysts, each of Bi_2S_3, $AgBi_3S_5$ and their composite $AgBi_3S_5$-Bi_2S_3 are exposed separately to sunlight keeping the identical condition such as concentration of dye (10 ppm), amount of catalyst (0.7 g L^{-1}) at pH 5. The Rh-B-degradation profile is depicted in **figure 5.10(a)** where C/C_0 versus time plot reveals $AgBi_3S_5$-Bi_2S_3 out performs others, the degradation percentages are 8, 26 and 36 (compare to 1% for without catalyst), for Bi_2S_3, $AgBi_3S_5$ and $AgBi_3S_5$-Bi_2S_3 respectively in 20 minutes. The rate constants (min^{-1}) are 0.001, 0.014 and 0.024 for Bi_2S_3, $AgBi_3S_5$, $AgBi_3S_5$-Bi_2S_3 respectively were shown in **figure 5.12(a)**. The degradation rate compliments the outcome of band gap of respective synthesized catalyst presented in **figure 5.4(b-d)** where $AgBi_3S_5$-Bi_2S_3 has shown lower band gap compare to others and degrade greater percentage. The photoluminescence spectra depicted in **figure 5.5(a)** also synchronize with the above result where lower intensity for $AgBi_3S_5$-Bi_2S_3 with respect to others shows that the separation of charge carriers is improved as a consequence of lower recombination rate which indirectly helps in subsequent increase of the quantum efficiency of the respective photocatalytic reaction.

5.3.9.1 Effect of pH

Now the effect of pH variation is studied with the best photocatalyst ($AgBi_3S_5$-Bi_2S_3) keeping other environment same as it is done at pH 5. The degradation percentage (%) s for pH 1,3,5,7 and 10 are 81, 94, 23, 21, 18 respectively and their associated rate constants (min^{-1}) are 0.023, 0.031, 0.019, 0.013 and 0.008 respectively were shown in **figure 5.12(b)**. The degradation percentage increases from 36 to 94 in 15 minutes and 99 in 20 minutes at pH 3 under natural light illumination (AI 250 × 100 LUX) which is near about 2.8 times better performance in degradation compare to that obtained at pH 5. The catalytic performance was not very significant at very low pH and pH of the solution adjusted by using 1 mol L^{-1} of HCl and NaOH. The outcome of degradation shown in **figure 5.10(b)** signifies that at very low pH increased concentration of Cl^- may play as a scavenger of h^+ and $OH^\bullet$ radical **[46]** and on the other hand when the pH in the basic range, OH^- adsorbed holes to produce $OH^\bullet$ radical which subsequently facilitate H_2O_2 production and plays a role in decomposition of dye **[47].**

5.3.9.2 Effect of catalyst dosage

Variation of catalyst dosage was performed using different concentration of catalyst from 0.3 g L^{-1} to 1.1 g L^{-1} at pH 3. The performance of photocatalytic Rh-B degradation reached at optimum level i.e., 99.5% at concentration 0.7 g L^{-1} which signifies in **figure 5.10 (c)** and the associate rate constant for respective dosages concentration range (0.3, 0.5, 0.7, 0.9 and 1.1 g L^{-1}) are 0.012 min^{-1}, 0.033 min^{-1}, 0.059 min^{-1}, 0.055 min^{-1} and 0.046 min^{-1} respectively were shown in figure **5.12(c)**. The above result signifies that the degradation efficiencies increase at the beginning due to maximum number of reaction sites expose to catalyst surfaces and in the later part the efficacy of catalyst performance decreases with higher concentration because of exposure of light scattering as well as self-quenching of this catalyst molecule at that excited state **[48-51].**

The UV-vis adsorption spectra of degradation of Rh-B at the optimum pH and concentration depicted in **figure 5.10(d**) reveals that the maximum adsorption peak has shifted from 555 nm to 503 nm subsequently with progression of degradation. It indicates that the hypso-chromic shift occurs, which signifies the formation of a N-de-ethylated intermediates in the HRMS profiles **[52,53].**

5.3.9.3 Effect of zeta potential at different pH

The variation of zeta potential (ζ) at different pH is presented in **figure 5.9(e).** (Verified the greater degradation percentage outcome from the pH 3). The values(mV) are 14.5, 8.8, -3.18, -4.47, -15.80, -18.4 for pH 1,2,3,4,5 and 8 respectively, sharp jump of potential is observed between pH 2 to 3 and the respective point of zero charge (PZC) for $AgBi_3S_5$-Bi_2S_3 is nearly 2.95 mV. The PZC value (2.95) being very near to pH (3) it indicates that the surface of $AgBi_3S_5$-Bi_2S_3 becomes almost zero in potential which facilitates the better adsorption of Rh-B dye followed by better electrostatic attraction and also increasing rate of adsorption of Rh-B on the COO^- part of Zwitter ionic part present in Rh-B dye.

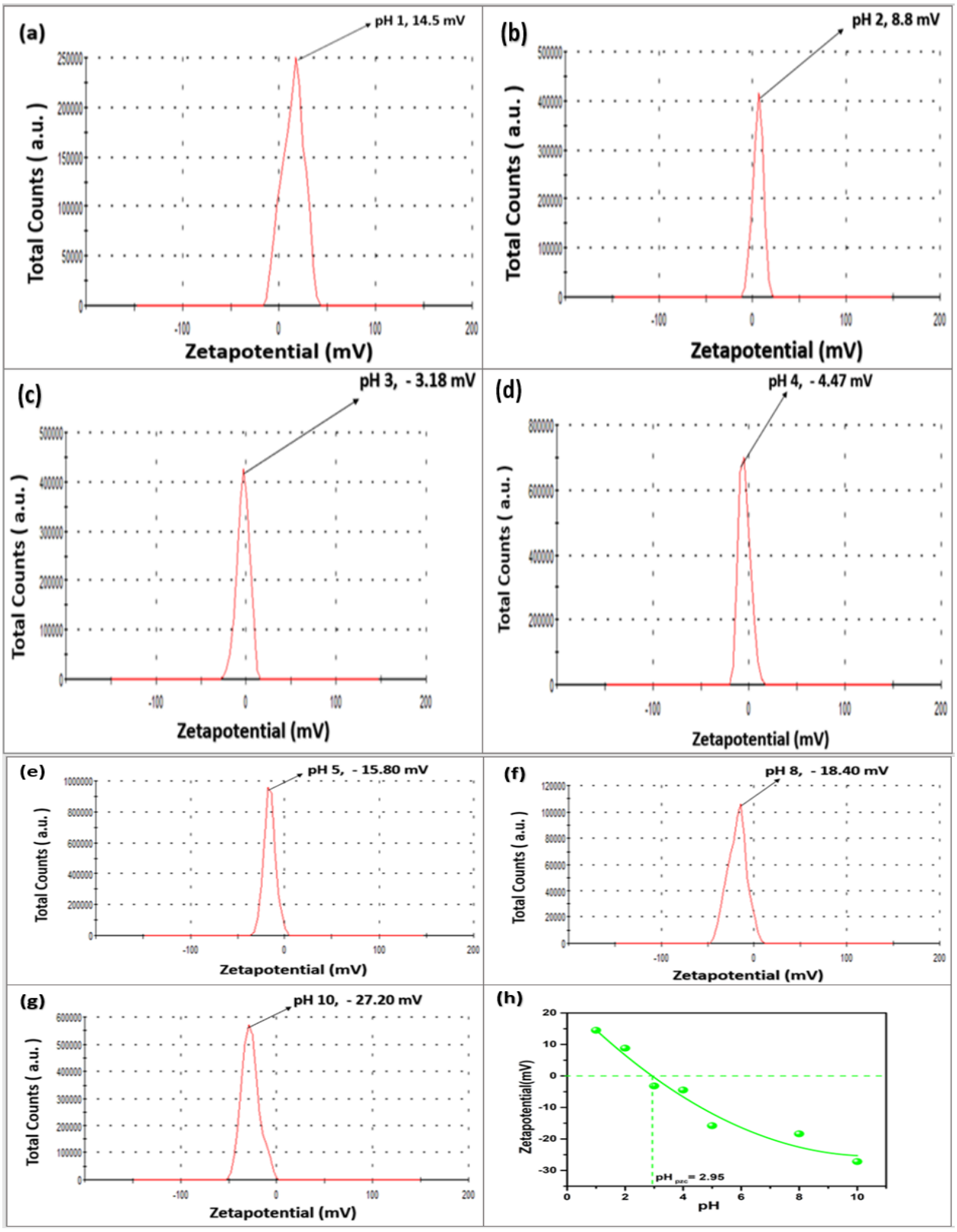

Figure 5.9: (a-g) are Zeta potential plot of different pH 1,2,3,4,5,8, 10 respectively of $AgBi_3S_5$-Bi_2S_3 and (h) represents plot of zeta potential values versus different pH.

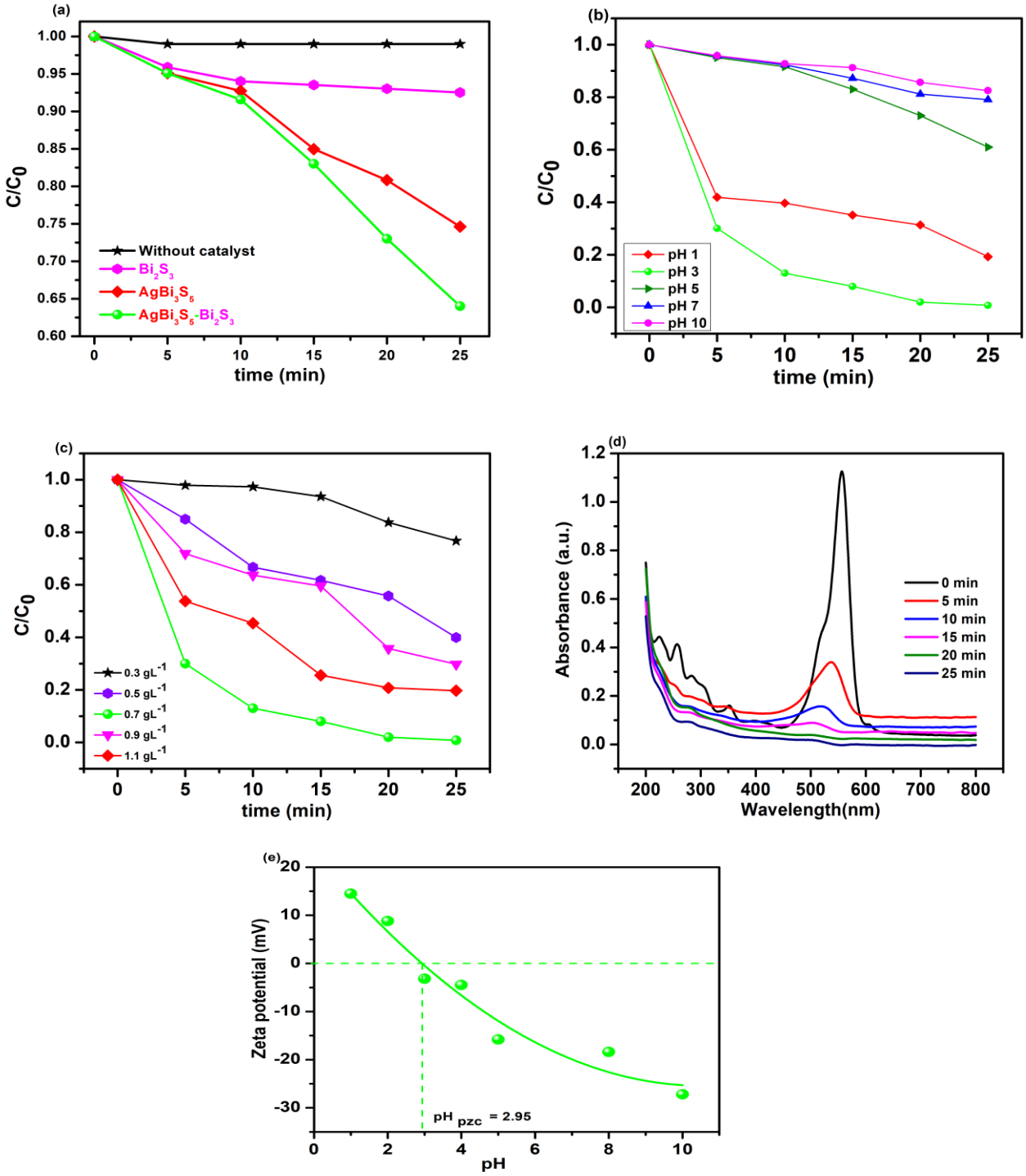

Figure 5.10: (a) Plot of C/C_0 Vs time for Rh-B (10 ppm) without catalyst, Rh-B with Bi_2S_3, $AgBi_3S_5$, $AgBi_3S_5$-Bi_2S_3 photocatalyst (0.7 gL^{-1}) respectively at pH 5 under natural light illumination (AI 250 × 100 LUX) (b) degradation of Rh-B at different pH with 0.7 g L^{-1} by $AgBi_3S$-Bi_2S_3. (c) effect of dosage of $AgBi_3S_5$-Bi_2S_3 at pH 3 (d)UV-vis spectra of Rh-B degradation with $AgBi_3S_5$-Bi_2S_3 (0.7 g L^{-1}) at pH 3. (e) effect of pH on the zeta potential of aqueous solution of $AgBi_3S_5$-Bi_2S_3 at 25°C.

5.3.10 Radical quenching experiments

Radical quenching experiments **[32, 42, 47]** were carried out to detect the photo reactive species and identify the electron transfer mechanism of photocatalytic degradation of Rhodamine-B by $AgBi_3S_5/Bi_2S_3$ n-n heterojunction under natural sunlight exposure. Different radical quencher like Benzo Quinone (BQ), Isopropyl alcohol (IPA), Ethelene-di ammine tetra acetic acid (EDTA) was taken in equal amount (0.1 m mole) as a probe to quench $^{\bullet}O_2^-$, $^{\bullet}OH$ and h^+ respectively. The figure 9 illustrates that the addition of EDTA into the dye severely arrest the degradation and follows the order: EDTA (2.22 %) > PBQ (41 %) > IPA (48 %) > No Scavenger (99.95 %) in 25 min exposure. Therefore, h^+ plays the key role in the degradation over the others.

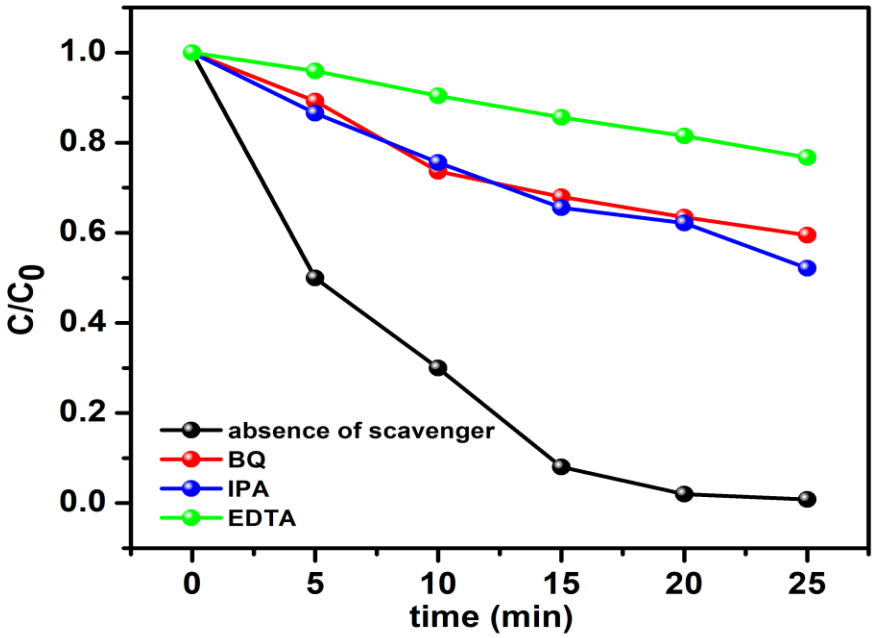

Figure 5.11: Effective contribution of IPA, BQ and EDTA towards photocatalytic degradation of Rhodamine-B under natural sunlight illumination (AI), 250 × 100 lux.

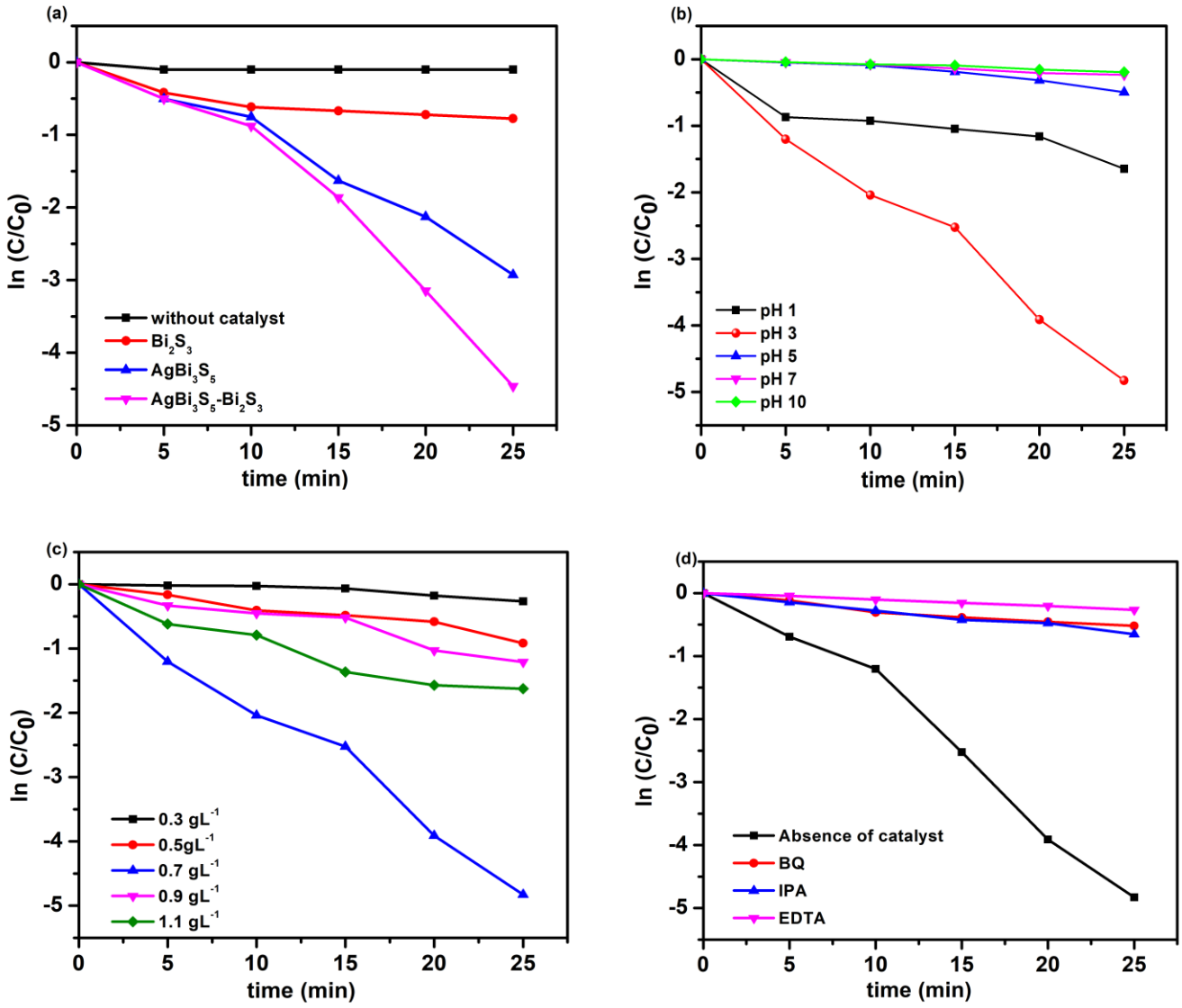

Figure 5.12: (a) Plot of ln C/C_0 vs. time for Rh-B (10 ppm) without catalyst, Rh-B with Bi_2S_3, $AgBi_3S_5$, $AgBi_3S_5$-Bi_2S_3 photocatalyst (0.7 g L^{-1}) respectively at pH 5 under natural light illumination (AI 250 × 100 LUX) (b) ln C/C_0 vs. time for degradation of Rh-B at different pH with 0.7 g L^{-1} by $AgBi_3S$-Bi_2S_3 (c) ln C/C_0 vs. time, effect of dosage of $AgBi_3S_5$-Bi_2S_3 at pH 3 (d) ln C/C_0 vs. time plot of BQ, IPA, BQ and EDTA towards photocatalytic degradation of Rhodamine-B under natural sunlight illumination (AI 250 × 100 LUX).

5.3.11 Mechanism of degradation of Rhodamine-B dye:

The band gap energy of $AgBi_3S_5$ and Bi_2S_3 photocatalyst calculated by Tauc plot of $(\alpha h\upsilon)^2$ Vs $h\upsilon$ (as shown in **figure 5.4**) [43,54] are 1.9 & 2.8 eV respectively. The valance band (VB) and conduction band (CB) edges of $AgBi_3S_5$ and Bi_2S_3 are calculated using following equation:

$$E_{VB} = \chi - Ee + 0.5\ Eg$$

$$E_{CB} = E_{VB} - Eg$$

Where χ is the absolute electronegativity of the semiconductor, obtained by geometric mean of the electronegativity of the constituent atom by the following expression

$\chi = [\ \chi(A).\ a.\ \chi(B).\ b.\ \chi(C).\ C]\ (1/\ (a + b + c))$ where a, b & c are the number of atoms of A, B and C in the semiconductor **[55]** Thus χ values of $AgBi_3S_5$ and Bi_2S_3 are 2.32 eV and 2.80 eV respectively. Top of VBs and bottom of CB values of $AgBi_3S_5$ lies at -1.23 eV and -3.13 eV respectively where same for Bi_2S_3 lies at -0.29 eV & -3 eV.

On the basis of the stated calculation, a schematic representation of band energy levels is presented in **Scheme 5.2** which shows that VB edges of Bi_2S_3 is more positive than that of $AgBi_3S_5$ whereas CB edges of $AgBi_3S_5$ is more negative than Bi_2S_3.

Thus, electron migrate from CB of $AgBi_3S_5$ to CB of Bi_2S_3 while holes migrate from VB of Bi_2S_3 to VB of $AgBi_3S_5$ forming type-II electron transfer mechanism **[56]** but in this mechanism the oxidation ability of holes on $AgBi_3S_5$- Bi_2S_3 photocatalyst was decreased which contradict the trapping experiment. The enhanced degradation rates are further explained by step scheme (S scheme) electron transfer forum. In **Scheme 2**, it can be exhibited that electron moves from CB of Bi_2S_3 to VB of $AgBi_3S_5$ by columbic attraction which restricts the electrons in the CB of $AgBi_3S_5$ and holes in VB of Bi_2S_3. Thus, S-scheme heterojunction displays significant separation of photo generated e^-- h^+ pairs & superiority in the inhibition of charge recombination **[57]** The electron in CB of $AgBi_3S_5$ reduce O_2 to $O_2^{\bullet -}$ and produce $O_2^{\bullet -}$ where in the VB, h^+ & $OH^\bullet$ generated that is ($h^+ + OH^- \longrightarrow OH^\bullet$) oxidizes Rh-B dye to CO_2 and H_2O which consistent with the result of trapping experiment.

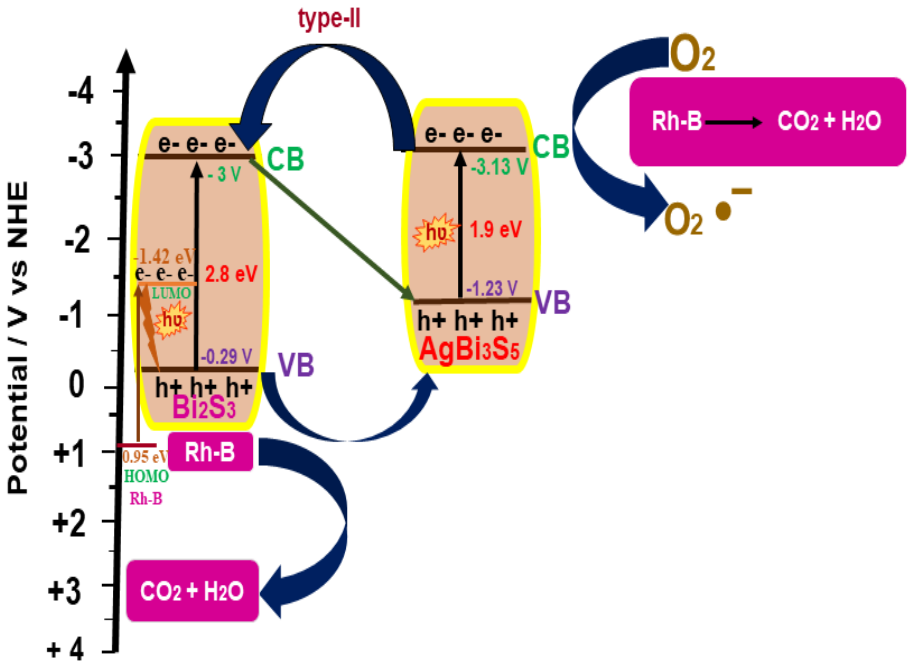

Scheme 5.2: Schematic illustration of photocatalytic degradation mechanism of Rh-B through n-n type $AgBi_3S_5$-Bi_2S_3 heterojunction under natural sunlight.

5.3.12 Identification of degradation product of Rh-B:

HR-MS study **(Figure 5.13)** reveals the intermediate product during the oxidation of Rh-B dye and the subsequent intermediates are A (m/z = 389), B (m/z = 372), C (m/z = 372) and J are formed due to N-de-ethylation product of Rh-B. The P_{ZC} value of $AgBi_3S_5$-Bi_2S_3 photocatalyst is 2.95, obtained from the zeta potential experiment which is less than pH 3, the observance implies that, the surface of catalyst negatively charged. Therefore, the negatively charged photocatalyst helps to adsorb the positively charged di-ethylamine group of Rh-B owing to electro static attraction **[47].** The formation of N-de-ethylation products were also supporting from the absorption spectra where successive shift of absorption maxima i.e., Hypso-chromic shift observed of Rh-B dye from 555 nm to 509 nm. The intermediates, E (m/z = 274), F (m/z = 212), G (m/z = 208), H (m/z = 208), I (m/z = 59) formed due to ring cleavage and oxidizing reaction via the attack of h^+ and $O_2^{\bullet-}$ on Rh-B dye.

The intermediates, B & C were the isomeric in the de-ethylation product of Rh-B and G was isomerized to obtain intermediates H. The above observance and their subsequent explanation led to two probable pathways on which Rh-B dye degradation passes through, one is N-de ethylation and another one is ring cleavage, the final out come from the degradation were CO_2 and H_2O [**32**, **47, 58-60**].

The two types of products of degradation, namely de-ethylation and ring cleavage presented in **scheme 5.3** indicate simultaneous absorption of sunlight by Rh-B and the catalyst and both photo-sensitization by Rh-B and catalyst excitation are responsible for degradation, as explained in our earlier study with other materials **[32].**

The reaction steps involved in this photocatalytic degradation of Rh-B are as following

Path-1

$$\text{Rh-B} + h\upsilon \longrightarrow \text{Rh-B}^*$$

$$\text{Rh-B}^* \longrightarrow \text{Rh-B}^{\bullet +} + \text{N-dethylated products}$$

Path-2

$$AgBi_3S_5 - Bi_2S_3 + h\upsilon \longrightarrow AgBi_3S_5\,(e^-) + Bi_2S_3\,(h^+)$$

$$Bi_2S_3\,(h^+) + \text{Rh-B} \longrightarrow CO_2 + H_2O$$

$$AgBi_3S_5\,(e\text{-}) + O_2 \longrightarrow O_2^{\bullet -}$$

$$O_2^{\bullet -} + \text{Rh-B} \longrightarrow CO_2 + H_2O + \text{Other carbonaceous products}$$

Here both the Bi based compounds are n-type in nature as their valence and conduction band potentials are both below zero in the standard hydrogen scale. From this one can expect that their electrons in the conduction bands have relatively higher energy so that they can effectively produce $^{\bullet}O_2^-$ radical for degradation. Moreover, the hole, h^+ in these materials is relatively stable, so it is easily produced in large number and can subsequently react with H_2O to produce $^{\bullet}OH$ that oxidizes Rh-B according to the equations:

$$h^+ + H_2O \longrightarrow H^+ + {}^{\bullet}OH$$

$$^{\bullet}OH + \text{Rh-B} \longrightarrow CO_2 + H_2O + \text{Other carbonaceous products}$$

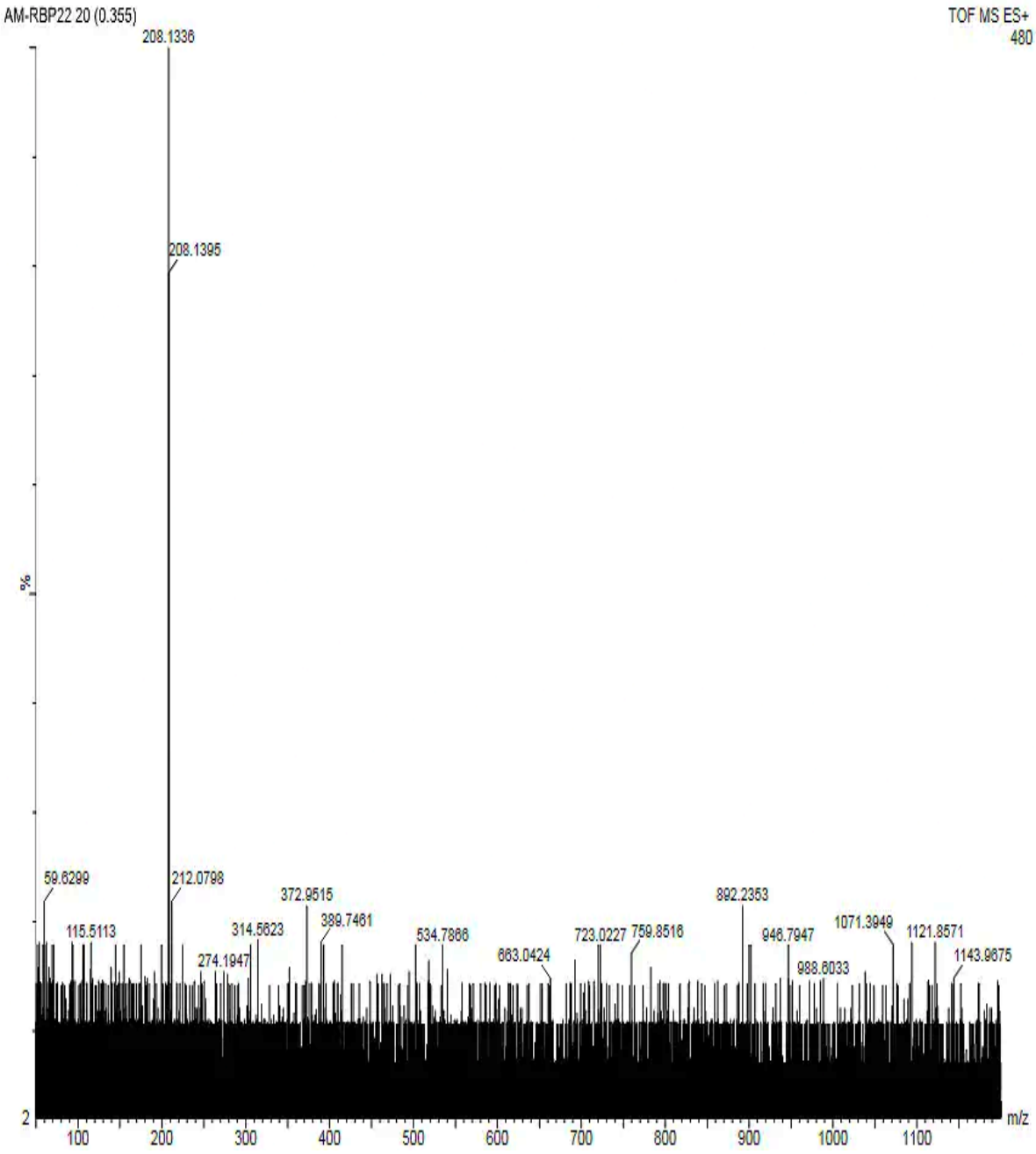

Figure 5.13: Mass spectrum (HRMS) of degradation product of Rhodamine- B dye.

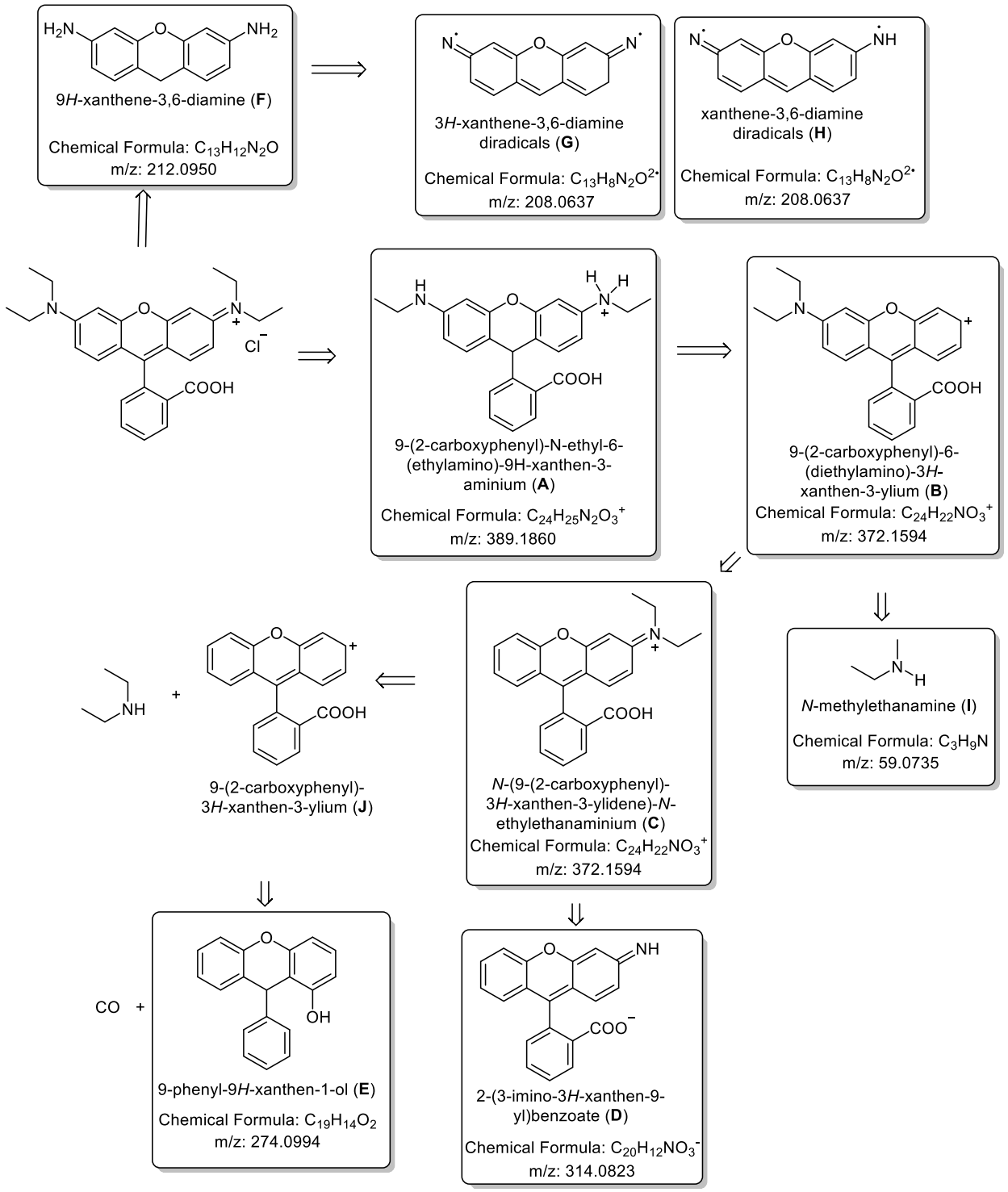

Scheme 5.3: The possible fragmentation of product formed from the Rhodamine-B degradation with $AgBi_3S_5$-Bi_2S_3 under natural sunlight.

5.3.13 Reusability and fate of photocatalyst:

To justify the reusability of the synthesized $AgBi_3S_5$-Bi_2S_3 photocatalyst towards degradation of Rh-B under natural sunlight, the used catalyst of the reaction mixture was collected after centrifugation followed by washing with water and alcohol for several times and then dried in a hot air oven at 70 ˚C. Then the procedure of kinetic measurements was repeated followed by the same experimental purification treatment for each of 5th times. The **figure 5.15(a)** represents the degradation profiles of the photocatalyst used at different extents(cycles). The profiles reveal that the degradation efficiency decreases by only about 5% after 5th cycle of operation of the used of photocatalyst. This is plausibly due to loss of very little amount of catalyst during washing after each cycle. (Completed which may be the probable reason to bring modification in pores of the photocatalyst.) The fate of the catalyst was investigated after collecting the catalyst at the end of 5th cycle of the degradation using XRD, FTIR, BET and FESEM techniques. The XRD study of the used catalyst reveals in **figure 5.15(b)** that the planes (113), (310), (312), (403), (313), (314), (405), (007), (116) arise at the corresponding 2Θ values (°): 28.53, 29.92, 31.39, 32.52, 34.913, 36.430, 37.165, 38.447, 40.82 respectively. The most intense peak designated by (312) matches well in XRD profiles of synthesized and used catalyst. But most of other peaks are shifted towards higher angle which might be due to the tensile strain of the catalyst arising by irradiation. It might be also due to mixing or/and adsorption of dye and its fragments/products (which can't be removed by washing several times with water and alcohol) on the catalyst surface and the change of the morphology of the catalytic surface, which is normally responsible for the change in the relative intensity of the peak. Besides, a new peak marked -by* is also developed here at 2Θ value of 46.9° corresponding to 112 planes of orthorhombic Bi_2S_3 demonstrating the change of morphology of the catalyst during the photochemical reaction. Since several differences are found in XRD profiles of the catalyst mixture before and after use, the stability of them cannot be overstated at the present stage of the study. More detail and sophisticated studies which include in-situ dynamics study are necessary for that. **Figure 5.15(c)** exhibits all the characteristic vibration modes of used $AgBi_3S_5$-Bi_2S_3, which are present in the FTIR profiles of synthesized mixed catalyst. The surface area and the corresponding average pore diameter found for the photocatalyst before degradation were 25.79 m^2/g and 5.29 nm respectively from the N_2 adsorption-desorption isotherm where after degradation the surface area became 31.77 m^2/g and the respective pore diameter 5.45 nm. The enhancement of the surface area and pore diameter as presented in **figures 5.15(d-e)** reflect that

the pores become more open due to the movement of the reactants to the catalyst surface along with the subsequent washing of the used catalyst for several times with water and alcohol to remove the adsorb dye and products from the surface of the photocatalyst after degradation. The above experimental evidence complements the catalyst fate remaining almost same even after 5th cycle of degradation.

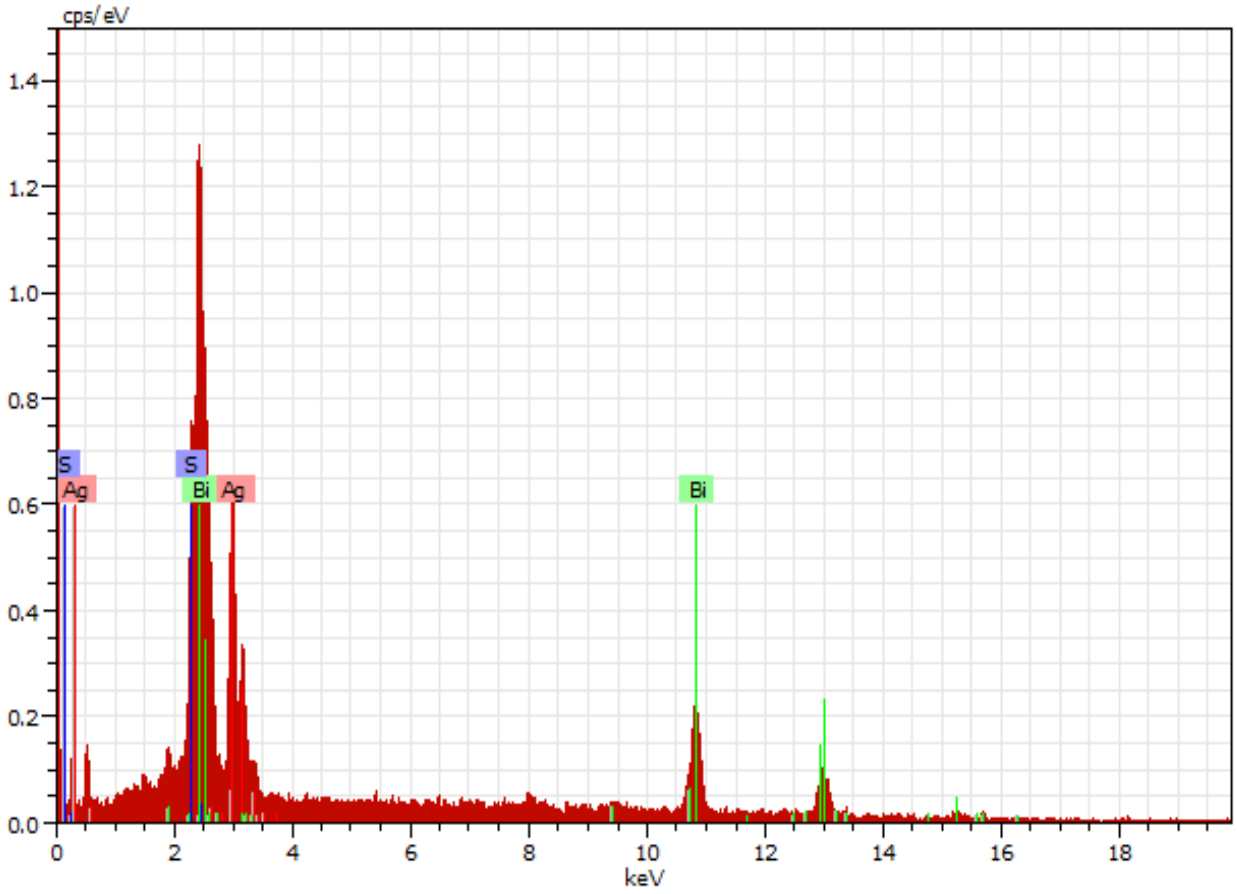

Figure 5.14: EDS spectrum of $AgBi_3S_5$-Bi_2S_3 after degradation.

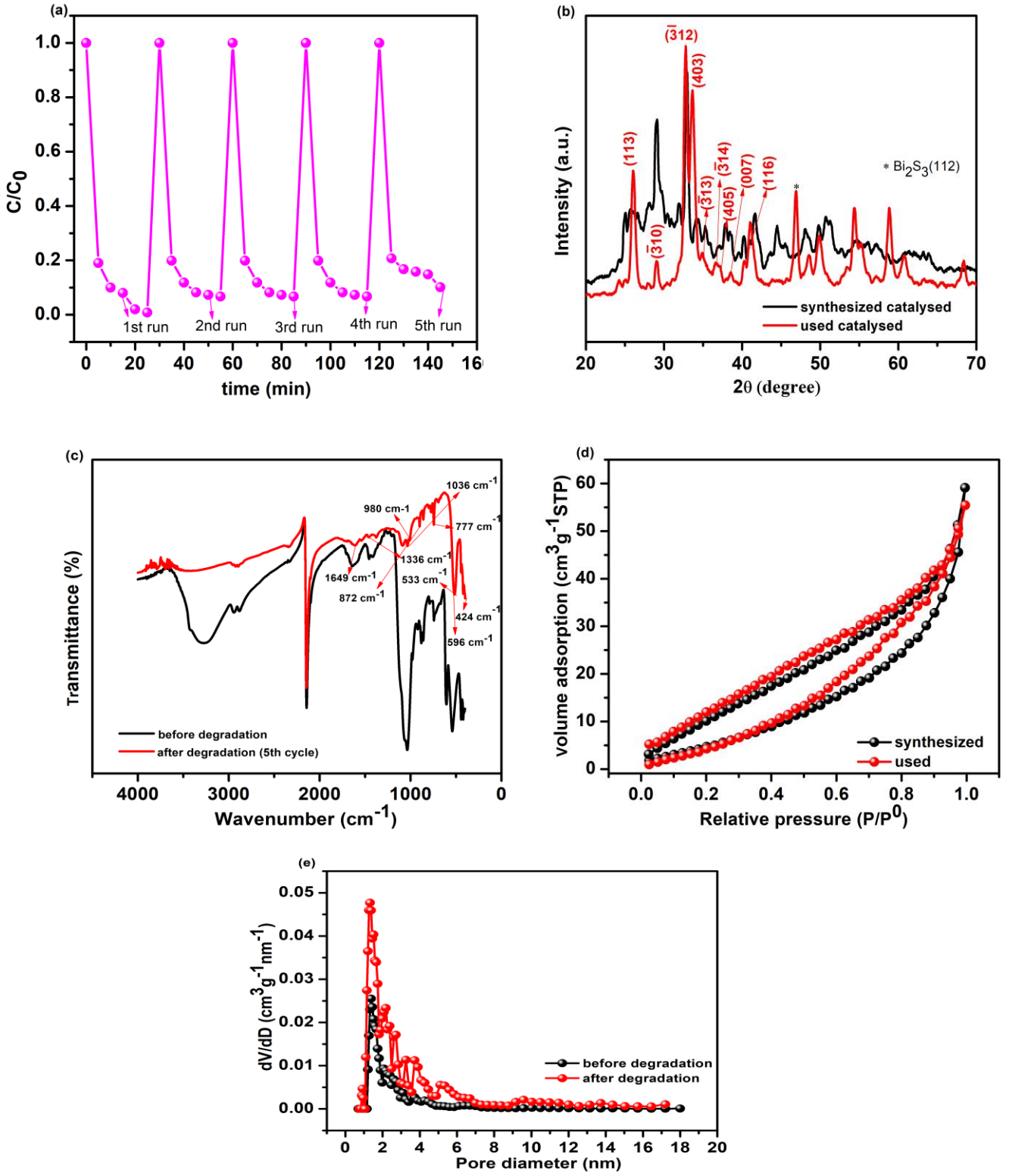

Figure 5.15: (a) Robustness of photo-catalytic efficacy of $AgBi_3S_5/Bi_2S_3$ (0.7 g L^{-1}) under natural sunlight exposure (AI= 250×100 lux) in 10 ppm) Rh-B solution at pH 3 even after 5th cycle of degradation (b-e) represent the fate of photo-catalyst using analyzing tools like XRD, FTIR, N_2 adsorption-desorption isotherm, pore size distribution respectively with this used $AgBi_3S_5$-Bi_2S_3 after 5th cycle of catalytic run.

5.4 Conclusions:

Nano spheres of monoclinic $AgBi_3S_5$, nanorods of orthorhombic Bi_2S_3 and their nanocomposite were separately synthesized in glycolic medium by hot chemical process at 90 °C. Diffraction, spectrophotometric and microscopic studies reveal that the synthesized particles have average dimensions below 10 nm. All the synthesized catalysts exhibit significant photocatalytic degradation of pollutant dye Rh-B at pH 3 where optimum adsorption of dye is expected to occur. Among the catalysts, the nanocomposite of $AgBi_3S_5$-Bi_2S_3 display excellent and synergistic catalytic activity. With it the degradation of Rh-B is almost (99.99%) completed on exposure to natural sunlight within 25 minutes at pH 3 using 0.7 g L^{-1} of the catalyst in the dye solution (10 ppm). The degradation efficiency is somewhat better or comparable among the S based catalysts found in the literature. The superiority of the catalyst might be due to judicious synthesis of two n-type semiconductors whose valence and conduction band potentials are above zero in the standard hydrogen scale and suitable for charge separation through z-scheme and S-S transition, which help charge separation and generation of photo-catalytically active radicals: $^{\bullet}O_2^-$ and $^{\bullet}OH$, responsible for degradation. The retention of 95% catalytic activity after 5th cycle of operation, might be due to modification of the morphology with an increase of porosity and surface area of the catalyst. The identified products reveal simultaneous de-ethylation and ring-opening reactions. The study may open new strategy for getting very highly efficient mixed catalyst.

References

1. UNW-DPAC. Challenges and Opportunities for Water in the Transition to a Green Economy, UN-Water Conference 'Water in the Green Economy in Practice: Towards Rio, Zaragoza, Spain; UN-Water Decade Programme on Advocacy and Communication, Ed. UNDESA (United Nations Department of Economic and Scoial Affairs), Water for Life, UN-WATER: Zaragoza, Spain, **2011**.
2. Siddiqui, S. I.; & Chaudhry, S. A. Nanohybrid composite Fe2O3-ZrO2/BC for inhibiting the growth of bacteria and adsorptive removal of arsenic and dyes from water. Journal of cleaner production. **2019**, 223, 849-868.
3. Siddiqui, S. I.; Manzoor, O.; Mohsin, M.; & Chaudhry, S. A. Nigella sativa seedbased nanocomposite-MnO2/BC: An antibacterial material for photocatalytic degradation, and adsorptive removal of Methylene blue from water. Environmental research. **2019**, 171, 328-340.
4. Water Scarcity Drafting Group Water Scarcity Management in the Context of WFD; MED Joint Process WFD /EUWI, **2006**
5. Vandevivere, P. C.; Bianchi, R.; Verstraete, W. Treatment and reuse of wastewater from the textile wet-processing industry: Review of emerging technologies. J. Chem. Technol. Biotechnol. **1998**, 72 (4), 289−302.
6. Sundar, V.; Gnanamani, A.; Muralidharan, C.; Chandrababu, N. K.; Mandal, A. B. Recovery and utilization of proteinous wastes of leather making: a review. Rev. Environ. Sci. Bio/Technol. **2011**, 10 (2), 151−163.
7. Pereira, L.; & Alves, M. Dyes—environmental impact and remediation. Environmental protection strategies for sustainable development. **2012**, 111-162.
8. Saratale, R. G.; Saratale, G. D.; Chang, J. S.; Govindwar, S. P. Bacterial decolorization and degradation of azo dyes: A review. J. Taiwan Inst. Chem. Eng. **2011**, 42 (1), 138−157.
9. Shivaraju, H. P.; Yashas, S. R.; & Harini, R. Application of Mg-doped TiO2 coated buoyant clay hollow-spheres for photodegradation of organic pollutants in wastewater. Materials Today: Proceedings. **2020**, 27, 1369-1374.
10. Mao, M.; Chen, F.; Zheng, C.; Ning, J.; Zhong, Y.; Hu, Y. Facile Synthesis of Porous Bi2 O3-BiVO4 P-n Heterojunction Composite Microrods with Highly Efficient Photocatalytic Degradation of Phenol. J. Alloys Compd. **2016**, 688, 1080–1087.

11. Peng, H.; & Guo, J. Removal of chromium from wastewater by membrane filtration, chemical precipitation, ion exchange, adsorption electrocoagulation, electrochemical reduction, electrodialysis, electrodeionization, photocatalysis and nanotechnology: a review. Environmental Chemistry Letters. **2020**, 18, 2055-2068.
12. Ochedi, F. O.; Liu, D., Yu, J.; Hussain, A.; & Liu, Y. Photocatalytic, electrocatalytic and photoelectrocatalytic conversion of carbon dioxide: a review. Environmental Chemistry Letters. **2021**, 19, 941-967.
13. Akhil, D.; Lakshmi, D.; Senthil Kumar, P.; Vo, D. V. N.; & Kartik, A. Occurrence and removal of antibiotics from industrial wastewater. Environmental chemistry letters. **2021**, 19, 1477-1507.
14. Xia, L.; Bai, J.; Li, J.; Zeng, Q.; Li, L.; Zhou, B. High-Performance BiVO4 Photoanodes Cocatalyzed with an Ultrathin α-Fe2O3 Layer for Photoelectrochemical Application. Appl. Catal. B Environ. **2017**, 204, 127–133.
15. Zhang, K.; Deng, J.; Liu, Y.; Xie, S.; & Dai, H. Photocatalytic removal of organics over BiVO4-based photocatalysts. In Semiconductor photocatalysis-materials, mechanisms and applications. IntechOpen. **2016**.
16. Khalid, N. R.; Majid, A.; Tahir, M. B.; Niaz, N. A.; Khalid, S. Carbonaceous-TiO2 Nanomaterials for Photocatalytic Degradation of Pollutants: A Review. Ceram. Int. **2017**, 43(17), 14552–14571.
17. Guo, Y.; Qi, P. S.; and Liu, Y. Z. A Review on Advanced Treatment of Pharmaceutical Wastewater. IOP Conference Series: Earth and Environmental Science, International Conference on Environmental and Energy Engineering (IC3E 2017) 22–24 March 2017, Suzhou, China. **2017**, 63, 012025.
18. Wu, Q.; Han, R.; Chen, P.; Qi, X.; Yao, W. Novel Synthesis and Photocatalytic Performance of BiVO4 with Tunable Morphologies and Macroscopic Structures. Mater. Sci. Semicond. Process. **2015**, 38, 271–277.
19. Zhao, Y.; Tao, C.; Xiao, G.; Su, H. Controlled Synthesis and Wastewater Treatment of Ag 2 O/TiO 2 Modified Chitosan-Based Photocatalytic Film. RSC Adv. **2017**, 7(18), 11211–11221.

20. Wang, Y.; Long, Y.; Zhang, D. Novel Bifunctional V2O5/BiVO4 Nanocomposite Materials with Enhanced Antibacterial Activity. J. Taiwan Inst. Chem. Eng. **2016**, 68, 387–395.
21. Liu, B.; Fang, Y.; Li, Z.; Xu, S. Visible-Light Nanostructured Photocatalysts—A Review. J. Nanosci. Nanotechnol. **2015**, 15(2), 889–920.
22. Wang, Y.; Long, Y.; Zhang, D. Novel Bifunctional V2O5/BiVO4 Nanocomposite Materials with Enhanced Antibacterial Activity. J. Taiwan Inst. Chem. Eng. **2016**, 68, 387–395.
23. Zhang, K.; Guo, L. Metal sulphide semiconductors for photocatalytic hydrogen production. Catal Sci Technol. **2013**, 3,1672–1690.
24. Zhang, J.; Wageh, S.; Al-Ghamdi, AA.; Yu, J. New understanding on the different photocatalytic activity of wurtzite and zincblende CdS. Appl Catal b Environ. **2016**, 192,101–107.
25. Begum, S.; Ranjan Mishra, S.; Ahmaruzzaman, M. Facile synthesis of NiO-SnO2 nanocomposite for enhanced photocatalytic degradation of bismarck brown. Inorg Chem Commun. **2022**, 143,109721.
26. Wang, L.; Zhu, B.; Zhang, J.; Ghasemi, J. B.; Mousavi, M.; & Yu, J. S-scheme heterojunction photocatalysts for CO2 reduction. Matter. **2022**, 5(12), 4187-4211.
27. Zhen, Y.; Yang, C.; Shen, H.; Xue, W.; Gu, C.; Feng, J.; ... & Liang, Y. Photocatalytic performance and mechanism insights of a S-scheme gC 3 N 4/Bi 2 MoO 6 heterostructure in phenol degradation and hydrogen evolution reactions under visible light. Physical Chemistry Chemical Physics. **2020**, 22(45), 26278-26288.
28. Zhang, J.; Wang, L.; Mousavi, M.; Ghasemi, J. B.; & Yu, J. Molecular-level engineering of S-scheme heterojunction: the site-specific role for directional charge transfer. Chinese Journal of Structural Chemistry. **2022**, 41(6), 2206003-2206005.
29. Ren, Y.; Li, Y.; Wu, X.; Wang, J.; & Zhang, G. S-scheme Sb2WO6/g-C3N4 photocatalysts with enhanced visible-light-induced photocatalytic NO oxidation performance. Chinese Journal of Catalysis. **2021**, 42(1), 69-77.
30. He, R.; Ou, S.; Liu, Y.; Liu, Y.; & Xu, D. In situ fabrication of Bi2Se3/g-C3N4 S-scheme photocatalyst with improved photocatalytic activity. Chinese Journal of Catalysis. **2022**,43(2), 370-378.

31. Benaissa, M.; Abbas, N.; Al Arni, S.; Elboughdiri, N.; Moumen, A.; Hamdy, M. S.; ... & Ahmed, M. A. BiVO3/g-C3N4 S-scheme heterojunction nanocomposite photocatalyst for hydrogen production and amaranth dye removal. Optical Materials. **2021**,118, 111237.
32. Bera, K. K.; Chakraborty, M.; Mondal, M.; Banik, S.; & Bhattacharya, S. K. Synthesis of α-β Bi2O3 heterojunction photocatalyst and evaluation of reaction mechanism for degradation of RhB dye under natural sunlight. Ceramics International. **2020**, 46(6), 7667-7680.
33. S, Sugarthi.; G, Bakiyaraj.; R, Abinaya.; M, Navaneethan.; J, Archana.; M, Shimomura. Effect of different growth temperature on the formation of ternary metal chalcogenides AgBiS2, Mater. Sci. Semicond. Process. **2020**, 107, 104781.
34. Kim, Y-Y.; Walsh, D. Metal sulfide nanoparticles synthesized via enzyme treatment of biopolymer stabilized nanosuspensions. Nanoscale. **2010**, 2(2):240–7.
35. Wu, D.; Jiang, Y.; Yuan, Y.; Wu, J.; Jiang, K. ZnO–ZnS heterostructures with enhanced optical and photocatalytic properties. J Nanoparticle Res **2011**,13(7):2875–86.
36. NIST X-ray Photoelectron Spectroscopy Database https://srdata. nist.gov/xps/Default.aspx, **2012.**
37. Bernechea, M.; Miller, N. C.; Xercavins, G.; So, D.; Stavrinadis, A.; Konstantatos, G. Solution-processed solar cells based on environmentally friendly AgBiS2 nanocrystals. Nat. Photonics. **2016**, 10, 521.
38. Pai, N.; Lu, J.; Senevirathna, D. C.; Chesman, A. S. R.; Gengenbach, T.; Chatti, M.; Bach, U.; Andrews, P. C.; Spiccia, L. Cheng, Y.-B.; Simonov, A. N. Spray deposition of AgBiS2 and Cu3BiS3 thin films for photovoltaic applications. J. Mater. Chem. C. **2018**, 6, 2483−2494.
39. Cheng, W.; Guan, W.; Lin, Y.; Lu, C. Rapid Discrimination of Adsorbed Oxygen and Lattice Oxygen in Catalysts by the Cataluminescence Method. Anal. Chem. **2022**, 94, 1382−1389.
40. Bai, P.; Tong, X.; Wan, J.; Gao, Y.; Xue, S. Flower-Like Bi2O2CO3-Mediated Selective Oxidative Coupling Processes of Amines Under Visible Light Irradiation. J. Catal. **2019**, 374, 257−265.
41. Esmaili-Hafshejani, J.; & Nezamzadeh-Ejhieh, A.; Increased photocatalytic activity of Zn (II)/Cu (II) oxides and sulfides by coupling and supporting them onto clinoptilolite

nanoparticles in the degradation of benzophenone aqueous solution. Journal of hazardous materials. **2016**, 316, 194-203.

42. Derikvandi, H.; & Nezamzadeh-Ejhieh, A.; Increased photocatalytic activity of NiO and ZnO in photodegradation of a model drug aqueous solution: effect of coupling, supporting, particles size and calcination temperature. Journal of hazardous materials. **2017**, 321, 629-638.
43. Tan, G.; Hao, S.; Zhao, J.; Wolverton, C.; and Kanatzidis, M.G. High thermoelectric performance in electron-doped AgBi3S5 with ultralow thermal conductivity. Journal of the American Chemical Society. **2017**, 139(18),6467-6473.
44. Qian, X.; Zhang, X.; Guo, H.; Ding, B.; Chen, M.; Wang, J.L.; Zhao, L.D.; and Wang, S.F. Enhancing thermoelectric performance of n-type AgBi3S5 through synergistically optimizing the effective mass and carrier mobility. Journal of Materiomics. **2023**, 9, 874-881.
45. Helal, A.; Harraz, F. A.; Ismail, A. A.; Sami, T. M.; & Ibrahim, I. A. Controlled synthesis of bismuth sulfide nanorods by hydrothermal method and their photocatalytic activity. Materials & Design. **2016**, 102, 202-212.
46. Shi, Y.; Luo, L.; Zhang, Y.; Chen, Y.; Wang, S.; Li, L.; ... & Jiang, F. Synthesis and characterization of α/β-Bi2O3 with enhanced photocatalytic activity for 17α-ethynylestradiol. Ceramics International. **2017**, 43(10), 7627-7635.
47. Bera, K. K.; Majumdar, R.; Chakraborty, M.; & Bhattacharya, S. K. Phase control synthesis of α, β and α/β Bi2O3 hetero-junction with enhanced and synergistic photocatalytic activity on degradation of toxic dye, Rhodamine-B under natural sunlight. Journal of hazardous materials. **2018**, 352, 182-191.
48. Sood, S.; Umar, A.; Mehta, S. K.; & Kansal, S. K. α-Bi2O3 nanorods: An efficient sunlight active photocatalyst for degradation of Rhodamine B and 2, 4, 6-trichlorophenol. Ceramics International. **2015**, 41(3), 3355-3364.
49. Kou, T.; Jin, C.; Zhang, C.; Sun, J.; & Zhang, Z. Nanoporous core–shell Cu@ Cu 2 O nanocomposites with superior photocatalytic properties towards the degradation of methyl orange. RSC advances. **2012**, 2(33), 12636-12643.

50. Mohammadyari, P.; & Nezamzadeh-Ejhieh, A. Supporting of mixed ZnS–NiS semiconductors onto clinoptilolite nano-particles to improve its activity in photodegradation of 2-nitrotoluene. Rsc Advances. **2015**, 5(92), 75300-75310.
51. Pouretedal, H. R.; Norozi, A.; Keshavarz, M. H.; & Semnani, A. Nanoparticles of zinc sulfide doped with manganese, nickel and copper as nanophotocatalyst in the degradation of organic dyes. Journal of hazardous materials. **2009**, 162(2-3), 674-681.
52. Watanabe, T.; Takizawa, T.; & Honda, K. Photocatalysis through excitation of adsorbates. 1. Highly efficient N-deethylation of rhodamine B adsorbed to cadmium sulfide. The Journal of Physical Chemistry. **1977**, 81(19), 1845-1851.
53. Takizawa, T.; Watanabe, T.; & Honda, K. Photocatalysis through excitation of adsorbates. 2. A comparative study of Rhodamine B and methylene blue on cadmium sulfide. The Journal of Physical Chemistry. **1978**, 82(12), 1391-1396.
54. Liu, X. C.; & Yang, M. Enhanced thermoelectric performance of AgBi 3 S 5 by antimony doping. Rare Metals. **2020**, 39, 289-295.
55. Bera, K. K.; Chowdhury, A.; Bera, S. K.; Das, M. R.; Bhattacharya, S. K. Pd Nanoparticle-Decorated Novel Ternary Bi2O2CO3 Bi2MoO6 CuO Heterojunction for Enhanced Photo-electrocatalytic Ethanol Oxidation. **2023**.
56. Yong, Z. J.; Lam, S. M.; Sin, J. C.; Mohamed, A. R.; Zeng, H.; Li, H.; ... & Lim, J. W. Incorporating photocatalytic fuel cell with dual S-scheme CuBi2O4/Bi2WO6/ZnO NRA photoanode for energy recuperation from municipal wastewater treatment under sunlight. Journal of Environmental Chemical Engineering. **2024**, 12(1), 111606.
57. Xu, Q.; Zhang, L.; Cheng, B.; Fan, J.; & Yu, J. S-scheme heterojunction photocatalyst. Chem. **2020**, 6(7), 1543-1559.
58. Chakraborty, M.; Bera, K. K.; Chatterjee, S.; Bhattacharya, S. K. Synthesis of mesoporous BiOI flower and facile in situ preparation of BiOI/BiOCl mixture for enhanced photocatalytic degradation of toxic dye, Rhodamine B, J. Photochem. Photobiol. **2021**, 8, 100077.
59. Barzegar, M. H.; Sabzehmeidani, M. M.; Ghaedi, M.; Avargani, V. M.; Moradi, Z.; Roy, V. A.; & Heidari, H. S-scheme heterojunction g-C3N4/TiO2 with enhanced photocatalytic activity for degradation of a binary mixture of cationic dyes using solar parabolic trough reactor. Chemical Engineering Research and Design. **2021**, 174, 307-318.

60. Li, W.; Wang, Z.; Li, Y.; Ghasemi, J. B.; Li, J.; & Zhang, G. Visible-NIR light-responsive 0D/2D CQDs/Sb2WO6 nanosheets with enhanced photocatalytic degradation performance of RhB: Unveiling the dual roles of CQDs and mechanism study. Journal of Hazardous Materials. **2022**, 424, 127595.

Chapter 6

Conclusion and future Prospects

CHAPTER 6

6.1 Conclusions

Our main goal as stated in the thesis title has been objectified with our findings. All the findings complement each other's in terms of catalytic efficacy in electrochemical, photochemical and photoelectrochemical applications and the outcomes throw light on the path is relatively mitigate the adverse effects of energy consumption to maintain environmental sustainability.

In chapter 2, hydrogen evolution reaction with newly synthesized $AgBi_3S_5$ catalyst was demonstrated.

In the study, we designed a new time-efficient environment-friendly synthesis route to prepare a low-cost, free-of-toxic element, versatile sulfur-based ternary bismuth chalcogenide, $AgBi_3S_5$ as ABS nano catalyst for mainly hydrogen evolution reaction. Ag and Bi compounds possess low band gaps. So, charge separation and availability of electrons for reduction are easy. The presence of two nuclei causes the molecule to be more defective in the nature of the crystal and S vacancy develops, which is responsible for greater H^+ adsorption required for HER. S possesses a slightly negative charge compared to Ag and Bi in the compounds. Due to S vacancy conduction capabilities of Ag and Bi increase. Moreover, greater S vacancy in ABS (due to the presence of two atoms of different sizes and valency) compared to AS and BS, causes S to become the potential centers of H^+ adsorption in ABS. So, a synergistic effect is found between Ag, Bi, and S. This study further advances the knowledge in this particular field. Following the same synthesis procedure, we also prepared Ag_2S as (AS), Bi_2S_3 as (BS), and $CuBiS_2$ as (CBS). Here in this study, $AgBi_3S_5$ was chosen because $AgBi_3S_5$ is quite stable and it occurs in nature as a pavonite mineral compared to the other intermates of Ag_2S and Bi_2S_3.In general, $CuBiS_2$ was chosen which are new compound in this application along with another specification as Cu is present in the same period of Ag and mixed catalysts often show synergistic behavior. It may also contain more defects and S-vacancies which will enhance the catalytic capabilities of synthesized materials. Pertaining to this investigation, it is explored that ABS performed better as a catalyst compared to others in an electrochemical hydrogen evolution reaction.

Nanoparticles of different sulfides like Ag_2S, Bi_2S_3, and particularly their composites $AgBi_3S_5$, and another variant $CuBiS_2$ are synthesized for the first time by similar facile liquid phase hot chemical treatments and are used as catalysts also for the first time for electrochemical hydrogen evolution reaction in aqueous acid solution and are characterized by various microscopic and

spectroscopic techniques. Amongst the various catalysts developed (such as ABS, AS, BS, and CBS), ABS shows the lowest overpotential value of 47 mV and the lowest Tafel slope value of 75.99 mV/dec compared to others. The catalytic capability of the synthesized materials follows the sequence: ABS > AS > BS > CBS which are in the same order as that of the electrochemical surface area of the materials and EIS values. ABS is a quite stable compound as confirmed from the post studies of the catalyst. Thus, at room temperature more charge separation, conductivity, and S vacancy are expected. These may increase H^+ adsorption. So, it shows more electrochemical surface area than others. Moreover, Bi of ABS may upshift the Centre of the d-band in ABS. Hence the desorption of adsorbed hydrogen in the Volmer- Heyrovsky step is facilitated. Thus, ABS outperforms the other components. The dynamic stability study reveals little deterioration of the best electrode made by $AgBi_3S_5$, even after 500 cycles in the AD study. Thus, the electrode based on $AgBi_3S_5$ can be used as a superior catalyst for HER in an acidic medium for the fabrication of green hydrogen fuel on a large scale. The study also provides a promising strategy to develop excellent stable Pt-group-metal-free multinuclear nano-catalysts. The study will also initiate the use of more ternary sulfide nanoparticles as catalysts in various energy studies in the near future.

In chapter 3, the as synthesized photocatalyst $AgBi_3S_5$-Bi_2S_3 nano composite was characterized by Rietveld analysis of XRD data along with FTIR and XPS studies. The morphological study like FESEM, TEM, EDS also support the characteristic data analysis and formation of nano composite and their elemental constitution. The performance of this nano composite in the hydrogen production reaction is convincible due to its catalytic ability revealed first time in absence of light as well as in presence of light where all the major determinates factors well synchronized and outperformed in presence of light compare to that in absence of light. The catalytic efficacy along with the robustness and longtime durability are also proved by the result outcome from the studied parameters like overpotential, Tafel slope, electron charge transfer kinetics, double layer capacitance, electrochemical surface area and chronoamperometric analysis, etc.

In chapter 4, the Cu_9S_5 nanomaterial was synthesized following designing of a new reaction scheme, within a short time in an environment friendly atmosphere and the used material was economically viable. The synthesized nanomaterial was characterized by XRD, FTIR, FESEM, EDS, TEM like techniques and the outcome confirmed so the successful formation of the synthesized nanomaterial. We used Cu_9S_5 as an alternate catalyst of highly expensive noble metal

like Pt, Pd in the valuable application of fuel oxidation for the first time and the electrochemical and photochemical results open a new door in the field of energy research though still a few limitations are still there for its improvement. Electrochemical experiment like cyclic voltammetry, chronoamperometry, photocurrent response measurement, electrochemical impedance spectral studies reveal that graphite carbon supported synthesized Cu_9S_5 performs better in presence of light compare to absence of light in anodic oxidation of 1 M CH_3OH in 1 M KOH. Moreover, it's better than 10 wt.% commercial platinum. The stability of the synthesized material is measured through continuously repeating cyclic voltammetry cycles at 50 mV/sec vs. SCE. The current density initially increases and remain constant around 70 cycles and after that little fall in current density is observed. But the result seems to be impressive in absence of any noble metal in the catalyst system current per surface area was impressive. This result is thus attractive to the researcher for providing a new in sight to improve the catalyst design of alkaline fuel oxidation reaction. The HPLC measurement identified the products in alkaline methanol oxidation in presence of light. The probable mechanism is also proposed on the basis of the product formation in this photo-assisted oxidation process.

In chapter 5, nano spheres of monoclinic $AgBi_3S_5$, nanorods of orthorhombic Bi_2S_3 and their nanocomposite were separately synthesized in glycolic medium by hot chemical process at 90 °C. Diffraction, spectrophotometric and microscopic studies reveal that the synthesized particles have average dimensions below 10 nm. All the synthesized catalysts exhibit significant photocatalytic degradation of pollutant dye Rh-B at pH 3 where optimum adsorption of dye is expected to occur. Among the catalysts, the nanocomposite of $AgBi_3S_5$-Bi_2S_3 display excellent and synergistic catalytic activity. With it the degradation of Rh-B is almost (99.99%) completed on exposure to natural sunlight within 25 minutes at pH 3 using 0.7 g L^{-1} of the catalyst in the dye solution (10 ppm). The degradation efficiency is somewhat better or comparable among the S based catalysts found in the literature. The superiority of the catalyst might be due to judicious synthesis of two n-type semiconductors whose valence and conduction band potentials are above zero in the standard hydrogen scale and suitable for charge separation through z-scheme and S-S transition, which help charge separation and generation of photo-catalytically active radicals: $^{\bullet}O_2^-$ and $^{\bullet}OH$, responsible for degradation. The retention of 95% catalytic activity after 5th cycle of operation, might be due to modification of the morphology with an increase of porosity and surface area of

the catalyst. The identified products reveal simultaneous de-ethylation and ring-opening reactions. The study may open new strategy for getting very highly efficient mixed catalyst.

6.2 Scope and Future Prospect

Earth-abundant, transition metal-based multinuclear and mixed sulfides, in the nanoscale range have emerged as potential electrocatalysts which are also economically feasible and better alternatives to precious metal-based catalysts for the application of electrochemical water splitting reactions. Mixed ion metal sulfide shows excellent characteristics of enhancing performance compared to mono metal sulfides in terms of higher electronic conductivity, higher specific capacitance, higher surface area, and inherent higher redox properties. The characteristics improvement of performance along with synergistic effect in metal ion metal sulfide emerged as a promising electrode material in the field of water splitting like application and their dynamic feature unveils the wings in the field of bifunctional electrocatalyst. Catalytic activity plays a pivotal role in bringing the best result out of water splitting. It depends on the variety of composition and structure of the catalyst and their adjustability features. Water splitting performance is greatly enhanced by varying stoichiometric adjustability of these materials. Electrocatalytic improvement in hydrogen evolution reaction is affected by some of the exposed S atoms and vacancies created because of that atom on the edges of the transition metal sulfide-based catalyst. As a consequence, S vacancies help to introduce new active sites on the inert basal plane of 2H-metal sulfide where the gap near the fermi level permits hydrogen binding directly with exposed metal sites. Another important role of the S atom in the case of the hydrogen evolution reaction is the formation of a place for hydrogen adhesion and separation when the metal atom is in the place of the effective site of the plane and the S atom can participate indirectly. Mononuclear and binuclear metal sulfides also be used as anode catalyst in fuel oxidation in presence and absence of visible light. It may have tremendous applications in future.

In addition to Ag, Bi, and S elements, other cost-effective earth-abundant elements like Ni, Mn, Fe, etc. can be used in our synthesized materials and the plenty of composition made from these elements. These will have versatile applications towards photocatalysis, solar cells, photovoltaic devices, photodynamic capabilities, efficiency in high optothermal conversion, synergistic imaging, photothermal driven anticancer treatment, applicable as an antibacterial agent, demonstrated in the treatment of multi-model malignant tumor.

LIST OF PUBLICATIONS

LIST OF PUBLICATION

Publications

Journal article

1. Designing $AgBi_3S_5$ Nanoparticle as an Efficient Electrocatalysts for Hydrogen Evolution Reaction, **Anupam Chowdhury**, Aditi De, Subrata Kundu and Swapan Kumar Bhattacharya, *Sustainable Energy & Fuels*, (2024), 8, 2941-2953.
2. Unfolding photocatalytic efficiency of newly one pot synthesized n-n $AgBi_3S_5$-Bi_2S_3 photocatalyst for removal of Rhodamine-B from aqueous system under natural light illumination, **Anupam Chowdhury**, Nandogopal Hudait, Kamal Kanti Bera, Ambikesh Mahapatra, Swapan Kumar Bhattacharya, ACS Sustainable Resource Management, (2024) https://doi.org/10.1021/acssusresmgt.4c00171
3. Pd Nanoparticle-Decorated Novel Ternary Bi2O2CO3-Bi2MoO6-CuO Heterojunction for Enhanced Photo-electrocatalytic Ethanol Oxidation Kamal Kanti Bera, **Anupam Chowdhury,** Symal Kanti Bera, Mahima Ranjan Das, Apurba Ray, Sachindranath Das & Swapan Kumar Bhatacharya, (2023). *ACS omega*, *8*(31), 28419-28435.
4. Synergistic photo-enhanced electrocatalysis of Pt–ZnO–Bi 2 O 3 heterojunction for methanol oxidation under visible light illumination. Kamal Kanti Bera, Malay Chakraborty, Symal Kanti Bera, **Anupam Chowdhury,** Mahima Ranjan Das, Mousumi Mondal & Swapan Kumar Bhatacharya, (2022). *Energy Advances*, *1*(11), 908-925.
5. Environment friendly $AgBi_3S_5$-Bi_2S_3 nano composite for efficient visible light driven photochemical H_2 evolution reaction. Anupam chowdhury et al……to be communicated soon.
6. Unveiling novel metal free electrochemical and photochemical anodic oxidation of methanol by newly synthesized Cu_9S_5. Anupam chowdhury et al……to be communicated soon.

PRESENTED ORAL AND POSTER IN CONFERENCES

Presented in International Seminar

1. Oral presented entitled “Electrochemical oxidation of urea on synthesized copper sulfide nano-particles supported by graphite carbon electrode” in International Seminar on Recent Advances in Chemistry and Material Science (RACMS-2022), Young Scientist Conclave (YSC-2022) & Research Scholar Competition (RSC-2022), organized by the Indian Chemical Society in association with the Bangladesh Chemical Society, Bangladesh and Department of Chemistry, Jadavpur University, Kolkata during July 30-31 & August 02-03,2022.
2. Oral presented entitled “Exploring new characteristic feature of $AgBi_3S_5$ towards hydrogen evolution reaction” in 4^{th} International Conference on Emerging smart materials in applied Chemistry (ESMAC-2023) & Interdisciplinary Science for Sustainability as a part of the diamond jubilee celebration of Indian Photobiology Society at Kalinga Institute of Industrial Technology (KIIT) Deemed to be University and CSIR-IMMT, Bhubaneswar, Odisha, India on 18^{th} -20^{th} November, 2023.
3. Poster presented entitled “Natural-light driven $AgBi_3S_5$-Bi_2S_3 S-scheme photocatalyst for organic pollutants removal from waste water” in International Symposium on Modern Perspectives of Chemistry in Biology, held by the department of chemistry, St. Xavier’s College (Autonomous), Kolkata on January 6, 2024